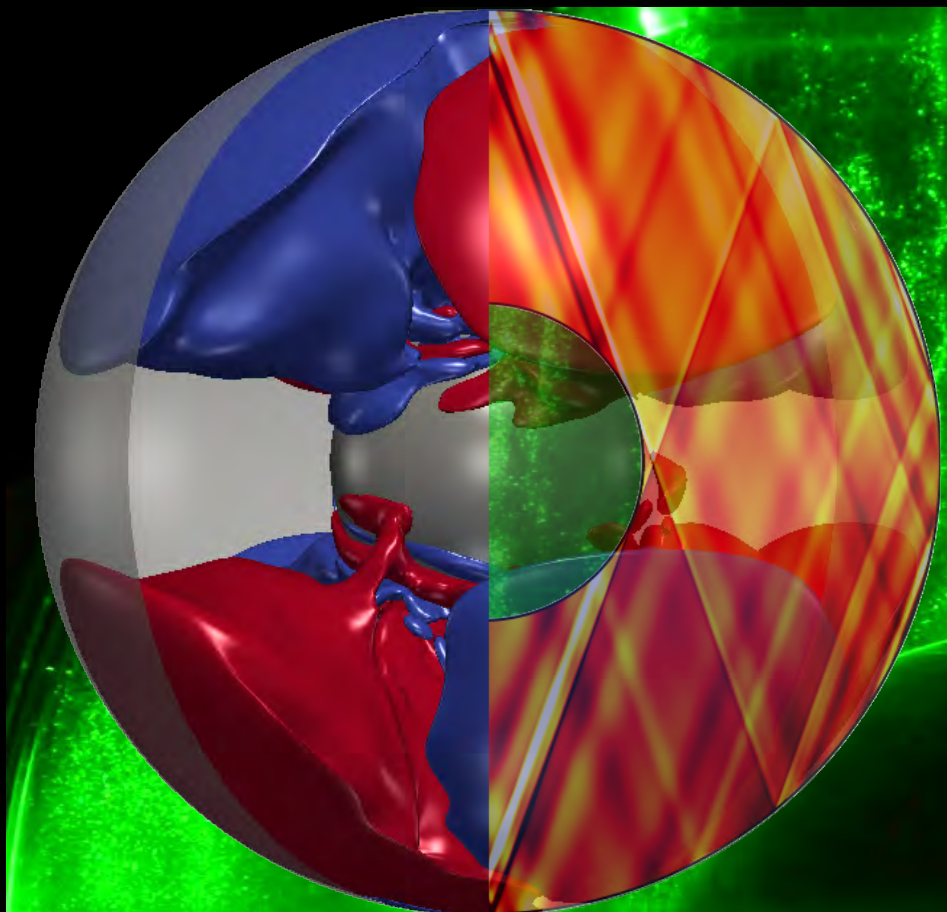


Inertial modes, turbulence and magnetic effects in a differentially rotating spherical shell



Ankit Barik

International Max Planck Research School
for Solar System Science
at the University of Göttingen

Inertial modes, turbulence and magnetic effects in a differentially rotating spherical shell

Dissertation

zur Erlangung des mathematisch-naturwissenschaftlichen Doktorgrades

“Doctor rerum naturalium”

der Georg-August-Universität Göttingen

im Promotionsprogramm PROPHYS

der Georg-August University School of Science (GAUSS)

vorgelegt von

Ankit Barik

aus Midnapore, Indien

Göttingen, 2017

Betreuungsausschuss

Dr. Johannes Wicht

Max-Planck-Institut für Sonnensystemforschung, Göttingen

Prof. Dr. Ulrich R. Christensen

Max-Planck-Institut für Sonnensystemforschung, Göttingen

Prof. Dr. Andreas Tilgner

Georg-August-Universität Göttingen

Mitglieder der Prüfungskommission

Referent: Prof. Dr. Ulrich R. Christensen

Max-Planck-Institut für Sonnensystemforschung, Göttingen

Korreferent: Prof. Dr. Andreas Tilgner

Georg-August-Universität Göttingen

Weitere Mitglieder der Prüfungskommission:

Prof. Dr. Laurent Gizon

Max-Planck-Institut für Sonnensystemforschung, Göttingen

Prof. Dr. Stefan Dreizler

Georg-August-Universität Göttingen

PD Dr. Olga Shishkina

Max-Planck-Institut für Dynamik und Selbstorganisation

Prof. Dr. Stan Lai

Georg-August-Universität Göttingen

Tag der mündlichen Prüfung: 08.05.2017

Bibliografische Information der Deutschen Nationalbibliothek

Die Deutsche Nationalbibliothek verzeichnet diese Publikation in der Deutschen Nationalbibliografie; detaillierte bibliografische Daten sind im Internet über <http://dnb.d-nb.de> abrufbar.

ISBN 978-3-944072-58-6

uni-edition GmbH 2017

<http://www.uni-edition.de>

© Ankit Barik



This work is distributed under a
Creative Commons Attribution 3.0 License

Printed in Germany

“The aim of the theorist is to know the train of wheels which the lever sets in motion - that binding of the parts which is the soul of the engine.”

- [Eddington](#) (1920)

This work is dedicated to my families (both Indian and German), my teachers, my friends, my love Anindita and my grandfather Bhima Charan Basu.

Contents

Summary	11
1 Introduction	13
1.1 Rotating spherical shells	13
1.2 Dynamo theory and interior modelling	15
1.3 Hydrodynamic and MHD experiments	17
1.4 The spherical Couette system	21
1.5 Outline of this work	23
2 Theory of inertial modes	25
2.1 Basics of fluid dynamics	25
2.1.1 Conservation equations	25
2.1.2 Rotating frame of reference	27
2.1.3 Non-dimensionalisation	28
2.2 Inertial Waves	29
2.2.1 Inertial oscillations of a fluid particle	29
2.2.2 Plane inertial waves	30
2.3 Inertial modes	33
2.3.1 The geostrophic mode	35
2.3.2 Inertial modes	36
2.4 Internal shear layers	37
2.5 Inertial modes in a sphere	38
2.6 Inertial modes in a spherical shell	42
2.7 Sustaining inertial modes: triadic resonances	45
2.8 Discussion	50
3 The spherical Couette system	51
3.1 Introduction	51
3.2 Proudman solution and Stewartson Layers	51
3.3 Stewartson layer instabilities	54
3.4 Overview of parameter regimes	55
3.4.1 Very low outer boundary rotation: $\Omega \leq 1$ or $E \geq 1$	57
3.4.2 Intermediate outer boundary rotation rate: $1 < \Omega < 10^3$ or $10^{-3} < E < 1$	58
3.4.3 High outer boundary rotation: $10^3 < \Omega < 3 \times 10^5$ or $3 \times 10^{-6} < E < 10^{-3}$	59

3.4.4	Very high outer boundary rotation: $\Omega > 3 \times 10^5$ or $E < 3 \times 10^{-6}$	60
3.5	Discussion	61
4	Numerical methods and diagnostics	65
4.1	Numerical methods	65
4.1.1	Non-dimensionalisation	65
4.1.2	Poloidal/Toroidal decomposition	67
4.1.3	Non-linear terms and time-stepping	69
4.1.4	The code	70
4.2	Identifying inertial modes	71
4.2.1	Using spherical harmonics	71
4.2.2	Using spectrograms	72
4.2.3	Structures of solutions	73
4.3	Discussion	75
5	Radial jet and torque scalings	77
5.1	Outer sphere stationary	77
5.2	Torque bistability	82
5.3	Summary and discussion	86
6	Triadic resonances in the wide-gap spherical Couette system	89
6.1	Introduction	89
6.2	Fast and Slow modes	90
6.3	Experimental methods	90
6.4	Results from experiments	91
6.5	Numerical methods	93
6.6	Results from simulations	93
6.6.1	Ekman number, $E \sim 10^{-4}$	93
6.6.2	Ekman number, $E = 10^{-5}$	103
6.7	Effect of background flow on inertial modes	108
6.8	Triadic interactions	112
6.8.1	Theoretical background	112
6.8.2	Triadic resonances in the inertial mode regime	114
6.9	Onset of inertial modes	117
6.10	Conclusion	118
7	The turbulent regime	121
7.1	Introduction	121
7.2	Theoretical background	121
7.3	Turbulent regime of spherical Couette flow	124
7.3.1	Temporal spectrum	124
7.3.2	Spatial spectra	127
7.3.3	Flow and Torque	129
7.3.4	A new mode	133
7.4	Critical Balance - criteria for transition?	133
7.5	Triadic resonances in the turbulent regime	134

7.6	Conclusion	135
8	MHD Theory	139
8.1	Pre-Maxwell and induction equations	139
8.2	The Lorentz force	141
8.3	Waves due to the Lorentz force	142
	8.3.1 Alfvén waves	142
	8.3.2 Magneto-Coriolis waves	144
	8.3.3 Lorentz force and differential rotation: Ferraro's law of isorotation	145
8.4	Magneto-Coriolis modes	146
8.5	Discussion	148
9	Magnetic Couette flow	149
9.1	Introduction	149
9.2	Non-dimensional parameters	151
9.3	Magnetic field as a diagnostic	151
9.4	Magneto-Coriolis modes	154
9.5	Flow and torque	159
9.6	Discussion	161
10	Conclusions and Outlook	163
	Bibliography	169
	Sources of figures	189
A	Orthogonality and eigenvalues of Inertial modes	193
	A.1 ω real and $ \omega \leq 2$	193
	A.2 Orthogonality	194
B	List of dimensionless numbers	195
	Publications	197
	Acknowledgements	199
	Curriculum vitae	201

Summary

Compact astrophysical objects like planets, moons and stars can be thought of as rotating spherical shells with a fluid filled in between. Magnetic field generation in these objects is thought to take place through a dynamo process driven by convection, though alternative mechanisms such as precession (Malkus 1968, Tilgner 2005) and differential rotation (Spruit 1999, 2002) have also been proposed. Convective dynamo models for planets (e.g. Glatzmaier and Roberts 1995, Gastine et al. 2014) and stars (Charbonneau and Steiner 2012) have become increasingly complex and make it difficult to attribute a certain observation to a physical process. A major component of the internal dynamics of these astrophysical objects is differential rotation. To avoid the complexities of “realistic” interior models, we numerically study a simplified system consisting of two concentric differentially rotating spherical boundaries with a fluid filled in between. This is the spherical analogue of the more famous cylindrical Taylor-Couette setup and is known as the spherical Couette setup. This allows us to focus on a single effect on the fluid dynamics of the interiors of astrophysical objects. In addition, simulations of this setup allows us to complement hydrodynamic (HD) and magnetohydrodynamic (MHD) experiments that use the same setup but have limited diagnostics. This setup is extremely interesting from the point of view of theoretical fluid mechanics and MHD as well, hosting a rich variety of fluid instabilities and HD and MHD phenomena such as free shear layers, rotational turbulence, waves in rotating fluids, magnetic shear layers, magneto-Coriolis modes and so on. Lastly, this setup also allows us to study the interaction of differential rotation with magnetic fields, varying each of them independently - something not possible in self-consistent dynamo simulations of planetary and stellar interiors.

In this study we explore several aspects of this system using numerical simulations. A large part of the work consists of direct comparisons of results from simulations and experiments, in particular those of Triana (2011) and Hoff et al. (2016b). We start by exploring the case with the outer boundary stationary and rotating the inner boundary. The thickness of the fluid radial jet that emerges in the system is scaled with the inner boundary rotation rate and the power law obtained agrees well with past studies. The same holds true for the torque on the inner sphere.

We now run simulations with the outer boundary rapidly rotating, and with both senses of differential rotation. For a positive differential rotation (inner sphere rotating prograde and faster than outer), we attempt at reproducing the torque bistability observed in experiments of Zimmerman (2010) and are able to reproduce some of the observed features, but not the bistability itself.

For negative differential rotation (inner sphere rotating slower or in opposite direction as compared to outer), we perform a more extensive study in parameter regimes at two different outer boundary rotation rates in order to explain the onset of fast wave-like modes

in the system called inertial modes that are equatorially antisymmetric. We find three distinct hydrodynamic regimes as observed by [Hoff et al. \(2016b\)](#). The inertial modes and other flow features observed in the simulations match well with the experiments. Using numerical experiments we find clues that these modes might be instabilities of the axisymmetric background flow.

We increase the differential rotation magnitude further and observe a temporal broadband spectrum, as also observed by [Hoff et al. \(2016b\)](#). This was considered to be a transition to turbulence in the experiments. With our numerical insights, we are able to point out that it is indeed a transition from rotation dominated inertial wave turbulence to a homogeneous and isotropic turbulent regime, finding a criterion for the transition in the process.

Finally, we impose a weak axial magnetic field on the setup, use it as a diagnostic and find excellent agreements with the experimental inertial mode diagnostics of [Kelley et al. \(2007\)](#). We also find that as the field strength is increased, it increases the growth rate of the inertial modes, as well as affecting their frequencies and structures.

Our numerical studies show that the spherical Couette system offers a host of intriguing phenomena which can provide insights into experiments and help better understand effects of differential rotation in stellar and planetary interiors.

1 Introduction

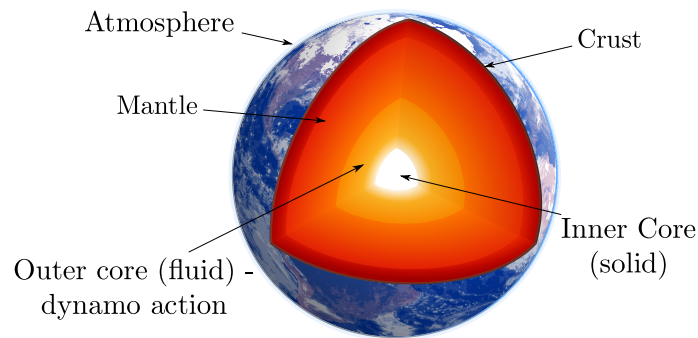
“The most beautiful thing we can experience is the mysterious. It is the source of all true art and science.”

Albert Einstein

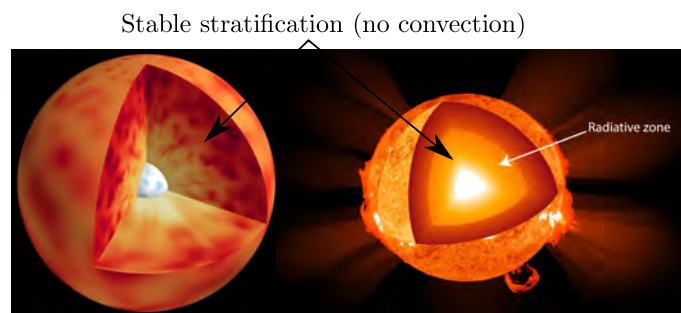
1.1 Rotating spherical shells

The structure of planets, moons, or stars is in the form of layered spherical shells. This renders rotating spherical shells as important models for the dynamics in their interiors. Breakthroughs in seismology ([Wiechert 1897](#), [Oldham 1906](#), [Gutenberg 1912](#), [Jeffreys 1926](#), [Lehmann 1936](#)) helped us to decipher the internal structure of the Earth, as shown in figure 1.1a. It consists of the crust, the mantle, and the outer and the inner core, out of which only the outer core is fluid. Planetary exploration has provided us insights into the structures of other planets in our solar system as well. Terrestrial planets such as Mercury, Venus and Mars are known to have a structure with a fluid outer core similar to that of the Earth (see [Spohn 2007](#)). The gas giants Jupiter and Saturn are thought to have a layer of liquid metallic hydrogen surrounded by a heavy element core at the bottom and a layer of hydrogen gas on top ([Stevenson 2008](#)). Even the Earth’s and the Galilean moons like Ganymede and Titan possess a layered spherical shell structure (see e.g. [Spohn 2007](#)).

The structure of stars is also in the form of spherical shells. Theories of stellar structure and evolution (e.g. [Kelvin 1862](#), [Lane 1870](#), [Emden 1907](#), [Eddington 1920](#), [Biermann 1932](#), [Cowling 1934](#), [Chandrasekhar 1939](#), [Bethe 1939](#)) have shaped the present day ideas of structures of stars of different masses and how they evolve. Depending on their mass, stars in their main sequence can be fully convective or have stably stratified radiative zones either below or above a zone of convection. Certain stars such as red giants or massive stars also have a spherical shell structure with a large stably stratified radiative zone. For details one can refer to the classic book by [Kippenhahn and Weigert \(1990\)](#). Recent advancements in helioseismology (e.g. [Schou et al. 1998](#)) and asteroseismology ([Aerts et al. 2010](#)) along with missions like SOHO ([Domingo et al. 1995](#)) and KEPLER ([Borucki et al. 2003](#)) have allowed us to have much better constraints on the interiors of stars and their magnetic fields. In fact, we now know a lot about the structure of the Sun along with detailed measurements of its differential rotation ([Schou et al. 1998](#)).



(a) Structure of the Earth.



Red Giant Sun
(b) Different layers in a red giant and the Sun

Heat Transfer of Stars



(c) Structures of different types of stars in main sequence.

Figure 1.1: Ubiquity of spherical shell structures from Earth (and other planetary bodies) to stars of different masses.^a

^aFigure attributes: (a) and figure of Sun in (b) is by wikipedia user Kelvinsong (c) is by www.sun.org - <http://www.sun.org/encyclopedia/stars> - all three under CC BY-SA 3.0 <http://creativecommons.org/licenses/by-sa/3.0>, via Wikimedia Commons. Figure of red giant by Paul G. Beck, Leuven University, Belgium.

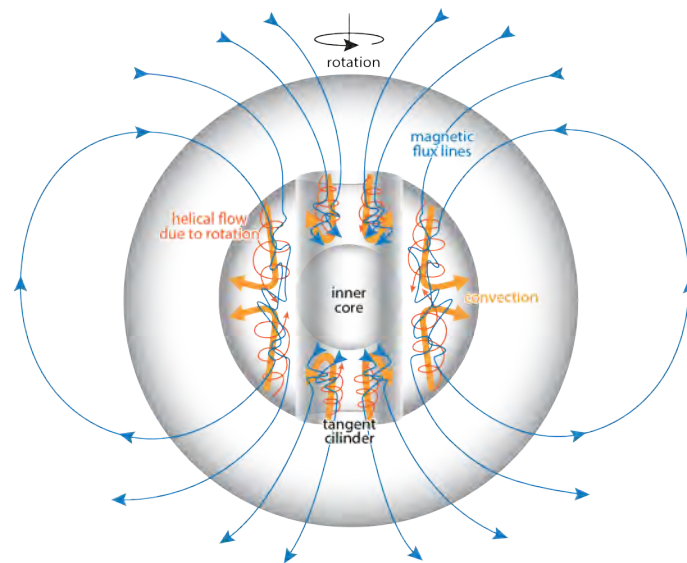


Figure 1.2: A typical convective dynamo model for the Earth, also applicable to other planets. Shown in orange are helical convective flows that twist magnetic field lines, shown in blue. Figure courtesy of Sabrina Sanchez.

1.2 Dynamo theory and interior modelling

Intimately tied to the structure of these compact astrophysical objects was the question of the origin of their magnetic fields. The origin of the magnetic field of the Earth was a mystery since the times of [Gilbert \(1600\)](#) and [Halley \(1683\)](#) who gave preliminary ideas in the form of permanent magnetism. The discovery of a fluid iron core provided one of the key hints towards the solution of this open question. This question became more intriguing when [Hale \(1908\)](#) discovered the magnetic nature of sunspots marking the discovery of the first extra-terrestrial magnetism. The mystery started to get resolved only when [Larmor \(1919\)](#) put forward his theory of a hydromagnetic dynamo to explain the magnetic fields of rotating bodies like the Earth and the Sun. This theory postulated that electric currents are generated in a conducting fluid when the fluid moves in the presence of an existing magnetic field. These induction currents, in turn, generate a magnetic field which amplifies the existing field.

In geophysics, undeterred by anti-dynamo theorems (e.g. [Cowling 1933, 1957](#)), this idea was taken up by pioneers like Walter Elsasser and E.C. Bullard who tried to materialise a quantitative theory of the geodynamo leading to seminal works such as [Elsasser \(1939, 1946, 1950\)](#), [Bullard \(1949\)](#), [Bullard et al. \(1950\)](#) and [Bullard and Gellman \(1954\)](#). These gave us much of the geodynamo theory in the form we use today. However, examples of self-sustaining dynamos even in a kinematic sense (with a prescribed flow field) were not found till the works of [Backus \(1958\)](#) and [Herzenberg \(1958\)](#).

Around a similar time, [Parker \(1955\)](#) and [Steenbeck et al. \(1966\)](#) came up with mean field models of dynamos which consisted of two mechanisms - generation of toroidal (non-radial) magnetic field from poloidal (non-azimuthal) field using shear generated due to azimuthal flows (called ‘ ω -effect’ after [Roberts 1972b](#)) and the interactions of small-scale velocity and magnetic fields giving rise to large-scale magnetic fields, called the

α -effect. This could give a whole assortment of dynamo mechanisms. Since conversion from toroidal to poloidal field was only possible through the α mechanism, one could have either an α or an ω -effect or both working alongside an α -effect to give rise to $\alpha\omega$, α^2 or $\alpha^2\omega$ dynamos.

Planetary dynamos

A typical model for the geodynamo is shown in figure 1.2. Convection inside the fluid outer core is influenced by rotation, resulting in helical fluid motion along columns. This in turn leads to the twisting of magnetic field lines, resulting in the aforementioned α -effect. Additional motions such as precession and tidal excitation can also give rise to helical flows. Possible processes generating an ω -effect through azimuthal flows could be thermal winds and differential rotation of the inner core. Simulations of the geodynamo using this model began with [Glatzmaier and Roberts \(1995\)](#) and [Kageyama and Sato \(1995\)](#) with further complexities added on later due to inclusion of compressibility and thermo-chemical convection ([Braginsky and Roberts 1995](#), [Glatzmaier and Roberts 1996](#)), variations in heat flux in the mantle ([Glatzmaier et al. 1999](#)), stable stratification at the top of the core ([Braginsky 1984, 1993](#), [Buffett and Seagle 2010](#), [Buffett 2014](#)) and differential inner core growth ([Monnereau et al. 2010](#), [Aubert et al. 2013](#)). However, there are tight power budget restrictions on convection inside the Earth ([Nimmo 2007](#)), especially in the light of new estimates for the thermal conductivity of liquid iron inside the Earth ([Pozzo et al. 2012](#), [Buffett 2012](#)). Alternative dynamo mechanisms beside convection have also been investigated, though to a limited extent. For example, [Malkus \(1968\)](#) proposed that precession driven flows could produce dynamo action, which was later verified numerically by [Tilgner \(2005\)](#) for large precession amplitudes. Differential rotation has been suggested as a possible dynamo mechanism for Saturn ([Cao et al. 2012](#)). Having achieved success on the geodynamo front, convective dynamos have also been applied for understanding magnetic fields in other planetary bodies like Mercury ([Christensen 2006](#), [Manglik et al. 2010](#)), Mars ([Milbury et al. 2012](#), [Dietrich and Wicht 2013](#)), Jupiter ([Stevenson 2008](#), [Gastine et al. 2014](#)) and Ganymede ([Christensen 2015](#)).

Stellar dynamos

Stellar dynamo models often rely on turbulent convection in spherical shells, taking into account fluid compressibility (see e.g. [Charbonneau and Steiner 2012](#)). However, [Spruit \(1999, 2002\)](#) showed that dynamos in stars can be driven just by using differential rotation in a stably stratified radiative zone. This is crucial for applications to massive stars and red giants. The analytical predictions of these works were verified through numerical box simulations by [Braithwaite \(2006\)](#). To explain the strong dipolar magnetic field of chemically peculiar A stars (called Ap stars), [Jouve et al. \(2015\)](#) also performed simulations with differentially rotating fluid-filled spherical shells to obtain instabilities which could provide a possible answer. Differential rotation has also been invoked in an attempt to explain the strong magnetic fields of magnetars ([Spruit 1999, 2008](#)). For a review on how differential rotation can drive a dynamo in non-convecting regions of stars, one can have a look at [Braithwaite and Spruit \(2015\)](#).

Differential rotation and angular momentum transport

One dimensional stellar evolution models usually parametrise angular momentum transport using diffusion and the interaction of differential rotation and magnetic fields (e.g. [Maeder and Meynet 2000](#), [Meynet and Maeder 2003](#), [Maeder and Meynet 2004](#), [2005](#), [Maeder 2008](#), [Maeder, A. et al. 2013](#)). These models require further development to explain stellar observations, especially for giants and clump stars ([Cantiello et al. 2014](#)). A recent focus has turned towards gravito-inertial waves or internal gravity waves (IGW), which are waves restored by gravity and the Coriolis force, to explain angular momentum transport in stars (e.g. [Talon and Charbonnel 2008](#), [Rogers et al. 2013](#), [Fuller et al. 2014](#)).

Angular momentum transport is also important in studies of accretion discs which are the first step towards formation of stellar and planetary systems. They can form through gravitational collapse of a cloud of gas and dust or through the accretion of matter in binaries from one companion to the other. Gravitational collapse of such a cloud impose Keplerian orbits onto its particles which are stable to the Rayleigh criterion ([Rayleigh 1917](#)). But the hydrodynamical models of the rate of angular momentum transport in such discs are not compatible with observations of fast accretion rates. This problem was solved by the introduction of the concept of the magnetorotational instability (MRI) by [Balbus and Hawley \(1998\)](#) who showed how a weak magnetic field can destabilise a Rayleigh stable flow and cause enhanced angular momentum transport.

Need to study differentially rotating fluid

From the discussions above, one can infer that a study of differentially rotating fluids in spherical shells and their interaction with magnetic fields has wide applications. The models used to study dynamics of planetary and stellar interiors are complex and hence make it difficult to attribute observations in numerical models to exact physical processes. In addition, the study of other physical processes involving differential rotation and magnetic fields (e.g. MRI) are crucial to understanding angular momentum transport in astrophysical objects. Such a study is further motivated by several hydrodynamic and MHD experiments which we briefly review below.

1.3 Hydrodynamic and MHD experiments

Need for experiments

Parameter regimes covered by numerical simulations are far away from those of astrophysical objects, especially in terms of diffusivities. Important parameters that depend on diffusivities are the Ekman number E which is a measure of relative importance of viscous to Coriolis forces and the magnetic Prandtl number Pm which is a measure of the fluid conductivity. As an example, in the Earth $E \approx 10^{-15}$ and $Pm \approx 10^{-6}$. Typical numerical geodynamo simulations are usually run at around $E \approx 10^{-5}$ and $Pm \approx 0.1$. Recent developments in computational power and better numerical codes have pushed the bound to $E = 10^{-7}$ and ([Schaeffer et al. 2017](#)) and even $E = 10^{-8}$ using artificial ‘hyperviscosity’ ([Aubert et al. 2017](#)). But such simulations are extremely computationally expensive and they are still several orders of magnitude away from realistic parameters. This means that

the small scales of fluid motion are not resolved correctly in simulations. In the absence of a proper theory of turbulence, one has to resort to experiments which can run in regimes where simulations fail.

Hydrodynamic experiments of rotating fluids

A large number of hydrodynamic laboratory experiments have been performed to understand the dynamics of rotating fluids as well as to explore mechanisms other than convection that could give rise to dynamos. These include experiments in precessing spheroids by [Malkus \(1968\)](#), [Vanyo \(1984\)](#) and [Vanyo et al. \(1995\)](#), who observed cylindrical differential rotation and columnar vortices, and by [Triana et al. \(2012\)](#) in a spherical shell who clearly identified the ‘spin-over’ mode which consists of a solid body rotation of the fluid about an axis different to that of the container and is a solution to the equation of motion in the presence of precession derived by [Poincaré \(1910\)](#). Other experiments studied elliptical instabilities (e.g. [Aldridge et al. 1997](#), [Lacaze et al. 2004](#), [Le Bars et al. 2010](#)) and zonal flows driven by tidal forcing (e.g. [Morize et al. 2010](#)) and libration (e.g. [Sauret et al. 2010](#)).

There have been a number of experiments in rotating spherical shells as well. These will be reviewed in section 1.4.

Dynamo flows and past experiments

Since the dawn of dynamo theory, several flows have been proposed that could generate and maintain a magnetic field against ohmic decay. Examples of such flows are given by [Ponomarenko \(1973\)](#), [Roberts \(1972a\)](#) in 1D and 2D Cartesian geometry, [Roberts \(1971\)](#) and [Dudley and James \(1989\)](#) in 2D spherical geometry, by [Lortz \(1968\)](#) in 3D cylindrical, the Arnold-Beltrami-Childress (ABC) flow in 3D Cartesian, and [Kumar and Roberts \(1975\)](#) in 3D spherical geometry. A more detailed list of such flows and a detailed introduction to dynamo theory in general can be found in [Roberts \(2007\)](#) and [Jones \(2008\)](#).

Three types of flows have been used to design successful experiments capable of maintaining dynamo action and sustaining a magnetic field. One was at Riga, Latvia ([Gailitis et al. 2000](#)) using the Ponomarenko flow, another at Karlsruhe, Germany ([Stieglitz and Müller 2001](#)) using the G. O. Roberts flow. A third experiment, at Cadarache in France, was based on the ‘von Kármán’ flow - the flow between two rotating discs ([Zandbergen and Dijkstra 1987](#)). The experiment, called the ‘von Kármán sodium’ or VKS experiment ([Bourgoin et al. 2002](#)) was also successful in generating and maintaining a magnetic field, but only with ferromagnetic propellers. Schematics of all three experiments are shown in figure 1.3.

Spherical shell MHD experiments

The experiments mentioned above, though all breakthroughs in themselves, were not very physical when it came to applications to real astrophysical objects. They were, at best, idealised forced representations of convective columns inside a rotating body of fluid with a very unrealistic geometry.

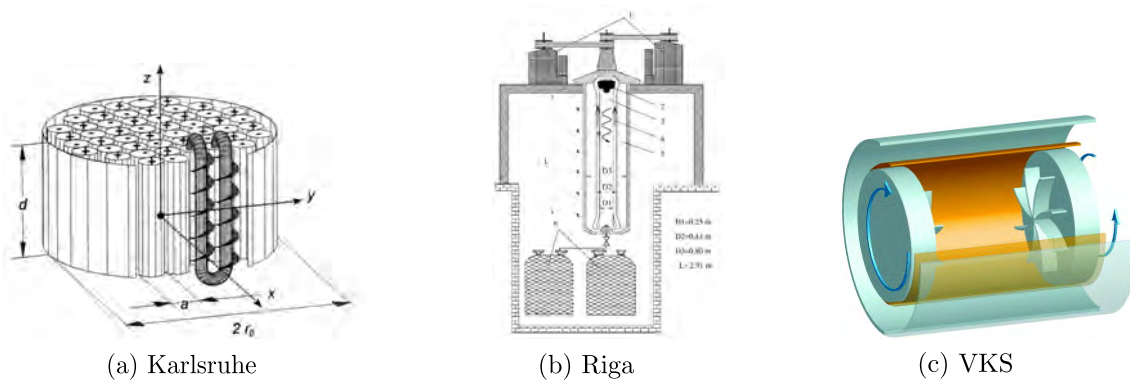


Figure 1.3: Schematics of three dynamo experiments - (a) one at Karlsruhe, Germany^a (b) one at Riga, Latvia^b and (c) the VKS experiment in Cadarache, France^c. All three were successful in producing and maintaining a magnetic field against ohmic decay through dynamo action.

^aTaken from Stieglitz and Müller (2001), with the permission of AIP Publishing, DOI: <http://dx.doi.org/10.1063/1.1331315>

^bReprinted figure with permission from Gailitis et al. (2000), copyright (2000) by the American Physical Society, DOI: <https://doi.org/10.1103/PhysRevLett.84.4365> and with permission from Frank Stefani

^cTaken from Boisson and Dubrulle (2011)



3 m, Maryland, USA



DTS, Grenoble, France



MPDX, Madison, USA

Figure 1.4: New spherical MHD experiments. The 3-metre spherical shell experiment in Maryland contains liquid sodium and is used to study MHD turbulence, the DTS experiment in Grenoble France has a permanently magnetised inner sphere to study motions of a conducting fluid in a dipolar magnetic field. The Madison Plasma Dynamo eXperiment (MPDX) is built to be able to reach parameters not achievable by liquid metal experiments. Sources of images: 3m : <http://complex.umd.edu/news.html>, DTS: Henri-Claude Nataf (director of the DTS group), MPDX: <http://plasma.physics.wisc.edu/mpdx>.

Experiments at Maryland, USA The group of Daniel Lathrop in Maryland, USA has built spherical shell experiments with sizes of 30 cm, 60 cm and 3 m with the space in the shell filled with liquid sodium, air or water. The results from these experiments have been the topic of six PhD theses (Sisan 2004, Kelley 2009, Zimmerman 2010, Triana 2011,

[Adams 2016](#), [Mautino 2016](#)). Magnetic instabilities with features similar to the MRI were observed in the 30 cm experiment, inertial modes (wave-like modes restored by Coriolis force, incompressible analogues of internal gravity waves (IGW) mentioned earlier) were observed in the 60 cm experiment, while extensive studies on turbulence, inertial modes and precession were performed with the 3m water experiments. Two of the most puzzling observations from the study were the excitation of inertial modes by differential rotation, which are otherwise known to be excited by external oscillatory mechanisms like precession, libration and tidal excitation ([Kelley et al. 2007](#), [Rieutord et al. 2012](#)), and a bistability in torque measurements in the turbulent state ([Zimmerman et al. 2011](#)).

DTS Experiment, Grenoble, France The group of Henri-Claude Nataf at Grenoble France, built a 21 cm setup where the inner sphere of 7.4 cm contains bricks of rare-earth Cobalt magnets to make it a permanently magnetised dipole. The experiment was called “Derviche Tourneur Sodium” (DTS, [Nataf and Gagnière 2008](#)). Several studies on the interaction of differential rotation with a dipolar magnetic field have been performed using this setup. The large scale steady state was measured and characterised by [Brito et al. \(2011\)](#) while [Figueroa et al. \(2013\)](#) performed numerical simulations of the same. The results show that the fluid rotations tend to be aligned with the field lines where the field is strong. Magnetic instabilities, more specifically magneto-Coriolis modes, were observed in this experiment. The identifications of these instabilities were verified by numerical simulations ([Schmitt et al. 2008](#), [Schmitt et al. 2013](#)).

MPDX, Madison, USA The Madison plasma dynamo experiment (MPDX), built by the group of Cary Forest, is a spherical experiment consisting of two 3 m hemispheres confining a hot weakly magnetised plasma using magnets. This experiment will reach parameters unattainable in liquid sodium experiments and give us further insights into astrophysical dynamos as well as other MHD processes like the MRI. Preliminary results from this experiment consist of a successful containment of the plasma and successful in-situ measurements of the plasma flow ([Cooper et al. 2014](#)).

Images of these experiments are provided in figure 1.4. More details and further reviews of the above experiments and more can be found in [Gailitis et al. \(2002\)](#), [Cardin and Olson \(2007\)](#), [Lathrop and Forest \(2011\)](#) and [Olson \(2013\)](#).

Need to numerically study a fluid-filled spherical shell

The hydrodynamic and MHD experiments outlined above are extremely useful in studying turbulent flows. However, their diagnostics are limited, for example, by the availability of and space for the number of sensors that can be used. This is especially true for MHD experiments with liquid sodium or plasmas where the whole volume of the working fluid cannot be seen directly. There is also a large degree of uncertainty associated with experiments. For example, physical properties of working fluids change with temperatures and keeping precise and constant rotation rates in a sphere is difficult. This motivates us to simulate a fluid-filled rotating spherical shell, to complement and provide further insight into the limited laboratory data. Numerical simulations are economically cheaper to run, have much better control on parameters and have access to the full solution at every grid point. This makes them ideal for detailed analyses. The diffusivities

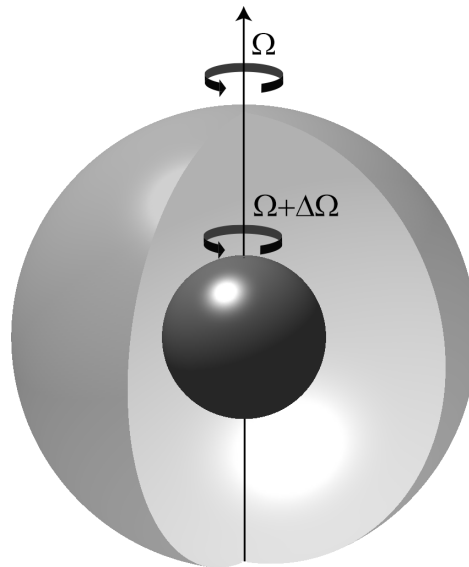


Figure 1.5: The spherical Couette system. The two concentric spheres rotate differentially and drive the fluid filled in the space in between. The outer sphere rotates with a rate Ω , while the inner sphere rotates with a rate $\Omega + \Delta\Omega$.

in numerical simulations are often much larger compared to experiments and are always several orders of magnitude away from values of real astrophysical objects. However, one can reach similar hydrodynamic regimes and often reproduce essential features of the flow observed in experiments (e.g. [Wicht 2014](#)) as well as large-scale features observed in astrophysical objects (e.g. [Christensen and Wicht 2007](#)).

1.4 The spherical Couette system

From the discussions in sections [1.1](#), [1.2](#) and [1.3](#), it is clear that simulations of fluid-filled differentially rotating spherical shells are imperative. Our objectives in this regard are twofold:

1. Study a simple model of stellar and planetary interiors to understand the effect of differential rotation and its interaction with magnetic fields
2. Compare with experimental results and help to gain insight into experimental observations through numerical simulations.

To achieve these objectives, we study the spherical Couette system which consists of two concentric differentially rotating spheres with a fluid filling the space inside, as shown in figure [1.5](#). This setup resembles interiors of astrophysical objects as well as experimental setups used for several hydrodynamic as well as the new generation of MHD experiments. Besides the above two motivations, the spherical Couette system also provides a unique opportunity to study classic fluid dynamical phenomena such as free shear layers, waves in rotating fluids as well as rotational turbulence.

Brief review

The spherical Couette setup has been a classic system of study in fluid mechanics. Its theoretical study goes back to Proudman (1956) who studied a small perturbation to solid body rotation when the outer sphere is rotating rapidly. He postulated the presence of a shear layer on the tangent cylinder circumscribing the inner sphere, which later became known as the Stewartson layer owing to the work of Stewartson (1966) who formulated its structure. Bratukhin (1961) determined the critical Reynolds number needed for the first non-axisymmetric instability for a stationary outer sphere and also formulated the solution of this instability. Numerical studies go back to Pearson (1967) and Munson and Joseph (1971a) who studied the axisymmetric flow in the system. Munson and Joseph (1971b) studied the hydrodynamic stability of the flow using energy theory, as a numerical eigenvalue problem. Munson and Menguturk (1975) presented results from linear analyses and experiments and explored the effect of radius ratio and flow Reynolds number.

Hollerbach (2003) performed direct numerical simulations (DNS) of a wide-gap spherical Couette flow and found that the azimuthal wavenumbers of the first non-axisymmetric instabilities are different depending on whether the inner sphere rotated faster or slower as compared to the outer, similar to experimental results in cylinders (Hide and Titman 1967). Hollerbach et al. (2004) performed DNS of this setup with radius ratio $r_i/r_o = 2/3$ and found that the wavenumber of the most unstable mode at onset of instability increases with outer boundary rotation, while in the supercritical regime mode transitions occur whereby the wavenumber of the instability decreases. Excellent agreements with experiments were also found in this study. Hollerbach et al. (2006) numerically studied instabilities of the system with outer boundary stationary for different radius ratios. They found that the basic state always consisted of a radial jet, but the instabilities depended on the radius ratio. Wicht (2014) studied this setup with a radius ratio of $r_i/r_o = 0.35$ with a much wider parameter range than in earlier studies. He recovered the instabilities that had been observed in previous wide-gap studies while finding new ones.

Experimental studies of this system go back to Sorokin et al. (1966) who tried to verify the criteria of Bratukhin (1961) for a critical Reynolds number for instability when the outer sphere is stationary, failing to find an agreement. The study of Munson and Menguturk (1975) has already been mentioned. Egbers and Rath (1995) studied instabilities of the system and their dependence on radius ratio when the outer sphere is stationary, finding that narrower gaps yield higher azimuthal wavenumbers of instability. Kelley et al. (2007) and Kelley et al. (2010) and Triana (2011) and more recently Hoff et al. (2016b) found inertial modes excited by differential rotation. Zimmerman et al. (2011) found a torque bistability in a turbulent flow under very rapid rotation.

Inertial modes

Inertial modes are wave-like modes of a rotating fluid restored by the Coriolis force. They have been claimed to be detected in the Earth's outer core (Aldridge and Lumb 1987). These modes have also been seen as gravito-inertial modes in a rapidly-rotating B3 star (Pápics et al. 2012) and in a hot Be star (Neiner et al. 2012) where the Coriolis force plays a major role in the force balance. They are strongly influenced by the background rotation and can in turn influence it - being capable of inducing strong zonal jets (Tilgner 2007b) and transporting angular momentum. The recent importance being

given to gravito-inertial modes in stars for angular momentum transport has already been discussed.

[Rieutord \(1991\)](#) studied the linear eigenvalue problem of inertial modes in a spherical shell in the presence of dissipation using an expansion in spherical harmonics. He found good agreement with experimental data and was even able to identify some of the modes identified in the Earth's core. [Rieutord and Valdetaro \(1997\)](#), [Tilgner \(1999a\)](#) and [Rieutord et al. \(2001\)](#) studied internal shears layers, ray geometries, wave attractors and the asymptotic spectrum of these modes. [Rieutord et al. \(2012\)](#) used the eigenvalue formulation of inertial modes to compare with data from the 3-metre experiment. [Baruteau and Rieutord \(2013\)](#) studied the effect of differential rotation on inertial modes in a spherical shell under a linear approximation.

These modes are thought to be excited due to precession, libration or tidal excitation in astrophysical objects ([Le Bars et al. 2015](#)). However, in the spherical Couette setup they have been seen to be excited in the absence of any of these mechanisms, but simply in the presence of differential rotation, both in experiments ([Kelley et al. 2007, 2010](#), [Triana 2011](#), [Hoff et al. 2016b](#)) as well as in simulations ([Matsui et al. 2011](#), [Wicht 2014](#)). Their onset is still an open question ([Rieutord et al. 2012](#), [Wicht 2014](#)).

Magnetic spherical Couette flow

Imposing an external magnetic field allows one to vary differential rotation and magnetic fields independently which is not possible in self-consistent dynamo simulations. This gives rise to new kinds of instabilities, depending on the imposed magnetic field geometry and strength as well as the magnetic boundary conditions. Examples of studies of magnetic effects in spherical Couette flow are numerical studies by [Hollerbach \(1994, 1997\)](#), [Dormy et al. \(1998\)](#), [Hollerbach \(2000\)](#), [Hollerbach and Skinner \(2001\)](#), [Schmitt et al. \(2008\)](#), [Schmitt et al. \(2013\)](#), [Hollerbach \(2009\)](#), [Gissinger et al. \(2011\)](#) and analytical studies by [Kleeorin et al. \(1997\)](#), [Starchenko \(1997\)](#), [Soward and Dormy \(2010\)](#).

A brief review of these works are provided in chapter 9. A detailed review can be found in [Rüdiger et al. \(2013\)](#).

1.5 Outline of this work

The preceding discussions showed us why a numerical study of rotating spherical shells is essential and briefly reviewed the work that has been done in this context. The present study focusses on simulations of the spherical Couette setup with a radius ratio of $r_i/r_o = 0.35$, similar to that of the Earth's core, and tries to answer some of the open questions. A large part is dedicated to the comparisons with experiments, in particular by [Triana \(2011\)](#) and [Hoff et al. \(2016b\)](#). The structure of the thesis is as follows.

Chapter 2 provides a background in the theory of rotating fluid mechanics, with special emphasis on inertial modes. We derive the continuity and Navier-Stokes equations and show how a plane wave ansatz in the presence of rotation gives rise to waves restored by the Coriolis force. Thereafter, we show how boundary conditions prohibit a continuous spectrum of frequencies and give rise to specific modes which now drift in azimuth. We discuss inertial modes in a sphere and spherical shell and how boundary conditions give

rise to internal shear layers. We end the chapter by discussing oscillatory mechanisms known to excite inertial modes in astrophysical objects.

Chapter 3 provides an overview of the different flow regimes and instabilities observed in the spherical Couette setup for our chosen radius ratio. We first introduce the solution of Proudman (1956) and Stewartson (1966) in the rapidly rotating case and briefly discuss the Stewartson layer instabilities. Thereafter we provide an overview of the parameter regimes and different instabilities observed by Wicht (2014).

Chapter 4 introduces the numerical methods employed in this study. This includes poloidal/toroidal decomposition of vector fields and their expansions in spectral space. We also introduce the code MagIC that was employed in the simulations. Finally, we end the chapter by explaining how inertial modes can be identified in our simulations using various methods.

Chapter 5 discusses the case when the outer boundary is stationary. We scale the thickness of the radial jet and the torque on the inner sphere with the inner boundary rotation rate. We compare with past experimental studies in a spherical shell as well as analytical and numerical studies of a sphere rotating in an unbounded fluid and find similarities. This chapter also discusses an attempt to study the torque bistability observed by Zimmerman et al. (2011) using simulations at much slower rotation rates.

Chapter 6 compares results of simulations at two different outer boundary rotation rates with experimental results observed by Hoff et al. (2016b). This chapter is based on the manuscript “Triadic resonances in the wide-gap spherical Couette system” by A. Barik, S. A. Triana, M. Hoff and J. Wicht, that has been submitted to the Journal of Fluid Mechanics. This work was carried out in collaboration with Santiago Triana from the Royal Observatory of Belgium and Michael Hoff from BTU Cottbus-Senftenberg. We perform simulations for the case when the inner sphere is rotating slower or in an opposite direction with respect to the outer one. At a low outer boundary rotation rate, as we increase the magnitude of differential rotation, we find the three hydrodynamic regimes identified by Hoff et al. (2016b). At a higher outer boundary rotation rate, a similar exercise is repeated and closer comparisons with experiments are performed. We identify triadic resonances of inertial modes in the system, similar to those observed by Hoff et al. (2016b). Finally, we use artificial symmetry restrictions in numerical simulations to determine the cause of onset of these fast EA modes.

Chapter 7 discusses the regime where a broadband temporal spectrum was observed in the simulations as well as in the experiments of Hoff et al. (2016b). We start by providing a brief theoretical background in rotating turbulence. Thereafter, we attempt to address the nature of the ‘turbulent’ regime and the cause for the transition to a broadband turbulence.

Chapter 8 provides a background in fundamentals of magnetohydrodynamics (MHD) and discusses waves due to the effect of the Lorentz force - namely Alfvén and magneto-Coriolis waves. We end the chapter by providing a background in magneto-Coriolis modes and studies of Hide (1966) and Malkus (1967).

Chapter 9 discusses the effect of an imposed axial magnetic field on the inertial modes observed in the spherical Couette flow. When the magnetic field is weak, it acts as a diagnostic and we find similar magnetic induction patterns as observed in experiments by Kelley et al. (2007). Increasing the magnetic field amplitude leads to flow modifications and new instabilities that we briefly describe.

The thesis ends with a conclusion and outlook towards plans of future studies.

2 Theory of inertial modes

*“C’est par la logique qu’on démontre,
c’est par l’intuition qu’on invente.”
(It is by logic that we prove, but by
intuition that we discover.)*

Henri Poincaré

This chapter introduces the reader to the basic equations of rotational fluid dynamics and provides a background in inertial mode theory. A more detailed insight into rotational fluid mechanics in general, can be found in the classic monograph by Greenspan (1968). For a more recent account of advancements in the field of inertial modes we refer to Le Bars et al. (2015).

2.1 Basics of fluid dynamics

2.1.1 Conservation equations

The basic equations of motion of a fluid simply represent fundamental laws of nature for a closed system:

- Conservation of mass
- Conservation of momentum
- Conservation of energy

These equations are derived in brief for a fluid moving with a velocity $\mathbf{u}(\mathbf{x}, t)$ and having mass density $\rho(\mathbf{x}, t)$, in a domain \mathcal{D} of three-dimensional space. Here \mathbf{x} and t represent position vector and time, respectively. In what follows, it is assumed that \mathbf{u} and ρ are smooth functions on \mathcal{D} and we consider a finite subregion W of \mathcal{D} , with surface ∂W .

Conservation of mass

The time rate of change of mass in this volume can be written as $\partial/\partial t \int_W \rho dV$ and is determined by the mass flux into the surface of the volume, $-\int_{\partial W} \rho \mathbf{u} \cdot \mathbf{n} dS$. Here, \mathbf{n} is the normal to the surface ∂W pointing outwards (hence the negative sign). Equating the two, one gets

$$\frac{\partial}{\partial t} \int_W \rho dV = - \int_{\partial W} \rho \mathbf{u} \cdot d\mathbf{S}, \quad (2.1)$$

where using the divergence theorem leads to

$$\int_W \left[\frac{\partial \rho}{\partial t} + \nabla \cdot (\rho \mathbf{u}) \right] dV = 0. \quad (2.2)$$

Since this holds for all W in \mathcal{D} , the following must hold at any point locally

$$\frac{\partial \rho}{\partial t} + \nabla \cdot (\rho \mathbf{u}) = 0. \quad (2.3)$$

Equation (2.3) is referred to as the *equation of continuity*. For an incompressible fluid ($\rho(\mathbf{x}, t) = \text{constant}$) this reduces to:

$$\nabla \cdot \mathbf{u} = 0. \quad (2.4)$$

Conservation of momentum

The conservation of momentum of the fluid in W can be derived using Newton's second law:

$$\begin{aligned} \text{Rate of change of momentum} &= \text{Force due to stress applied on surface } \partial W \\ &+ \text{Force applied on the whole volume.} \end{aligned}$$

If $\boldsymbol{\sigma}$ represents the resultant of the stresses on the surface, and the sum of all forces acting on the volume is denoted by \mathbf{F} , then one can write

$$\frac{d}{dt} \int_W \rho \mathbf{u} dV = \int_{\partial W} \boldsymbol{\sigma} \cdot \mathbf{n} dS + \int_W \mathbf{F} dV. \quad (2.5)$$

The divergence theorem allows us to write the above equation as:

$$\int_W \left[\frac{D}{Dt} (\rho \mathbf{u}) - \nabla \cdot \boldsymbol{\sigma} - \mathbf{F} \right] dV = 0, \quad (2.6)$$

where $D/Dt = \partial/\partial t + \mathbf{u} \cdot \nabla$ is the *material derivative*. Since this must hold for all W in \mathcal{D} , the following must be true locally as well,

$$\frac{D}{Dt} (\rho \mathbf{u}) = \nabla \cdot \boldsymbol{\sigma} + \mathbf{F}. \quad (2.7)$$

Equation (2.7) represents conservation of momentum and is known as the Navier-Stokes equation. Decomposing $\boldsymbol{\sigma}$ into isotropic (pressure) and anisotropic (deviatoric stress) parts, $\boldsymbol{\sigma} = -P\mathbf{I} + \boldsymbol{\tau}$, we get the more commonly used form of the Navier-Stokes equation:

$$\frac{D}{Dt} (\rho \mathbf{u}) = -\nabla \cdot P\mathbf{I} + \nabla \cdot \boldsymbol{\tau} + \mathbf{F}. \quad (2.8)$$

Here, $\boldsymbol{\tau}$ is the rate of strain tensor. For Newtonian fluids, this is given by:

$$\tau_{ij} = 2\mu \left(\epsilon_{ij} - \frac{1}{3} \nabla \cdot \mathbf{u} \right), \quad (2.9)$$

where,

$$\epsilon_{ij} = \frac{1}{2} (\nabla u_i + \nabla u_j^T), \quad (2.10)$$

and μ is the dynamic viscosity of the fluid. Substituting the above expressions in equation (2.8), we get for an incompressible fluid ($\nabla \cdot \mathbf{u} = 0$)

$$\rho \frac{D\mathbf{u}}{Dt} = -\nabla \cdot P\mathbf{I} + \nabla \cdot (\mu (\nabla \mathbf{u} + \nabla \mathbf{u}^T)) + \mathbf{F}, \quad (2.11)$$

which, for a constant μ , can be written as:

$$\frac{D\mathbf{u}}{Dt} = -\frac{1}{\rho} \nabla P + \nu \nabla^2 \mathbf{u} + \frac{\mathbf{F}}{\rho}, \quad (2.12)$$

where, $\nu = \mu/\rho$ is the kinematic viscosity. Equation (2.12) is the form of the Navier-Stokes equation that we would use in the subsequent sections.

Conservation of energy

Multiplying the Navier-Stokes equation (2.12), by \mathbf{u} , we get the equation for energy:

$$\underbrace{\frac{\partial}{\partial t} u^2}_{\text{Rate of change of KE}} = \underbrace{-\mathbf{u} \cdot \nabla u^2}_{\text{Advection of KE}} + \underbrace{\frac{1}{\rho} (-\nabla P + \mathbf{F}) \cdot \mathbf{u}}_{\text{Work done by forces}} + \underbrace{\nu (\mathbf{u} \cdot \nabla^2 \mathbf{u})}_{\text{Viscous dissipation}}. \quad (2.13)$$

This does not give us an evolution equation, but a condition that must hold true at all times.

2.1.2 Rotating frame of reference

In a rotating frame of reference, rotating with a constant angular velocity $\boldsymbol{\Omega}$, the velocity is given according to the equation

$$\mathbf{u}_{inert} = \mathbf{u}_{rot} + \boldsymbol{\Omega} \times \mathbf{r}, \quad (2.14)$$

where subscripts *inert* and *rot* indicate quantities in inertial and rotating frames of reference, respectively. Using a similar transformation, one can write the acceleration as

$$\left(\frac{\partial \mathbf{u}}{\partial t} \right)_{inert} = \left(\frac{\partial \mathbf{u}}{\partial t} \right)_{rot} + \underbrace{2\boldsymbol{\Omega} \times \mathbf{u}_{rot}}_{\text{Coriolis acceleration}} + \underbrace{\boldsymbol{\Omega} \times \boldsymbol{\Omega} \times \mathbf{r}}_{\text{Centrifugal acceleration}} + \underbrace{\left(\frac{\partial \boldsymbol{\Omega}}{\partial t} \right)_{inert} \times \mathbf{r}}_{\text{Poincaré acceleration}}. \quad (2.15)$$

The third term on the RHS, conventionally called the Poincaré acceleration, comes into the picture only when $\boldsymbol{\Omega}$ is evolving in time as is the case, for example, for precession. However, it is equal to zero here since we only consider an $\boldsymbol{\Omega}$ which is constant in time.

Substituting into equation (2.12), we get in a rotating frame of reference,

$$\frac{D\mathbf{u}}{Dt} = -\frac{1}{\rho}\nabla P - 2\boldsymbol{\Omega} \times \mathbf{u} - \boldsymbol{\Omega} \times \boldsymbol{\Omega} \times \mathbf{r} + \nu\nabla^2\mathbf{u} + \frac{\mathbf{F}}{\rho}. \quad (2.16)$$

The third term on the RHS can be written as $\boldsymbol{\Omega} \times \boldsymbol{\Omega} \times \mathbf{r} = -\nabla|\boldsymbol{\Omega} \times \mathbf{r}|^2/2$ and the body force is assumed to be conservative so that $\mathbf{F} = -\rho\nabla\Phi$. These terms can be grouped together with the pressure term as

$$\frac{D\mathbf{u}}{Dt} = -\nabla\left(\frac{P}{\rho} + \frac{1}{2}|\boldsymbol{\Omega} \times \mathbf{r}|^2 + \Phi\right) - 2\boldsymbol{\Omega} \times \mathbf{u} + \nu\nabla^2\mathbf{u}, \quad (2.17)$$

giving rise to an effective pressure, $p = P/\rho + \frac{1}{2}|\boldsymbol{\Omega} \times \mathbf{r}|^2 + \Phi$. Thus, one can see that inclusion of gravity and centrifugal accelerations only changes the effective pressure, and thus don't need to be considered separately. Thus, the final form of the Navier-Stokes equation for a fluid in a rotating frame of reference is as follows:

$$\frac{\partial\mathbf{u}}{\partial t} + \mathbf{u} \cdot \nabla\mathbf{u} = - \underbrace{\nabla p}_{\text{Pressure gradient}} - \underbrace{2\boldsymbol{\Omega} \times \mathbf{u}}_{\text{Coriolis force}} + \underbrace{\nu\nabla^2\mathbf{u}}_{\text{Viscous force}}. \quad (2.18)$$

Taylor - Proudman theorem

Consider equation (2.18) for the steady state of an inviscid fluid in the limit of rapid rotation with the fluid velocity in the rotating frame being small in magnitude so that inertia can be neglected. In such a situation the equation reduces to

$$\nabla p + 2\boldsymbol{\Omega} \times \mathbf{u} = 0. \quad (2.19)$$

Taking the curl of the above equation and using $\nabla \cdot \mathbf{u} = 0$ yields

$$\boldsymbol{\Omega} \cdot \nabla\mathbf{u} = 0, \quad (2.20)$$

which means that the fluid velocity is invariant along the axis of rotation. This remarkable result was found first theoretically by [Hough \(1897\)](#) but is usually credited to [Proudman \(1916\)](#) who showed it experimentally and [Taylor \(1917\)](#) who also provided a theoretical explanation.

2.1.3 Non-dimensionalisation

It is easy to see that we have $n = 3$ variables in equation (2.18) and $k = 2$ dimensions (L, T). Thus, using the Buckingham π theorem, we would have $n - k = 1$ non-dimensional number characterising the flow.

Let L and $\tau_v = 1/\Omega$ to be the characteristic length and time scales, respectively. Using these, one can derive the non-dimensional form of the Navier-Stokes (2.18) and continuity (2.4) equations,

$$\frac{\partial\mathbf{u}}{\partial t} + \mathbf{u} \cdot \nabla\mathbf{u} = -\nabla p - 2\hat{\mathbf{z}} \times \mathbf{u} + E\nabla^2\mathbf{u}, \quad (2.21)$$

$$\nabla \cdot \mathbf{u} = 0, \quad (2.22)$$

where we have retained the original notation for the non-dimensional variables for simplicity. \hat{z} is the unit vector along the axis of rotation. E is called the Ekman number and is given by

$$E = \frac{\nu}{\Omega L^2} = \frac{\text{Viscous}}{\text{Coriolis}}, \quad (2.23)$$

$$(2.24)$$

Thus, the Ekman number defines the relative importance of viscous forces with respect to the Coriolis force. Thus, a low E number implies lower effect of viscosity and greater effect of rotation on the fluid.

2.2 Inertial Waves

2.2.1 Inertial oscillations of a fluid particle

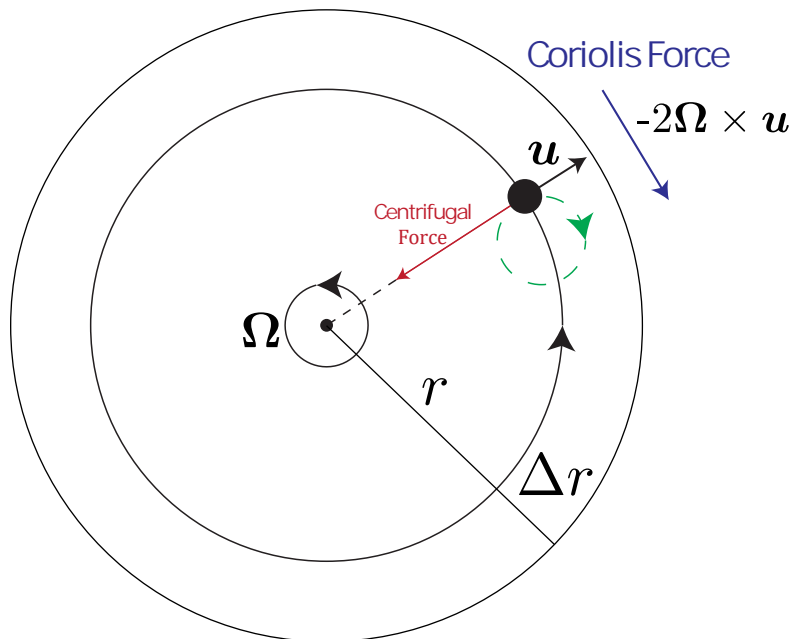


Figure 2.1: Simple demonstration of inertial oscillations of a rotating fluid. The fluid particle in black moves out of the line of solid body rotation whereby the Coriolis force (blue) acts upon it to make it go in oscillatory circles (green).

Consider a body of fluid in solid body rotation with rotation rate Ω . Consider a fluid particle/parcel of unit mass perturbed by a velocity \mathbf{u} , in a plane perpendicular to the rotation axis. Without loss of generality, we consider a radial perturbation, since the effect of a tangential perturbation would be to move the parcel radially outwards (or inwards) due to residual unbalanced centrifugal force and a resultant radial perturbation. If this fluid particle moves from a radius r to a radius $r + \Delta r$, then by conservation of angular momentum, its new angular velocity would be

$$\Omega^* = \left(\frac{r}{r + \Delta r} \right)^2 \Omega < \Omega. \quad (2.25)$$

The centrifugal force per unit mass of the fluid at a radius of r is $\Omega^2 r$ and is balanced by the pressure gradient at that radius. This displacement will lead to a larger centrifugal force $\Omega^{*2}(r + \Delta r)$ on the particle that is smaller than the pressure gradient $\Omega^2(r + \Delta r)$. Thus, there will be a net restoring force on the particle, given by:

$$\begin{aligned} F &= \Omega^2(r + \Delta r) - \Omega^{*2}(r + \Delta r) \\ &= \Omega^2(r + \Delta r) - \Omega^2 r \left(1 - 3\Delta r/r + O(\Delta r^2) \right) \\ &= 4\Omega^2 \Delta r. \end{aligned} \quad (2.26)$$

Thus, the equation of motion of the particle is given by:

$$\ddot{\Delta r} + 4\Omega^2 \Delta r = 0, \quad (2.27)$$

which is the equation of a simple harmonic oscillator with angular frequency 2Ω . Thus, the particle oscillates back and forth radially with an angular frequency of 2Ω . But, as the particle moves radially, the Coriolis force starts acting on it and makes it move rightward all the time, making it go in circles in a sense retrograde to that of Ω . The resulting path of the particle is shown in green in figure 2.1. Such oscillations are called *inertial oscillations* of a rotating fluid (Bjerknes et al. 1933, Fultz 1959).

During the whole analysis, we assumed the particle to be in a plane perpendicular to the rotation axis, where the effect of rotation is felt the most. Now imagine a particle with a velocity perturbation only along the rotation axis. It will keep rotating in solid body rotation while moving with a uniform velocity along the rotation axis. It wouldn't feel any effect of rotation and thus, would have an oscillation frequency of 0. It is thus clear that inertial oscillations of a fluid have frequencies between 0 and 2Ω and are continuously varying depending on the ratio of horizontal to vertical motion.

Below, we derive the properties of inertial waves starting from the Navier-Stokes equation.

2.2.2 Plane inertial waves

Consider an unbound fluid rotating as a solid body with angular velocity Ω . Let us denote a small perturbation to the fluid velocity as \mathbf{u} . The equation of evolution of this perturbation is given by the Navier-Stokes equation (2.21). The analysis that follows is based on chapter 4 of Greenspan (1968) which one can refer to for further details.

For small E , that is, in the case of a fast rotating fluid with low viscosity and small $|\mathbf{u}|$, one can ignore the non-linear and viscous terms and resort to linear theory as follows:

$$\frac{\partial \mathbf{u}}{\partial t} = -\nabla p - 2\hat{\mathbf{z}} \times \mathbf{u}, \quad (2.28a)$$

$$\nabla \cdot \mathbf{u} = 0. \quad (2.28b)$$

We use the wave ansatz for velocity and pressure:

$$\mathbf{u} = \mathbf{Q}e^{i(\mathbf{k}\cdot\mathbf{r}-\omega t)}, \quad (2.29a)$$

$$p = \Phi e^{i(\mathbf{k}\cdot\mathbf{r}-\omega t)}. \quad (2.29b)$$

where \mathbf{k} is the wave vector and ω is the angular frequency of the wave. The continuity equation then gives

$$\mathbf{Q} \cdot \mathbf{k} = 0. \quad (2.30)$$

Thus, the velocity of the fluid is perpendicular to the direction of propagation of the wave and the wave is transverse.

Taking the curl of the momentum equation twice and using the identity, $\nabla \times \nabla \times \mathbf{u} = \nabla(\nabla \cdot \mathbf{u}) - \nabla^2 \mathbf{u} = -\nabla^2 \mathbf{u}$, yields

$$\frac{\partial^2 \nabla^2 \mathbf{u}}{\partial t^2} + 4(\hat{\mathbf{z}} \cdot \nabla)^2 \mathbf{u} = 0. \quad (2.31)$$

Substituting the wave ansatz, we get,

$$-\omega^2 \mathbf{k}^2 + 4(\hat{\mathbf{z}} \cdot \mathbf{k})^2 = 0, \quad (2.32)$$

giving the dispersion relation

$$\omega = \pm 2(\hat{\mathbf{z}} \cdot \hat{\mathbf{k}}), \quad (2.33)$$

where $\hat{\mathbf{k}}$ is the unit vector in the direction of \mathbf{k} . In the dimensional form this reads

$$\omega = \pm 2\Omega(\hat{\mathbf{z}} \cdot \hat{\mathbf{k}}). \quad (2.34)$$

Thus, we see that the linearised Navier-Stokes equation (2.28) admits wave solutions with the dispersion relation given by equation (2.34). Thus, the perturbation to the solid body rotation of a fluid evolves in the form of travelling waves restored by the Coriolis force. These waves are called *inertial waves*.

This peculiar dispersion relation shows that inertial waves have a continuous spectrum of frequencies between 0 and 2Ω and that their frequency depends not on the magnitude of the wave vector but only on the angle it forms with the rotation axis. In the last section, we derived the same result for a fluid particle. The ratio of horizontal to vertical motion was essentially a measure of the angle of the particle's motion with respect to the rotation axis.

The phase and group velocities of these waves, in their dimensional forms, are given by

$$\mathbf{C}_p = \frac{\omega}{\mathbf{k}} = \pm 2\Omega \frac{\hat{\mathbf{z}} \cdot \hat{\mathbf{k}}}{|\mathbf{k}|} \hat{\mathbf{k}}, \quad (2.35a)$$

$$\mathbf{C}_g = \nabla_{\mathbf{k}} \omega = \pm 2\Omega \frac{\hat{\mathbf{k}} \times \hat{\mathbf{z}} \times \hat{\mathbf{k}}}{|\mathbf{k}|}. \quad (2.35b)$$

Their magnitudes are

$$\begin{aligned} C_p &= 2\Omega \cos \theta, \\ C_g &= (2\Omega/k) \sin \theta, \end{aligned} \tag{2.36}$$

where θ is the angle between the rotation axis and the direction of propagation. It can be seen that the peculiar dispersion relation (2.34) leads to the fact that the phase and group velocities are perpendicular to each other implying that the energy of the wave travels perpendicular to the wavefronts themselves. The fluid particles oscillate in planes perpendicular to the direction of propagation of the wave making it a *transverse wave*. In addition, the projection of oscillations of the fluid particles onto a transverse plane would be in the form of circles making the wave *circularly polarised*. Figure 2.2 illustrates these features of a plane inertial wave.

The dispersion relation of inertial waves is very similar to internal gravity waves which are caused when a fluid that is stably stratified in density is perturbed. In that case, the frequency is determined by the angle between the wave vector and the direction of gravity. The similarity is not surprising, since a fluid in solid body rotation is also stably stratified, in terms of angular momentum. This is the reason the two waves are often studied together. In the present study, we restrict ourselves to fluids with constant density, and thus to inertial waves alone.

Reflection at boundaries

Inertial waves are *monoclinical*, i.e., they maintain a constant angle with respect to the rotation axis, as illustrated in figure 2.3. Thus, their law of reflection is very different from sound or light waves which maintain a constant angle with the normal to the reflecting boundary. Since their frequency only depends on the angle between the wavevector and the rotation axis, inertial waves retain their frequency upon reflection.

Inertial wave rays can be focussed or defocussed depending on the angle at which they reflect and the direction in which they travel. The situations have been illustrated in figure 2.3. When the angle of incidence with respect to the rotation axis (θ) is less than the angle the boundary makes with the rotation axis (α), the rays are focussed, i.e, the distance between them decreases while getting reflected ‘upward’. The opposite happens while the rays get reflected ‘downward’. The situation reverses when $\theta > \alpha$. Such focussing can lead to limit cycles of rays where they get focussed along the same path again and again and lead to standing waves, which are often seen clearly as internal shear layers in experiments (e.g. Maas 2001) as well as in numerical computations (e.g. Rieutord et al. 2001, Tilgner 2007a).

Since rays are focussed or defocussed during reflection, it would imply that the distance between two rays of inertial waves changes, thus changing the wavelength. However, the energy carried by the waves remains the same (ignoring any energy absorbed by the boundary). Thus, reflection would provide an efficient means of energy transfer from one wavelength to another. For more details on this, one can have a look at the seminal study by Phillips (1963).

For more details on inertial waves, we refer to Greenspan (1968), Lighthill and Lighthill (2001) and Maas (2005).

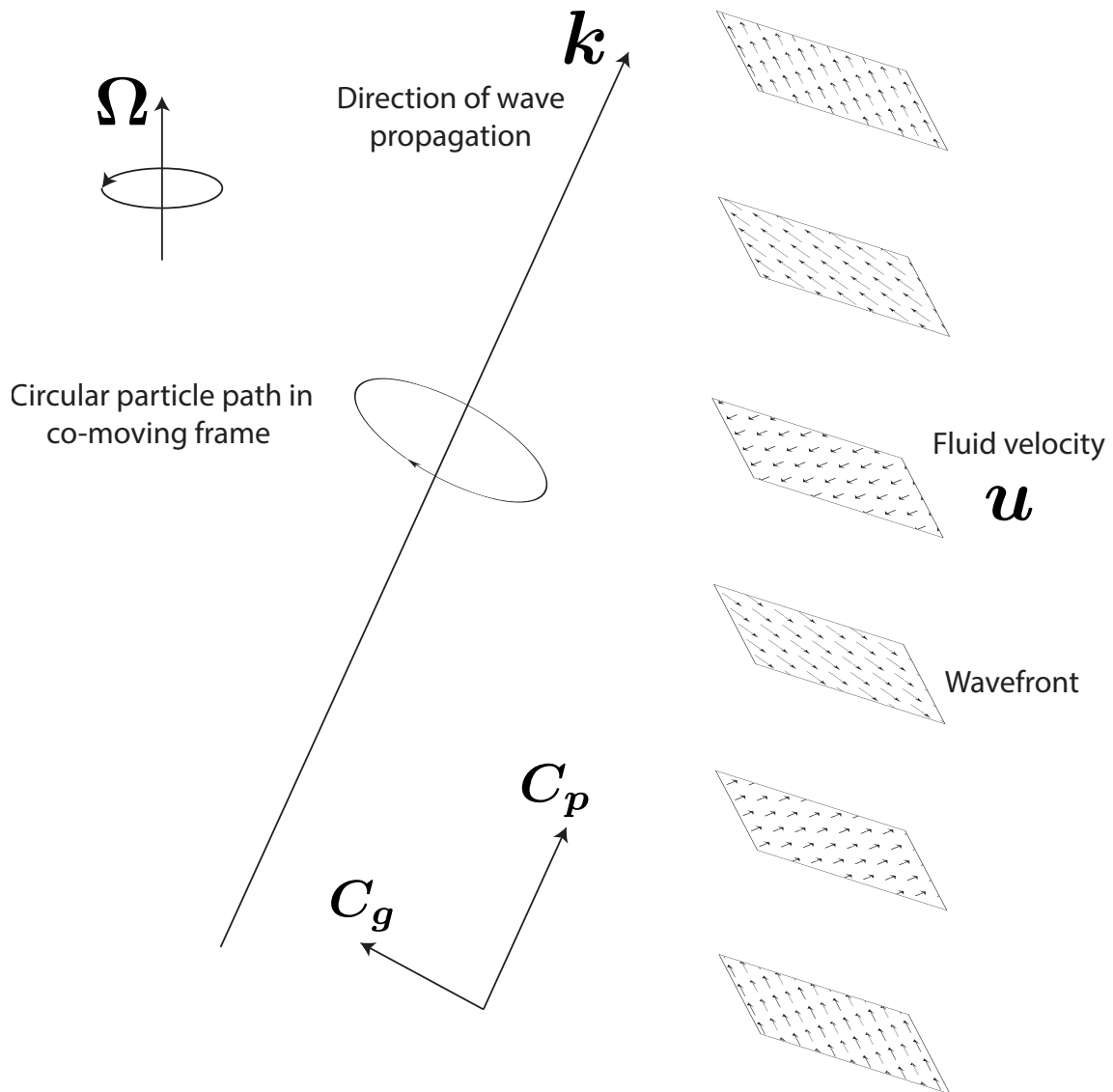


Figure 2.2: Propagation of inertial waves. The phase velocity is perpendicular to the group velocity meaning that the energy of the wave propagates perpendicularly to the wavefronts. The velocity of fluid particles is restricted to planes perpendicular to the phase velocity - the waves are transverse.

2.3 Inertial modes

Inertial waves propagate in an unbounded fluid in solid body rotation. However, in a bounded container, the waves cannot take up a continuous spectrum and global modes of oscillation are set up which are known as *inertial modes*. However, plane inertial waves may still travel inside the fluid and get reflected at the boundary, as the wave equation in an unbounded fluid still holds locally. This section is based on chapter 2 of [Greenspan \(1968\)](#) to which the reader can refer for further details.

Imagine a container with fluid filled inside rotating at an angular velocity Ω . Given

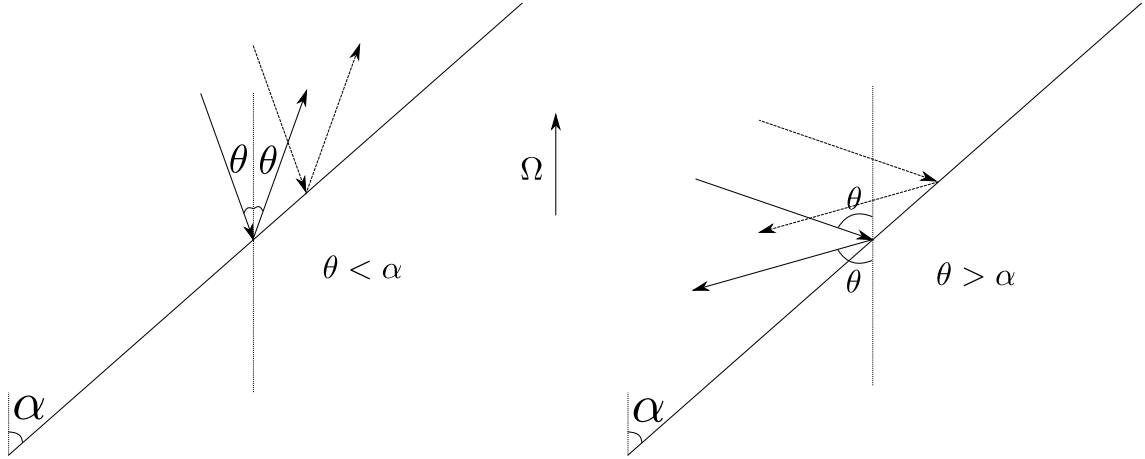


Figure 2.3: Reflection of inertial waves. The rays maintain their angle θ with the rotation axis and thus, the wave maintains a constant frequency. The rays in both cases get focussed if travelling along the directions shown and defocussed if travelling in the opposite direction.

an initial condition for the velocity of the fluid, we would like to see how this velocity evolves towards solid body rotation. To solve this initial value problem we resort to the Navier-Stokes equation (2.21). If the initial condition on the fluid velocity is close to solid body rotation - the final state of the fluid - then the problem can be investigated using linear theory. We start with the linear Navier-Stokes equation:

$$\frac{\partial \mathbf{u}}{\partial t} = -\nabla p - 2\hat{\mathbf{z}} \times \mathbf{u} + E\nabla^2 \mathbf{u}, \quad (2.37a)$$

$$\nabla \cdot \mathbf{u} = 0, \quad (2.37b)$$

combined with an initial condition and boundary conditions on the surface ∂W of the container:

$$\mathbf{u}(\mathbf{r}, 0) = \mathbf{u}_0(\mathbf{r}), \quad (2.38a)$$

$$\mathbf{u}(\mathbf{r}, t) = 0 \quad \text{on } \partial W. \quad (2.38b)$$

The solutions, \mathbf{u} and p can be evaluated by splitting them into a number of normal modes, using $E^{1/2}$ as an expansion parameter (Greenspan 1965):

$$\begin{aligned} \mathbf{u} = \mathbf{q}_0(\mathbf{r}, \tau) + \sum A_n \mathbf{Q}_n(\mathbf{r}) e^{s_n t} + E^{1/2} \left[\mathbf{q}_1(\mathbf{r}, \tau) + \sum \mathbf{q}_{n1}(\mathbf{r}, t, E^{1/2}) \right] + \dots \\ + \tilde{\mathbf{q}}_0 + \sum \tilde{\mathbf{q}}_{n0} + E^{1/2} \left[\tilde{\mathbf{q}}_1 + \sum \tilde{\mathbf{q}}_{n1} \right] + \dots, \end{aligned} \quad (2.39a)$$

$$\begin{aligned} p = \phi_0(\mathbf{r}, \tau) + \sum A_n \Phi_n(\mathbf{r}) e^{s_n t} + E^{1/2} \left[\phi_1(\mathbf{r}, \tau) + \sum \phi_{n1}(\mathbf{r}, t, E^{1/2}) \right] + \dots \\ + \tilde{\phi}_0 + \sum \tilde{\phi}_{n0} + E^{1/2} \left[\tilde{\phi}_1 + \sum \tilde{\phi}_{n1} \right] + \dots, \end{aligned} \quad (2.39b)$$

where ‘...’ represent higher order terms in $E^{1/2}$ representing higher order viscous corrections in each case. $\tau = E^{1/2}t$ represents the “Ekman spin-up” time - the time taken for a fluid to spin-up to solid body rotation from rest. The tilde over a variable indicates the perturbation induced by the viscous boundary layer attached to the surface of the container. Thus, for each variable, the expansion represents the following:

$$\begin{aligned} \text{Variable} = & \text{Inviscid modes} + E^{1/2}[\text{Viscous correction to inviscid modes}] + \dots \\ & + \text{perturbation induced by boundary layer} \\ & + E^{1/2}[\text{Viscous correction to BL induced perturbation}] + \dots \end{aligned} \quad (2.40)$$

These expansions are augmented by an expansion of the exponents s_n ,

$$s_n = s_{n0} + E^{1/2}s_{n1} + \dots, \quad (2.41)$$

where, $s_{n0} = i\omega_n$ and s_{n1} represents viscous decay of an inviscid mode. Thus, ω_n would represent the oscillation frequency of the n^{th} inviscid mode. Note that $\omega = 0$ for \mathbf{q}_0 and ϕ_0 .

Here we restrict our discussion to the inviscid modes. Refer to pages 38 - 63 of chapter 2 of Greenspan (1968) to get more in-depth analysis of the above problem in general.

2.3.1 The geostrophic mode

Consider the zero order problem of the expansion (2.39), with a slow time-dependence of $\tau = E^{1/2}t$. Since the time dependence is too slow for the problem of spin up to solid body rotation, this mode is considered to be independent of time, having a zero frequency. This problem consists of \mathbf{q}_0 and ϕ_0 and can be formulated as

$$2\hat{z} \times \mathbf{q}_0 = -\nabla\phi_0, \quad (2.42a)$$

$$\nabla \cdot \mathbf{q}_0 = 0, \quad (2.42b)$$

with the boundary condition $\mathbf{q}_0 \cdot \hat{\mathbf{n}} = 0$ on the container surface ∂W . Taking the curl of the momentum equation, we get

$$(\hat{z} \cdot \nabla) \mathbf{q}_0 = 0, \quad (2.43)$$

showing that \mathbf{q}_0 is invariant along the axis of rotation and thus satisfies the Taylor-Proudman theorem. A flow in which pressure and Coriolis forces perfectly balance each other is called a geostrophic flow. Thus, this stationary mode with zero frequency ($\omega = 0$) is called the **geostrophic mode**. It can be shown that this mode sits in a container along contours of constant height and possesses a finite mean circulation (circulation of depth averaged velocity) along these contours:

$$\oint_C \langle \mathbf{Q} \rangle \cdot d\mathbf{s} \neq 0$$

, where $\langle \mathbf{Q} \rangle$ is the velocity averaged along the rotation axis and C is a geostrophic contour. For example, in a sphere, the only mode that can be geostrophic must have an azimuthal symmetry of $m = 0$. However, in a cylinder, it can take any azimuthal symmetry.

2.3.2 Inertial modes

Now, consider the next problem in the expansion (2.39), that of the inviscid modes $\mathbf{Q}_n e^{-i\omega_n t}$ and $\Phi_n e^{-i\omega_n t}$. Since these modes are separable, we can drop the subscripts while discussing them here and consider a single mode. The linear Navier-Stokes equations for a mode can be written as follows

$$-i\omega \mathbf{Q} = -\nabla\Phi - 2\hat{\mathbf{z}} \times \mathbf{Q}, \quad (2.44a)$$

$$\nabla \cdot \mathbf{Q} = 0, \quad (2.44b)$$

with the boundary condition $\mathbf{Q} \cdot \hat{\mathbf{n}} = 0$ on the surface of the container ∂W . Note again that $\omega = 0$ will lead to the equations for the geostrophic mode. In terms of pressure alone, the problem can be formulated as

$$\nabla^2 \Phi - \frac{4}{\omega^2} (\hat{\mathbf{z}} \cdot \nabla)^2 \Phi = 0, \quad (2.45)$$

with the boundary condition

$$-\omega^2 \hat{\mathbf{n}} \cdot \nabla \Phi + 4(\hat{\mathbf{n}} \cdot \hat{\mathbf{z}})(\hat{\mathbf{z}} \cdot \nabla \Phi) - 2i\omega(\hat{\mathbf{z}} \times \hat{\mathbf{n}}) \cdot \nabla \Phi = 0, \quad (2.46)$$

on ∂W . Equation (2.45) is called the ‘*Poincaré equation*’, a term coined by [Cartan \(1922\)](#). This is a hyperbolic equation with boundary conditions and is thus ill-posed. Hence, it will not have solutions for all ω . Thus, even though inertial waves and inertial modes satisfy the same linearised momentum equation, the boundary conditions on inertial modes lead to the fact that they cannot have a continuous spectrum of frequencies like inertial waves. In addition, the solution for inertial modes is no longer in the form of plane waves, but are dependent on the geometry of the container which also decides whether one would find smooth solutions or not.

In general, however, one should expect singularities in the solution. We’ll see later that these singularities give rise to internal shear layers in the presence of viscous dissipation. But before that, let us glance upon some important properties of inertial modes:

- The eigenvalues, ω , of inertial modes are real and their absolute values lie between 0 and 2Ω . This is similar to the property of plane inertial waves. However, the spectrum is discontinuous and, in the absence of a simple dispersion relationship like equation (2.34), one has to mathematically find it from first principles. The proof is provided in the appendix A.
- Inertial modes are orthogonal. The integral over the volume of the product of two inertial modes is $\int_W \mathbf{Q}_i \mathbf{Q}_j = \delta_{ij}$, where δ_{ij} is the Kronecker delta function. This makes it very easy to project a solution onto a set of inertial modes.
- Inertial modes do not possess a mean circulation about a geostrophic contour,

$$\oint_C \langle \mathbf{Q} \rangle \cdot d\mathbf{s} = 0$$

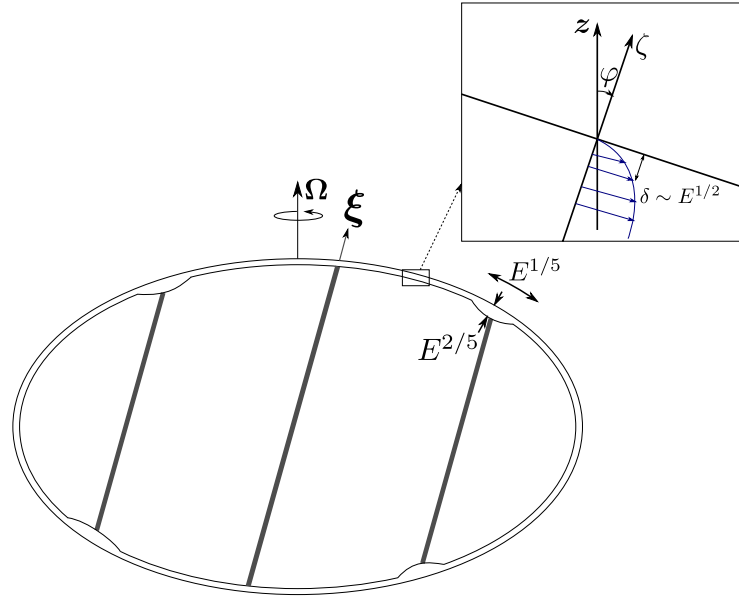


Figure 2.4: Boundary layer eruptions and the resulting internal shear layers associated with an inertial mode. The shear layers are conical in 3D while they appear as rays in 2D. δ represents the local boundary layer thickness, ζ is the boundary layer coordinate, φ represents the angle between the rotation axis and the normal to the boundary layer. $\xi = \nabla \times \mathbf{u}$ is the fluid vorticity. Illustration based on [Le Bars et al. \(2015\)](#)

2.4 Internal shear layers

As mentioned before, the problem of inertial modes in a container is ill-posed in general. Let us see the consequences it has. Consider the linearised Navier-Stokes equation (2.28). Introducing the viscous dissipation term, we get,

$$\frac{\partial \mathbf{u}}{\partial t} = -\nabla p - 2\hat{\mathbf{z}} \times \mathbf{u} + E\nabla^2 \mathbf{u}. \quad (2.47)$$

Proceeding as before to derive a wave equation yields

$$\left(\frac{\partial}{\partial t} - E\nabla^2 \right)^2 \nabla^2 \mathbf{u} + 4 \frac{\partial^2 \mathbf{u}}{\partial z^2} = 0. \quad (2.48)$$

For an inertial mode, $\mathbf{u} = \mathbf{Q}e^{-i\omega t}$, we can write the above equation in terms of a boundary layer coordinate ζ ,

$$\left(-i\omega - E \frac{\partial^2}{\partial \zeta^2} \right)^2 \frac{\partial^2 \mathbf{Q}}{\partial \zeta^2} + 4 \cos^2 \varphi \frac{\partial^2 \mathbf{Q}}{\partial \zeta^2} = 0. \quad (2.49)$$

where, φ is the angle between the rotation axis and the normal to the boundary layer, as shown in figure 2.4. This would represent the colatitude in case of a spherical container.

If δ be the local boundary layer thickness, then one can approximate $\partial^2/\partial \zeta^2 \sim 1/\delta^2$, and we get

$$|\delta| = \frac{E^{1/2}}{(\omega \pm 2 \cos \varphi)^{1/2}}. \quad (2.50)$$

Thus, the boundary layer thickness is no longer a simple $E^{1/2}$ as in the case of a classical Ekman layer, but is dependent on the angle φ . In particular, at angles where $\omega = \pm 2 \cos \varphi$, one would get singularities. In the presence of viscosity, these occur as boundary layer ‘eruptions’ which have a thickness of $E^{1/5}$ and a spatial extent of $E^{2/5}$ (Roberts and Stewartson 1963).

The equation for inertial modes is a hyperbolic differential equation. Thus, a discontinuity in the boundary conditions will propagate along the characteristics. The propagation of information in a hyperbolic system can only take place through waves, in this case, inertial waves. Thus, the discontinuities in the Ekman layer propagate inward along the characteristic cones and spawn internal shear layers, studied first by Bondi and Lyttleton (1953). These shear layers are nothing but plane inertial waves excited by discontinuities at the boundary. Although they resemble rays when seen in two dimensions, in three dimensions they are cones of the characteristics of the Poincaré equation (2.45). These cones, as visualised by Bondi and Lyttleton (1953) for a sphere, are shown in figure 2.5.

The discussion here showed that a *no-slip* boundary condition, giving rise to Ekman layers, makes the inertial mode problem ill-posed in general. However, for specific geometries like the spherical-shell which will be discussed later, even *free-slip* and impenetrable boundary conditions makes the problem ill-posed and gives rise to internal shear layers. Further discussions on internal shear layers will take place when we talk about inertial modes in a spherical shell.

2.5 Inertial modes in a sphere

Inertial modes in a sphere (“spheroid of finite ellipticity”, of which the sphere is a special case) were considered by Bryan (1889), who also gave a solution in terms of pressure, being an implicit solution in terms of velocity. Noticing the difficulty with this solution, Kudlick (1966) expressed Bryan’s solution in terms of a double polynomial F_N , which made it easy to find explicit analytical solutions for small $N \leq 4$. Zhang et al. (2001) came up with a complete set of analytical solutions for inertial modes in a sphere. We discuss these developments in more detail below.

To investigate inertial modes in a sphere, let us turn to equations (2.44). For velocity of the mode, \mathbf{Q} , and pressure, p we use the following ansatz in cylindrical coordinates:

$$\mathbf{Q} = \left(u_s(s, z), u_\phi(s, z), u_z(s, z) \right) e^{i(m\phi - \omega t)}, \quad (2.51a)$$

$$p = \Phi e^{i(m\phi - \omega t)}. \quad (2.51b)$$

Writing down and rearranging the equations for the different components, it can be easily shown that (e.g. Greenspan 1964, Kudlick 1966, Zhang et al. 2001)

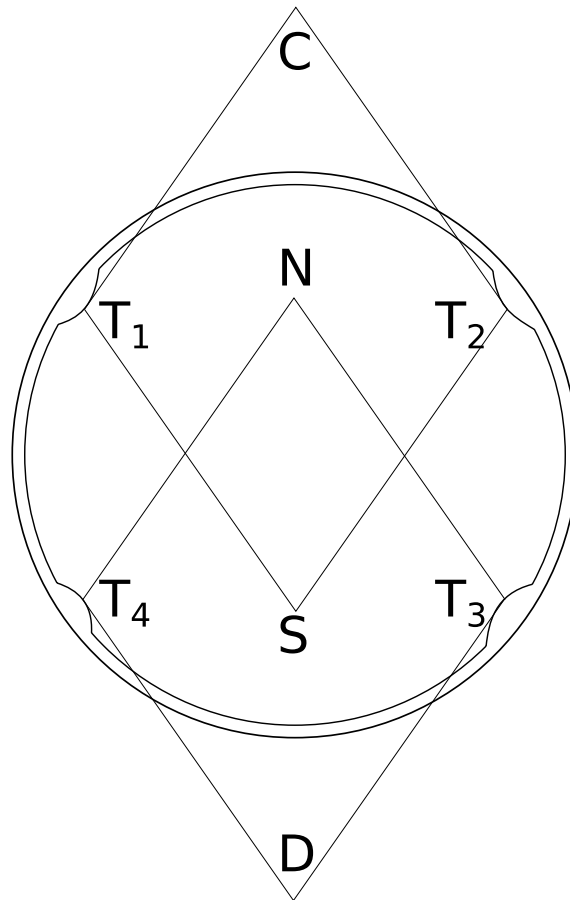


Figure 2.5: Internal shear layers spawned from the Ekman layer of a rotating sphere. The lines show the characteristic cones of the Poincaré equation, which also mark the positions of the internal shear layers. Figure based on an illustration in [Bondi and Lyttleton \(1953\)](#). In the figure, T_i represent the points in the Ekman layer from which the internal shear layers emanate. N and S represent the points where the rays meet inside the sphere while C and D are the points where rays would theoretically meet outside the sphere.

$$u_s = \frac{i}{4 - \omega^2} \left(\frac{2m\Phi}{s} - \omega \frac{\partial \Phi}{\partial s} \right), \quad (2.52a)$$

$$u_\phi = \frac{1}{4 - \omega^2} \left(\frac{\omega m \Phi}{s} - 2\omega \frac{\partial \Phi}{\partial s} \right), \quad (2.52b)$$

$$u_z = -\frac{i}{\omega} \frac{\partial \Phi}{\partial z}. \quad (2.52c)$$

Solution by Bryan

[Bryan \(1889\)](#) provided an implicit solution for Φ in terms of spheroidal coordinates

(μ, η, ϕ) :

$$s = \left(\frac{4}{4 - \omega^2} - \eta^2 \right)^{1/2} (1 - \mu^2)^{1/2}, \quad (2.53a)$$

$$z = \left(\frac{4}{\omega^2} - 1 \right)^{1/2} \eta \mu, \quad (2.53b)$$

giving the surface of the sphere as $\mu = \cos \theta$, $\eta = (4/\omega^2 - 1)^{-1/2}$. The separable solutions in terms of these coordinates are (Greenspan 1964)

$$\Phi_{lm} = P_{lm}(\eta/c_{lm})P_{lm}(\mu)e^{im\phi}, \quad (2.54)$$

where P_{lm} is an associated Legendre polynomial of degree l and order m , and $c_{lm} = (1 - 4/\omega^2)^{-1/2}$. Thus, on the surface,

$$\Phi_{lm} = P_{lm}(f(\omega))Y_{lm}(\theta, \phi), \quad (2.55)$$

where, $Y_{lm} = P_{lm}(\cos \theta)e^{im\phi}$ represents a spherical harmonic of degree l and order m and $f(\omega) = \eta/c_{lm}$ is a function of ω . Thus, on the surface of the sphere, the pressure structure of an inertial mode looks like a spherical harmonic of degree l and order m , with its amplitude depending on the eigenvalue ω . The eigenvalues associated with these eigenmodes, ω_{lm} are given by solving the eigenvalue equation

$$mP_{lm}(\omega/2) = 2 \left(1 - \frac{\omega^2}{4} \right) \frac{d}{d\omega} P_{lm}(\omega/2). \quad (2.56)$$

Using recurrence relations of associated Legendre polynomials, this can be simplified to

$$[l(\omega/2) + m] P_{lm}(\omega/2) = (l + m)P_{l-1,m}(\omega/2). \quad (2.57)$$

In general, this equation has $l - m - \nu_{lm}$ solutions, where

$$\nu_{lm} = \begin{cases} 0, & \text{if } l - m \text{ is even} \\ 1, & \text{if } l - m \text{ is odd} \end{cases} \quad (2.58)$$

The eigenvalues and eigenfunctions are thus denoted using three indices, (l, m, n) where n denotes the n^{th} eigenvalue. Note that the notation used here is different in order to that used by Greenspan (1968) - (n, m, k) . The correspondence is $l \rightarrow n, m \rightarrow k, n \rightarrow m$.

Kudlick's extension

The above solution is not amenable to obtaining explicit solutions in terms of velocity. Kudlick (1966) expressed the solution for pressure in the form of a polynomial as follows (using a similar notation)

$$\Phi_{lm} = C_{lm}^2 \left(\frac{z}{\alpha\beta} \right)^{\nu_{lm}} \left(\frac{s}{\alpha} \right)^m \prod_{j=1}^N (D_j + A_j s^2 + B_j z^2), \quad (2.59)$$

where,

$$\begin{aligned}
 C_{lm} &= \frac{(2l)!}{2^l l! (l-m)!}, \\
 \nu_{lm} &= \begin{cases} 0, & \text{if } l-m \text{ is even} \\ 1, & \text{if } l-m \text{ is odd} \end{cases}, \\
 \alpha &= \left(1 - \frac{\omega^2}{4}\right)^{-1/2}, \quad \beta = \left(\frac{4}{\omega^2} - 1\right)^{1/2} \\
 D_j &= x_j^2(x_j^2 - 1), \quad A_j = x_j^2(1 - \omega^2/4), \quad B_j = (\omega^2/4)(1 - x_j^2) \\
 &x_j \text{ are the } N = l - m - \nu_{lm} \text{ zeros of } P_{lm} \text{ excluding 0 and 1.}
 \end{aligned}$$

The explicit solution by Zhang et al. (2001)

Kudlick's extension of Bryan's solution allowed one to compute explicit solutions by first using the zeros of P_{lm} to determine the pressure using equation (2.59) and thereafter using equations (2.52) to determine the velocity components u_s, u_ϕ, u_z . This proved to be quite easy for small N . However, analytical expressions for the roots x_j do not exist for $N > 4$, making obtaining analytical solutions for $N > 4$ impossible (Zhang et al. 2001).

Zhang et al. (2001) found explicit solutions for velocity for all N by using Bryan's coordinate transformation and expressing the terms cleverly in terms of cylindrical coordinates s and z . They found expressions for the two distinct classes of inertial modes:

- Equatorially symmetric:

$$(u_s, u_\phi, u_z)(z) = (u_s, u_\phi, -u_z)(-z) \quad (2.61)$$

These modes would have $l - m = \text{even}$ in Greenspan notation

- Equatorially antisymmetric:

$$(u_s, u_\phi, u_z)(z) = (-u_s, -u_\phi, u_z)(-z) \quad (2.62)$$

These modes would have $l - m = \text{odd}$ in Greenspan notation

Their main motivation behind this was to show that the dissipation integral over the whole volume vanished identically for any mode in a full sphere,

$$\int_W \mathbf{Q}_{lmn}^* \cdot \nabla^2 \mathbf{Q}_{lmn} dV = 0. \quad (2.63)$$

Mode structures

The use of indices l and m will become apparent here. The surface structure of each inertial mode in a full sphere is in the form of a spherical harmonic $Y_{lm}(\theta, \phi)$. However, it is only when one looks at the full 3D structure does one realize that each mode has a complex radial structure as well. It is the difference in radial structures that the role of the third index n comes in. This has been illustrated in figure 2.6.

In what follows, we would be always be dealing with a single eigenmode for each combination of l and m . Hence, the third index n becomes redundant and will be dropped.

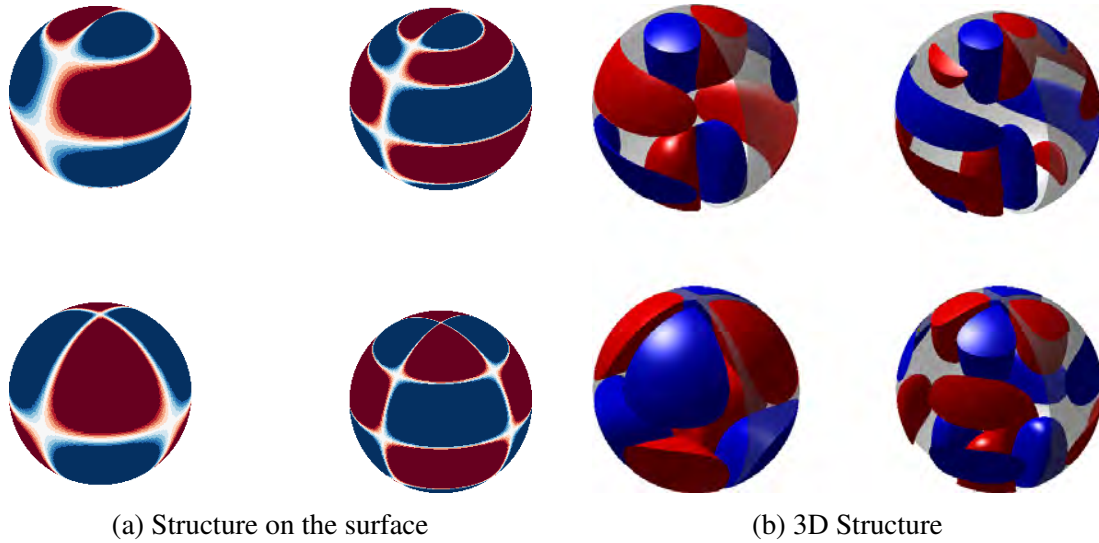


Figure 2.6: Structure of inertial modes of a full sphere. Shown here are isosurfaces of cylindrically radial velocity, u_s , red being outward and blue inward, based on the analytical solution by Zhang et al. (2001). (a) shows the structure on the surface. Note how each mode resembles the spherical harmonic Y_{lm} on the surface. (b) shows the 3D structure. This shows that the modes have a complex radial structure as well. The difference in radial structure is where the third index n comes in to distinguish between different modes with same surface structure.

Internal shear layers

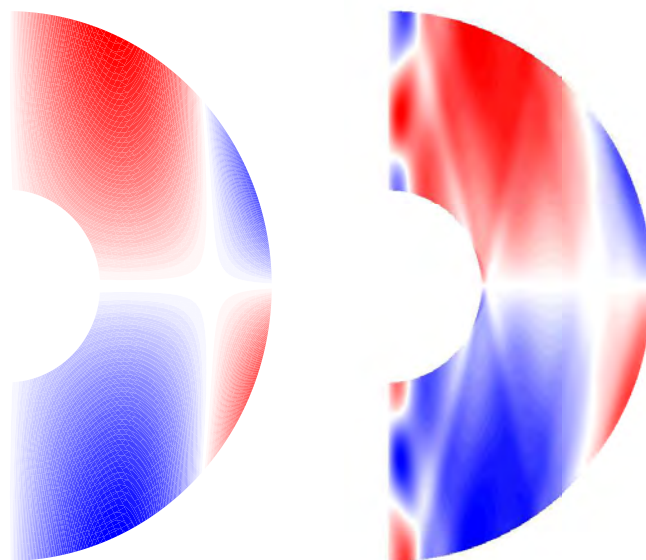
The analytical solutions derived above for inertial modes in a full-sphere are well-behaved and the problem for inertial modes in a full-sphere is well-posed *only* when impenetrable boundary conditions $\mathbf{Q} \cdot \hat{\mathbf{n}} = 0$ are used. However, these solutions do not satisfy the more realistic *no-slip* boundary condition $\mathbf{Q} = 0$. This inevitably gives rise to internal shear layers, as first noted by Bondi and Lyttleton (1953) and discussed in section 2.4. In the *no-slip* case, the above-mentioned analytical solutions become the solutions in the bulk of the fluid which can be treated as inviscid, while viscous effects are incorporated in a boundary layer analysis which brings in discontinuities with it.

2.6 Inertial modes in a spherical shell

Unlike in the case of a sphere, the inertial mode problem in a spherical shell is ill-posed. As a result, formulating analytical solutions for a spherical shell is not possible. Analytical solutions for waves in a spherical shell of infinitesimally small thickness were found by Longuet-Higgins (1964, 1965) and were later computationally explored in a later work, Longuet-Higgins (1968). These works presented solutions of “of Laplace’s tidal equations for a thin, uniform layer of fluid on the surface of a rotating sphere.” (Longuet-Higgins 1968), and were applicable to waves in the Earth’s atmosphere and oceans.

However, an attempt at formulating analytical solutions of a spherical shell of finite

thickness was first made by [Stewartson and Rickard \(1969\)](#). Their work considered expansion of velocity components and pressure in powers of the parameter $\epsilon = (r_o - r_i)/(r_o + r_i)$, where r_o and r_i represent radii of inner and outer boundaries, respectively. It was found that a singularity occurs at every term after the second in the expansion for pressure and a singularity of one order higher at every term (thus, starting from the second) of the velocity components. These singularities take place whenever the colatitude satisfies $\cos\theta = \pm\omega/2$. These are the circles along which the cones of the characteristics of the Poincaré equation meet the boundaries. In the presence of viscosity, these singularities are ‘smoothed’ out as internal shear layers. In two-dimensions, the projection of these cones looks like rays reflecting at boundaries. These ‘rays’ follow the same reflection law as plane inertial waves, suggesting that they are inertial waves spawned by discontinuities in the boundary conditions. A comparison of structures for a full sphere mode with a corresponding spherical shell mode shows the internal shear layers clearly. This can be seen in figure 2.7. Note that both modes, although similar in structure can be clearly distinguished by the presence of the internal shear layers.



(a) Full sphere (5, 2)

(b) Spherical shell (5, 2)

Figure 2.7: Comparison of the structure of an inertial mode, (5, 2), for a full sphere and a spherical shell. The internal shear layers for the spherical shell can be clearly seen. Colormaps show zonal velocity, u_ϕ , in a meridional plane - red being positive (eastward) blue being negative (westward). The direction of rotation is along \hat{z} .

Effect of inner sphere

In three dimensions, the inertial eigenmodes of a spherical shell resemble those of a full sphere to a large extent, as shown in figure 2.8, though small deviations can be noted because of the presence of the inner sphere. The full-sphere mode uses the analytical

solution by [Zhang et al. \(2001\)](#), while the spherical shell eigenmode was computed using SINGE. Note that both were computed using *free-slip* boundary conditions.

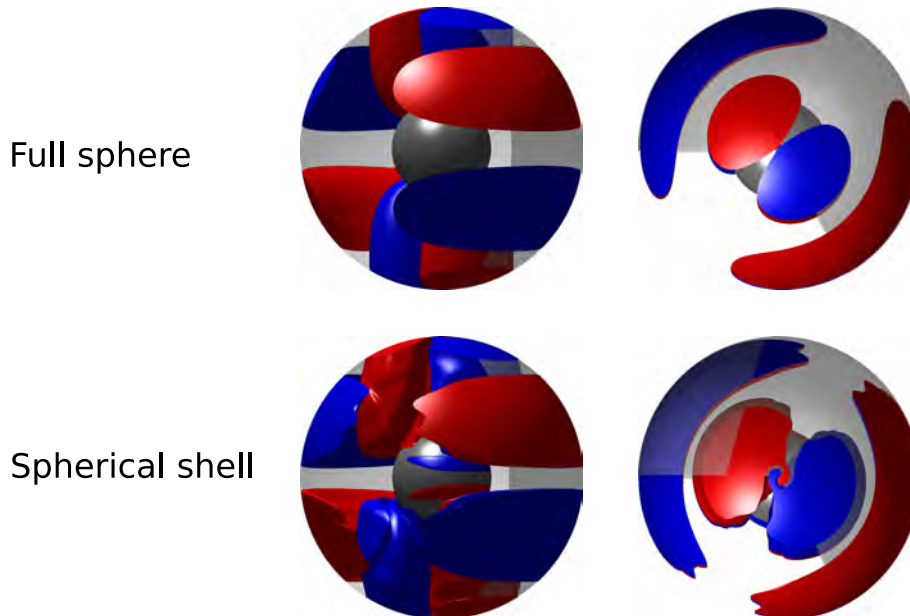


Figure 2.8: Comparison of 3D structures of the $(4, 1)$ mode for a full-sphere and a spherical shell. The structures are very similar with small differences. Shown here are isosurfaces of cylindrically radial velocity, u_s , with red being positive (outward) and blue being negative (inward). The inner sphere has been rendered in case of the full sphere illustration for the purpose of comparison.

The effect of the presence of an inner sphere was studied in detail by [Aldridge \(1967\)](#). He performed libration experiments using a spherical shell setup and computed eigenvalues for different spherical shell modes using visualisation and kinetic energy resonances as well as complemented his experimental results with theoretical models. He estimated eigenvalues of a spherical shell using two different methods - first, in a crude way using the fact that inertial mode eigenvalues can be written in terms of the ratio of kinetic energies, $\omega^2 = KE_z/KE_s$, and second in a better way using a variational principle. He noted that all modes of the family $(n, 1)$, where n is an integer, showed a *decrease* in frequency as compared to the full sphere, with the $(1, 1)$ mode showing a smaller shift compared to $(2, 1)$, $(3, 1)$ and $(4, 1)$ modes. However, for the $(2, 2)$ mode there was an increase in the eigenvalue as compared to a sphere.

Since the inertial mode problem in a spherical shell is analytically intractable, numerical investigations were necessary. The first numerical inertial eigenmode computation in a spherical shell was carried out by [Rieutord \(1991\)](#) who also compared frequencies and viscous decay factors with experiments of [Aldridge \(1967\)](#) and concluded that the identification of inertial modes in the Earth's core using gravimeters by [Aldridge and Lumb \(1987\)](#) is likely to be correct. In the present study, we use the eigenvalue code SINGE ([Vidal and Schaeffer 2015](#)) to compute inertial modes of a spherical shell.

Internal shear layers

The inertial mode problem in a spherical shell, being ill-posed, consists of singularities in the solutions for velocity and pressure, as found by [Stewartson and Rickard \(1969\)](#). These discontinuities travel along the characteristics of the hyperbolic Poincaré equation and in the presence of viscosity, take the form of internal shear layers. These shear layers are spawned from ‘critical latitudes’ that satisfy $\sin \theta = \omega/2$, and are tangent to the inner sphere at the critical latitude. They ‘reflect’ from boundaries following the same law as plane inertial waves, keeping their angle with the rotation axis always constant at θ . Thus, the angle that these shear layers emanate from is the same as the latitude from which they begin. The discontinuities on the boundaries become ‘bumps’ on the Ekman layer in the presence of viscosity. [Roberts and Stewartson \(1963\)](#) found that these ‘bumps’ have a size of the order of $E^{1/5} \times E^{2/5}$. The shear layers themselves have a width that scales as $E^{1/3}$ ([Walton 1975](#), [Kerswell 1995](#)).

Let us take the example of the ‘spinover mode’ in a spherical shell. This is the (2, 1) mode in Greenspan notation and is one of the simplest inertial mode to study in a sphere/spherical shell, with a non-dimensional frequency of $\omega = 1$. In the rotating frame of reference, it is simply the rotation of the fluid along an axis different from the rotation axis of the sphere/spherical shell (see [Greenspan 1968](#), for details). Since $\omega = 1$, critical latitudes occur at $\sin^{-1}(1/2) = 30^\circ$ and the shear layers make an angle of 30° with the rotation axis. The various scalings of the Ekman layers and the shear layers can be seen in figure 2.9. For more details of these scalings, one can have a look at [Kerswell \(1995\)](#), [Walton \(1975\)](#) and [Hollerbach and Kerswell \(1995\)](#), who confirmed them with numerical simulations.

The relationship between these shear layers and plane inertial waves was already discussed in section 2.4. Their reflections can lead to focussing of ‘ray’ paths along periodic orbits, and one can analyse the system from a dynamical systems point of view, borrowing the concept of attractors. Examples of such studies in a spherical shell are [Tilgner \(1999a\)](#), [Rieutord et al. \(2000\)](#), [Rieutord et al. \(2001\)](#) and [Rabitti and Maas \(2013, 2014\)](#).

2.7 Sustaining inertial modes: triadic resonances

From the above analysis, it is clear that inertial modes in a sphere are travelling waves which travel along the azimuth with wavenumber m and drift speed ω/m . They are normal modes of the system which make up any transient flow in the bulk rotating fluid, ignoring viscous corrections. In the presence of viscous dissipation, the transient eventually decays away and the fluid attains solid-body rotation in an Ekman spin-up time scale, $\tau \sim E^{1/2}t$, during which the inertial modes also decay away. Thus, all inertial modes decay in an Ekman spin-up time scale of $\tau = E^{1/2}t$ ([Greenspan 1968](#)).

To sustain inertial modes in a rotating fluid against viscous dissipation, one needs a constant source of energy to feed these modes. For astrophysical bodies, this is usually in the form of a mechanical forcing like precession, libration or tidal forces. The common mechanism of exciting inertial modes or inertial instabilities from mechanical forcing is through triadic resonances which involve two inertial modes coupled together with the fundamental response of the system to the forcing.

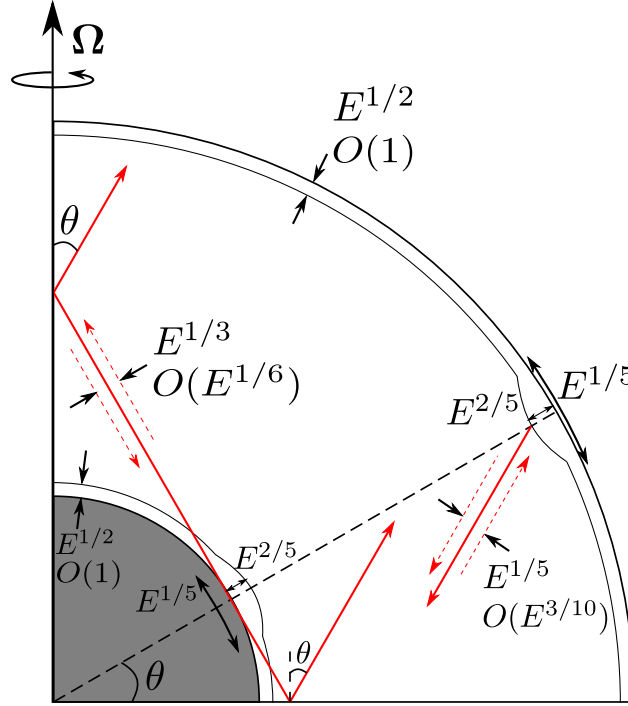


Figure 2.9: A diagram of the viscous response to a spinover velocity field in a spherical shell. The internal shear layers spawned by singularities in the Ekman layer, are shown in red. The various scalings of the thickness of the shear layers as well as the ‘bumps’ in the Ekman layer are shown. The corresponding velocity magnitudes are shown with the $O()$ notation. $\theta = \sin^{-1}(\omega/2)$ is the critical latitude. Figure based on an illustration in [Kerswell \(1995\)](#).

To elucidate the above statement, we follow a general recipe of inertial instabilities provided in [Tilgner \(2007a\)](#). Let us begin with the linearised Navier-Stokes equation (2.28) and write the velocity and pressure into a fundamental response and a perturbation so that, $\mathbf{u} = \mathbf{u}_0 + \mathbf{u}'$ and $p = p_0 + p'$. Substituting this in equation (2.28) and noting that \mathbf{u}_0 and p_0 satisfy (2.28), we get an equation for the evolution of \mathbf{u}' .

$$\frac{\partial \mathbf{u}'}{\partial t} + 2\hat{\mathbf{z}} \times \mathbf{u}' + \nabla p' + (\mathbf{u}_0 \cdot \nabla \mathbf{u}' + \mathbf{u}' \cdot \nabla \mathbf{u}_0) = 0 \quad (2.64)$$

where we have assumed $u' \ll u_0$ and have ignored terms quadratic in \mathbf{u}' . The last term in brackets can be written as a perturbation to the Coriolis force,

$$\frac{\partial \mathbf{u}'}{\partial t} + 2\hat{\mathbf{z}} \times \mathbf{u}' + \nabla p' + \epsilon \mathcal{V} \mathbf{u}' = 0 \quad (2.65)$$

where, ϵ is small parameter and \mathcal{V} is a linear operator operating on \mathbf{u}' (note that the non-linear term involving \mathbf{u}' and \mathbf{u}_0 is linear in both vectors individually).

The solutions of the unperturbed equation are inertial modes as mentioned in section 2.3.2. Since, inertial modes form an orthogonal set in terms of both pressure and velocity ([Greenspan 1968](#)), we can project the corresponding perturbations on to the inertial modes. Thus,

$$\mathbf{u}' = \sum c_j(t) \mathbf{Q}_j e^{-i\omega_j t}, \text{ and } p' = \sum c_j(t) \Phi_j e^{-i\omega_j t}, \quad (2.66)$$

which would give us, for the j^{th} term,

$$\sum_j \left[\mathbf{Q}_j \frac{dc_j}{dt} + c_j (-i\omega_j \mathbf{Q}_j + 2\hat{\mathbf{z}} \times \mathbf{Q}_j + \nabla \Phi_j + \epsilon \mathcal{V} \mathbf{Q}_j) \right] e^{i\omega_j t} = 0. \quad (2.67)$$

Noting that by definition, $-i\omega_j \mathbf{Q}_j + 2\hat{\mathbf{z}} \times \mathbf{Q}_j + \nabla \Phi_j = 0$, and we are left with

$$\sum_j \left[\mathbf{Q}_j \frac{dc_j}{dt} + c_j \epsilon \mathcal{V} \mathbf{Q}_j \right] e^{-i\omega_j t} = 0 \quad (2.68)$$

Expanding c_j in terms of the parameter ϵ ,

$$c_j = c_j^{(0)} + \epsilon c_j^{(1)} + \epsilon^2 c_j^{(2)} + \dots \quad (2.69)$$

we get, at order 0, $(\partial/\partial t)c_j^{(0)} = 0$. At order 1, we get,

$$\sum_k \mathbf{Q}_k \frac{dc_k^{(1)}}{dt} e^{-i\omega_k t} + \sum_j c_j^{(0)} \mathcal{V} \mathbf{Q}_j e^{-i\omega_j t} = 0 \quad (2.70)$$

Thus, the projection of the perturbation on an inertial mode \mathbf{Q}_k can be obtained as

$$\frac{dc_k^{(1)}}{dt} = - \sum_j c_j^{(0)} e^{i(\omega_k - \omega_j)t} \int \mathbf{Q}_k^\dagger \mathcal{V} \mathbf{Q}_j dV \quad (2.71)$$

Now, if the fundamental mode \mathbf{u}_0 and hence, \mathcal{V} has an azimuthal symmetry of m_0 and a time dependence $e^{i\omega_0 t}$, then separating the time and ϕ dependences from the integral on the RHS, we get,

$$\frac{dc_k^{(1)}}{dt} = - \sum_j c_j^{(0)} e^{i(\omega_0 + \omega_k - \omega_j)t} \int_\phi e^{i(m_0 + m_j - m_k)\phi} d\phi \int \mathbf{Q}_k^\dagger(S) \mathcal{V} \mathbf{Q}_j(S) dS \quad (2.72)$$

where S represents the coordinate system after the ϕ -dependence has been removed. From the the last equation two things are clear:

- The integral over ϕ is non-zero only when $m_0 = |m_j - m_k|$
- A resonance occurs when, $\omega_0 = |\omega_j - \omega_k|$ and $c_k^{(1)} \rightarrow \infty$

The above two criteria define selection rules for the instability of a fundamental flow. When such a resonance occurs between three different modes (fundamental mode and two inertial modes), it is called a *triadic resonance*. In practice, amplitudes never go to infinity, but get saturated due to non-linear effects and viscous dissipation.

Note that the above discussion leads to two distinct scenarios:

- The fundamental mode has an azimuthal dependence of m_0 . This will become unstable to two inertial modes and three will form a triadic resonance.

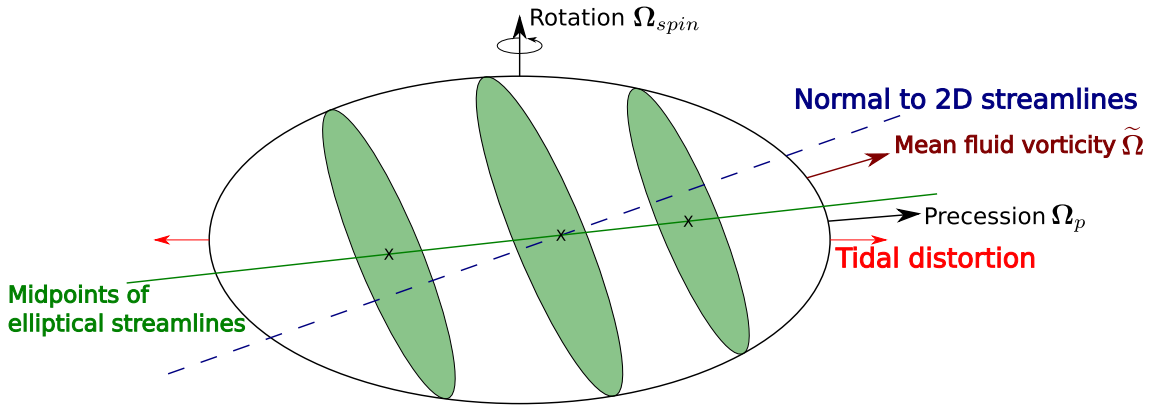


Figure 2.10: Poincaré flow in a precessing spheroid. Note the elliptical streamlines that are not perfectly aligned leading to a strain. Figure based on an illustration in [Le Bars et al. \(2015\)](#).

- The background flow with $m = 0$ can become unstable to only a single inertial mode, the coupling in this case being through the self-interaction of the inertial mode.

Below we discuss briefly how mechanical forcings give rise to inertial instabilities in astrophysical objects, which are often modelled as spheroids.

Precession

The basic flow response to a precessing spheroid is a solution given by [Poincaré \(1910\)](#), which looks like:

$$\mathbf{u} = \tilde{\boldsymbol{\Omega}} \times \mathbf{r} + \nabla\psi \quad (2.73)$$

where, $\tilde{\boldsymbol{\Omega}}$ is the mean vorticity of the flow and ψ is a potential needed to satisfy impenetrable boundary conditions. The flow consists of elliptical streamlines such that the centres of the ellipses are not aligned, shown in figure 2.10.

This flow can become unstable due to two reasons. One is the well-known elliptical instability, which is the instability of a strained vortex with elliptical streamlines. Such a strained vortex becomes unstable to two inertial modes, and the basic vortex flow forms a triadic resonance with the two inertial modes. This instability acts in the plane of the streamlines. A detailed review of the elliptical instability has been given by [Kerswell \(2002\)](#). The second is the shearing instability due to shear strain of misaligned centres, acting cross-plane. This shearing instability also gives rise to two inertial modes forming a triadic resonance. The detailed analysis of both mechanisms can be found in [Kerswell \(1993\)](#).

Tides

The excitation of inertial modes and their sustenance due to tidal forces takes place via the elliptical instability. In this case, it is called the *Tide-driven elliptical instability* or TDEI

(Le Bars et al. 2015). Since a tidal force deforms the fluid boundary periodically into a spheroid, the basic flow response is in the form of elliptical streamlines. These elliptical streamlines act like a strained vortex and become unstable to two inertial modes which form a triadic resonance with them. If the tidal deformation is due to a gravitational companion with orbital velocity $\mathbf{\Omega}_{orb}$ with respect to the reference frame of the outer boundary of the fluid (e.g: CMB in case of planets), then the corresponding elliptical distortion will also rotate with the same rate. The basic flow response is given by

$$\mathbf{u} = \left(1 - \frac{\Omega_{orb}}{\Omega}\right) \left(- (1 + \beta)x_2 \hat{\mathbf{e}}_1 + (1 - \beta)x_1 \hat{\mathbf{e}}_2\right) \quad (2.74)$$

where, x_1 and x_2 are the coordinates perpendicular to the rotation axis, and $\hat{\mathbf{e}}_1$ and $\hat{\mathbf{e}}_2$ are the respective unit vectors, with x_1 being along the major axis of the spheroid. β is the ellipticity of the spheroid, defined as $\beta = (a_1^2 - a_2^2)/(a_1^2 + a_2^2)$, a_1 and a_2 being the lengths of the major and minor axes, respectively.

Since, the excited inertial modes form a triadic resonance with the elliptical streamlines having an azimuthal symmetry $m_0 = 2$ and time dependence $\omega_0 = 2\Omega_{orb}$, thus they must satisfy $|m_1 - m_2| = 2$ and $\omega_1 \pm \omega_2 = 2\Omega_{orb}$. Now, since inertial modes must have $\omega \leq 2\Omega$, they can only be excited for $-2\Omega \leq \Omega_{orb} + \Omega \leq 2\Omega$ or $-\Omega \leq \Omega_{orb} \leq 3\Omega$.

Some of the relevant works in this regard are those by Craik (1989), Cébron et al. (2012a), Lacaze et al. (2004, 2005), Le Bars et al. (2007, 2010).

Libration

Libration or more specifically longitudinal libration refers to the modulation of the rotation rate of an astrophysical object. Mathematically, this refers to an outer boundary rotation of the form

$$\Omega = \Omega_0(1 + \epsilon \sin(f\Omega_0 t)). \quad (2.75)$$

ϵ and f are referred to as the libration amplitude and frequency, respectively. The basic flow is given by (Kerswell and Malkus 1998)

$$\mathbf{u} = \epsilon \sin(ft) \left(- (1 + \beta)x_2 \hat{\mathbf{e}}_1 + (1 - \beta)x_1 \hat{\mathbf{e}}_2\right) \quad (2.76)$$

The excitation of inertial modes takes place due to the elliptical instability, often called *libration-driven elliptical instability* or LDEI (Le Bars et al. 2015). The elliptical instability couples elliptical streamlines of the flow with $m = 2$ to two inertial modes. LDEI is excited only for $f < 4$, since inertial modes must have frequencies between $\pm 2\Omega$. The global analysis using inertial modes was done by Kerswell and Malkus (1998). Other works in this regard include Wu and Roberts (2013), Cébron et al. (2012a,b), Zhang et al. (2013) and Grannan et al. (2014).

A review of all the above methods of exciting inertial instabilities can be found in Le Bars et al. (2015).

2.8 Discussion

This chapter introduced the fundamentals of rotational fluid dynamics and the theory of inertial modes. We also reviewed inertial mode structures in spheres and spherical shells and how boundary effects can give rise to internal shear layers. Finally we explored the phenomenon of triadic resonances and how different excitation mechanisms give rise to inertial modes. These concepts, in particular those of inertial modes in spherical shells and the concept of triadic resonances will be used in the next chapter which studies the excitation of inertial modes in a spherical shell using only differential rotation.

3 The spherical Couette system

“I don’t believe in empirical science. I only believe in a priori truth.”

Kurt Gödel

This chapter introduces the reader to the spherical Couette system with some basic concepts like that of the Stewartson Layer. Some preliminary simulation results are also presented.

3.1 Introduction

The spherical Couette system consists of two concentric differentially rotating spheres with a fluid filled in the space in between. This is shown in figure 3.1. The outer and inner spheres have radii r_o and r_i , respectively. Generally, we shall use the subscript o for the outer sphere and i for the inner one.

The two spheres rotate with dimensional rotation rates of Ω_o and Ω_i . Using the gap-width $L = r_o - r_i$ as length scale and the viscous diffusion time $\tau_v = L^2/\nu$ as time-scale, these rates are parametrised with the following non-dimensional quantities

- the Ekman number $E = \nu/\Omega_o L^2 = 1/\Omega$, where Ω is the non-dimensional rotation rate of the outer boundary, and
- the differential rotation $\Delta\Omega/\Omega = (\Omega_i - \Omega_o)/\Omega_o$, often referred to as the Rossby number, Ro .

Thus, $\Delta\Omega/\Omega > 0$ implies that the inner sphere rotates faster than the outer sphere, while $\Delta\Omega/\Omega < 0$ implies that it rotates slower. All results are presented in the frame of reference rotating with the outer boundary.

3.2 Proudman solution and Stewartson Layers

This system was first studied by Proudman (1956), who gave an asymptotic solution for the case when the outer sphere is rapidly rotating and the differential rotation has a very

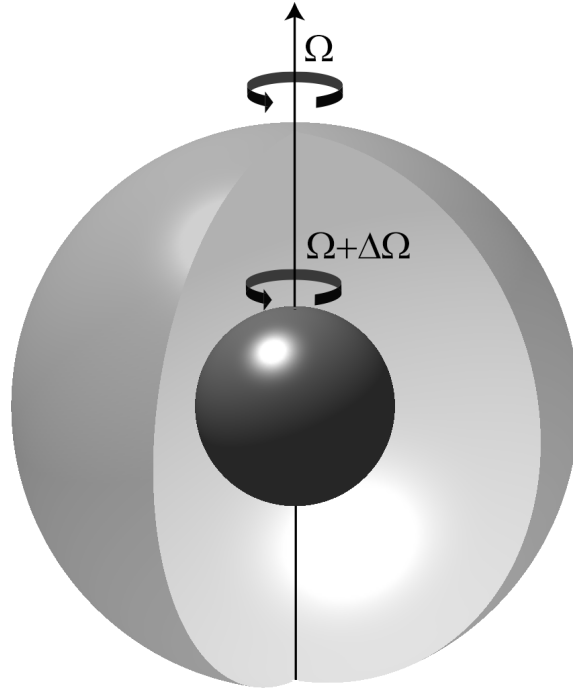


Figure 3.1: The spherical Couette system. The outer and inner spheres with radii r_o and r_i rotate with rotation rates Ω and $\Omega + \Delta\Omega$, respectively.

small value. In such a state the flow is laminar and axisymmetric and is described by the solution

$$u_\phi = \frac{s'(1 - s'^2)^{1/4}}{(1 - s'^2)^{1/4} + (1 - s'^2/r_i^2)^{1/4}}, \quad (3.1a)$$

$$\psi = \frac{s'^2}{2r_o^{1/2} \left((1 - s'^2)^{1/4} + (1 - s'^2/r_i^2)^{1/4} \right)}, \quad (3.1b)$$

where, $s' = s(1 - r_i/r_o)$ is the cylindrical radius scaled with the outer boundary radius and ψ is a stream function from which u_r and u_θ can be determined.

The form of the solution is shown in figure 3.2. The cylinder tangent to the inner sphere at the equator forms a very important boundary. This cylinder is often called the ‘tangent cylinder’ or TC. Fluid inside the TC rotates at roughly half the differential rotation rate, while fluid outside the TC is in solid body rotation with the outer boundary. Due to this discontinuity, a shear layer forms at the TC. While its presence was predicted by Proudman (1956), Stewartson (1966) was the first to describe the detailed structure. He found that it is, in fact, not a single but three nested layers which are illustrated in figure 3.3a.

The three layers are:

1. The outermost shear layer, seen in figure 3.3 in red with high density of contour lines in panel 3.3b, serves to adjust the jump in the fluid rotation rate $\bar{\omega}$ and it hosts most of the meridional circulation. The thickness of this layer scales as $E^{1/4}$.

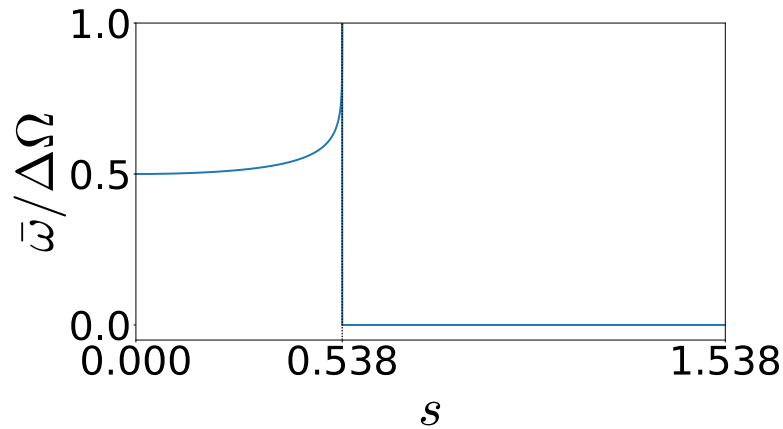


Figure 3.2: The Proudman solution. $\bar{\omega} = u_\phi/s$ represents the rotation rate of the fluid, scaled with the differential rotation $\Delta\Omega$. The fluid rotates at half the outer boundary rotation rate inside the tangent cylinder (marked with dotted line), while the fluid outside the tangent cylinder rotates in solid body rotation with the outer boundary.

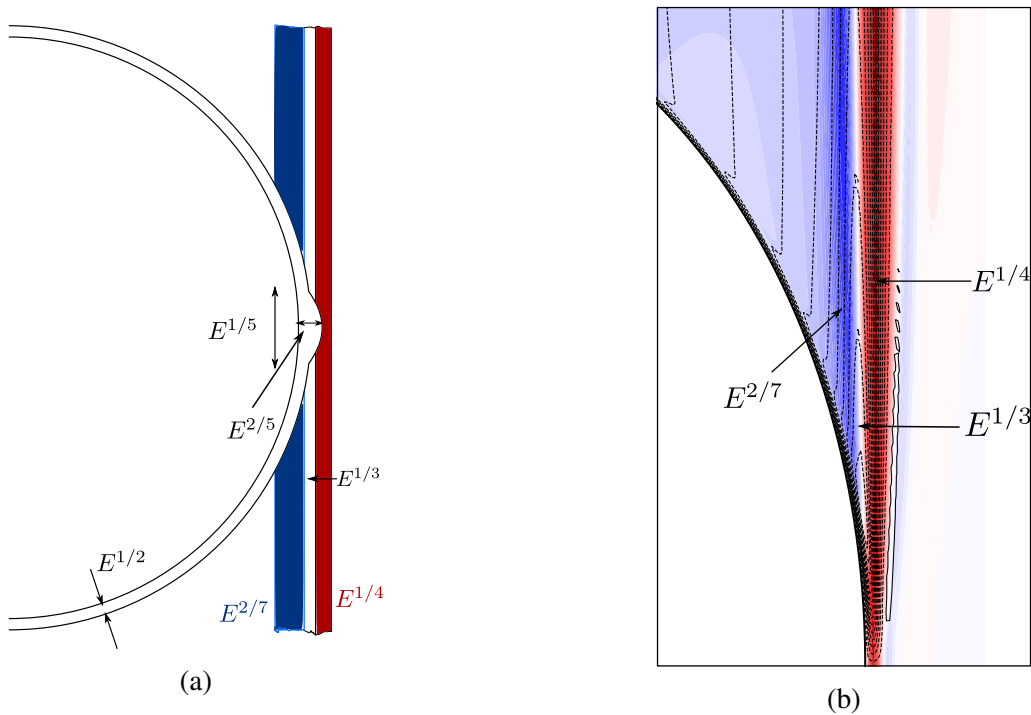


Figure 3.3: The structure of the nested shear layers described by Stewartson (1966). (a) shows a schematic of the nested shear layer structure, based on an illustration in Stewartson (1966). The Ekman layer on the inner sphere has also been shown. (b) shows the same structure in a simulation at $E = 3 \times 10^{-6}$. Colours show radial velocity, u_r - blue (red) being negative (positive). Contours show meridional circulation - solid lines indicate clockwise while dotted lines indicate counter-clockwise circulation.

2. The innermost shear layer, seen in a darker shade of blue, serves to remove a singularity in the first derivative of $\bar{\omega}$. Its thickness scales as $E^{2/7}$.
3. The thin layer in between, difficult to make out in figure 3.3b, serves to remove a discontinuity in the second derivative of $\bar{\omega}$. Its thickness scales as $E^{1/3}$.

3.3 Stewartson layer instabilities

In the absence of any external forces, the instabilities in a rotating system can be of broadly two types - the first is due to the violation of the stability criterion of [Rayleigh \(1917\)](#), $\partial(\bar{\omega}s^2)/\partial s > 0$ and second is in the form of waves drifting in azimuth due to an instability of a shear flow ([Busse 1968](#)). The first type occurs in a classical Taylor-Couette setup with two concentric differentially rotating cylinders in the form of Taylor vortices ([Taylor 1917](#)). This is an extremely well-studied system and one can see [Chossat and Iooss \(1994\)](#) for details. For a spherical Couette setup, one can get either type depending on the gap-width. For a narrow gap, the first non-axisymmetric instabilities occur in the form of Taylor rolls as in the Taylor-Couette setup. For a wide gap, the instabilities take the form of drifting waves caused by shear flow instabilities. This dependence on gap-width was explored by [Egbers and Rath \(1995\)](#) as well as [Hollerbach et al. \(2006\)](#).

Instabilities of shear layers in rotating fluids were studied by [Busse \(1968\)](#), who found a scaling law for a critical Rossby number, $|Ro_c| \sim E^{3/4}$ for rotating cylinders, without any difference in the nature of instabilities for $Ro > 0$ or $Ro < 0$. [Hide and Titman \(1967\)](#) and [Früh and Read \(1999\)](#) performed experiments with rapidly rotating cylindrical setups, but with a difference in the way the differential rotation was applied. [Hide and Titman \(1967\)](#) used a disc in the middle of the cylinder while [Früh and Read \(1999\)](#) used a split disk setup with a disk embedded in each of the end boundaries of the cylinder. The setups are shown in figure 3.4. Due to a difference in the fluid flow inside and outside the tangent cylinders (tangent to the disks and parallel to rotation axis), shear layers form on the TC. These layers were first described by [Stewartson \(1957\)](#) and are therefore also known as Stewartson layers (vertical dashed lines in figure 3.4).

[Früh and Read \(1999\)](#) (setup (b) in figure 3.4) observed no difference in the nature of instabilities of the Stewartson layer for $Ro > 0$ or $Ro < 0$, which was in accordance with the prediction of [Busse \(1968\)](#). [Hide and Titman \(1967\)](#) (setup (a) in figure 3.4), however, found that the sign of differential rotation matters - one gets high wavenumber instabilities with $Ro > 0$, while for $Ro < 0$, they found an instability with azimuthal wavenumber $m = 1$.

This dichotomy in instabilities is also observed for the spherical Couette flow ([Hollerbach 2003](#)). For $Ro > 0$, one finds large wavenumber instabilities while for $Ro < 0$, one finds instabilities with small wavenumbers. Especially, for low differential rotation, one can find an $m = 1$ instability which seems to be quite special, as will be explained later in chapter 6 while discussing the onset of inertial modes.

In general, Stewartson layers occur only when the outer boundary is rapidly rotating. There are several different kinds of instabilities that take place when the outer boundary rotates slowly or at intermediate rates. An overview of parameter regimes is thus, required. This has been described below.

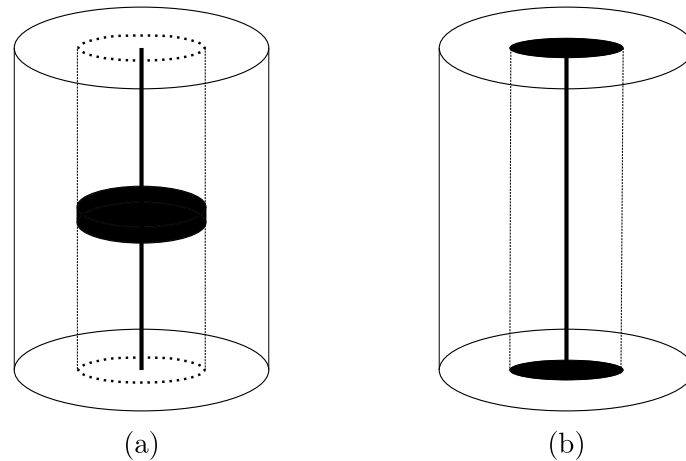


Figure 3.4: Experimental setups of (a) [Hide and Titman \(1967\)](#) and (b) [Früh and Read \(1999\)](#). [Hide and Titman \(1967\)](#) used a central disc setup and observed a dichotomy in the instabilities depending on the sign of differential rotation, while no such dichotomy was observed by [Früh and Read \(1999\)](#) who used a split disc setup. The vertical dotted lines show the position of the Stewartson layer. Figure based on [Hollerbach \(2003\)](#).

3.4 Overview of parameter regimes

The most comprehensive study of the instabilities of the spherical Couette flow for a wide gap of $r_i/r_o = 0.35$ was performed by [Wicht \(2014\)](#). The main results are summarised in figure 3.5. The salient points to note are:

- For very low outer boundary rotation ($\Omega \leq 1$ or $E \geq 1$), the first instability takes place in the form of a radial jet, as found by [Hollerbach \(2003\)](#), [Hollerbach et al. \(2006\)](#), [Guervilly and Cardin \(2010\)](#), [Gissinger et al. \(2011\)](#).
- For intermediate outer boundary rotations ($1 < \Omega < 10^3$ or $10^{-3} < E < 1$), the instabilities for $Ro > 0$ are similar to the equatorial jet instabilities observed for low outer boundary rotation, while instabilities for $Ro < 0$ are in the form of double-roll and helical instabilities.
- For high outer boundary rotation ($\Omega > 10^3$ or $E < 10^{-3}$), the basic flow state is geostrophic and the instabilities are in the form of Stewartson layer instabilities, with high wavenumbers observed for $Ro > 0$ and low wavenumbers for $Ro < 0$.
- For very high outer boundary rotation ($\Omega > 3 \times 10^5$ or $E < 3 \times 10^{-6}$), the Coriolis force seems to dominate dynamics and the wavenumber dichotomy between $Ro > 0$ and $Ro < 0$ seems to vanish.

These results are discussed in more detail below.

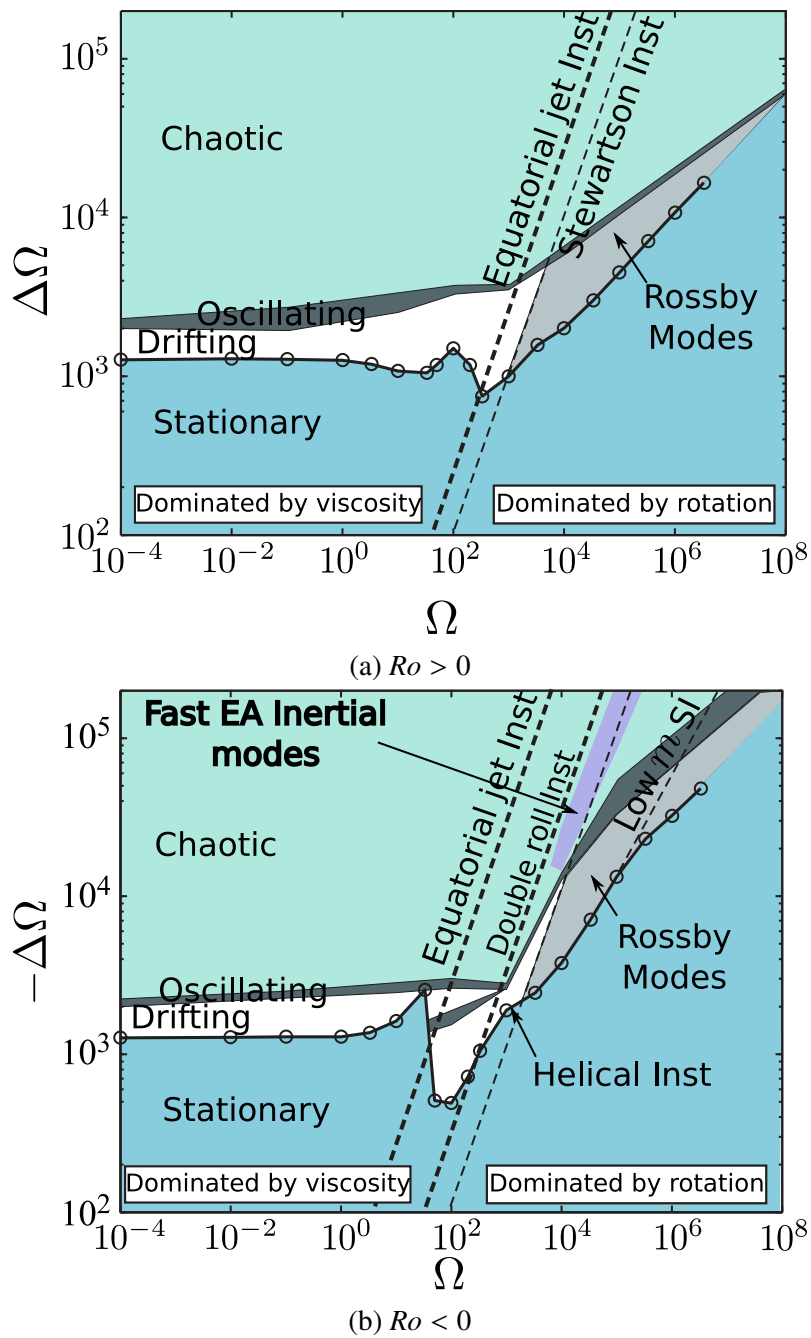


Figure 3.5: Summary of instabilities for the spherical Couette flow across different parameter regimes. Note the similarities for small and very large $Ro = \Delta\Omega/\Omega$ and clear differences for intermediate Ro between (a) $Ro > 0$ and (b) $Ro < 0$. Figure adapted from one by Johannes Wicht.

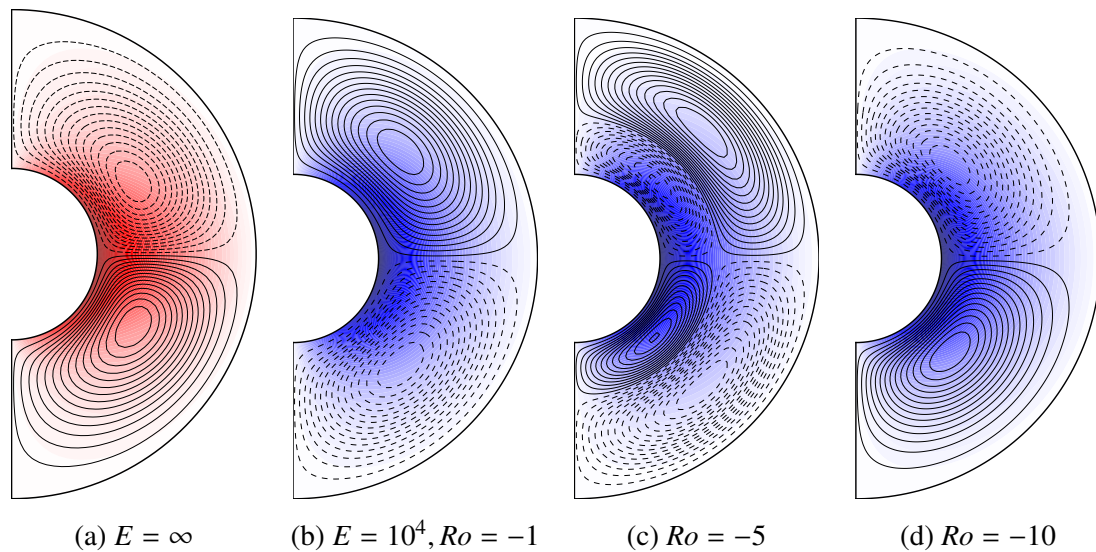


Figure 3.6: The axisymmetric state for $\Omega \leq 1$ or $E \geq 1$. The colours show the zonal velocity, u_ϕ , with red being positive and blue negative, while the contours show meridional circulation, with solid lines indicating clockwise and dotted lines indicating counter-clockwise circulation. (a) is for a case where the outer boundary is stationary and thus, $E = \infty$ or $\Omega = 0$. The case for positive differential rotation is the same as (a) even when the outer boundary rotates at a small rate. However, there is a change in the direction of the meridional circulation when $Ro < 0$. This change is shown in (b), (c) and (d) for $E = 10^4$ or $\Omega = 10^{-4}$.

3.4.1 Very low outer boundary rotation: $\Omega \leq 1$ or $E \geq 1$

Axisymmetric state

The axisymmetric solution in this case mostly consists of the inner sphere driving zonal flow and of two rolls of meridional circulation, similar to Taylor rolls of the Taylor-Couette setup. This is illustrated in figure 3.6, which shows the background zonal velocity map and the meridional circulation due to Ekman pumping. For the case when the outer boundary is stationary, there is absolutely no difference in the axisymmetric states for both signs of differential rotation. However, when the outer boundary rotates slowly, the initial directions of meridional circulation depends on the sign of Ro , i.e., whether the inner sphere rotates faster or slower with respect to the outer. For $Ro < 0$, as the magnitude of Ro is increased, there is a reversal in the direction of meridional circulation, as illustrated in panels (b), (c) and (d) of figure 3.6. For $Ro > 0$, there is no such effect.

Non-axisymmetric instabilities

As mentioned before, when the outer sphere is held stationary, there is absolutely no dependence of the dynamics of the fluid on the sense of inner sphere rotation. Also, we saw that when the outer sphere rotates slowly, both senses of differential rotation resemble each other at high values of differential rotation. Thus, for the non-axisymmetric instabilities, the sense of inner sphere rotation does not matter when the outer boundary



Figure 3.7: The radial jet that emergence due to rotation of the inner sphere when the outer boundary rotates very slow or is stationary. Shown here are isosurfaces of radial velocity, u_r , for $\Delta\Omega = 1000$ and $E = \infty$.

rotates slowly. Due to the outward flow of the meridional circulation, a radial jet starts to develop as illustrated in figure 3.7, which is axisymmetric in the beginning, but soon falls prey to a non-axisymmetric instability with azimuthal wavenumber $m_c = 3$. The jet develops a wavy nature that is equatorially antisymmetric, while the background flow is still symmetric with respect to the equator. As the differential rotation is increased, the radial jet gets progressively thinner and breaks down and becomes turbulent at very strong rotation rates.

3.4.2 Intermediate outer boundary rotation rate: $1 < \Omega < 10^3$ or $10^{-3} < E < 1$

Axisymmetric state

The axisymmetric state here resembles that of the case with very low outer boundary rotation, but Coriolis effects already start to play a role in making the flow more geostrophic as seen in figure 3.8. The direction and structure of meridional circulation depends on the sign of the differential rotation, with $Ro < 0$ displaying a double-roll structure.

Non-axisymmetric state

The non-axisymmetric states show a dichotomy for different signs of differential rotation. For $\Delta\Omega/\Omega = Ro > 0$, one finds the equatorial jet instability again, while for $Ro < 0$, one gets two special instabilities, called ‘double-roll’ and ‘helical’ instabilities, respectively by [Wicht \(2014\)](#). Their structures are shown in figure 3.9. The equatorial jet instability takes over after $|Ro|$ reaches a high value for negative differential rotation.

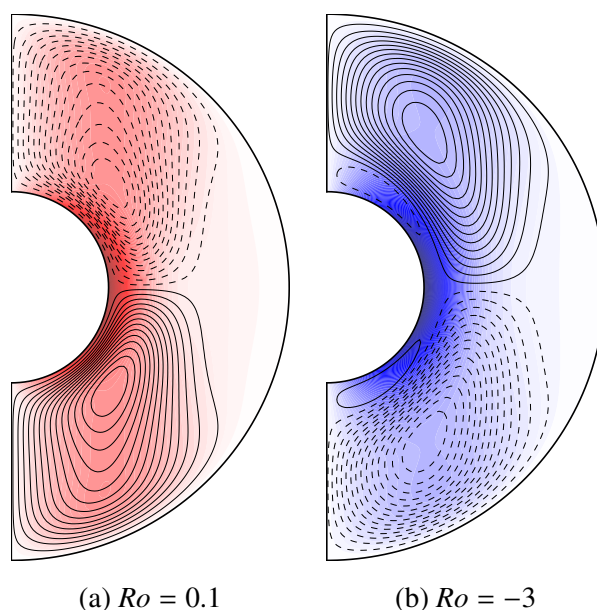


Figure 3.8: The axisymmetric state for intermediate values of outer boundary rotation. Shown above are flow solutions at $E = 10^{-2}$. The Taylor-roll like structure of the meridional circulation is reminiscent of the case with outer boundary stationary, but Coriolis effects can be seen starting to play a role in making the flow more geostrophic. Also, the cases for $Ro > 0$ and $Ro < 0$ are different, with $Ro < 0$ showing a double-roll structure.

3.4.3 High outer boundary rotation: $10^3 < \Omega < 3 \times 10^5$ or $3 \times 10^{-6} < E < 10^{-3}$

Axisymmetric state

For an intermediate value of outer boundary rotation, the axisymmetric flow solution becomes progressively geostrophic as one increases Ω from 10^3 towards higher values, or equivalently decreases E from 10^{-3} onwards. This progressive transition towards a more geostrophic regime can be seen in figure 3.10, where the colors of zonal velocity as well as the contours of meridional circulation can be seen getting progressively aligned with the rotation axis. The Stewartson shear layer adjusting the flow inside and outside the tangent cylinder becomes progressively narrower and becomes more localised on it.

Non-axisymmetric state

The case for high outer boundary rotation shows the dichotomy for different signs of differential rotation, mentioned towards the beginning of this section. The azimuthal wavenumber, m , for the first non-axisymmetric instability is high for $Ro > 0$ while low wavenumber instabilities set in for $Ro < 0$. In particular, an $m = 1$ instability recurs for a range of Ekman numbers. In addition, equatorially antisymmetric inertial modes are a dominant large scale feature in this regime as well as for lower Ekman numbers.

The theory of inertial modes has already been discussed in chapter 2. A study of inertial modes in this system and their onset mechanism will be provided in the chapter 6.

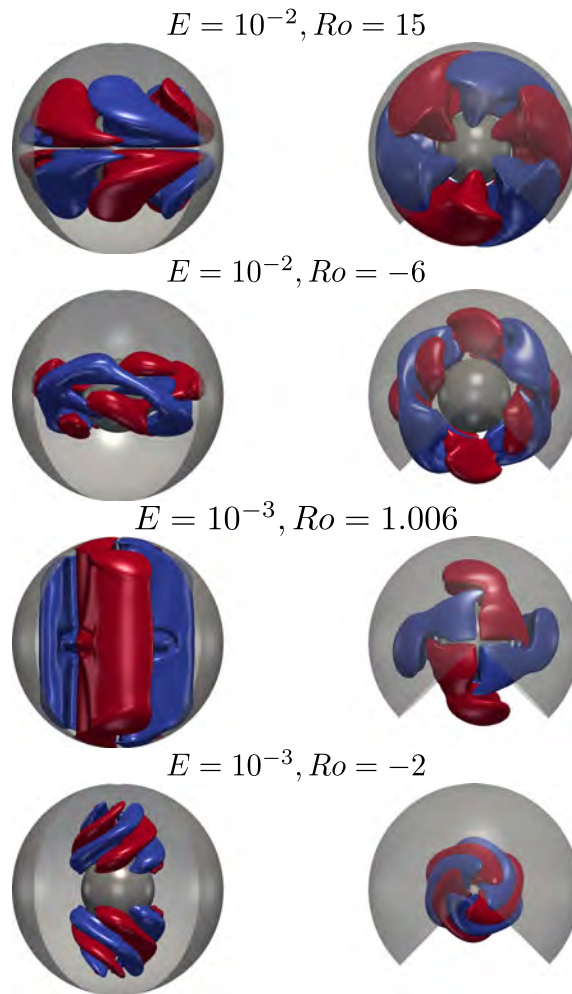


Figure 3.9: Different instabilities at onset for intermediate outer boundary rotation rates. There is a clear difference in the nature of instabilities at onset. The ‘double-roll’ and ‘helical’ instabilities can be seen for negative differential rotation for $E = 10^{-2}$ and 10^{-3} , respectively.

3.4.4 Very high outer boundary rotation: $\Omega > 3 \times 10^5$ or $E < 3 \times 10^{-6}$

Axisymmetric state

The dynamics here are dominated by Coriolis forces due to the high outer boundary rotation. This also gives rise to a strong Taylor-Proudman constraint which leads to the basic axisymmetric state being geostrophic. The solution is the one given by Proudman (1956) with a Stewartson layer located on the tangent cylinder. The instabilities taking place in the system are due to the destabilisation of this layer. The axisymmetric state at $E = 3 \times 10^{-6}$ is shown in figure 3.12.

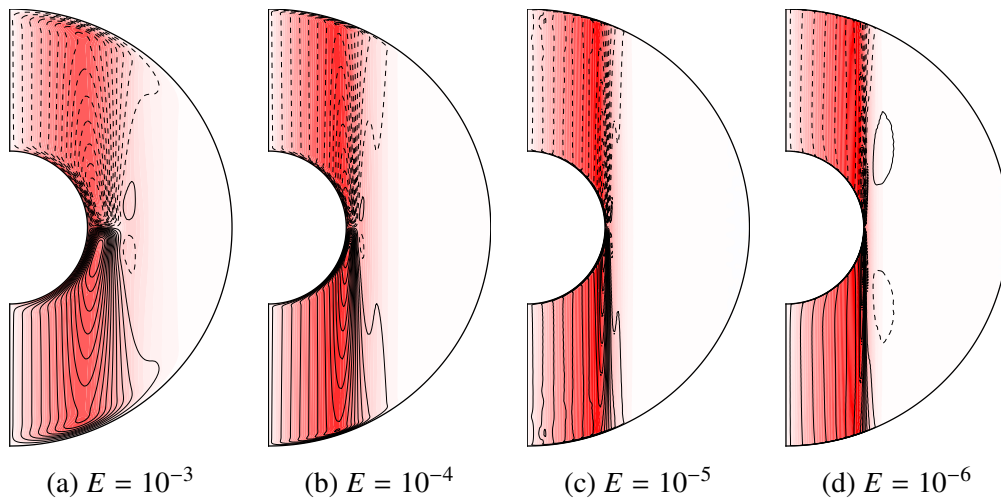


Figure 3.10: Axisymmetric solutions at different outer boundary rotation rates. As the outer boundary rotates faster, the flow solution progressively approaches a geostrophic regime. The colours show zonal velocity, u_ϕ while the contours show meridional circulation, solid lines showing clockwise and dotted lines showing anti-clockwise circulation. The flow can be seen approaching the strong shear layer solution given by Proudman (1956) at $E = 10^{-5}$.

Non-axisymmetric state

For a very high outer boundary rotation, the effect of the Coriolis force is so large that the nature of the fundamental instabilities are again independent of the sign of differential rotation. This is shown in figure 3.13 which shows the solutions at onset for both signs of differential rotation. The structures in both cases are nearly geostrophic and have high azimuthal wavenumbers.

For very high values of outer boundary rotation rate, the E dependence of the critical quantities, namely, Ro_c and m_c start to follow simple scaling laws, at least in the parameter regime investigated. These scaling laws are given as:

$$Ro_c \propto \begin{cases} E^{0.63}, & \text{for } Ro > 0 \\ E^{0.66}, & \text{for } Ro < 0 \end{cases} \quad (3.2a)$$

$$m_c \propto E^{-0.3} \quad (3.2b)$$

The similarity in scaling laws and the nature of solutions suggest that the sign of differential rotation ceases to matter, at least for the first instability, when the outer boundary is rotating at a very high rate. Note that even though the scaling of Ro_c is similar, the values are different with higher $|Ro_c|$ values needed for $Ro < 0$.

3.5 Discussion

Figure 3.14 shows the critical values for differential rotation and azimuthal wavenumbers at onset. The vertical lines separate the regions where the outer boundary rotation is either

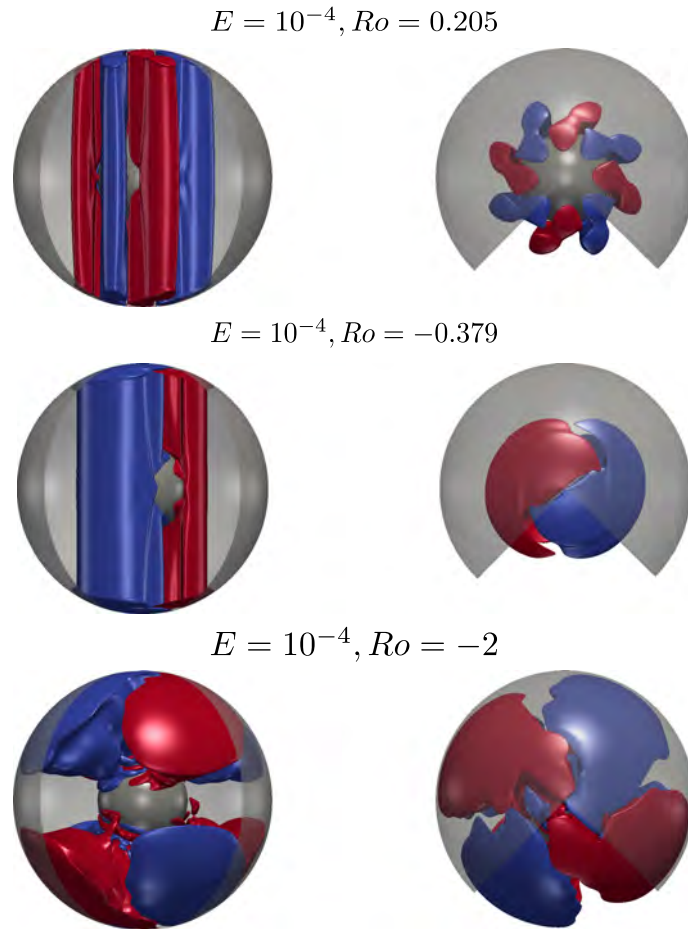


Figure 3.11: Different instabilities at $E = 10^{-4}$. The solutions at onset at $Ro = 0.205$ and $Ro = -0.379$ show a clear dichotomy with an $m = 1$ mode dominating the solution for $Ro < 0$. An equatorially antisymmetric inertial mode is seen for high differential rotation values for $Ro < 0$. Shown here are isosurfaces of cylindrically radial velocity, u_s with red being positive (outwards) and blue negative (inwards).

very low or very high, rendering the direction of inner sphere rotation rather irrelevant for the onset of the first instability, in terms of critical values or scaling of the critical values. In between these two extremes lies a region where the sign of differential rotation determines the dynamics of the fluid. In particular, an $m = 1$ branch suddenly seems to appear for $Ro < 0$, whose explanation has been sought by [Hollerbach \(2003\)](#) as well as [Schaeffer and Cardin \(2005\)](#). For more details about the instabilities the reader is referred to [Wicht \(2014\)](#).

The spherical Couette system provides a host of different instabilities as well as interesting fluid dynamic phenomena such as inertial modes as well as turbulence. In the following chapters, we will study several other features of it, not just in terms of hydrodynamics, but also in terms of hydromagnetic instabilities, including dynamo mechanisms.

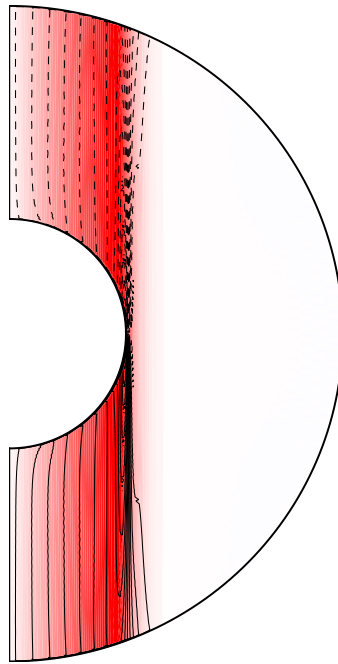


Figure 3.12: The axisymmetric state for high outer boundary rotation rate. Here, $E = 3 \times 10^{-6}$ and $Ro = \Delta\Omega/\Omega = 3 \times 10^{-6}$. The solution is the one given by Proudman (1956), with fluid inside the tangent cylinder rotating at half the rotation rate of the differential rotation, while fluid outside the TC rotates in solid body rotation with the outer boundary. The Stewartson layer is located on the TC.

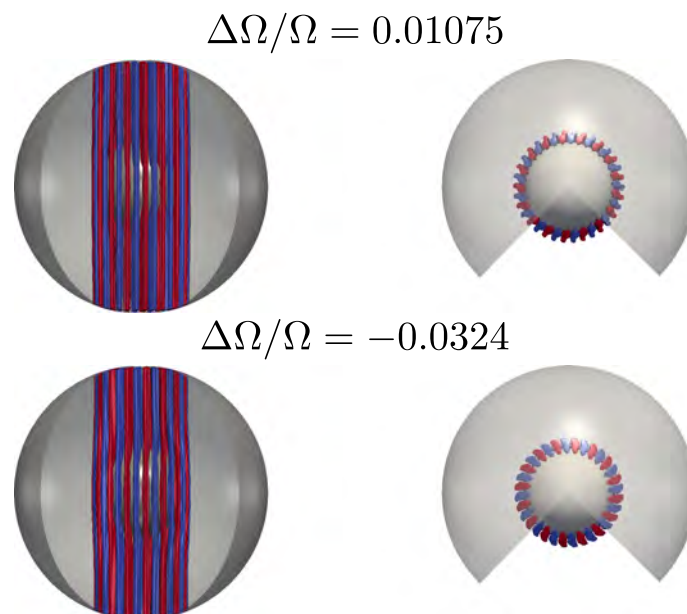
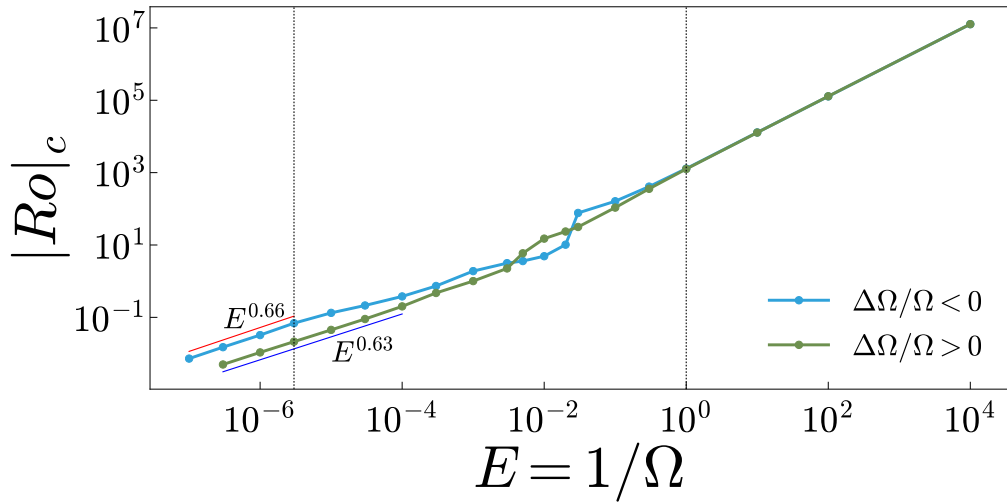
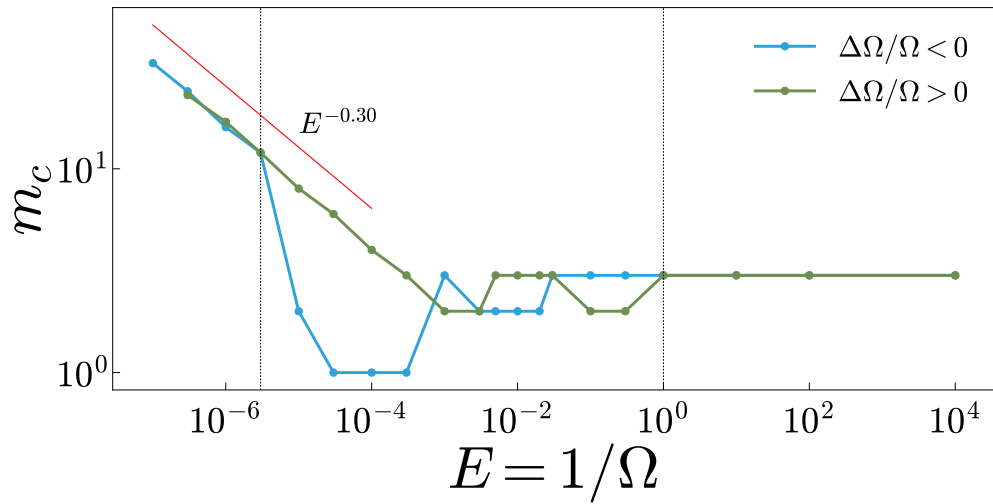


Figure 3.13: Solutions at onset at $E = 10^{-6}$. Shown here are isosurfaces of cylindrically radial velocity, u_s , with red being positive (outward) and blue being negative (inward). Note the similarity between the solutions at onset for the two signs of differential rotation under high outer boundary rotation. Also refer to figure 22 of Wicht (2014).



(a)



(b)

Figure 3.14: Critical values for onset of the first non-axisymmetric instabilities (a) shows the magnitude of critical differential rotation, quantified with $R_{o_c} = (\Delta\Omega/\Omega)_c$, while (b) shows the azimuthal wavenumbers, m_c , at onset. The vertical lines separate regions of very low and very high outer boundary rotation where there is seemingly no dichotomy between the two signs of differential rotation.

4 Numerical methods and diagnostics

“Young man, in mathematics you don’t understand things. You just get used to them.”

John von Neumann

This chapter provides an overview of how the spherical Couette system is simulated using pseudo-spectral methods on a spherical grid. We use the 3D spherical shell MHD code MagIC (Wicht 2002) to simulate the system, some details of which have also been provided. This chapter further discusses how the outputs of the code are analysed to provide useful information, such as identification of inertial modes and building spectrograms to compare with experiments.

4.1 Numerical methods

4.1.1 Non-dimensionalisation

To simulate the spherical Couette system, we solve the Navier-Stokes and continuity equation. When magnetic fields are involved we also solve the induction equation and Maxwell’s equations (introduced in chapter 8). These equations are solved in spherical coordinates (r, θ, ϕ) using the width of the spherical shell, $L = r_o - r_i$ is as the length scale and the viscous diffusion time $\tau_v = L^2/\nu$ is as the time scale. The magnetic field is non-dimensionalised using the quantity $(\rho\mu_0\lambda\Omega)^{1/2}$, where $\lambda = 1/\mu_0\sigma$ is the magnetic diffusivity, μ_0 and σ being the magnetic permittivity of vacuum and conductivity of the fluid, respectively. Using these, the non-dimensional forms of the equations are

$$E \left(\frac{\partial \mathbf{u}}{\partial t} + \mathbf{u} \cdot \nabla \mathbf{u} \right) = -\nabla p - 2\hat{\mathbf{z}} \times \mathbf{u} + \frac{1}{Pm} (\nabla \times \mathbf{B}) \times \mathbf{B} + E \nabla^2 \mathbf{u}, \quad (4.1)$$

$$\frac{\partial \mathbf{B}}{\partial t} = \nabla \times (\mathbf{u} \times \mathbf{B}) + \frac{1}{Pm} \nabla^2 \mathbf{B}, \quad (4.2)$$

$$\nabla \cdot \mathbf{u} = 0 \quad , \quad \nabla \cdot \mathbf{B} = 0 \quad (4.3)$$

where, $E = \nu/\Omega_o L^2 = 1/\Omega$ is the Ekman number and $Pm = \nu/\lambda$ is the magnetic Prandtl number. Here, Ω_o is the rotation rate of the outer boundary and Ω is its non-dimensional form.

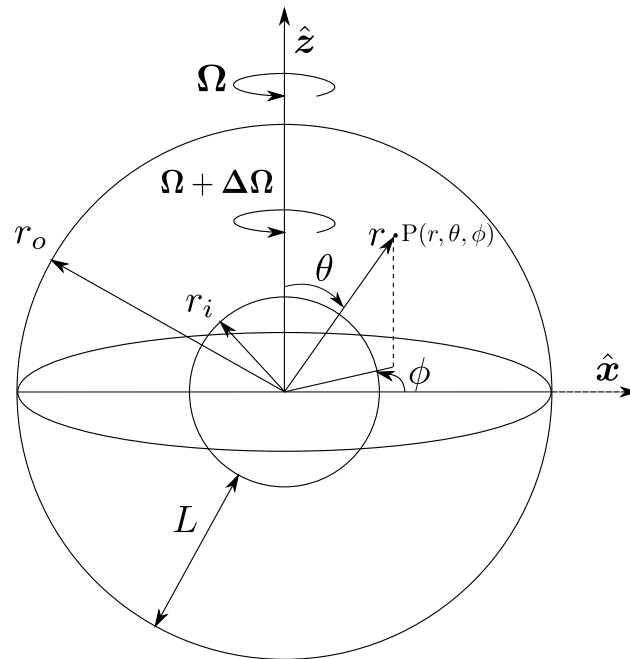


Figure 4.1: The spherical shell geometry used for simulating the spherical Couette system. The spherical coordinates are shown using a point $P(r, \theta, \phi)$. The outer boundary rotates along \hat{z} with a rotation rate Ω while the inner boundary rotates with a rotation rate $\Omega + \Delta\Omega$. $L = r_o - r_i$ is used as the length scale, where r_o and r_i denote the radii of outer and inner boundaries, respectively.

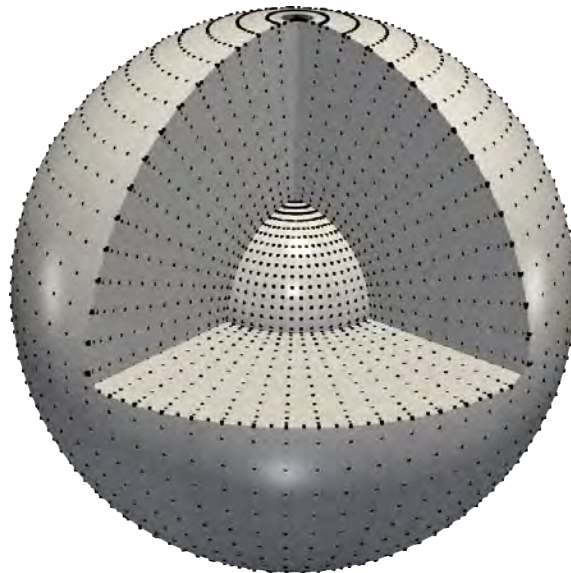


Figure 4.2: The spherical grid in (r, θ, ϕ) used for simulating the spherical Couette system. The N_ϕ points in longitude are equidistant in angles from 0 to 2π , the N_θ points in latitude are zeros in θ of the Legendre polynomial of degree N_θ in $\cos \theta$, while the N_r radial grid points are the extrema of the Chebyshev polynomial of order $N_r - 1$.

Boundary conditions

The above equations are combined with the following boundary conditions:

- **Mechanical** The mechanical boundary conditions are no-slip at the boundaries, thus,

$$\begin{aligned} \mathbf{u}(r_o) &= 0, \\ \mathbf{u}(r_i) &= (0, 0, \Delta\Omega r_i \sin \theta), \end{aligned} \quad (4.4)$$

where r_i and r_o are now in non-dimensional units.

- **Magnetic** We treat the regions outside the two boundaries as electrical insulators in this study. This implies the boundary condition that the magnetic field \mathbf{B} must be continuous across the boundary.

4.1.2 Poloidal/Toroidal decomposition

The spherical Couette system is simulated using pseudo-spectral methods on a spherical grid, shown in figure 4.2. The first step in the process is a poloidal/toroidal decomposition of vectors. Velocity and magnetic field vectors, being solenoidal, are decomposed in terms of two scalar potentials - the toroidal potentials (denoted here by z and g) and the poloidal potentials (denoted here by w and h)

$$\begin{aligned} \mathbf{u} &= \nabla \times \nabla \times w \hat{\mathbf{r}} + \nabla \times z \hat{\mathbf{r}}, \\ \mathbf{B} &= \nabla \times \nabla \times g \hat{\mathbf{r}} + \nabla \times h \hat{\mathbf{r}}. \end{aligned} \quad (4.5)$$

Note that the different components can be obtained from the scalar potentials as

$$\begin{aligned} u_r &= -\nabla_H^2 w, \\ u_\theta &= \frac{1}{r \sin \theta} \left(\frac{\partial}{\partial r} \sin \theta \frac{\partial w}{\partial \theta} + \frac{\partial z}{\partial \phi} \right), \\ u_\phi &= \frac{1}{r \sin \theta} \left(\frac{\partial}{\partial r} \frac{\partial w}{\partial \theta} - \sin \theta \frac{\partial z}{\partial \theta} \right), \end{aligned} \quad (4.6)$$

where,

$$\nabla_H^2 = \frac{1}{r^2} \left(\frac{1}{\sin \theta} \frac{\partial}{\partial \theta} \sin \theta \frac{\partial}{\partial \theta} + \frac{1}{\sin^2 \theta} \frac{\partial^2}{\partial \phi^2} \right)$$

is the horizontal part of the Laplacian operator. The expressions for the scalar potentials in terms of the vector fields are

$$\begin{aligned} \hat{\mathbf{r}} \cdot \mathbf{u} &= -\nabla_H^2 w, \\ \hat{\mathbf{r}} \cdot (\nabla \times \mathbf{u}) &= -\nabla_H^2 z. \end{aligned} \quad (4.7)$$

Using the above expressions, one can derive the evolution equations for the poloidal and toroidal potentials for velocity by substituting the expressions in the radial component of the Navier-Stokes equation and the curl of the Navier-Stokes equation, respectively. Similarly, the evolution equations for the magnetic field potentials can be obtained from the radial components of the induction equation (4.2) and the curl of the induction equation, respectively.

Angular expansion

The scalar potentials and other scalars in the equations are expanded in spherical surface harmonics, $Y_{lm}(\theta, \phi) = P_{lm}(\cos \theta)e^{im\phi}$

$$w = \sum_{l=0}^{l_{max}} \sum_{m=0}^l w_{lm}(r) Y_{lm}(\theta, \phi) \quad (4.8)$$

where, l and m are degree and order of spherical harmonics and P_{lm} is an associated Legendre polynomial. l_{max} represents the maximum degree of expansion.

The transformation from $(r, \theta, \phi) \rightarrow (r, l, m)$ is performed in two steps. First the transformation $(r, \theta, \phi) \rightarrow (r, l, \phi)$ takes place through a Legendre transform using Gauss-Legendre quadrature. Thereafter, the transformation $(r, l, \phi) \rightarrow (r, l, m)$ takes place through a Fourier transform.

The grid in longitude has a uniform spacing of $2\pi/N_\phi$, where N_ϕ is the total number of longitudinal grid points. The grid in latitude uses the Gauss-Legendre nodes which are zeros in θ of the Legendre polynomial $P_{N_\theta}(\cos \theta)$, where N_θ is the number of latitudinal grid points. Usually, $N_\theta = N_\phi/2$ to ensure equatorial isotropy. In addition, $l_{max} = [\min(2N_\theta, N_\phi)]/3$ is used to avoid aliasing.

Radial expansion

The coefficients of spherical harmonics (e.g. $w_{lm}(r)$) are expanded in radius using a Chebyshev basis. Chebyshev polynomials are given by

$$C_n(x) = \cos(n \cos^{-1}(x)), \quad -1 \leq x \leq 1 \quad (4.9)$$

The scalars are expanded in radius as

$$w_{lm}(r) = \sum_{n=0}^N w_{nlm} C_n(r) \quad (4.10)$$

The radius ($r_i \leq r \leq r_o$) is mapped onto the Chebyshev domain ($-1 \leq x \leq 1$) using a linear mapping

$$x(r) = 2 \frac{r - r_i}{r_o - r_i} - 1 \quad (4.11)$$

The N_r grid points in radius are chosen to be the extrema of the Chebyshev polynomial C_{N_r-1} , given by

$$x_k = \cos\left(\pi \frac{k-1}{N_r-1}\right), \quad k = 1, 2, 3, \dots, N_r \quad (4.12)$$

This makes it easier to evaluate the expansion as the values of C_n at these points are given by

$$C_n(x_k) = \cos\left(\pi \frac{n(k-1)}{N_r - 1}\right) \quad (4.13)$$

Substituting this in the radial expansion, we get

$$w_{lm}(x_k) = \sum_{n=0}^N w_{nlm} \cos\left((k-1) \frac{n\pi}{N_r - 1}\right) \quad (4.14)$$

which is a cosine transform and can be easily evaluated using Fast Fourier Transforms (FFTs). The radial dealiasing condition is $N_r > N$.

4.1.3 Non-linear terms and time-stepping

The terms which do not decouple in spherical harmonics, which include the Coriolis term and the non-linear terms, are evaluated in real space. For example, the components of the term $\mathbf{u} \cdot \nabla \mathbf{u}$ is evaluated using the components of \mathbf{u} and the components of $\nabla \mathbf{u}$ in real space, with the gradients in $\nabla \mathbf{u}$ computed in spectral space.

The time-stepping is performed using a mixed implicit/explicit method. The terms that decouple in spherical harmonics are treated implicitly. Other terms, namely, the Coriolis and non-linear terms are treated explicitly. For a general partial differential equation in time

$$\frac{\partial}{\partial t} x + \mathcal{I}(x, t) = \mathcal{E}(x, t) \quad (4.15)$$

where, \mathcal{I} and \mathcal{E} denote the implicit and explicit terms. The implicit time-stepping is

$$\frac{x(t + \Delta t) - x(t)}{\Delta t} = -\alpha \mathcal{I}(x, t + \Delta t) - (1 - \alpha) \mathcal{I}(x, t) \quad (4.16)$$

where, $\alpha = 0.5$ gives the classic Crank-Nicolson scheme. For the explicit time-stepping a second order Adams-Bashforth scheme is used.

$$\frac{x(t + \Delta t) - x(t)}{\Delta t} = \frac{3}{2} \mathcal{E}(x, t) - \frac{1}{2} \mathcal{E}(x, t - \Delta t) \quad (4.17)$$

Combining the two, the final time-stepping scheme is given by

$$\frac{x(t + \Delta t)}{\Delta t} + \alpha \mathcal{I}(x, t + \Delta t) = \frac{x(t)}{\Delta t} - (1 - \alpha) \mathcal{I}(x, t) + \frac{3}{2} \mathcal{E}(x, t) - \frac{1}{2} \mathcal{E}(x, t - \Delta t) \quad (4.18)$$

In our numerical scheme, such an equation is solved for each scalar coefficient like w_{nlm} .

For further details on numerical MHD simulations in spherical shells, one can refer to [Christensen and Wicht \(2007\)](#).

The Courant–Friedrichs–Lewy (CFL) condition

This is a necessary condition for the convergence of numerical solutions of partial differential equation formulated by Courant et al. (1928). For a discrete length scale in Δx and a discrete time step Δt and velocity u , the generic condition in one dimension can be written as

$$C = \frac{u\Delta t}{\Delta x} < C_{max}, \quad (4.19)$$

where C is called the Courant number and C_{max} depends on the problem.

In our numerical scheme we must take care of two different types of velocities - the fluid velocity $|\mathbf{u}|$, the Alfvén velocity $|\mathbf{u}_{alf}|$ (when magnetic field is present, defined in chapter 8), two different length scales - radial Δr and horizontal Δh and the rotation time scale. The maximum velocity and smallest length scale over the whole system is used to compute the necessary time step Δt needed to satisfy the CFL condition. This is also compared to the rotation rate of the system so that the rotational physics as well as the fastest velocities are correctly resolved in the solution.

4.1.4 The code

The code we use for simulations is called MagIC (Wicht 2002). It is open source and freely available at <https://github.com/magic-sph/magic>. The website (magic-sph.github.io) as well as the manual provides details of the equations and their numerical implementation.

Because of a pseudo-spectral implementation, MagIC needs to transform quantities back-and-forth between real space and spectral space. The transforms along with their time-complexities for computation are given below:

- Radial direction: Chebyshev transform, can be modelled as a discrete cosine transform which can be computed using FFT algorithms. Complexity: $\mathcal{O}(N_r \log N_r)$
- Longitudinal direction: Fourier transform, computed using FFT. Complexity: $\mathcal{O}(N_\phi \log N_\phi)$
- Latitudinal direction: Legendre transform, computed using Gauss quadrature. Complexity: $\mathcal{O}(N_\theta^3)$

MagIC uses a hybrid MPI + OpenMP parallelization with MPI between nodes and shared memory parallelization (OpenMP) inside each node. The grid is partitioned into spherical shells and is distributed among different MPI ranks. Among the individual ranks, the computations in l, m space is parallelised using OpenMP, since spherical harmonic modes are decoupled. The Chebyshev transform, however, needs communication among different ranks which is carried out using MPI.

The parallelizing algorithm is such that the maximum number of MPI ranks we can use is $N_r - 1$, and N_r must be of the form $4 \times \text{integer} + 1$. However, recently the code has been updated to be able to use a finite-difference scheme in radius, where such restrictions do not apply. The wall-time per time step of the code scales in a near ideal manner with the number of processors used, as shown in figure 4.3. These tests were performed on Haswell processors of the Cray XC40 of the Konrad supercomputing cluster belonging to

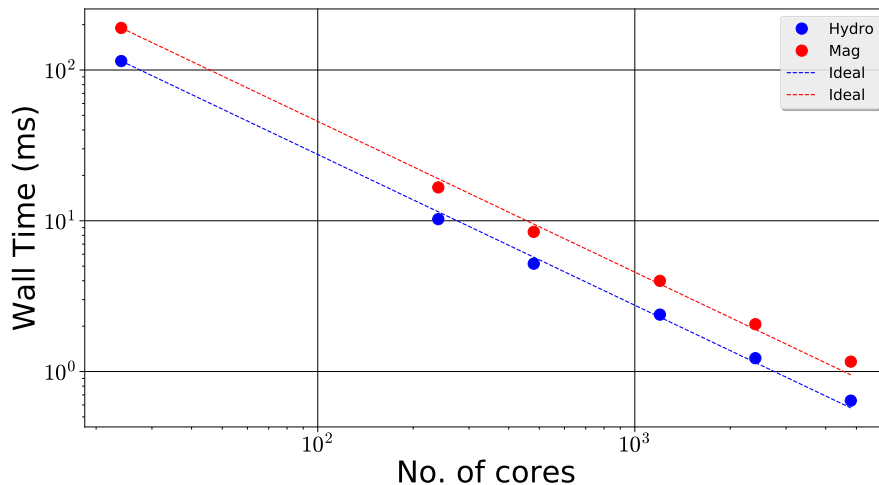


Figure 4.3: Variation of wall-time per time step in milliseconds with the number of processors used. One can see that for both hydrodynamic and MHD simulations, the code scales nearly ideally for the maximum number of processors that can be used. The tests were performed with a resolution of $N_r \times N_\theta \times N_\phi = 201 \times 1024 \times 2048$ on Haswell processors of the Cray XC40 of the Konrad supercomputing cluster in Berlin, a part of the HLRN.

the North-German Supercomputing Alliance (Norddeutscher Verbund zur Förderung des Hoch- und Höchstleistungsrechnens – HLRN). An extreme resolution of $N_r \times N_\theta \times N_\phi = 201 \times 1024 \times 2048$ was used for the test simulations.

For many of the simulations presented in this study, the spherical harmonics transforms have been carried out using the SHTNS library (Schaeffer 2013). Following tools were used for post-processing the data from simulations and for visualisations: IPython (Pérez and Granger 2007), NumPy and Scipy (van der Walt et al. 2011), Matplotlib (Hunter 2007), Paraview (Ayachit 2015) and MATLAB (MATLAB 2017).

4.2 Identifying inertial modes

4.2.1 Using spherical harmonics

One of the advantages of pseudo-spectral simulations is the direct access to the individual poloidal and toroidal coefficients, w_{lm} and z_{lm} . A careful study of the behaviour of these coefficients provides an easy way of identifying the presence of inertial modes in the system. In what follows we shall use the abbreviations ES for equatorially symmetric and EA for equatorially antisymmetric.

The equatorial symmetry of the flow field can easily be related to that of these coefficients. Recall that the velocity field is decomposed into poloidal and toroidal potentials, which are in turn expanded in terms of spherical harmonics. Now, a spherical harmonic is symmetric with respect to the equator when $l - m = \text{even}$. The curl ($\nabla \times$) operator is an antisymmetric operator (Gubbins and Zhang 1993). Let us write the expansion for \mathbf{u}

Flow Field	Toroidal	Poloidal
Equatorially antisymmetric (EA)	$l + m = \text{even}$	$l + m = \text{odd}$
Equatorially symmetric (ES)	$l + m = \text{odd}$	$l + m = \text{even}$

Table 4.1: Symmetry of flow field and the corresponding conditions on degree and order of spherical harmonics of poloidal and toroidal potentials

below.

$$\mathbf{u} = \nabla \times \nabla \times \sum w_{lm} Y_{lm} \hat{\mathbf{r}} + \nabla \times \sum z_{lm} Y_{lm} \hat{\mathbf{r}} \quad (4.20)$$

where coefficients are functions of radius and Y_{lm} of angles θ and ϕ . Now, if $Y_{lm} \hat{\mathbf{r}}$ is ES ($l - m = \text{even}$), then its curl (which is the case for z) will transform it into an EA vector, while a double curl (as in the case of w) will transform it back into an ES vector. Keeping these in mind, a relationship between the symmetry of \mathbf{u} and those of w and z can be derived, as shown in table 4.1.

An equatorially antisymmetric inertial mode of azimuthal wavenumber m_0 would manifest itself as oscillations of spherical harmonic coefficients of the corresponding symmetry, i.e., $w_{l_1 m_0}$ and $z_{l_2 m_0}$, where $l_1 - m_0 = \text{odd}$ and $l_2 - m_0 = \text{even}$. A Fourier analysis of the oscillations of these coefficients would provide the drift frequency of the inertial mode.

As an example, let us take the (3, 2) inertial mode identified by [Wicht \(2014\)](#). Figure 4.4 shows that the toroidal coefficient, z_{22} ($l + m = \text{even}$) is the dominant oscillatory coefficient while the same is true for the poloidal coefficient w_{32} ($l + m = \text{odd}$).

The Fourier analyses of the coefficients z_{22} and w_{32} , show a single strong peak at the same frequency of $\omega/\Omega = 0.72$, where ω is the angular frequency of the Fourier transform. This is shown in figure 4.4b.

4.2.2 Using spectrograms

Experimentalists regularly make use of spectrograms to identify flow features and instabilities. Observable quantities used are PIV measurements of zonal velocity, u_ϕ ([Hoff et al. 2016b](#)), measurements of cylindrically radial magnetic field, b_s using Hall sensors ([Kelley et al. 2007](#)), and pressure measurements using pressure probes ([Triana 2011](#)).

To build a spectrogram, one performs the Fourier transform of a time series obtained from a sensor or a group of sensors, which would provide a power spectrum of the time series. Plotting the map of such a power spectrum against differential rotation $\Delta\Omega/\Omega$ makes a spectrogram. Frequencies having high energy content stand out in such a spectrogram as drift frequencies of distinct modes and instabilities. An example is shown in figure 4.5a, based on data from the 3-metre experiment in Maryland. The various dominant inertial modes can be seen as ‘bright’ spectral lines with high power. A list of the identified modes can be found in [Triana \(2011\)](#).

For our simulations, we use time series of diagnostic quantities from 8 different grid points, on a single radial surface, radially symmetrically spaced in latitude and longitude. This is shown in figure 4.5b.

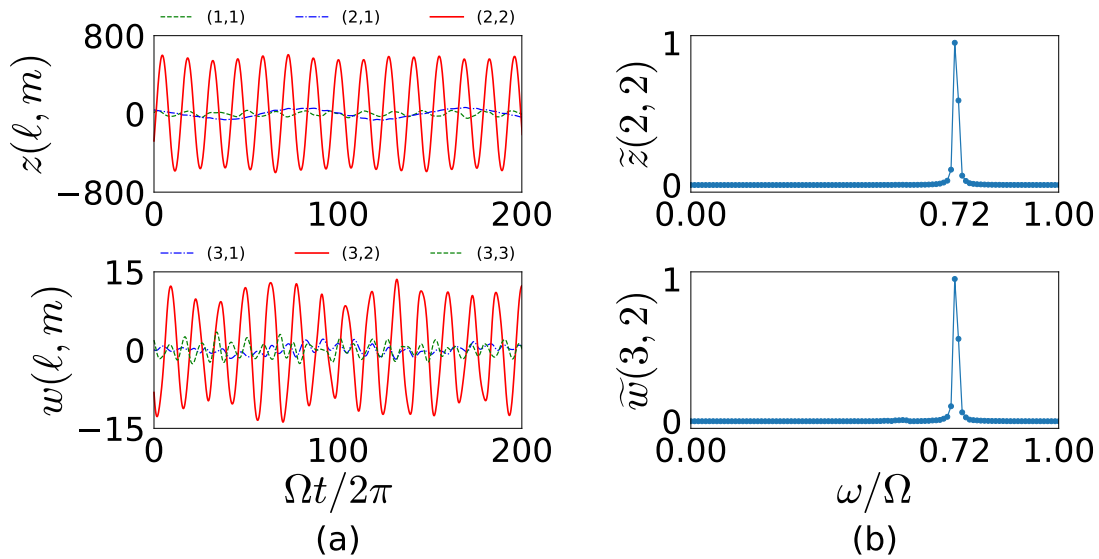


Figure 4.4: (a) Oscillations of spherical harmonic coefficients of toroidal ($z(\ell, m)$) and poloidal ($w(\ell, m)$) potentials. $z(2, 2)$ and $w(3, 2)$ are the dominant oscillatory coefficients. (b) Fourier transform of time series of $z(2, 2)$ and $w(3, 2)$ coefficients, denoted by tilde, showing a peak in frequency at the same position, $\omega/\Omega = 0.72$

The time series from different sensors are first cross-correlated against the time-series from one of the sensors, chosen as a reference. Thereafter, each time series is shifted by the time lag for which the cross-correlation with the reference time series is the highest. This takes care of the drift of the diagnostic quantity across sensors and brings the time series to a common time reference.

4.2.3 Structures of solutions

As shown in section 2.6, inertial modes in spherical shells have very specific structures. Some of them look very similar to the full-sphere modes and can be easily identified with the Greenspan notation (l, m) . We can compare the fluctuating part of a flow component or pressure from a snapshot of the solution to a standard eigenmode of a full sphere, as given by the analytical formulae of Zhang et al. (2001), or the pressure solution given by Bryan (1889), as well as eigenmodes of a spherical shell which are computed using the eigenvalue solver SINGE (Vidal and Schaeffer 2015). Such a comparison has been shown as an example in figure 4.6 where isosurfaces of cylindrically radial velocity, u_s of a snapshot of a simulation has been compared with the analytical solution of the $(3, 2)$ mode in a full sphere, based on Zhang et al. (2001) as well as a spherical shell eigenmode, computed using SINGE. If a mode is not dominantly visible in the full solution, but its oscillations can be found in the spherical harmonics, then the mode structure can be filtered out by filtering out the spherical harmonics of a given azimuthal and equatorial symmetry.

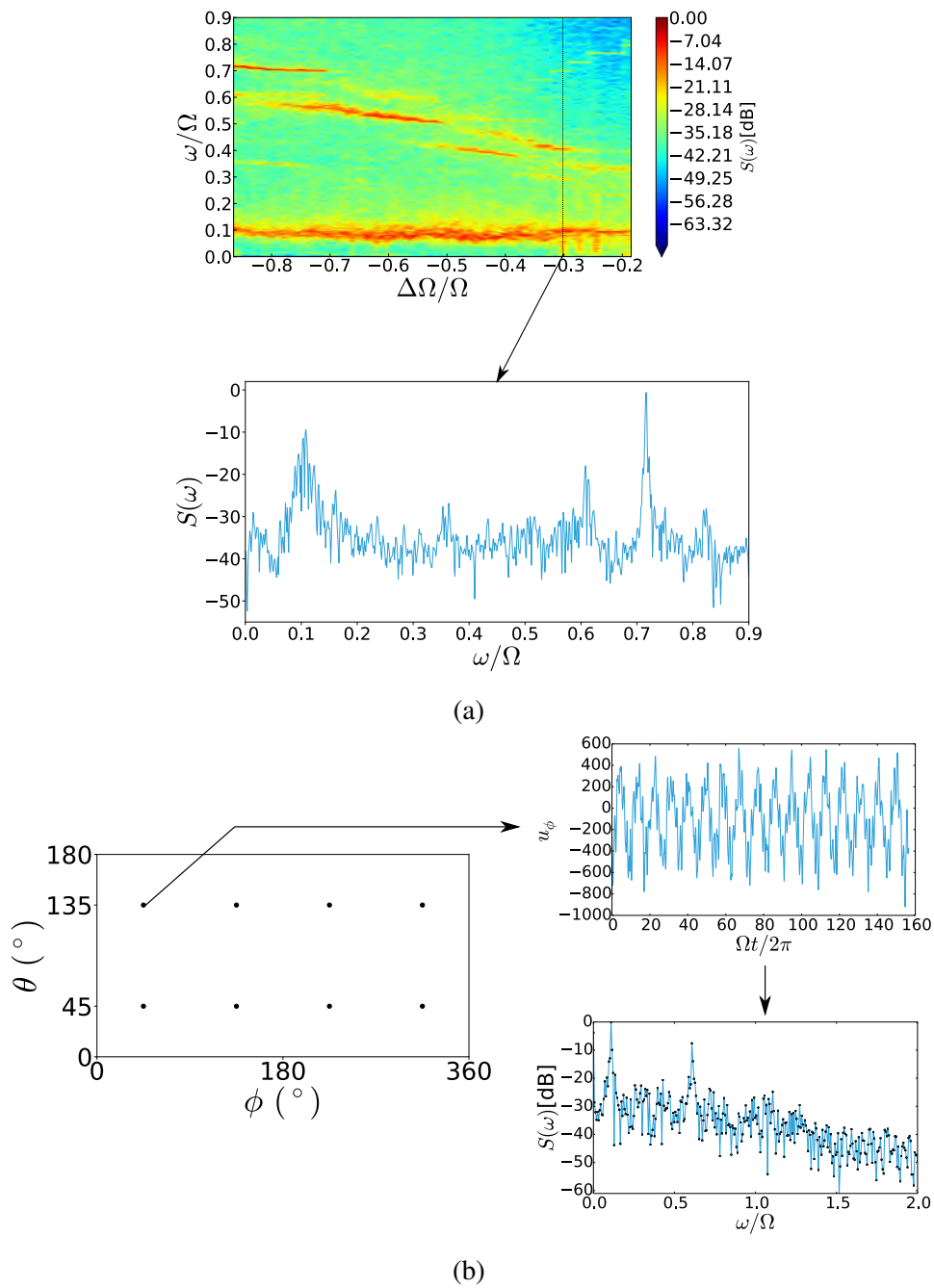


Figure 4.5: (a) The colormap shows a spectrogram built using time series data from pressure probes of the 3-metre experiment in Maryland, USA. The plot below it shows the power spectrum at a single value of differential rotation. Data supplied by Santiago Triana. (b) Location of artificial sensors used in simulations. All the probes are situated on one spherical surface of fixed radius and are placed in a radial symmetric way in latitude and longitude. The time series of a diagnostic quantity (zonal velocity u_ϕ in the above plot) is obtained from these sensors and Fourier transformed to provide a power spectrum $S(\omega)$.

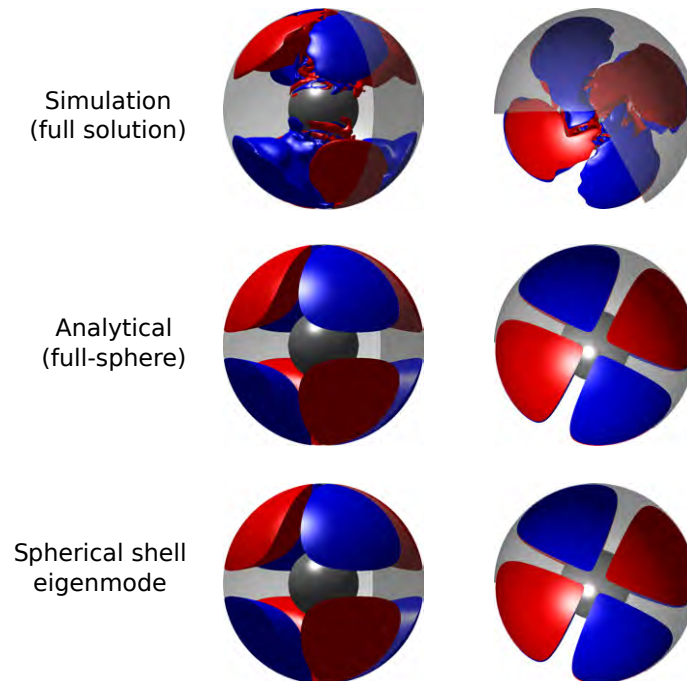


Figure 4.6: The structure of the solution from a simulation compared with the analytical structure of the $(3, 2)$ mode in a full sphere and in a spherical shell. Shown here are isosurfaces of cylindrically radial velocity, u_s . Red denotes positive (outward flow) while blue denotes negative (inward flow).

4.3 Discussion

This chapter introduced the numerical methods used to simulate the spherical Couette system as well as the code MagIC that has been used in this study. Finally, we introduced how we identify inertial modes in our system using spherical harmonic oscillations, spectrograms constructed using virtual probes as well as direct comparisons of flow structures with eigenmodes of a full sphere or spherical shell. These concepts will be used in the next chapter where inertial mode identification will be a key topic of discussion.

5 Radial jet and torque scalings

“This work contains many things which are new and interesting. Unfortunately, everything that is new is not interesting, and everything which is interesting, is not new.”

Lev Landau

This chapter talks about some preliminary results obtained in this study. These results pertain to the radial jet mentioned in section 3.4.1 and the scaling of the torque measured at the inner boundary as well as a hunt for a torque bistability as found in the 3-metre experiment at Maryland (Zimmerman 2010).

5.1 Outer sphere stationary

Section 3.4.1 discussed the axisymmetric state for the outer sphere stationary. We found that a slight rotation of the inner sphere led to a meridional circulation from which a radial jet emerged at high values of inner sphere rotation. In the scaling chosen here, the azimuthal velocity of the inner core boundary has the form of a Reynolds number,

$$Re_i = \Omega_i r_i^2 / \nu = \left(\frac{a}{1-a} \right)^2 \Delta\Omega, \quad (5.1)$$

where, $a = r_i/r_o$ is the radius ratio. With this definition, three distinct dynamic regimes can be identified, that of low, intermediate and high Reynolds numbers.

For low Re_i , Bratukhin (1961) and Haberman (1962) provide analytical results for the laminar flow which was re-derived by Wicht (2014) who compared it with numerical solutions with an excellent agreement. The analytical flow solution can be written as

$$u_\phi = r \sin \theta \frac{(r_i/r)^3 - a^3}{1 - a^3} \Delta\Omega, \quad (5.2a)$$

$$\psi = f(r) \sin \theta \cos \theta, \quad (5.2b)$$

where u_ϕ and ψ represent the zonal velocity and the stream function, respectively. f is a complex function of radius and depends on Ω , $\Delta\Omega$ and a .

For intermediate Re_i , a radial jet starts to develop at the equator. This jet becomes unstable to a non-axisymmetric instability with azimuthal wavenumber $m = 3$ at a critical

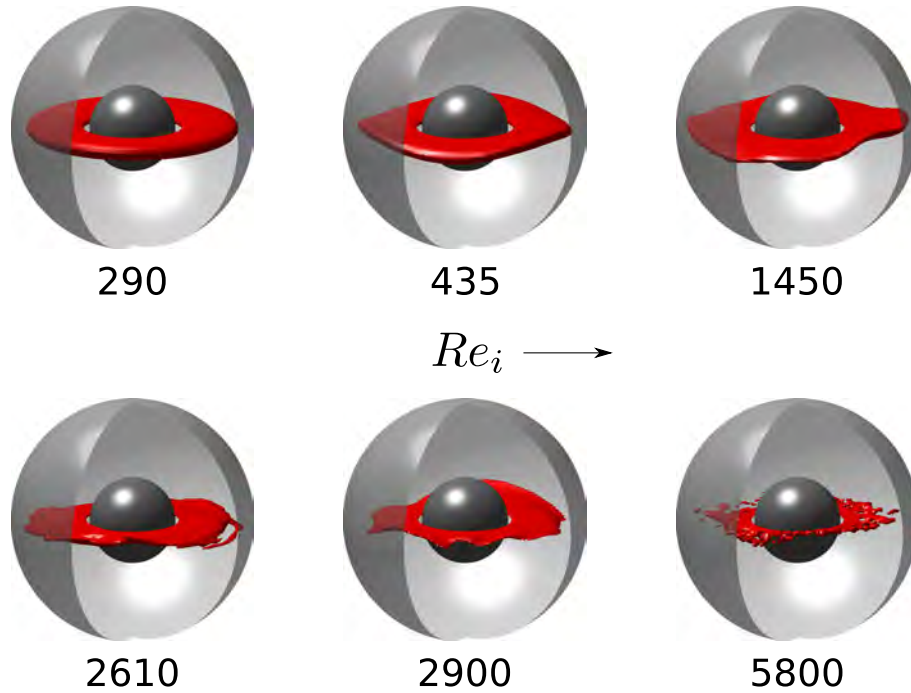


Figure 5.1: The radial jet, at $E = \infty$. Isosurfaces show radial velocity, red meaning positive (outward). This jet becomes thinner and shorter and becomes unstable to non-axisymmetric instabilities. For very high Reynolds numbers, Re_i , the jet becomes turbulent.

Reynolds number of $Re_i = 370$ (Wicht 2014). This equatorial jet instability has also been seen by other studies such as Hollerbach (2003), Hollerbach et al. (2006), Guervilly and Cardin (2010) and Gissinger et al. (2011). At high Re_i , the fluid becomes turbulent and the jet cannot be uniquely identified any more. The structure of the radial jet and its various transitions have been shown in figure 5.1 for different values of Re_i .

Comparison with sphere in unbounded fluid

Our system has a wide-gap and in the case when the outer sphere is stationary, is bound to share some features with studies of a sphere rotating in an unbounded fluid. We explore certain aspects of this similarity that can also explain some numerical observations.

Brief review

As mentioned before, the radial jet develops at intermediate values of Re_i . It is the result of the fluid being thrown out centrifugally at the equator of the inner sphere. To quantify this effect, we look at analyses of an inner sphere rotating in an unbounded fluid at rest and compare with our numerical results.

The boundary layer over a sphere rotating in a fluid at rest, was studied by Howarth (1951) who used series expansion in θ as well as a momentum integral method, similar to what von Kármán (1921) did for a rotating disc. His result showed that there are two boundary layers originating from diametrically opposite poles of the sphere. Similar to

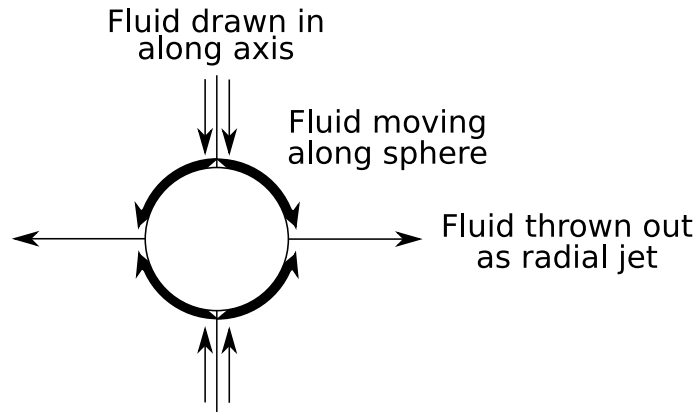


Figure 5.2: The model of laminar boundary layer on a sphere rotating in a bulk fluid, given by [Howarth \(1951\)](#) and refined by [Stewartson \(1958\)](#). Fluid drawn in along the axis of rotation along both poles of the sphere, moves on the surface of the sphere. Finally when the two boundary layers collide, the fluid is thrown out in the form of a radial jet.

the disc problem, fluid is drawn in along the axis at the poles, and thereafter moved along surface of the sphere, radially outwards. Since this happens at both poles, the fluid in the boundary layers is bound to collide at the equator, where the solution of [Howarth \(1951\)](#) breaks down due to the parabolic nature of the equations. The schematic of the boundary layer flow is shown in figure 5.2. The assumption of the theory was that the zonal velocity flux in the boundary layer is much larger compared to the non-zonal components:

$$\int_0^\delta u_\theta^2 dr \ll \int_0^\delta u_\phi^2 dr \quad (5.3)$$

Other notable theoretical studies on the boundary layer on a rotating sphere are [Stewartson \(1958\)](#), [Fox \(1964\)](#), [Banks \(1965\)](#) and [Manohar \(1967\)](#). [Stewartson \(1958\)](#) conjectured that the flow at the equator would evolve as a radial jet with a profile given by that due to [Landau \(1944a\)](#) and [Squire \(1955\)](#), often referred to as the Landau-Squire jet. [Singh \(1970\)](#) showed using analytical theory and numerical investigations that “ordinary boundary layer theory is capable of describing the outflow near the equator as a narrow radial jet”. These theoretical results agreed well with the torque measurements in the experiments of [Bowden and Lord \(1963\)](#) who studied a rotating sphere in a fluid at rest in a much larger cylinder. These experiments also showed the emergence of a radial jet from the equator. [Dennis et al. \(1981\)](#) showed numerically that the expanse of the region around the equator where the boundary layers collide is of $O(Re_i^{-1/2})$.

Width of radial jet

We determine the latitudinal width of the jet for each longitude for the spherical surface where it has its maximum. The mean over all longitudes then provides an estimate of the jet width

$$\delta = \langle r \Delta \theta \rangle_\phi \quad (5.4)$$

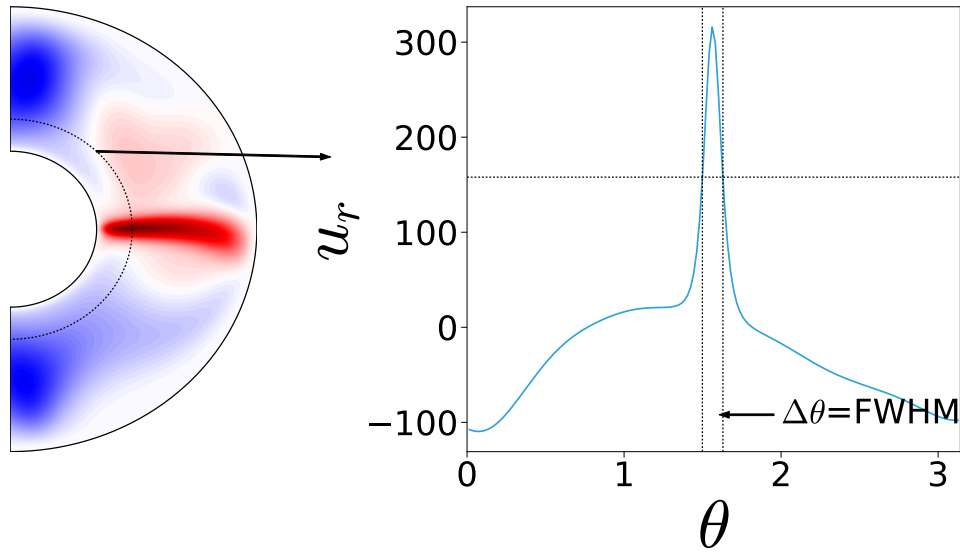


Figure 5.3: Determination of the width of the jet. The left panel shows how the radial level is chosen based on $u_{r_{max}}$. This gives u_r as a function of colatitude θ . The width of the jet is computed using the FWHM of the function $\Delta\theta$ as $\delta = r\Delta\theta$.

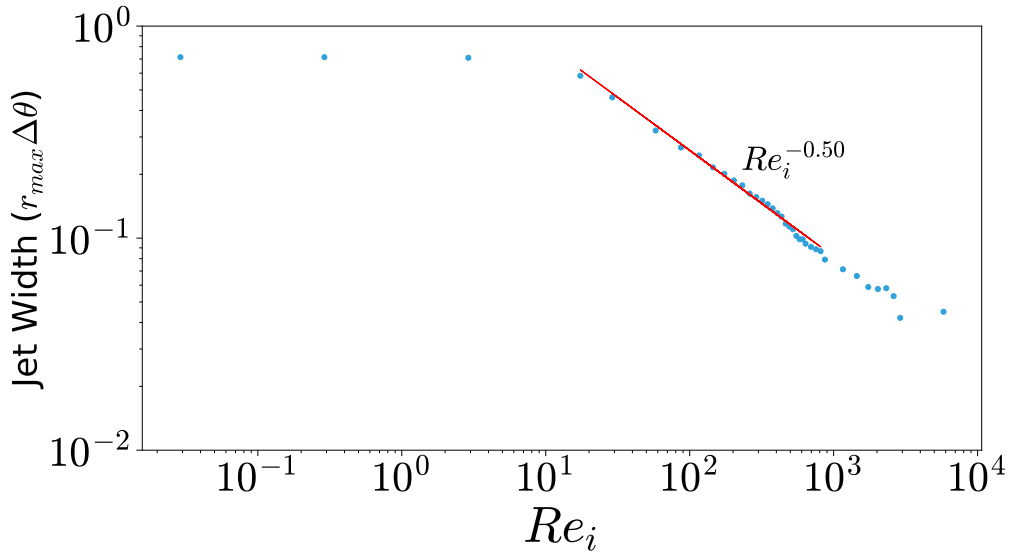


Figure 5.4: Scaling of the width of the radial jet. The scaling agrees to a great extent to the proposed region of discontinuity near the equator of $\mathcal{O}(Re_i^{-1/2})$ by Stewartson (1958) and shown by Dennis et al. (1981). The agreement is better at higher Re_i . The scattered points towards the end indicate a regime where the jet starts to become turbulent.

where $\Delta\theta$ is given by the full width at half maximum (FWHM) of the function $u_r(\theta)$ on the chosen spherical surface. This has been illustrated in figure 5.3.

Figure 5.4 shows the variation of the width of the radial jet with the Reynolds number.

One can distinguish the three regimes of low, intermediate and high Re_i . For low Re_i , the jet width is constant and a well-defined jet hasn't started to form yet. At high Re_i , the fluid becomes turbulent and we begin to lose a well-defined jet. Thus, scaling the jet-width makes sense in the regime of intermediate Re_i . The width of the radial jet in this regime varies as

$$\delta \propto Re_i^{-0.5}. \quad (5.5)$$

This is excellent agreement with the analytical investigation of [Stewartson \(1958\)](#) and the numerical results of [Dennis et al. \(1981\)](#), which showed that the boundary layer collision happens around a region of $O(Re^{-1/2})$, which is where the radial jet emerges from. This scaling also agrees with that of the viscous boundary layer thickness, as found by [Finke and Tilgner \(2012\)](#).

Torque on the inner sphere

Figure 5.5 shows the numerical torque measurement on the inner sphere as a function of Re_i . For low values of Reynolds numbers, as expected, the flow does not play a crucial role in determining angular momentum transport and the torque scales nearly linearly with the rotation rate of the inner sphere (Re_i). Once the radial jet starts to form, it acts as a more efficient mode of transporting angular momentum and thus, a higher torque is necessary to keep the inner sphere rotating at a constant rate. This leads to a deviation from the linear scaling.

Analyses by [Howarth \(1951\)](#), [Bowden and Lord \(1963\)](#) and [Singh \(1970\)](#), verified by the experiments of [Bowden and Lord \(1963\)](#), show that the torque on a sphere rotating in a fluid at rest should scale as

$$T \propto \rho \nu^{1/2} r_i^4 \Omega_i^{3/2}, \quad (5.6)$$

(see [Bowden and Lord 1963](#)). This torque scaling was also found by [Sorokin et al. \(1966\)](#) for a spherical Couette experiment with the outer sphere stationary, with a larger radius ratio of $r_i/r_o \approx 0.6$. Translated to the scaling used here, this shows that the dimensionless torque obeys

$$G \propto Re_i^{3/2} \quad (5.7)$$

Figure 5.5 shows that, at high rotation rates, the non-dimensional torque on the inner sphere from our numerical results scales as $Re_i^{1.47}$ which is very close to that found by the theoretical and experimental results mentioned above.

For even higher rotation rates, unachievable in simulations due to numerical difficulties, one would expect a deviation from the scaling found here. [Lathrop et al. \(1992\)](#) deduced, on dimensional grounds, that for very large Reynolds numbers the torque would approach an asymptotic scaling of $G \propto Re^2$. This analysis was for a Taylor-Couette system. However, experiments of [Zimmerman \(2010\)](#) at high $Re_i \sim 10^8$ showed an approach to this limit. The scaling obtained in the experiment was $G \propto Re_i^{1.89}$.

The above results show that for the spherical Couette flow with outer boundary stationary, there lies a regime of intermediate Reynolds numbers where the theory of [Howarth](#)

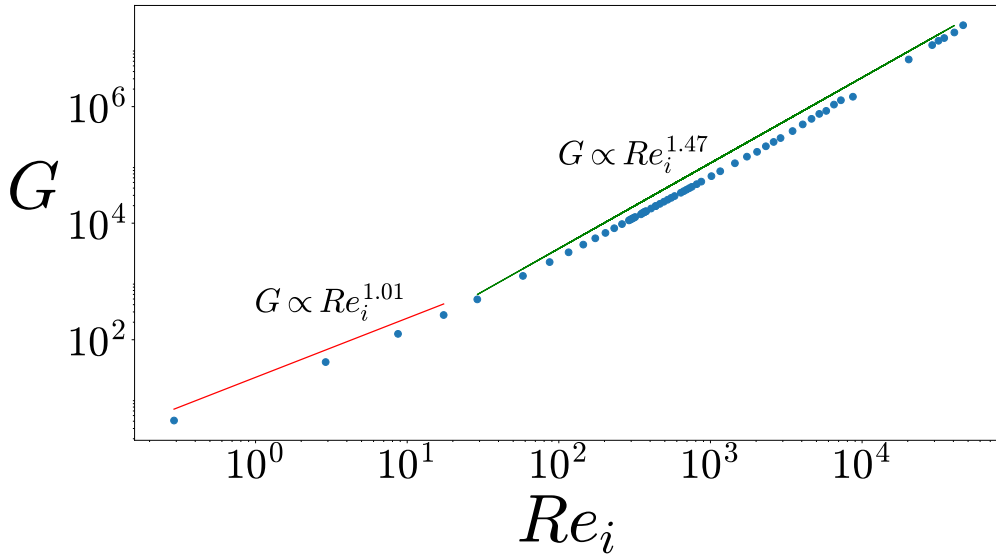


Figure 5.5: Scaling of the torque with the Reynolds number Re_i . One can see that at rotation rates after a radial jet has formed, the scaling agrees well with that proposed by [Howarth \(1951\)](#).

(1951) and others for an inner sphere rotating in a stationary fluid works quite well. However, for low Re_i , when the boundary layer is not well-pronounced or for very high Re_i , where the fluid is turbulent, the same doesn't hold true. For low Re_i , we fortunately have analytical solutions like those by [Bratukhin \(1961\)](#), [Haberman \(1962\)](#) and [Wicht \(2014\)](#) which explain the fluid dynamics excellently. However, for very high Reynolds numbers, such as those in the 3-metre experiment ([Zimmerman 2010](#)), the fluid is too turbulent to be treated analytically or numerically making the role of experiments important in complementing numerical modelling.

5.2 Torque bistability

There was an unexplained bistability in the torque that was observed in the 3-metre experiment in Maryland ([Zimmerman et al. 2011](#)) between $Ro = \Delta\Omega/\Omega = 1.8$ and $Ro = 2.75$ at all Ekman numbers ($E \leq 10^{-7}$ for the experiments). It consisted of a sudden jump in the torque to a very high value and then a relatively slow decay to a low state, as shown in figure 5.6a. The high state (marked 'H') in figure 5.6a was characterised by a broadband spectrum in temporal frequency, while the low state (marked 'L') was characterised by two peaks - at $\omega/\Omega = 0.18$ and $\omega/\Omega = 0.71$ where ω is the Fourier angular frequency. The high state has small peaks at $\omega/\Omega = 0.40$ and $\omega/\Omega = 0.53$ and a "broader buildup around $\omega/\Omega = 0.22$ " ([Zimmerman 2010](#)). These spectra are shown in figure 5.6b.

The reason for this bistability is unknown, but [Zimmerman \(2010\)](#) speculated some possible reasons based on experimental observations. He concluded that there must be a mechanism by which fast zonal flow is created and destroyed close to the inner sphere in a cyclical manner. In the low torque state, shown in figure 5.7a, the fluid just outside

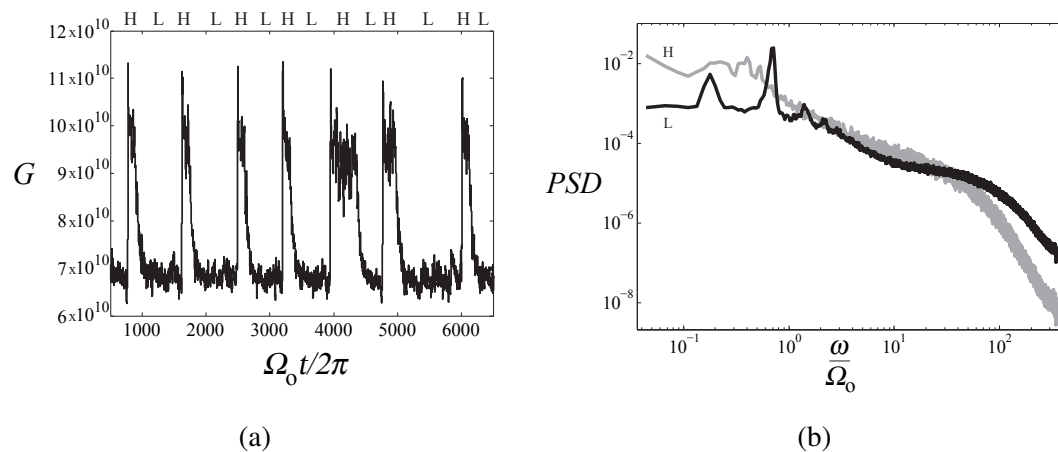


Figure 5.6: Torque bistability observed in the 3-metre experiment. ‘H’ and ‘L’ refer to ‘high’ and ‘low’ states respectively^a. The parameters are $E = 2.1 \times 10^{-7}$ and $Ro = 2.13$. (a) shows the measurements of the torque sensor, (b) shows the spectra of wall shear stress in the two states.

^aReprinted from Zimmerman et al. (2011), with the permission of AIP Publishing. DOI: <http://dx.doi.org/10.1063/1.3593465>

the zone of this fast azimuthal flow is not in solid body rotation with the outer sphere, but rather is slowing down over a long period of time, during which Ekman pumping transports angular momentum from this region to the ‘fast’ part of the flow quicker than the ‘fast’ zone pumps angular momentum out - resulting in a net localised rise in angular momentum and hence, torque. The boundary between the two regions might host Rossby waves (whose peaks are visible in the spectrum) and possibly complex vortex structures called “tripolar vortices” (van Heijst and Kloosterziel 1989). In the high torque state, shown in figure 5.7b, this special fast zone is destroyed and there is efficient mixing of angular momentum by turbulence, leading to a ‘flatter’ zonal velocity profile and hence, a higher torque.

We attempt to reproduce this torque bistability in our numerical simulations, at a much higher Ekman number of $E = 10^{-4}$ due to numerical difficulties. Our hope was that a ramp from low to high values of differential rotation and then the other way round would show a hysteretic behaviour and might produce a bistability in the time-averaged torque. We perform two ramps in Ro - one from $Ro = 1$ to $Ro = 5$ (marked ‘L2H’ in figure 5.8) and another the other way round (marked ‘H2L’ in figure 5.8). Unfortunately the value of the time-averaged torque at different Ro showed negligible difference between the two ramps.

However, we observed short transients which had a higher torque state, which then settled down to a lower torque state as shown in figure 5.9 for $Ro = 4$, starting from a flow solution at $Ro = 3$. The difference between the high and low states was, of course, much smaller than that observed by Zimmerman (2010), but one must keep in mind that our Ekman number and thus, our fluid viscosity is three orders of magnitude larger than that in the experiment, and would hence provide less “dramatic” results. This transition is nothing like the bistability observed in the experiments. However, we follow an analysis similar to Zimmerman (2010) in order to try to capture some of the observed features.

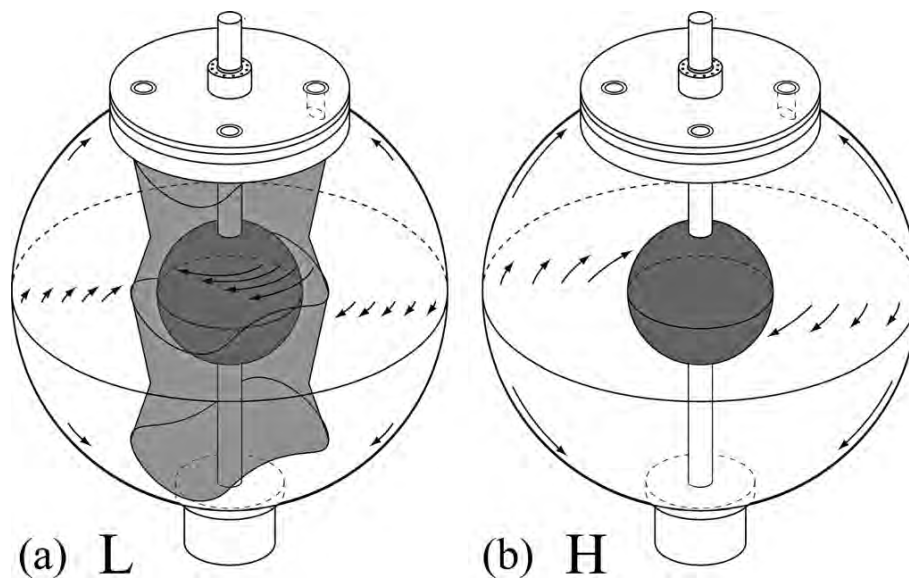


Figure 5.7: Schematic figures by Zimmerman (2010) speculating the possible flow states during the low torque state (figure (a)) and the high torque state (figure (b)).^a

^aReprinted from Zimmerman et al. (2011), with the permission of AIP Publishing. DOI: <http://dx.doi.org/10.1063/1.3593465>

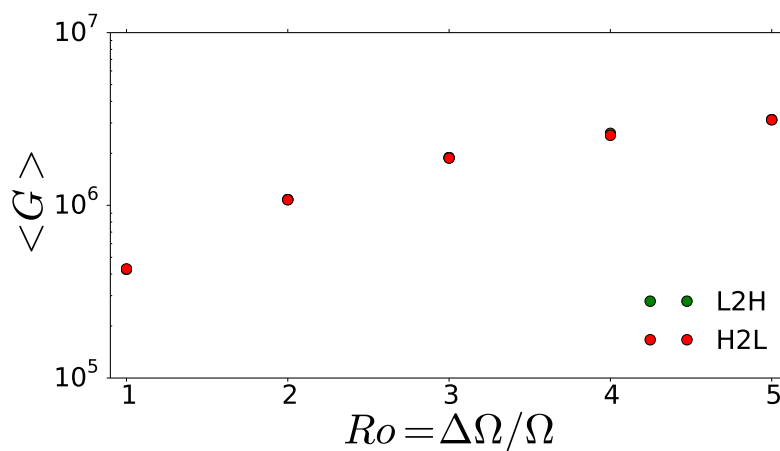


Figure 5.8: Time-averaged torque at different differential rotation rates. Numerical ramps are from $Ro = 1$ to $Ro = 5$ and back. The ramp from low to high Ro ('L2H') are marked with green circles while the one which is other way round ('H2L') is marked with red circles.

Figure 5.10 shows the spectra of the time series of torque in the two states. This is similar to obtaining the spectra of wall shear stress in experiments since the wall shear stress varies linearly with the torque. The spectra in the figure shows some similarities to that of the experiments - the 'high' state exhibits a broadband spectrum with no clear peaks while the 'low' state has a peak at $\omega/\Omega = 0.43$. However, this peak could not be associated with a particular mode in the flow as was found by Zimmerman (2010)

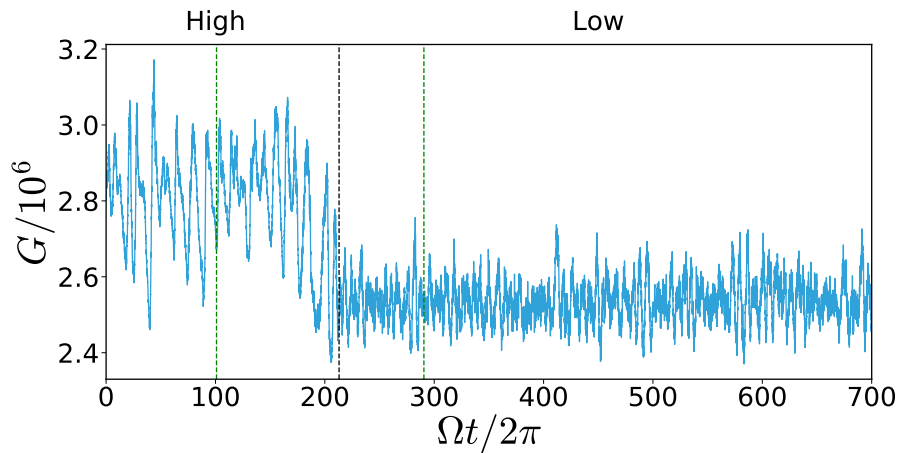


Figure 5.9: Time series of torque (G) on the inner sphere at $E = 10^{-4}$ and $Ro = 4$. Black dashed line marks the transition from a high torque state to a low one. Green dashed lines marks times at which flow solutions are shown in figure 5.11.

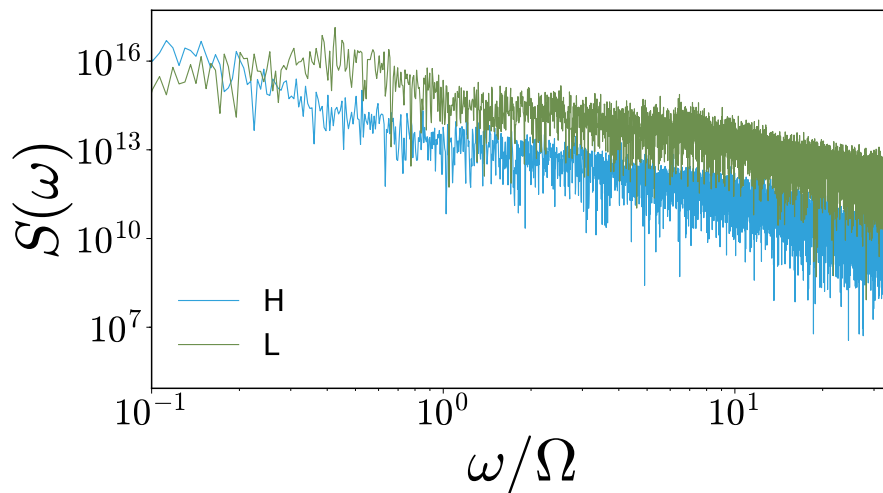
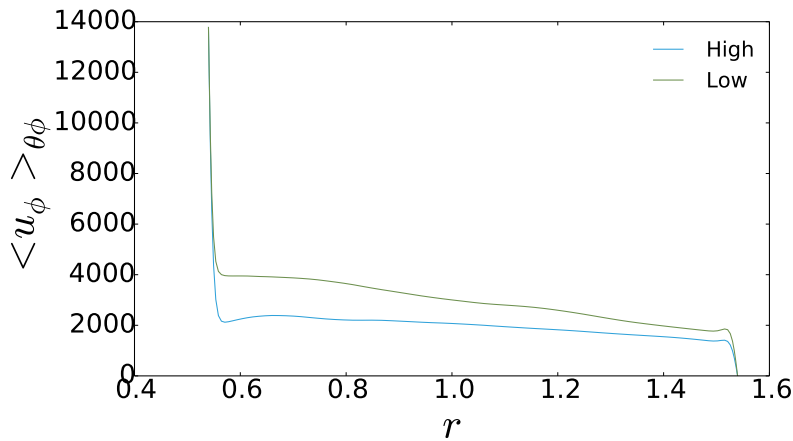
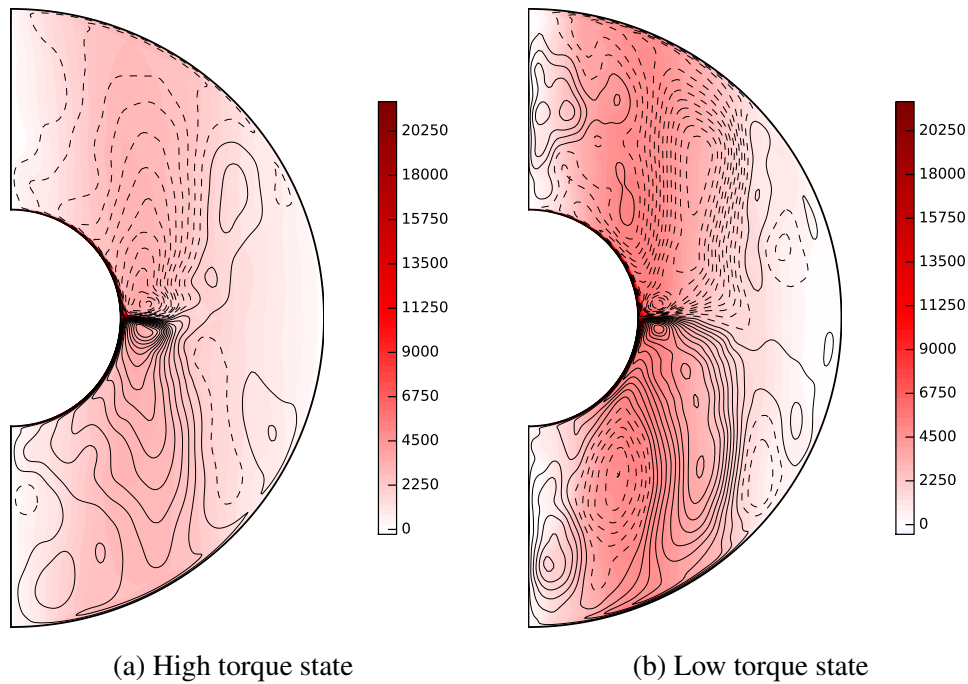


Figure 5.10: Power spectra ($S(\omega)$) of the torque series in the two states at $E = 10^{-4}$ and $Ro = 4$. The high torque state ‘H’ shows a broadband spectrum with no clear peaks while the low state ‘L’ shows a clear peak at $\omega/\Omega = 0.43$.

and Zimmerman et al. (2011). Comparing the flow structures in the two states in figure 5.11 we find that the solution in the high torque state consists of two large scale circulation cells while the flow in the low torque state consists of more small scale structures. Another noticeable difference is the fact that in the low torque state, the fluid around the tangent cylinder seems to have a larger azimuthal velocity as compared to that in the high torque state and zonal velocity profile looks more flat for the high torque case. This is similar to the idea of Zimmerman (2010) (figure 5.7) of a zone of high zonal velocity surrounding the tangent cylinder. However to achieve a bistability, one would need a destruction of this zone of high zonal flow. As to why this would happen remains an open question.



(c) Profiles of u_ϕ at low and high torque states.

Figure 5.11: (a) and (b) show flow solutions at the two different torque states. Colors show Azimuthal average of zonal velocity with red being positive (velocity into plane) while lines represent meridional circulation with solid (dashed) lines meaning clockwise (anti-clockwise). (c) shows profiles of u_ϕ averaged in θ and ϕ .

5.3 Summary and discussion

In this chapter, we first investigated the spherical Couette system with the outer sphere stationary. We found that with the increase in the inner sphere rotation rate, the onset of a radial jet takes place, as has been observed in past studies of the spherical Couette flow (Hollerbach 2003, Hollerbach et al. 2006, Guervilly and Cardin 2010, Gissinger et al. 2011, Wicht 2014) as well as those for a sphere rotating in an unbounded fluid (e.g.

Bowden and Lord 1963, Dennis et al. 1981). Observing that the jet gets thinner with the rotation rate of the inner boundary, we tried to scale the thickness of the jet with the Reynolds number of the flow at the inner boundary equator Re_i and found a scaling of $\delta \propto Re_i^{-1/2}$, which was proposed for a sphere rotating in an unbounded fluid (Stewartson 1958, Dennis et al. 1981). In addition, we found that the torque on the inner sphere has three distinct regimes. For very low $Re_i < 20$, the radial jet has not formed yet and the torque scales linearly with Re_i . However, there is a regime change beyond the point where the jet starts to form and we find a scaling of $G \propto Re_i^{3/2}$, a scaling found for the case of an inner sphere in an unbounded fluid (Howarth 1951, Bowden and Lord 1963) as well as for a spherical Couette flow experiment with a larger radius ratio than ours (Sorokin et al. 1966). For very large Re_i , the torque scaling, observed in experiments (Zimmerman 2010), gets closer to an asymptotic scaling of Re_i^2 proposed for the Taylor-Couette setup (Lathrop et al. 1992).

Hollerbach et al. (2006) found that the development of a radial jet when the outer boundary stationary is a common feature for several different radius ratios. However, the open question remains on whether the similarity with studies of a rotating sphere in an unbounded fluid would still hold at all radius ratios. Intuitively, one would assume the similarities to break down once the gap width of the shell becomes narrow. But this limit is still to be exactly determined.

At a finite outer boundary rotation of $E = 10^{-4}$, we attempt to reproduce the torque bistability observed in experiments at Maryland (Zimmerman et al. 2011). We fail to find such a bistability at our simulation parameters, but observe certain similarities while comparing a transient high torque state to a low torque state when the solution has statistically saturated. We observe that the temporal spectrum of torque has no clear peaks in the high torque state, unlike the low torque state which has a clear peak at $\omega/\Omega = 0.43$. We couldn't find a mode of flow that exactly matched this frequency. Comparing the flow solutions in the two states, we found that the flow in the low torque state consists of a region of high zonal velocity close to the tangent cylinder and a less flat zonal velocity profile as compared to the high torque state, which is very similar to the schematic picture proposed by Zimmerman (2010). Even though we observed such similarities, we still failed to answer the key question of what might be the reason for such a region of high azimuthal velocity to break down and be rebuilt again in a cyclical manner. Simulations at lower Ekman numbers might be able to get closer to finding the answer to this yet unanswered question.

6 Triadic resonances in the wide-gap spherical Couette system

“Probably every theory will someday experience its “No” - most theories, soon after conception.”

Albert Einstein

6.1 Introduction

In the last few chapters, we learned about the spherical Couette system as well as had an understanding of inertial modes in a sphere and spherical shell. We saw in chapter 2 that inertial modes in astrophysical objects are thought to be excited due to three mechanisms - precession, libration and tidal excitation. However, several experiments with the spherical Couette setup (Kelley et al. 2007, Kelley 2009, Kelley et al. 2010, Triana 2011, Rieutord et al. 2012, Hoff et al. 2016b) as well as direct numerical simulations (Matsui et al. 2011, Wicht 2014) have found the onset of inertial modes at certain critical differential rotation rates which have raised several questions. First and foremost is the fact that these modes onset in the absence of any external oscillatory mechanisms as thought to be the case for astrophysical objects. Secondly, the modes that have been observed in these studies are equatorially antisymmetric. This is surprising as the driving of the spherical Couette system is symmetric with respect to the equator and the Taylor-Proudman constraint tries to impose geostrophy, especially at high rotation rates such as that of the 3-metre experiment (e.g. Triana 2011). Lastly, these modes are more prominent for negative differential rotation, $Ro < 0$. Wave-like oscillations have also been reported for positive differential rotation (Zimmerman 2010) but their structures and symmetries haven't been clearly characterised.

Most of the contents of this chapter have been reproduced from the article: A. Barik, S. A. Triana, M. Hoff, J. Wicht, “*Triadic resonances in the wide-gap spherical Couette system*” that has been submitted to the Journal of Fluid Mechanics.

Contribution: I ran all the simulations with MagIC, performed all the analyses and wrote the first draft of the paper. After thorough revisions, much of the original structure and text is preserved. S. A. Triana ran the simulations using XSHELLS, M. Hoff provided the experimental data and J. Wicht contributed to writing of the final draft, physical interpretations of the results and supervision of research.

Past attempts at explaining the onset and selection of modes involve using the theory of over-reflection (Kelley et al. 2010) or being thought to be excited due to a critical layer at the tangent cylinder (Rieutord et al. 2012). The theory of over-reflection comes from sound waves Ribner (1957) and states that when a sound wave meets a shear flow at angles above a certain critical angle, the reflected wave can be amplified implying that energy is transferred from the shear flow to the sound wave. Kelley et al. (2010) used this idea and applied it to inertial waves stating that the Stewartson shear layer can act as a source of energy for over-reflecting inertial waves and in the process, certain modes get preferentially amplified. They used the critical angle of the internal shear layers of the modes as the critical angle for over-reflection and used the exact same formulae that were derived for sound waves by Ribner (1957). Their analysis broadly matched experimental observations, but there quite some exceptions. Besides, an analysis of over-reflection for an inertial wave must be done on similar lines as sound waves. The critical layer hypothesis of Rieutord et al. (2012) states that if there is a critical layer in the fluid that rotates with the drift rate of an inertial mode, it might resonantly excite one. However, this is a speculation and leaves much to be desired in terms of further investigations.

6.2 Fast and Slow modes

Inertial modes in a full sphere can be equatorially symmetric or antisymmetric. The equatorially symmetric modes that we find in simulations are the slow inertial modes described by Zhang et al. (2001) which are “nearly geostrophic”. This implies that they satisfy the Taylor-Proudman constraint to a large extent, i.e., the pressure gradient and Coriolis forces roughly balance each other,

$$-i\omega\mathbf{u} = -\nabla p/\rho - 2\Omega\hat{\mathbf{z}} \times \mathbf{u} \approx 0. \quad (6.1)$$

In such a scenario, the frequency of these modes, ω , are ‘small’ in magnitude as compared to the boundary rotation Ω and can thus change by a large fraction even for a small mismatch between pressure gradient and the Coriolis force. This is in contrast to the equatorially antisymmetric modes for which no such slow modes are found and which completely defy the Taylor-Proudman constraint and have larger magnitudes of frequencies as compared to the slow, nearly geostrophic, modes. Owing to this clear distinction between frequencies of these two classes of modes, the equatorially antisymmetric modes were referred to as ‘fast inertial modes’ by Wicht (2014). Thus, while the fast modes are easily identified by their frequencies, the same cannot be said of the slow columnar modes whose frequencies are susceptible to the slightest of changes in the force balance.

6.3 Experimental methods

Experimental studies have characterised the flow by building spectrograms using time series of various different quantities like zonal velocity, u_ϕ , using PIV measurements (Hoff et al. 2016b), cylindrical radial magnetic field, b_s , using Hall sensors (Kelley et al. 2007) and pressure using pressure probes (Triana 2011). The Hall sensors measure changes in the magnetic field induced in the fluid due to an imposed axial magnetic field.

The set-up for the spherical Couette experiments at BTU Cottbus-Senftenberg, Germany, consists of two concentric rotating spheres with radii $r_i = 40$ mm and $r_o = 120$ mm, with an aspect ratio of $r_i/r_o = 1/3$ and shell gap of width $L = 80$ mm. The fluid in the gap is a silicone oil of viscosity $\nu = (0.65 \pm 0.07)$ mm²/s. Two ramps in differential rotation were performed at Ekman numbers of $E = 3.04 \times 10^{-5}$ and $E = 1.52 \times 10^{-5}$. The flow is visualised in the meridional plane using Kalliroscope particles and a vertical laser sheet. In the horizontal plane, the flow was characterised using particle image velocimetry (PIV), using hollow spherical glass spheres as tracers. A Fourier analysis of the horizontal flow components gave spectrograms which were used to identify hydrodynamic regimes. Further details of the experimental setup and analysis techniques can be found in Koch et al. (2013), Hoff et al. (2016b) and Hoff et al. (2016a).

6.4 Results from experiments

Hoff et al. (2016b) describe three distinct hydrodynamic regimes encountered while increasing the magnitude of differential rotation ($|Ro|$) from small to large values for a fixed outer boundary rotation rate ($\Omega = 1/E$),

- i. **Fundamental instability** : At a critical differential rotation rate, Ro_c , the flow changes state from a purely axisymmetric configuration to a non-axisymmetric one, with a well-defined azimuthal symmetry, having wavenumber $m_c = 1$ in both cases shown in figure 6.1. Thereafter, this is the dominant large-scale feature in this regime, along with its higher harmonics, as seen in the spectrogram in figure 6.1. The onset of this first non-axisymmetric instability has been observed and studied before in other experimental and theoretical works, as mentioned in chapter 3.
- ii. **Inertial Modes** : As one keeps increasing the differential rotation rate, at a critical value around $Ro \approx -0.6$, one finds an onset of a pair of inertial modes, the dominant one being the (5, 2) mode in Greenspan notation. There are also sub-dominant $m = 1$ and $m = 3$ modes that also come in as two branches beside the (5, 2) mode. These modes are ‘fast’ and antisymmetric with respect to the equator. The pairs form triadic resonances with the first $m = 1$ instability (Hoff et al. 2016b). The two branches have not been distinctly identified by the authors. Thereafter, these modes go away as the differential rotation is increased further and the $m = 1$ first instability becomes the prominent large-scale structure again for a short range in Ro . Soon after, around $Ro \approx -0.9$ one finds a second onset of ‘fast’ inertial modes - the dominant one being the (3, 2) mode. There are two branches associated with this mode, again. The ‘lower’ branch (in terms of frequency) has been identified as the (4, 1) mode. The ‘upper’ branch is an $m = 3$ mode, which has not been distinctly identified. These modes again form triadic resonances with the fundamental $m = 1$ mode.
- iii. **Turbulence** : Further increasing the differential rotation beyond a critical values of $Ro = -2.011$ and $Ro = -1.730$ for $E = 3.04 \times 10^{-5}$ and $E = 1.52 \times 10^{-5}$, respectively leads the system to transition into a turbulent regime, seen as the regime of broadband peaks in the spectrograms. The triadic resonance that existed in the regime above is still seen to exist here.

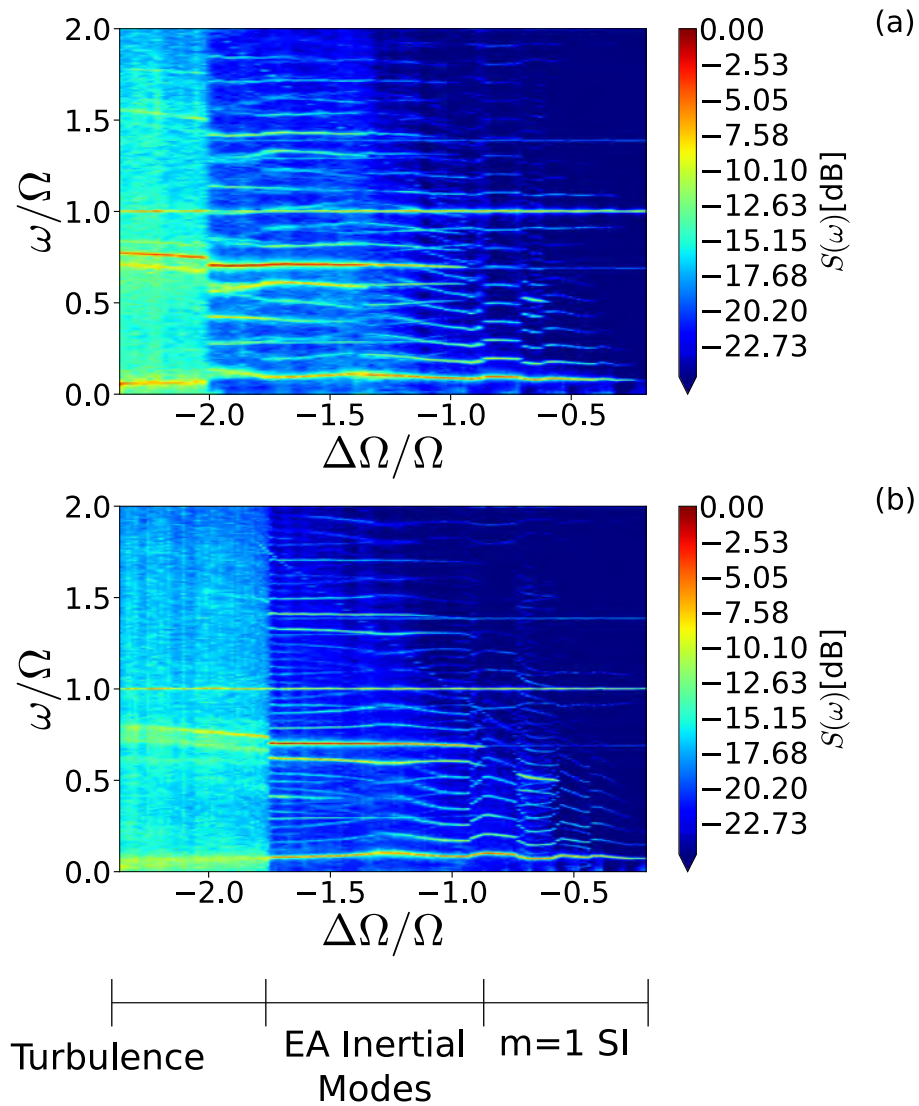


Figure 6.1: Spectrogram from PIV measurements of azimuthal velocity from experiments at BTU Cottbus-Senftenberg, u_ϕ at (a) $E = 3.04 \times 10^{-5}$ and (b) $E = 1.52 \times 10^{-5}$. One can see three distinct hydrodynamic regimes described by Hoff et al. (2016b). Abbreviations: SI = Stewartson layer Instability, EA = Equatorially Antisymmetric.

6.5 Numerical methods

The Navier-Stokes and continuity equations are solved using two independent codes: MagIC (Wicht 2002) and XSHELLS (Figueroa et al. 2013). Both codes use a poloidal/toroidal decomposition of the velocity field

$$\mathbf{u} = \nabla \times \nabla \times \hat{\mathbf{r}}w + \nabla \times \hat{\mathbf{r}}z \quad (6.2)$$

where w and z are the poloidal and toroidal potentials, respectively. Spherical harmonics are used for the spectral representation of these scalar potentials and pressure in latitude and longitude. For example,

$$w(r, \theta, \phi, t) = \sum_{l=0}^{l_{\max}} \sum_{m=0}^l w_{lm}(r, t) Y_{lm}(\theta, \phi). \quad (6.3)$$

The codes differ in the radial representation of the variables w , z and p . In MagIC, they are expanded in terms of Chebyshev polynomials and the radial grid consists of Gauss-Lobatto nodes. XSHELLS uses second-order finite differences in radius.

The reader is encouraged to have a look at Christensen and Wicht (2007) and Figueroa et al. (2013) for further details on the numerical methods. Some of the simulations using MagIC and all the simulations using XSHELLS presented here used the SHTns library (Schaeffer 2013) for spherical harmonic transforms. The identification of inertial modes using spherical harmonics has already been discussed in chapter

Tables 6.1 and 6.2 give a list of the ‘fast’ inertial modes identified in our simulations and compares it with experimental data as well as data obtained from analytical predictions (e.g. Greenspan 1968, Zhang et al. 2001) and eigenmode computations using SINGE. The frequency ranges provided in tables reflect the fact that the drift frequencies of the modes are not constant but change with differential rotation (Ro) and outer boundary rotation ($\Omega = 1/E$).

6.6 Results from simulations

To explore the parameter space, we typically keep the rotation rate of the outer boundary constant (constant E) and vary the differential rotation (Ro). We start by discussing numerical results at an Ekman number of 10^{-4} where a scan through a large range of Ro is numerically possible and the three hydrodynamic regimes found in the experiments are accessible. Thereafter, we present results for $E = 10^{-5}$, which is so close to the experimental values that we also attempt a more detailed comparison. Some important parameters of the experiments and simulations are provided in table 6.3.

6.6.1 Ekman number, $E \sim 10^{-4}$

In this case, the outer boundary rotation rate was kept constant at $E = 10^{-4}$ and the differential rotation was varied from $Ro = -1$ to $Ro = -3.5$. We present here results from two sets of such simulations:

The MagIC simulations were performed at $E = 10^{-4}$ using an aspect ratio of $r_i/r_o = 0.35$. The radius ratio has been chosen in accordance with that of the Earth and the 3-metre

Exp/Simulation	Frequency (ω/Ω)	E	$ Ro $
(3,2) mode			
Full sphere	0.667		
Spherical shell ¹	0.667	10^{-5}	
3m ²	0.700 - 0.760	$\leq 10^{-7}$	0.70 - 1.25
60 cm ³	0.683 - 0.698	$\leq 10^{-7}$	0.816
BTU C-S (24 cm) ⁴	0.698 - 0.715	3.04×10^{-5}	0.945 - 1.989
BTU C-S (24 cm)	0.688 - 0.708	1.52×10^{-5}	0.888 - 1.727
MagIC ⁵	0.717 - 0.741	10^{-4}	1.33 - 2.9
XSHELLS ⁶	0.719 - 0.783	10^{-4}	1.335 - 2.9
MagIC	0.670 - 0.710	10^{-5}	0.85 - 1.4
XSHELLS	0.690 - 0.705	10^{-5}	0.85 - 1.17
(5,2) mode			
Full sphere	0.467		
Spherical shell	0.466	10^{-5}	
3m	0.508 - 0.573	$\leq 10^{-7}$	0.50 - 0.77
60 cm	0.492 - 0.531	$\leq 10^{-7}$	0.6
BTU C-S (24 cm)	0.515 - 0.529	3.04×10^{-5}	0.631 - 0.693
BTU C-S (24 cm)	0.508 - 0.536	1.52×10^{-5}	0.600 - 0.729
MagIC	0.504 - 0.588	10^{-5}	0.55 - 0.75
XSHELLS	0.500 - 0.540	10^{-5}	0.55 - 0.7

- 1 : Using SINGE ([Vidal and Schaeffer 2015](#))
- 2 : From [Triana \(2011\)](#)
- 3 : Frequency ranges from [Kelley et al. \(2007\)](#). $|Ro|$ values are single representative values from Santiago Triana.
- 4 : From [Hoff et al. \(2016b\)](#) and [Hoff et al. \(2016a\)](#).
- 5 : Frequencies determined using spherical harmonics
- 6 : Frequencies determined from spectrograms

Table 6.1: List of the most dominant inertial modes observed and identified and comparisons with experiments. For simulations at $E = 10^{-5}$, the modes seem to occur at similar ranges of $|Ro|$ as all the experiments spanning a huge range of Ekman numbers.

Exp/Simulation	Frequency (ω/Ω)	E	$ Ro $
(4,1) mode			
Full sphere	0.612		
Spherical shell	0.602	10^{-5}	
3m	0.605 - 0.639	$\leq 10^{-7}$	1.42 - 2.20
60 cm	0.602 - 0.627	$\leq 10^{-7}$	1.32
BTU C-S (24 cm)	0.591 - 0.615	3.04×10^{-5}	1.041 - 1.989
BTU C-S (24 cm)	0.596 - 0.625	1.52×10^{-5}	0.888 - 1.727
MagIC	0.609 - 0.756	10^{-4}	1.33 - 2.9
MagIC	0.588 - 0.617	10^{-5}	0.85 - 1.4
XSHELLS	0.596 - 0.705	10^{-4}	1.335 - 2.9
XSHELLS	0.600 - 0.614	10^{-5}	0.85 - 1.17
(6,1) mode			
Full sphere	0.440		
Spherical shell	0.419	10^{-5}	
3m	0.444 - 0.500	$\leq 10^{-7}$	> 0.8 - 1.4
60 cm	0.435 - 0.450	$\leq 10^{-7}$	1.13
BTU C-S (24 cm)	0.403 - 0.429	3.04×10^{-5}	1.583 - 1.989
BTU C-S (24 cm)	0.407 - 0.414	1.52×10^{-5}	1.540 - 1.727
(4,3) mode			
Full sphere	0.500		
Spherical shell	0.499	10^{-5}	
3m	0.512 - 0.511	$\leq 10^{-7}$	0.33 - 0.40
60 cm	0.509 - 0.511	$\leq 10^{-7}$	0.44
MagIC	0.582 - 0.693	10^{-5}	0.55 - 0.75
XSHELLS	0.578 - 0.619	10^{-5}	0.55 - 0.70
(10,3) mode			
Full sphere	0.850		
Spherical shell	0.855	10^{-5}	
MagIC	0.822 - 0.859	10^{-4}	1.33 - 2.9
MagIC	0.751 - 0.808	10^{-5}	0.85 - 1.4
XSHELLS	0.790 - 0.843	10^{-4}	1.33 - 2.5
XSHELLS	0.776 - 0.798	10^{-5}	0.85 - 1.17
(5,0) mode			
Full sphere	0.570		
Spherical shell	0.570	10^{-5}	
MagIC	0.496 - 0.630	10^{-4}	1.33 - 2.4
XSHELLS	0.476 - 0.501	10^{-4}	1.35 - 2.1

Table 6.2: List of less dominant inertial modes and comparisons with experiments and theory. Sources of data same as in table 6.1.

	E	r_i/r_o	Step in Ro
Experiment	$3.04 \times 10^{-5}, 1.52 \times 10^{-5}$	1/3	0.02
MagIC	10^{-4}	0.35	0.1
MagIC	10^{-5}	0.35	0.05
XSHELLS	1.125×10^{-4}	1/3	0.05
XSHELLS	10^{-5}	1/3	0.05

Table 6.3: Parameters for simulations and experiments. The experiments at BTU C-S were run at other Ekman numbers as well, we provide here the one with which we closely compare the simulations.

experiment in Maryland. Time series for the non-axisymmetric part of u_ϕ are stored for eight different points spread out symmetrically in latitude and longitude ($\theta = \pi/4, 3\pi/4$ and $\phi = 0, \pi/2, \pi, 3\pi/2$) at $r = 0.7r_o$. These are stacked after shifting them by the time lag providing the highest cross-correlation value. A Fourier transform of the stack yields a spectrum of u_ϕ giving the power in different frequencies. Combining the spectra at different Ro finally provides the spectrogram shown in figure 6.2(a).

The XSHELLS simulations were run at a slightly larger $E = 1.125 \times 10^{-4}$ and the aspect ratio was $r_i/r_o = 1/3$, same as the experiments at BTU C-S. In this set of simulations, we collect time series data for three components of velocity, u_x , u_y and u_z at 8 different points symmetrically spread out in latitude and azimuth. The Fourier transforms of the time series from all points are then averaged to build a spectrogram. Hereafter, we refer to the MagIC simulations as ‘SIM1’ and the XSHELLS simulations as ‘SIM2’.

Figure 6.2(a) and 6.2(b) compare both numerical spectrograms using velocity from SIM1 and SIM2, respectively. Both show similar hydrodynamic regimes and instabilities, but there are differences because of the smaller resolution in Ro and longer integration times used for SIM2. This results in better constraints on mode onsets and a higher frequency resolution. We broadly find the three distinct regimes, that have been identified in the experiments at BTU C-S (see section 6.4 and refer to Hoff et al. 2016b), namely the fundamental instability, inertial modes and turbulence.

6.6.1.1 Fundamental Instability

The onset of the first non-axisymmetric Stewartson layer instability (SI) takes place when $Ro = -0.379$. It has a wavenumber $m = 1$, is nearly geostrophic and drifts in azimuth with a frequency $\omega/\Omega = 0.086$ (Wicht 2014). Figure 6.3 shows isosurfaces of cylindrically radial velocity, illustrating the two counter rotating circulation cells that have also been identified in the spherical Couette experiments at BTU C-S. This instability resides primarily inside the tangent cylinder.

This $m = 1$ mode has been identified as the (5, 1) mode by Hoff et al. (2016b). Wicht (2014) identified the (5, 1) mode as being the most probable candidate for identification of this mode, while commenting that it has the wrong sign for frequency.

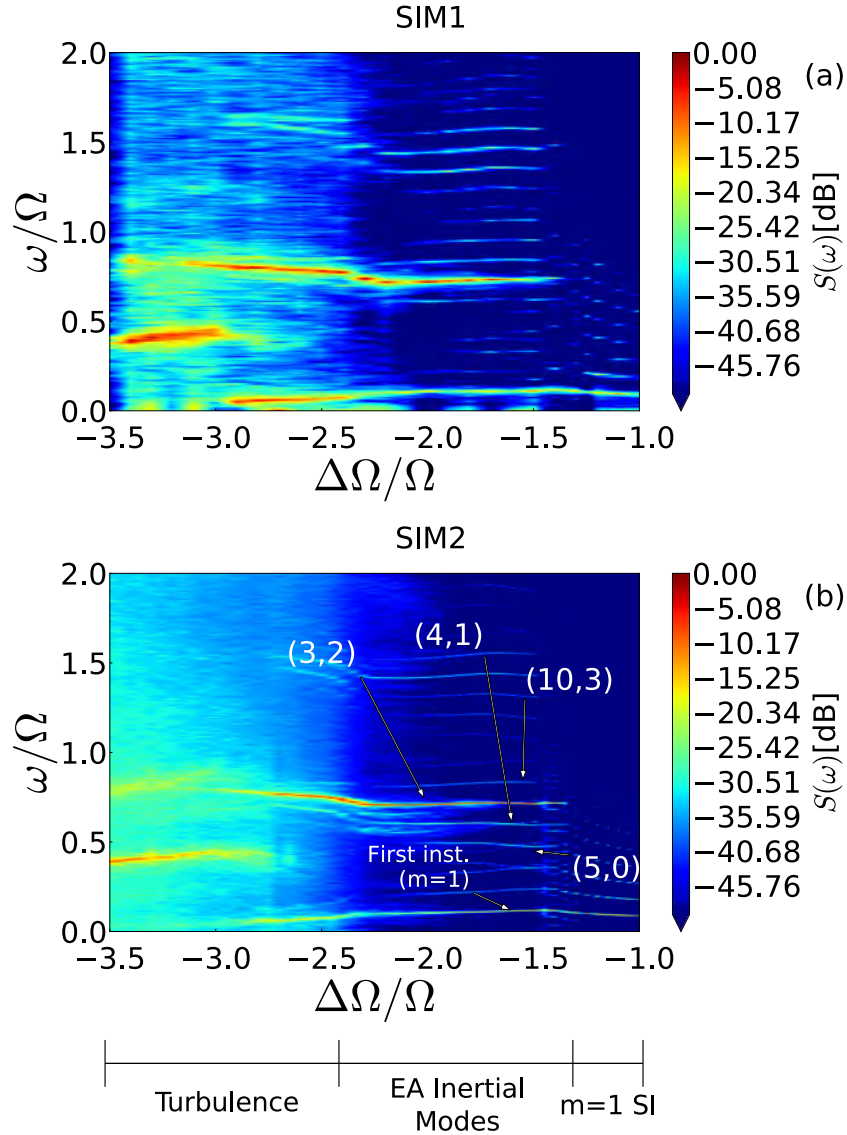


Figure 6.2: (Colour online) (a) Spectrogram of u_ϕ for $E = 10^{-4}$ at $r = 0.7r_o$, obtained from MagIC. (b) Spectrogram at $E = 1.125 \times 10^{-4}$ obtained from XSHELLS. In both cases, one can clearly identify the onset of the EA inertial modes at $Ro \approx -1.3$. There are three regimes visible: $m = 1$ drifting instability till $Ro \approx -1.3$, onset of inertial modes at $Ro \approx -1.3$, transition to turbulence at $Ro \approx -2.3$.

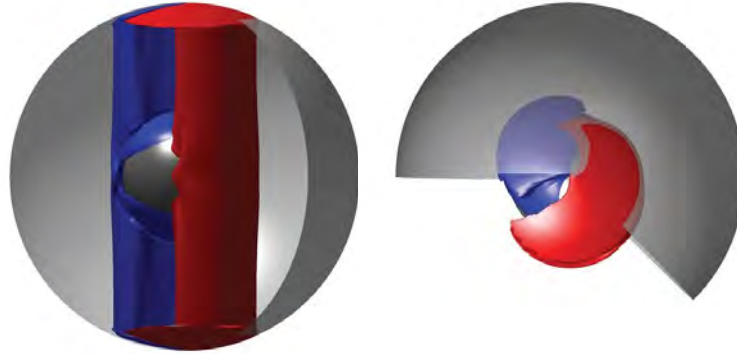


Figure 6.3: (Colour online) Structure of the fundamental $m = 1$ instability. Shown here are isosurfaces of non-axisymmetric cylindrically radial velocity (u_s). Red is positive (outward) while blue is negative (inward). The instability lives primarily inside the tangent cylinder.

6.6.1.2 Oscillations

Around $Ro = -1.25$ one can see the total kinetic energy of the flow oscillating. The spectrum is shown in figure 6.4a. Figure 6.4b shows that the oscillations are caused due to the onset of a second mode with a different drift frequency. Nonlinear interactions feed energy to higher wavenumbers and one observes a spectrum of several modes. However, the dominant large-scale feature of the flow is still the $m = 1$ SI mode.

6.6.1.3 Inertial Modes

As the differential rotation reaches a critical value of $Ro = -1.33$, ‘fast’ equatorially antisymmetric inertial modes are excited, as seen in the spectrograms in figure 6.2.

Since these are the first EA modes in the system, their onset is clearly marked by a growth of the equatorially antisymmetric kinetic energy. Figure 6.5a shows the growth of some of the individual mode energies (truncated at $l = 6$ in spherical harmonic expansion). One can see that modes with different azimuthal wavenumbers grow at the same rate, indicating that these modes are coupled together via nonlinear interactions. Figure 6.5b shows the steady state. Most of the kinetic energy is carried by modes with $m \leq 3$ and $m = 2$ clearly dominates.

By analysing the $m = 2$ spectral contributions more closely the $(3, 2)$ inertial mode was unambiguously identified based on its frequency and structure. It can be seen in the spectrograms in figure 6.2 as the ‘brightest’ line in this regime. Figure 6.6 compares the solution at $Ro = -2$ to the $(3, 2)$ mode for a full sphere and a spherical shell. The latter two are practically identical. A possible explanation is that they are ‘toroidal’ modes with $l - m = 1$. Since these modes have no radial velocity, the presence of the inner sphere is not communicated to larger radii. While the full numerical solution looks similar to the eigenmodes, it has also been evidently modified by the background flow due to the shear on and inside the tangent cylinder.

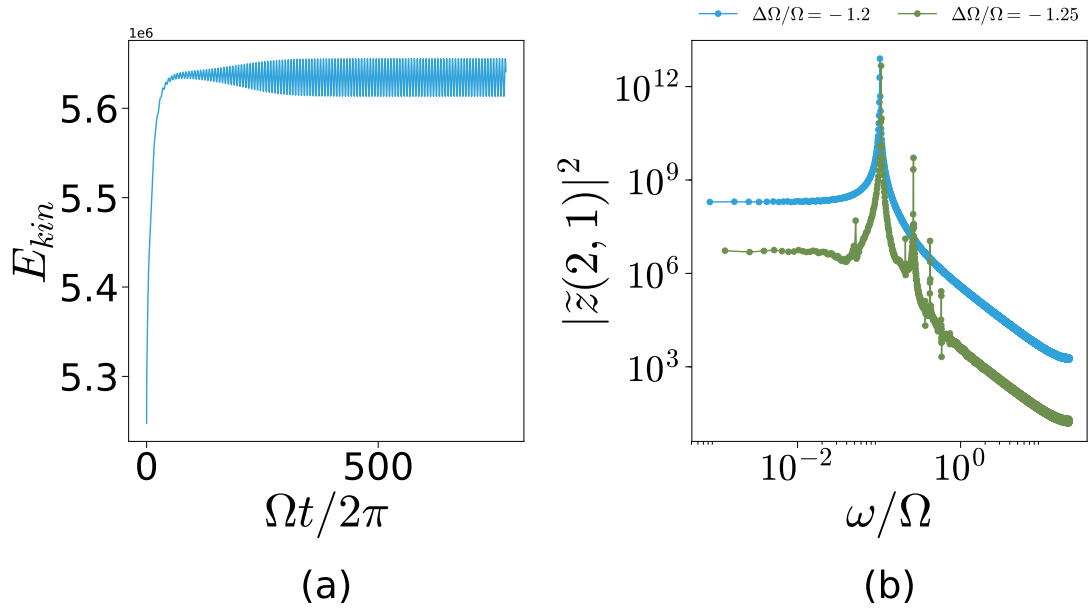


Figure 6.4: Regime of oscillating kinetic energy. (a) shows the oscillating nature of the total kinetic energy of flow at $Ro = -1.25$. (b) shows the power spectrum of the toroidal coefficient z_{21} representing the $m = 1$ equatorially symmetric modes present in the system at two different rates of differential rotation.

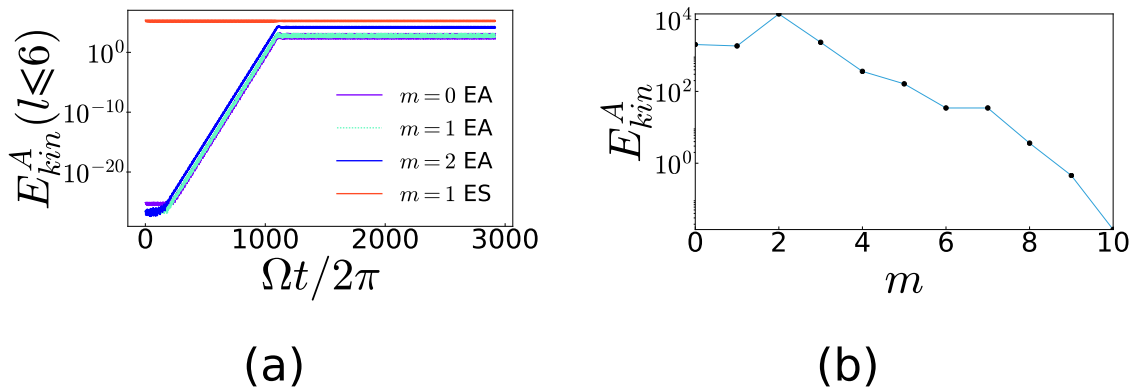


Figure 6.5: Onset of inertial modes at $E = 10^{-4}$ and $Ro = -1.33$. (a) shows the growth in terms of energy (SH expansion $l \leq 6$) of some of the individual modes at $r = 0.5r_o$. Shown in (a) is also the fundamental instability, $m = 1$ SI. (b) shows the spectrum for equatorially antisymmetric kinetic energy, E_{kin}^A , at $r = 0.5r_o$. EA = Equatorially Antisymmetric, ES = Equatorially Symmetric

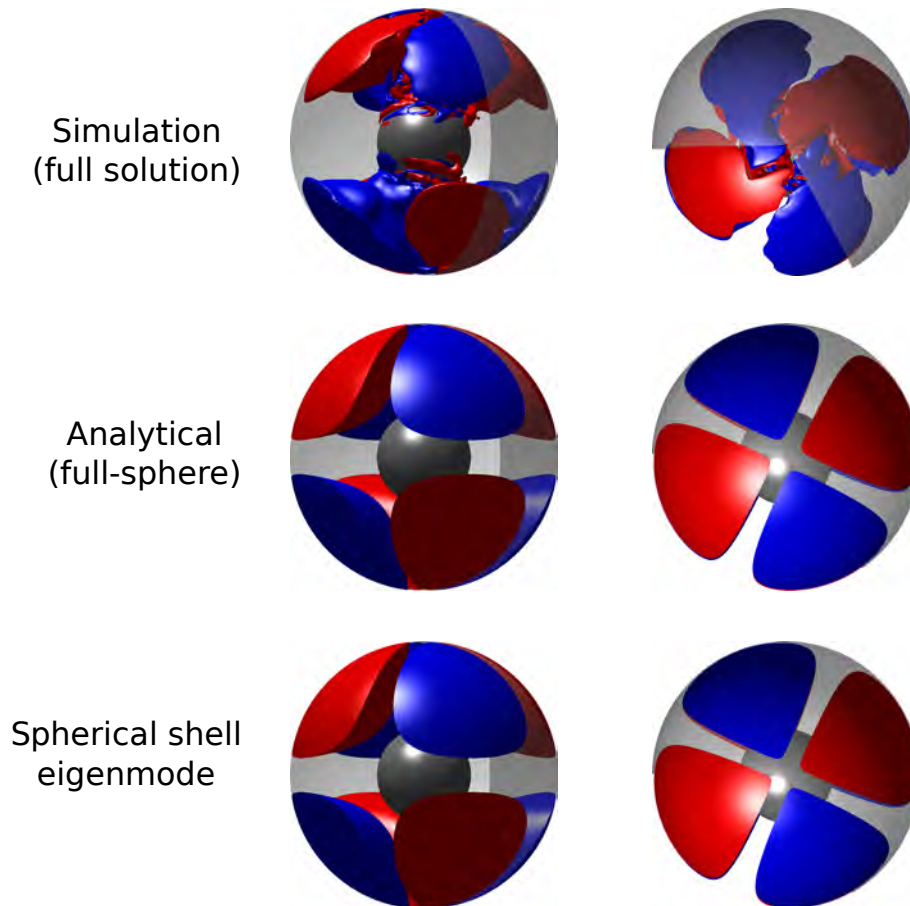


Figure 6.6: (Colour online) Comparison of flow structures between simulation (top row), analytical prediction for a full sphere (middle row) based on [Zhang et al. \(2001\)](#) and spherical shell eigenmode computed using SINGE (bottom row) for the (3, 2) mode at $E = 10^{-4}$, $Ro = -2$. Shown here are isosurfaces of non-axisymmetric cylindrically radial velocity (u_s). Red is positive (outward) while blue is negative (inward). The inner sphere has been shown for the full sphere mode for comparison. Note that no filtering has been performed on the solution. The whole solution is dominated by this mode at this parameters. The similarities are self-evident.

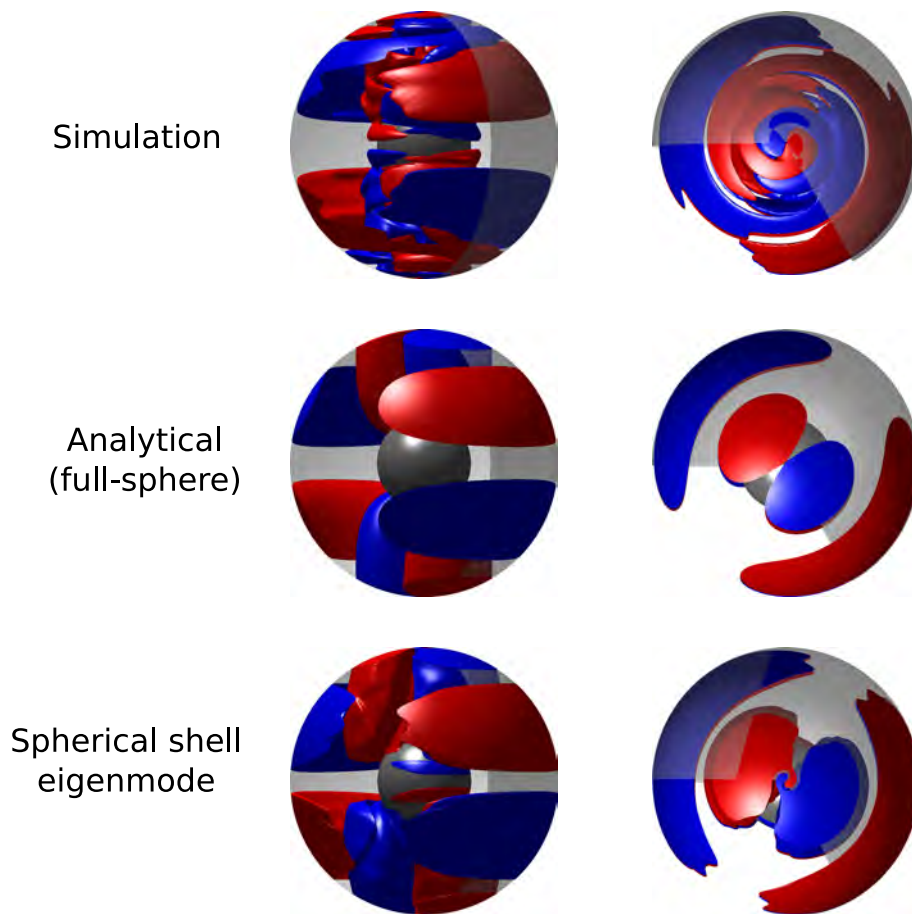


Figure 6.7: (Colour online) Comparison of flow structures between simulation (top row), analytical prediction for a full sphere (middle row) based on Zhang et al. (2001) and spherical shell eigenmode (bottom row) for the (4, 1) mode at $E = 10^{-4}$, $Ro = -2$. Shown here are isosurfaces of non-axisymmetric cylindrically radial velocity (u_s). Red is positive (outward) while blue is negative (inward). The inner sphere has been shown for the full sphere mode for comparison. The mode was filtered out using relevant spherical harmonics. The mode structure in the simulation somewhat resembles the theoretical structures, but has been twisted up by the background flow. The effect of background flow is discussed in section 6.7.

Table 6.1 compares the frequencies of the (3, 2) mode found in different experimental setups as well as the two numerical simulations presented here and the eigenvalues for a full sphere and a spherical shell. Both eigenvalues agree perfectly. However, numerical and experimental values show a slight deviation. Possible reasons can be differences in Ekman numbers, differential rotation or more generally, the effect of the background flow. Since the values in table 6.1 span four decades in Ekman number, the dependence on Ekman number can only be weak. The dependence on differential rotation is likely larger and will be discussed in section 6.7.

Besides the two most dominant lines in the spectrogram for the $m = 1$ SI and the (3, 2) mode, there are several other lines which are less dominant, but nevertheless clearly

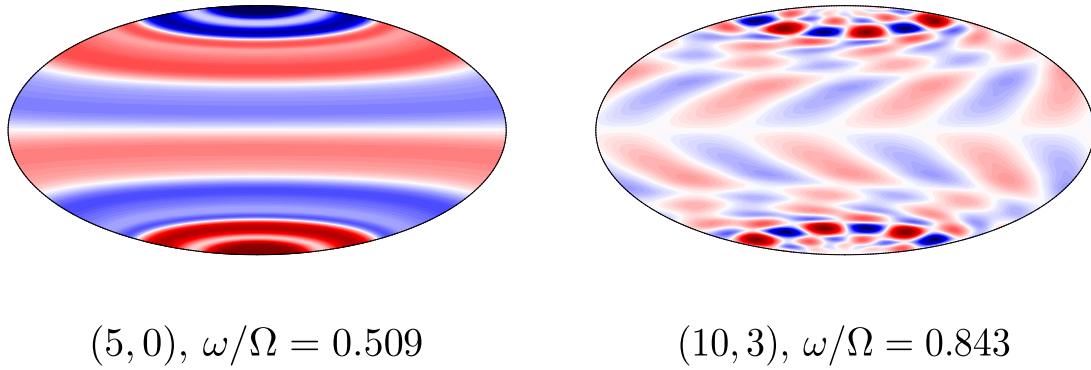


Figure 6.8: EA inertial modes with $m = 0$ and $m = 3$, not identified by Hoff et al. (2016b) and Hoff et al. (2016a). Simulation parameters are $E = 10^{-4}$, $Ro = -1.5$. Shown here is pressure at the outer boundary on a Hammer projection. Red is positive (outwards) while blue is negative (inwards). Note that the $(10, 3)$ mode is not the only $m = 3$ mode present, but is the one that corresponds to the spectrogram line around $\omega/\Omega = 0.85$.

visible against the background. Among the less dominant modes, the $(4, 1)$ mode can be easily identified. It can be seen as a relatively ‘bright’ line around $\omega/\Omega = 0.6$ in the spectrograms in figure 6.2. We tried to visualise this mode by filtering out spherical harmonic contributions with azimuthal wavenumber, $m = 1$ and equatorially antisymmetric. Figure 6.7 compares the result with $(4, 1)$ eigenmodes of a full sphere and a spherical shell. Once more, an overall similarity is convincing enough but also reveals the impact of the background flow. The frequency agrees with eigenvalues and experimental values to a great extent, as can be seen in table 6.2.

The line in the spectrogram around $\omega/\Omega = 0.85$ is an $m = 3$ mode which can be identified as a $(10, 3)$ mode based on its frequency (table 6.2). Analysis of the spectral flow contribution shows that another $m = 3$ mode is present in the system. Filtering out the $m = 3$ equatorially antisymmetric contributions of spherical harmonics reveals a dominant $(10, 3)$ structure. The dominant axisymmetric EA mode is the $(5, 0)$ mode. These modes are shown in figure 6.8.

As discussed by Hoff et al. (2016b) the ‘fast’ inertial modes appear in pairs that form a triadic resonance with the fundamental instability. These triadic resonances will be discussed in more detail in section 6.8.

6.6.1.4 Turbulence

Around $|Ro| = 2.3$, the spectrograms show a transition to a regime where small scale flows form a broadband spectrum. The frequencies of the dominant $(3, 2)$ and the fundamental mode are more strongly influenced by the background flow, including a sudden jump in the frequency of the $(3, 2)$ mode, similar to observations by Hoff et al. (2016b). The inertial mode $(3, 2)$ is still the dominant large-scale structure of the flow. Around $Ro = -2.7$, one finds a new mode onset which has an $m = 2$ and is equatorially symmetric. However, this mode has not been identified yet. The details of the turbulent regime will be discussed in chapter.

6.6.2 Ekman number, $E = 10^{-5}$

This Ekman number corresponds well with that of the experiments of Hoff et al. (2016b). Strong computational requirements prevented us from venturing into the turbulent regime, but we concentrate on the fundamental instability and the ‘fast’ inertial modes. Figure 6.9 shows the clear similarities of the respective MagIC and XSHELLS numerical spectrograms at $E = 10^{-5}$ with the experimental results at $E = 1.52 \times 10^{-5}$. Differences arise, as before, due to differences in resolution in Ro which was 0.05, 0.01 and 0.02, for MagIC, XSHELLS and the experiments, respectively, and in the duration for which time series data were collected in the three cases. Note that the regimes covered in Ro by the individual simulations and the experiments are different. We discuss the different flow transitions in the spectrograms as follows.

6.6.2.1 Fundamental instability

The first non-axisymmetric instability found using MagIC is the primary Stewartson layer instability with an azimuthal wavenumber of $m = 2$ that sets in at $Ro = -0.133$. A secondary $m = 1$ instability already comes in at $Ro = -0.16$ and from there on dominates the solution. Frequency and structure analysis identifies it as the fundamental Stewartson layer instability discussed for $E = 10^{-4}$ above.

Numerical exploration at a lower Ekman number of 3×10^{-6} and the experimental results of Triana (2011) confirm that this mode continues to set in as a secondary instability for smaller Ekman numbers and negative differential rotation. Figure 6.10 shows the critical wavenumber in panel (a) and the critical differential rotation in panel (b) at onset of the first non-axisymmetric instability for different Ekman numbers for $Ro < 0$. In addition to that, the onset of the secondary $m = 1$ instability has also been shown. A straight line fit has been used to extrapolate the onset of this instability to lower Ekman numbers. For example, at $E = 3 \times 10^{-6}$, the first instability sets in for $Ro = -0.0213$ and has a wavenumber of $m_c = 12$. The secondary $m = 1$ instability clearly dominates at $Ro = -0.09$, as shown in figure 6.11. The experimental parameters of the 3-metre experiment are clearly located beyond the extrapolated $m = 1$ onset, which may explain the prominence of this instability in their data (Triana 2011).

Hoff et al. (2016b) find an $m = 1$ mode at onset at all their Ekman numbers, the critical $|Ro|$ for which have been shown in figure 6.10b. The critical values seem to be slightly above those determined by MagIC simulations. The XSHELLS simulations confirm the critical $|Ro|$ and m_c observed at BTU C-S for $E = 10^{-5}$. Both use the same aspect ratio of $r_i/r_o = 1/3$ that slightly differs from the $r_i/r_o = 0.35$ used for MagIC and could explain the discrepancy.

6.6.2.2 Fast inertial modes

An analysis of the MagIC results shows that equatorial symmetry is broken at $Ro = -0.35$, but the equatorial antisymmetric energy remains too low to identify the underlying mode. At around $Ro = -0.4$, the total kinetic energy starts to show minor oscillations which can be attributed to nonlinear interactions between different modes. This shows as a distinct regime in the spectrograms. At $Ro = -0.55$, the kinetic energy becomes chaotic due to the onset of a ‘fast’ inertial mode - identified as the (5, 2) mode.

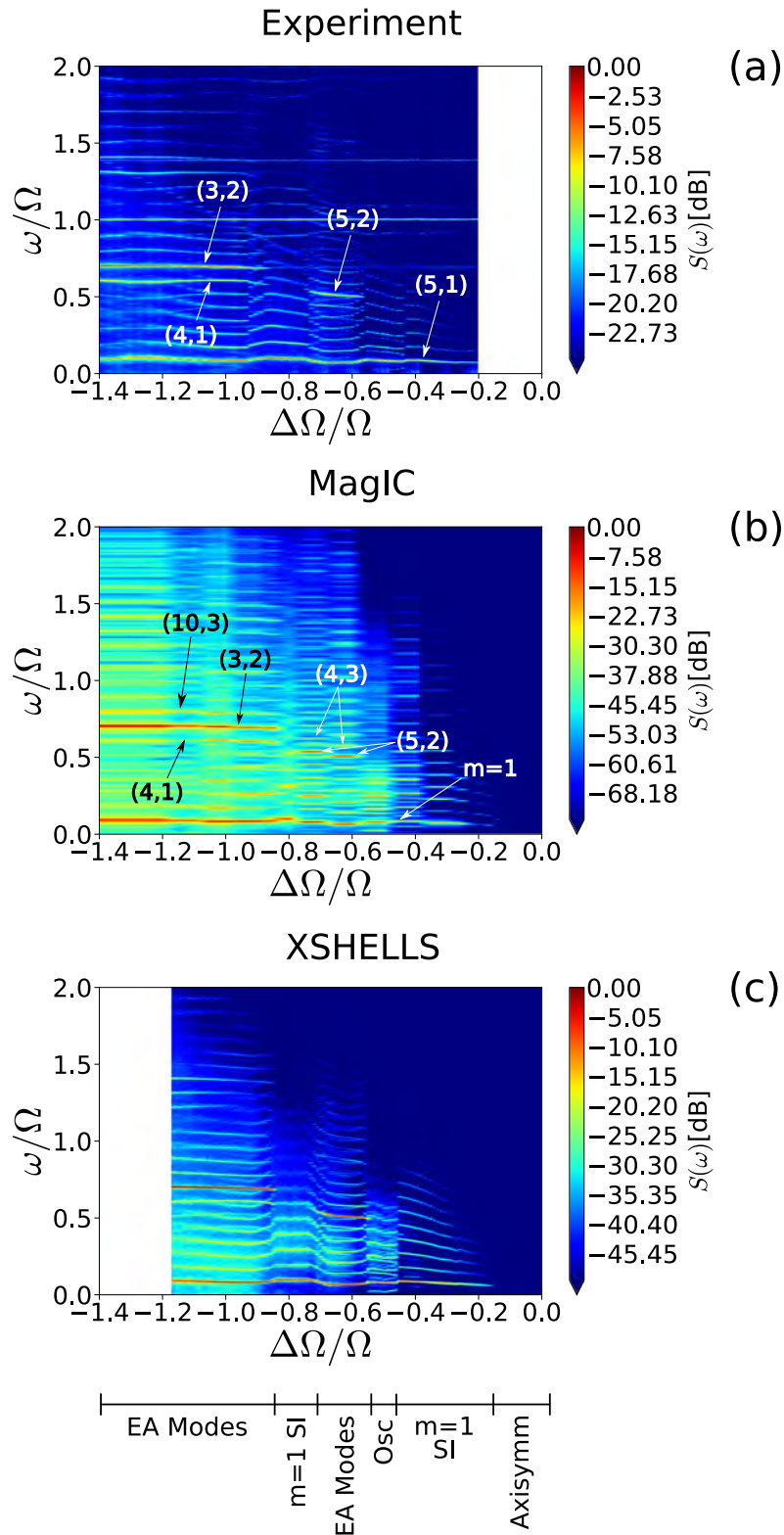


Figure 6.9: Spectrograms at (a) $E = 1.52 \times 10^{-5}$, obtained from experiments at BTU-CS and at $E = 10^{-5}$ ((b) and (c)) obtained using MagIC and XSHELLS, respectively. The similarity in the different observed regimes can be clearly seen. All the major modes identified in the simulations have been marked in (b). EA = Equatorially antisymmetric, SI = Stewartson layer Instability, Osc = Oscillatory regime.

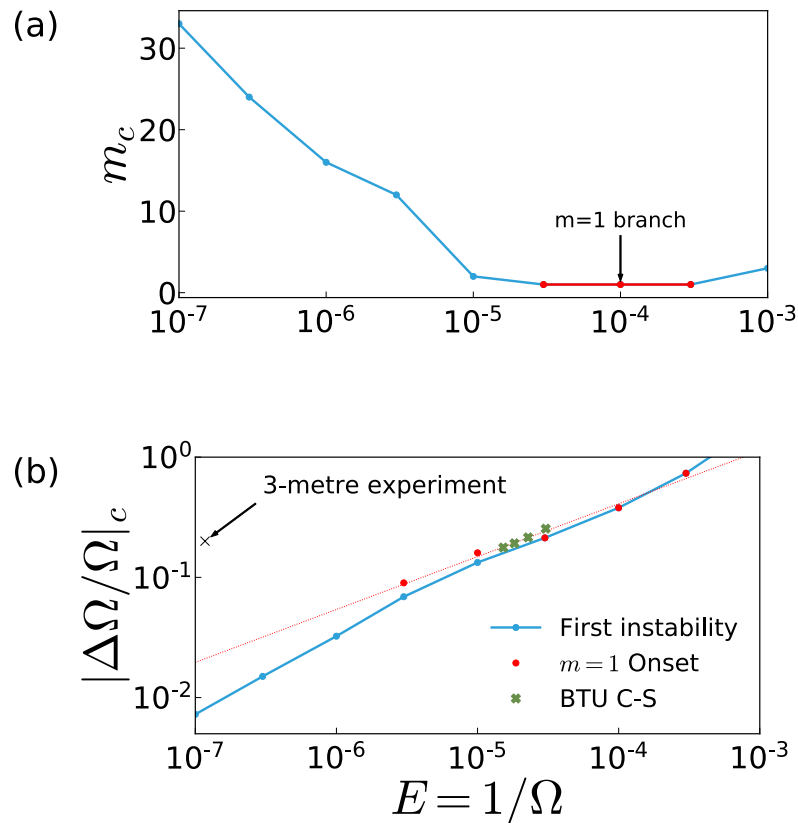


Figure 6.10: Critical values for onset of first non-axisymmetric instability at different Ekman numbers. (a) shows the critical wavenumber m . (b) shows the critical differential rotation. Red circles in (b) mark the onset of the fundamental $m = 1$ mode seen as a secondary instability at low Ekman numbers. A straight line approximation shows that the 3-metre experiment was always supercritical to the $m = 1$ onset.

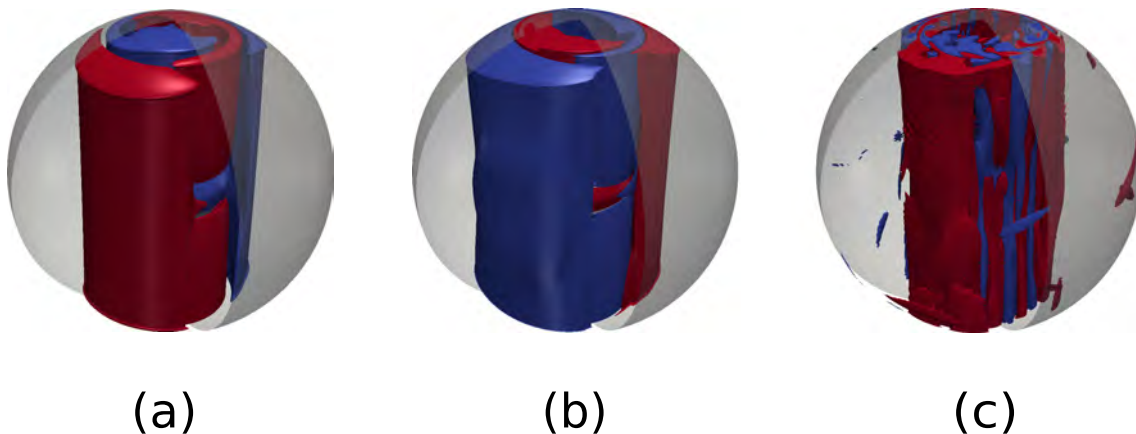


Figure 6.11: The $m = 1$ fundamental mode at (a) $E = 10^{-4}$, (b) $E = 10^{-5}$ and (c) $E = 3 \times 10^{-6}$. At $E = 10^{-4}$, the mode is the first non-axisymmetric instability to set in. At lower Ekman numbers, it comes in as a secondary instability.

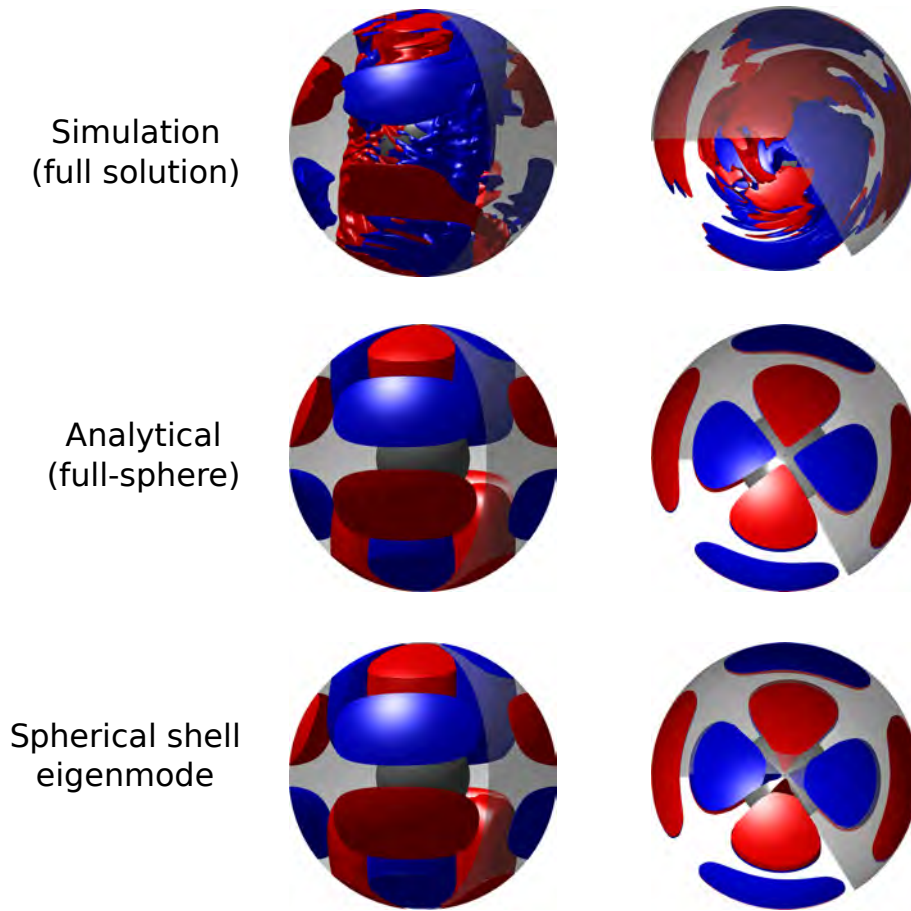


Figure 6.12: (Colour online) Comparison of flow structures between simulation (top row), analytical prediction for a full sphere (middle row) based on [Zhang et al. \(2001\)](#) and spherical shell eigenmode computed using SINGE (bottom row) for the (5,2) mode at $E = 10^{-5}$, $Ro = -0.6$. Shown here are isosurfaces of non-axisymmetric cylindrically radial velocity (u_s). Red is positive (outward) while blue is negative (inward). The inner sphere has been shown for the full sphere mode for comparison. Note that no filtering has been performed on the solution. The whole solution is dominated by this mode at this parameters. The similarities are self-evident.

A comparison with the analytical structure shown in figure 6.12 as well as an agreement in frequency confirms the identification of this mode. We further compare the MagIC simulations with the experimental PIV measurements from BTU-CS in figure 6.13. Note that the field of view in the experiment only covers a section of the planar circle (see figure 2(b) in [Hoff et al. \(2016a\)](#)). Hence, the velocity field had to be reconstructed for a full circular geometry.

An analysis of the MagIC results shows that a (4, 3) inertial mode sets in together with the dominant (5, 2) mode. A third mode present at the same time has been identified as an $m = 1$ mode with a frequency close to that of the (6, 1) ‘fast’ inertial mode. However, its structure seems too complex and distorted to verify this identification.

At $Ro = -0.8$, the ‘fast’ inertial modes disappear, the equatorially antisymmetric

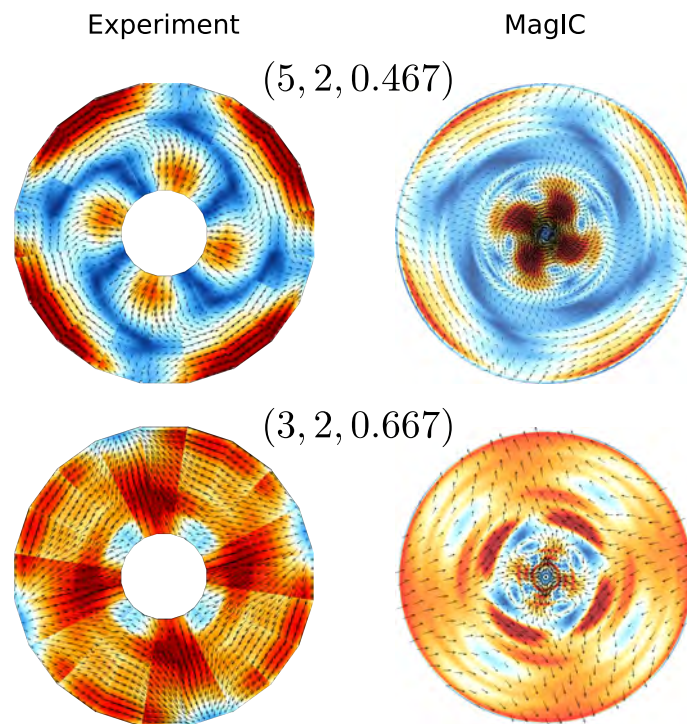


Figure 6.13: Comparison of z -slices of velocity magnitudes from experiments and simulations. The experimental data have been taken at $z/r_o = 1/3$, while the simulation data has been shown at $z/r_o = 0.35$. The structures look very similar for both modes - (5, 2) and (3, 2). For the (5, 2) mode the data have been taken at $Ro = -0.68$ for the experiment and at $Ro = -0.7$ for the simulation. For the (3, 2) mode, the corresponding numbers are $Ro = -1.11$ and $Ro = -1.1$, respectively. Colours represent velocity magnitudes - horizontal velocity for experiments and total velocity for simulations. The arrows indicate local flow speed and direction.

kinetic energy decreases significantly and the fundamental $m = 1$ Stewartson instability becomes the dominant large-scale structure in the solution again.

At $Ro = -0.85$, we see the emergence of ‘fast’ EA inertial modes yet again. The (3, 2) mode, which has already been identified at $E = 10^{-4}$ is the dominant mode. Figure 6.13 shows the clear similarities of the structure from the numerical simulations and the PIV measurements obtained in the experiments at BTU C-S.

The other sub-dominant modes identified in this regime are the (10, 3) and (4, 1) modes, pairs of which also form triadic resonances with the $m = 1$ mode, explained in more detail in section 6.8. The (4, 1) mode has a structure which could resemble a twisted (4, 1) as well as a distorted (6, 1) mode (figure 6.14). Since its frequency matches well with that of the spherical shell eigenvalue of the (4, 1) mode, we classify it as such. The $m = 3$ modes seen at this Ekman number have been compared to their spherical shell eigenmodes in figure 6.15.

These modes remain dominant till the point the simulations were run, $Ro = -1.4$ for MagIC and $Ro = -1.17$ for XSHELLS, whereby computational demands made it increasingly difficult to increase differential rotation magnitudes. Hoff et al. (2016b) finds

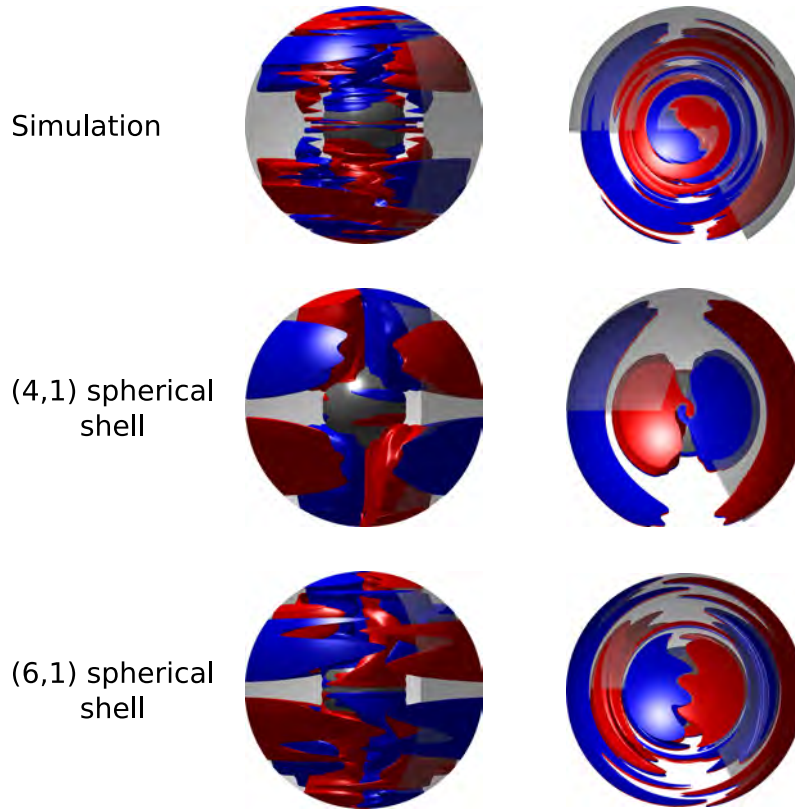


Figure 6.14: Comparison of structure of $m = 1$ EA mode at $Ro = -1$. The structure of the solution could be said to match a twisted (4, 1) mode or a distorted (6, 1) mode. Since its frequency matches well with that of the theoretical value for the (4, 1) mode, we classify it as such. Shown here are isosurfaces of cylindrically radial velocity. Red (online) represents outwards while blue represents inwards.

the transition to turbulence in this regime to be at $Ro = -1.73$ at $E = 1.52 \times 10^{-5}$.

6.7 Effect of background flow on inertial modes

Table 6.1 and 6.2 show that the frequencies of the inertial modes in the simulations as well as in the experiments (BTU C-S, 3 metre, 60 cm) match the theoretical predictions very closely, while for other cases, like for the (4, 3) mode, the difference can be as large as 40%. The structures of the modes found in simulations and experiments are mostly distorted close to or inside the tangent cylinder. The comparison of eigenvalues for a spherical shell and a full sphere in tables 6.1 and 6.2 show that the presence of an inner sphere has a relatively small effect, at most 5% seen for the (6, 1) mode. The presence of a background shear flow has, obviously, a much larger impact.

To explore this, we artificially excite inertial waves at different Ro and analyse how their resonance frequency changes. Following Rieutord et al. (2012), the excitation is an artificially imposed boundary forcing of the form

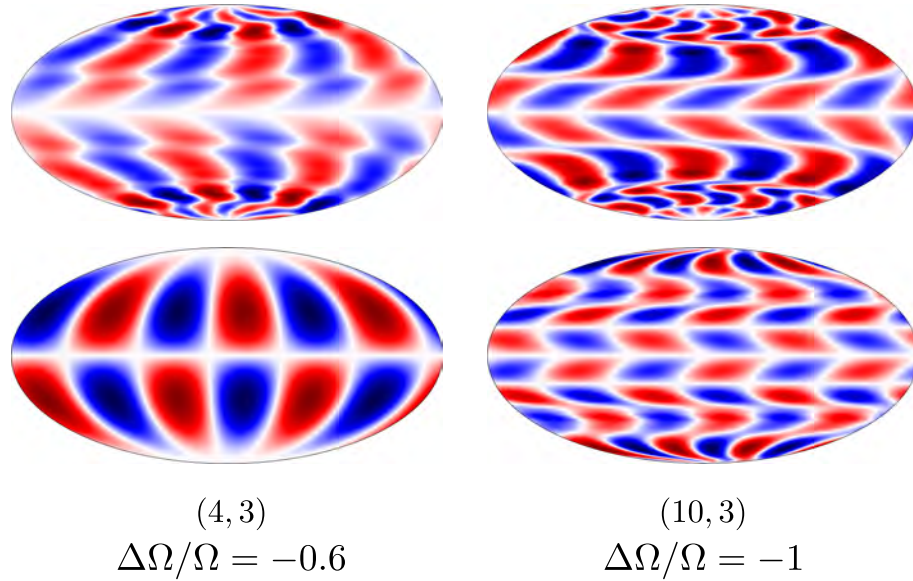


Figure 6.15: Comparison of structure of the $m = 3$ EA modes at $Ro = -0.6, -1$. The modes have frequencies $\omega/\Omega = 0.585$ and 0.806 can be identified as the $(4, 3)$ and $(10, 3)$ modes, respectively. The solutions closely match the respective eigenmodes of the spherical shell in terms of frequencies as well as structures. Shown here are contour maps of pressure at the outer boundary on a Hammer projection.

$$\mathbf{u}(\theta, \phi) = \left(\frac{1}{\sin \theta} \frac{\partial Y_m^m}{\partial \phi} \hat{\mathbf{e}}_\theta - \frac{\partial Y_m^m}{\partial \theta} \hat{\mathbf{e}}_\phi \right) e^{i\omega t} \quad (6.4)$$

where $\mathbf{u}(\theta, \phi)$ is the velocity on a fixed spherical surface, and $\hat{\mathbf{e}}$ represent unit vectors in θ and ϕ directions.

Figure 6.16 shows the resonances at eight different Ro for an $m = 2$ excitation which efficiently excites the $(3, 2)$ mode. Figure 6.17 shows how the resonance frequency depends on Ro . For no differential rotation, we recover the spherical shell eigenvalue. Lowering Ro , the frequency of 0.73 found for the onset of the $(3, 2)$ mode at $Ro = -1.33$ is gradually approached. The onset of the kinetic energy oscillations at $Ro = -1.25$ prevented us from going closer to the onset value of the inertial mode.

Figure 6.18 shows the effect of background flow on the $(3, 2)$ inertial mode. Until $Ro = -1.2$, the mode is artificially excited while the other panels illustrate the mode being naturally excited in the system. However, with increase in differential rotation, the mode starts to get distorted at around $Ro = -0.5$ - the part inside the tangent cylinder getting slowly twisted. This is due to the vastly different nature of the background flow inside and outside the tangent cylinder, shown in figure 6.19. As approximated by Proudman (Proudman 1956), the bulk of the flow outside the tangent cylinder is in solid body rotation with the outer boundary and thus has a weaker effect on the inertial mode as compared to the flow inside.

Internal shear layers are a characteristic feature of inertial modes in a spherical shell because of the ill-posed nature of the problem (e.g. Stewartson and Rickard 1969). They emanate from critical latitudes for which $\cos \theta = \omega/2\Omega$, travel along the characteristics

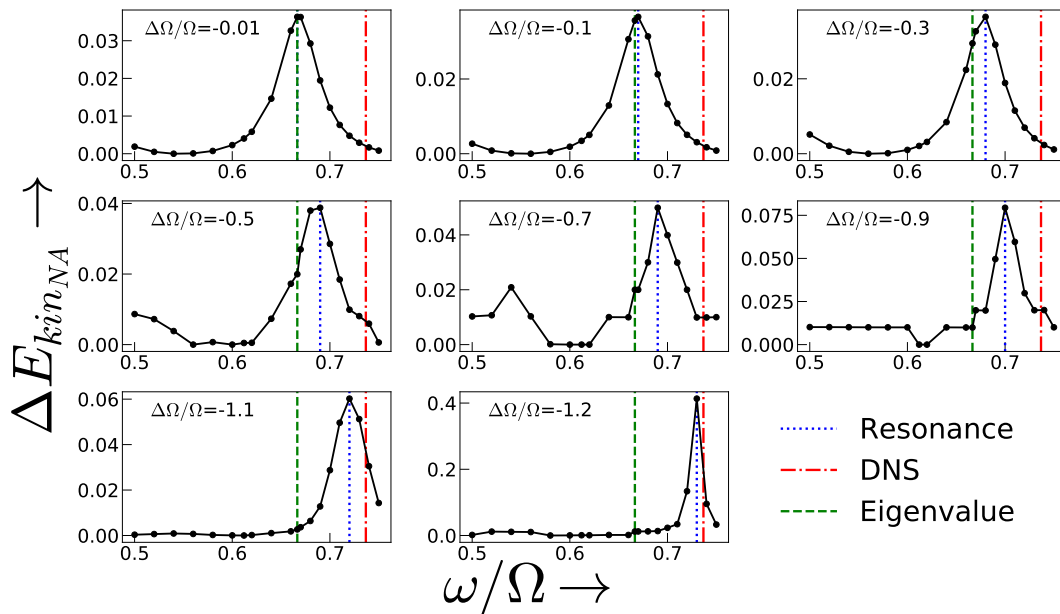


Figure 6.16: (Colour online) Influence of background rotation on inertial mode frequency for mode (3, 2) in Greenspan notation, at $E = 10^{-4}$. For very small differential rotation, we recover the analytical prediction for a full sphere. Increase of Ro to more negative values changes the normal mode frequency and shifts it towards the value we observe in simulations. The onset of inertial modes for simulations at this Ekman number is at $Ro = -1.3$.

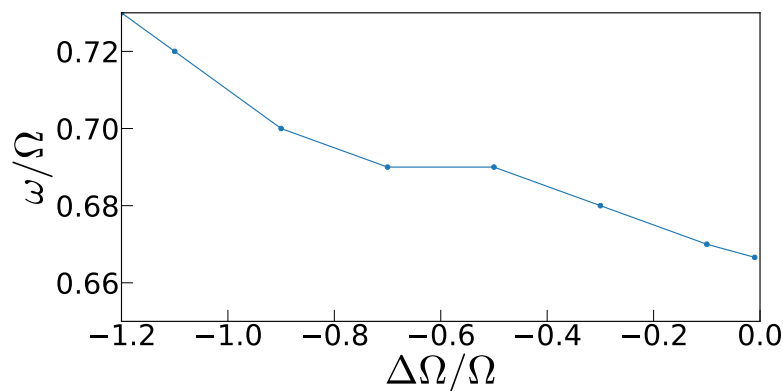


Figure 6.17: Change in normal mode frequency vs Ro for the (3, 2) mode at $E = 10^{-4}$. The frequency changes from the analytical value for full sphere to the one found in our simulations.

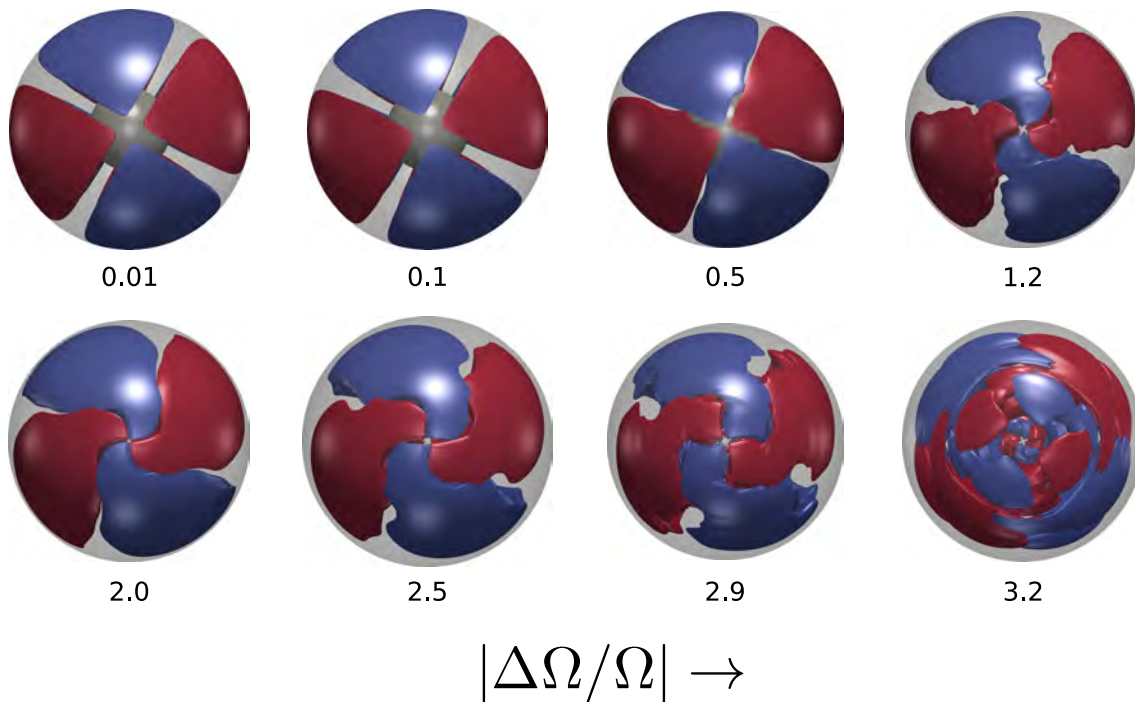


Figure 6.18: Change in the structure of $(3, 2)$ mode. The labels indicate $|Ro|$. One can see that the mode keeps getting twisted inside the tangent cylinder and breaks down after a certain point. The top panel shows the mode structures that have been excited artificially, while the bottom panel shows the mode that onsets naturally. Shown here are isosurfaces of cylindrically radial velocity u_s .

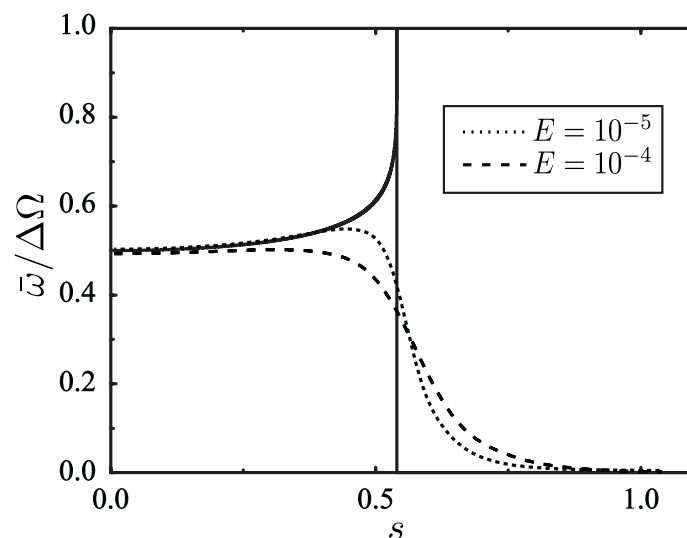


Figure 6.19: A typical axisymmetric flow solution. It shows axisymmetric z -averaged zonal flow at $E = 10^{-4}$ and 10^{-5} . The general form of the solution is independent of Ro . The position of the tangent cylinder coincides with the solid vertical line.

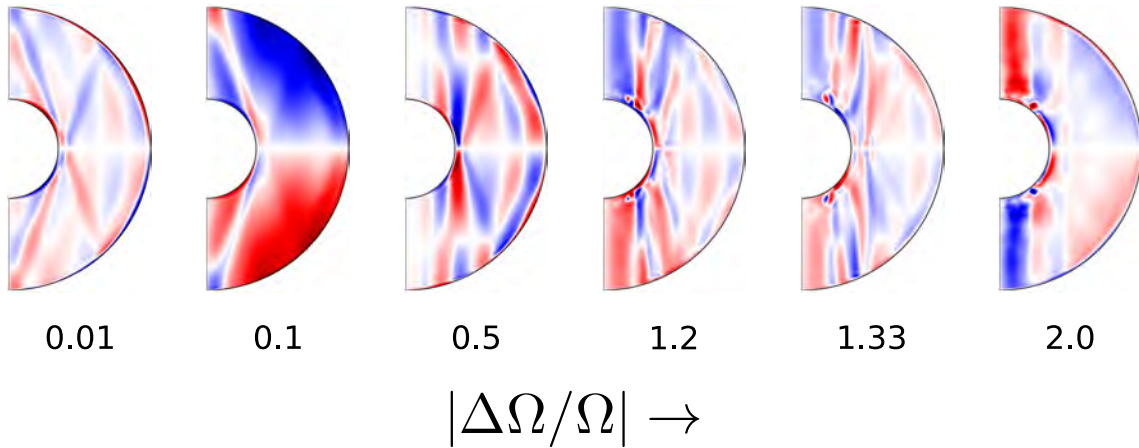


Figure 6.20: The figure shows meridional slices of zonal velocity u_ϕ of the filtered (3, 2) mode as Ro changes. The internal shear layers seen initially seem to get aligned more and more with the rotation axis as the frequency of the mode increases.

of the inertial wave equation and always maintain the same angle of $\cos^{-1}(\omega/2\Omega)$ with respect to the rotation axis. Since they are so thin, they have only been detected once in experiments (Triana 2011) and only for the ‘spin-over’ mode, which is not present in our system.

To illustrate how the shear layers change with differential rotation, we filter out the (3, 2) mode and compare meridional sections of zonal velocity u_ϕ in figure 6.20. With no differential rotation, the internal shear layers mode are perfectly emanating as straight rays from the expected critical latitudes at the critical angle. However, as one increases the differential rotation, the shear layers seem to get aligned more and more with the rotation axis.

6.8 Triadic interactions

6.8.1 Theoretical background

The phenomenon of triadic resonance inevitably appears in any physical problem involving non-linear wave interactions. Coupled harmonic oscillators, photon decay and waves in plasma (see e.g Bellan 2008) are just a few examples. In a geophysical context, they have been studied in the context of internal waves in oceans (McComas and Bretherton 1977) and resonant interactions of Rossby waves (Pedlosky 1987) and their instability (Zhang and Pedlosky 2007). Triadic resonances are also observed when a flow becomes unstable to inertial modes as explained in chapter 2. We first present the basic idea and then elaborate how it can apply to the present scenario.

The non-linear interaction between two waves would obey a general form like

$$e^{i(\mathbf{k}_1 \cdot \mathbf{x} \pm \omega_1 t)} e^{i(\mathbf{k}_2 \cdot \mathbf{x} \pm \omega_2 t)} = e^{i((\mathbf{k}_1 + \mathbf{k}_2) \cdot \mathbf{x} \pm (\omega_1 + \omega_2) t)} \quad (6.5)$$

where \mathbf{k} and ω represent wavevector and angular frequency, respectively. If the system has a normal mode (\mathbf{k}_3, ω_3) such that

$$\mathbf{k}_3 = \mathbf{k}_1 \pm \mathbf{k}_2, \quad \omega_3 = \omega_1 \pm \omega_2 \quad (6.6)$$

it can get resonantly excited due to the non-linear interactions of the waves with subscripts 1 and 2.

Consider two inertial modes \mathbf{Q}_1 and \mathbf{Q}_2 , with azimuthal and time dependences $e^{i(m_1\phi - \omega_1 t)}$ and $e^{i(m_2\phi - \omega_2 t)}$, respectively and the velocity and pressure perturbations \mathbf{u} and p due to their nonlinear interaction, denoted by \mathbf{u} . \mathbf{u} follows

$$\frac{\partial \mathbf{u}}{\partial t} + 2\hat{\mathbf{z}} \times \mathbf{u} + \nabla p + (\mathbf{Q}_1 \cdot \nabla \mathbf{Q}_2 + \mathbf{Q}_2 \cdot \nabla \mathbf{Q}_1) e^{i((m_1 \pm m_2)\phi - (\omega_1 \pm \omega_2)t)} = 0 \quad (6.7)$$

Expanding \mathbf{u} and p in terms of inertial modes \mathbf{Q}_j and Φ_j , respectively,

$$\mathbf{u} = \sum_j c_j \mathbf{Q}_j e^{i(m_j\phi - \omega_j t)}, \quad p = \sum_j c_j \Phi_j e^{i(m_j\phi - \omega_j t)} \quad (6.8)$$

where, $c_j \equiv c_j(t)$, we get

$$\begin{aligned} \sum_j \left[\mathbf{Q}_j \frac{\partial c_j}{\partial t} + c_j (-i\omega_j \mathbf{Q}_j + \nabla \Phi_j + 2\hat{\mathbf{z}} \times \mathbf{Q}_j) \right] e^{i(m_j\phi - \omega_j t)} \\ = -(\mathbf{Q}_1 \cdot \nabla \mathbf{Q}_2 + \mathbf{Q}_2 \cdot \nabla \mathbf{Q}_1) e^{i((m_1 \pm m_2)\phi - (\omega_1 \pm \omega_2)t)} \end{aligned} \quad (6.9)$$

By definition, $-i\omega_j \mathbf{Q}_j + \nabla \Phi_j + 2\hat{\mathbf{z}} \times \mathbf{Q}_j = 0$, for any inertial mode \mathbf{Q}_j . Thus, we get

$$\sum_j \mathbf{Q}_j \frac{\partial c_j}{\partial t} e^{i(m_j\phi - \omega_j t)} = -(\mathbf{Q}_1 \cdot \nabla \mathbf{Q}_2 + \mathbf{Q}_2 \cdot \nabla \mathbf{Q}_1) e^{i((m_1 \pm m_2)\phi - (\omega_1 \pm \omega_2)t)} \quad (6.10)$$

Let us project the perturbation \mathbf{u} onto an inertial mode \mathbf{Q}_k . Since inertial modes are orthogonal, we multiply both sides by \mathbf{Q}_k^\dagger and integrate over the whole volume of the container. We get

$$\frac{\partial c_k}{\partial t} = -e^{-i(\omega_1 \pm \omega_2 - \omega_k)t} \int_\phi e^{i(m_1 \pm m_2 - m_k)\phi} d\phi \int \mathbf{Q}_k^\dagger \cdot (\mathbf{Q}_1 \cdot \nabla \mathbf{Q}_2 + \mathbf{Q}_2 \cdot \nabla \mathbf{Q}_1) d\tau \quad (6.11)$$

where τ represents a ϕ -slice.

Equation (6.11) defines different ‘‘selection’’ rules for the inertial mode \mathbf{Q}_k that could potentially be resonantly excited by the nonlinear interaction:

1. The wavenumbers have to match

$$m_k = m_1 \pm m_2 \quad (6.12)$$

for the integral over ϕ to be non-zero.

2. The frequencies have to fulfil $\omega_1 \pm \omega_2 - \omega_k = 0$ for there to be a resonance.

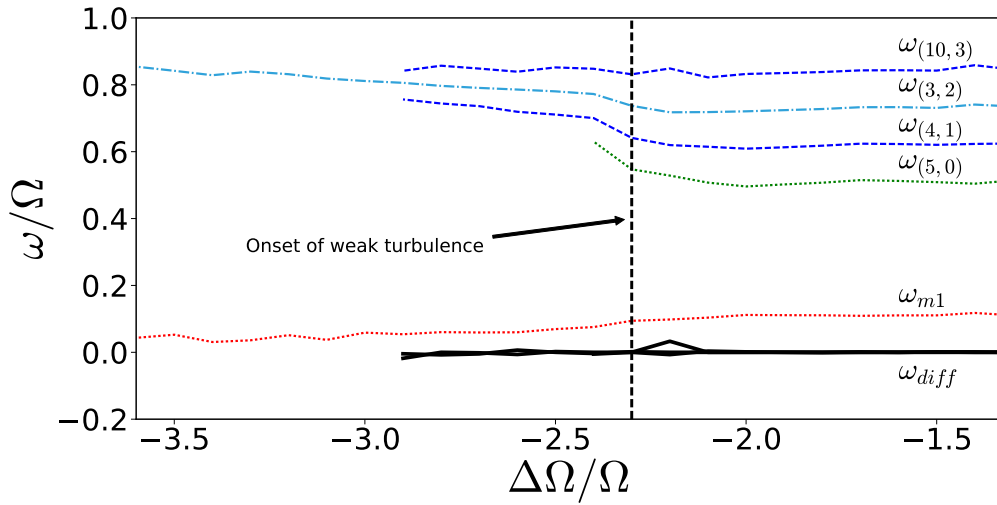


Figure 6.21: Triadic resonances at $E = 10^{-4}$. ω_{diff} refers to the lines of various differences: $\omega_{(3,2)} - \omega_{(4,1)} - \omega_{m1}$, $\omega_{(10,3)} - \omega_{(3,2)} - \omega_{m1}$ and $\omega_{(4,1)} - \omega_{(5,0)} - \omega_{m1}$. ω_{diff} is close to zero at all times.

3. The integral over τ provides additional selection rules. An obvious one concerns the equatorial symmetry. The product of two vector fields of opposite equatorial symmetry vanishes when integrated over volume. Thus, the integral over τ is non-zero only when \mathcal{Q}_k^\dagger has the same equatorial symmetry as the nonlinear term involving \mathcal{Q}_1 and \mathcal{Q}_2 . If \mathcal{Q}_1 and \mathcal{Q}_2 have opposite equatorial symmetries, then \mathcal{Q}_k has to be equatorially antisymmetric. If both of them possess the same equatorial symmetry, \mathcal{Q}_k has to be equatorially symmetric.
4. The τ integral may also define additional constraints for the radial and latitudinal structure that are not explored here.

6.8.2 Triadic resonances in the inertial mode regime

All the identified ‘fast’ inertial modes form pairwise triadic resonances with the fundamental $m = 1$ Stewartson layer instability. For example, at $E = 10^{-4}$, we identify the pairs $[(3, 2), (4, 1)]$, $[(10, 3), (3, 2)]$ and $[(4, 1), (5, 0)]$. The triads obviously fulfil the wave number criteria and figure 6.21 confirms that their frequencies indeed add up to nearly zero. As for spherical harmonics, inertial modes are equatorially symmetric (antisymmetric) when the difference $l - m$ is even (odd). The equatorially symmetry criterion is thus also fulfilled.

Figure 6.22 shows the 3D structure of the nonlinear advective acceleration of the triad $[(3, 2), (4, 1)]$ and the fundamental $m = 1$ mode in the left column. This is compared with the effective acceleration of the mode with the respective wavenumber, frequency, and equatorial symmetry on the right. While the driving has a richer radial and latitudinal structure, only the simpler modes are resonantly driven.

To check that the triads also preserve a consistent phase locking, we compute the bicoherence, defined as

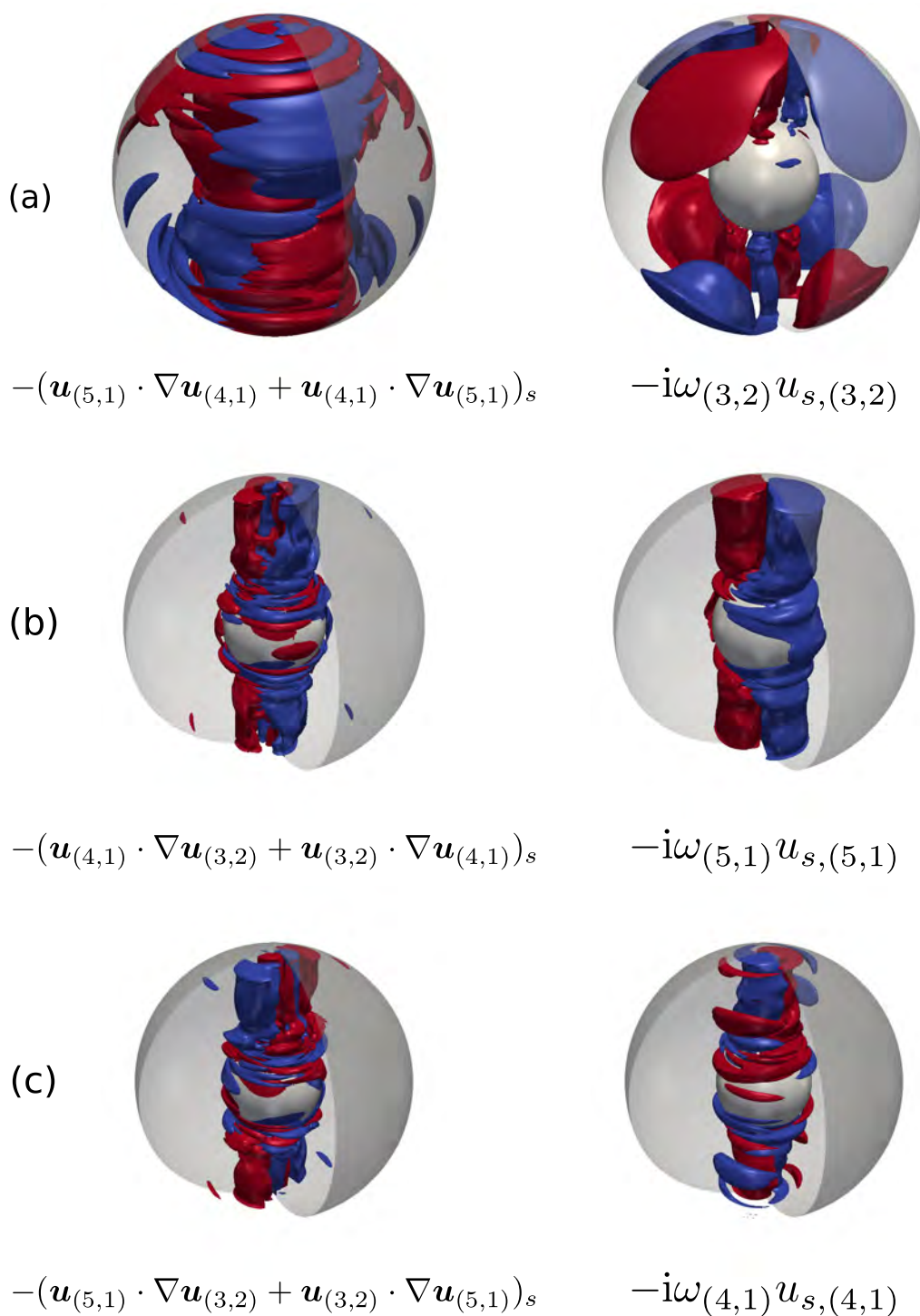


Figure 6.22: (Colour online) Comparison of the 3D structure of the advective acceleration due to the nonlinear interaction of two modes on the left with the structure of the effective acceleration of the third mode of the triad on the right, at $E = 10^{-4}$ and $Ro = -2$. Shown here are isosurfaces of cylindrically radial (s) components. Red denotes outward (positive), while blue denotes inward (negative). Subscripts 32, 41 and $m1$ denote the (3, 2), (4, 1) and the $m = 1$ fundamental instability, respectively.

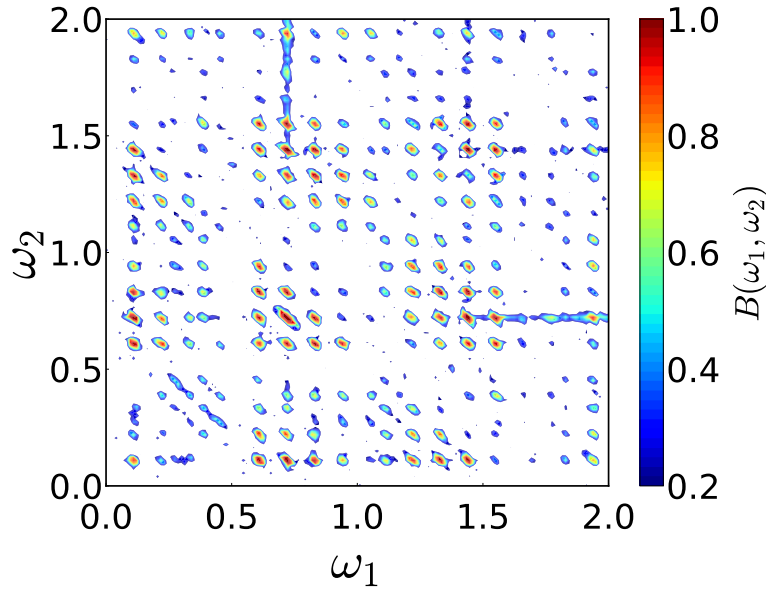


Figure 6.23: Bicoherence of u_ϕ time series taken at $r = 0.7r_o$, computed for $E = 10^{-4}$ and $Ro = -2$. All frequencies are non-dimensionalised by Ω . Compare with figure 6 from Hoff et al. (2016b).

$$B(\omega_1, \omega_2) = \frac{|\sum_n F_n(\omega_1)F_n(\omega_2)F_n^*(\omega_1 + \omega_2)|^2}{|F_n(\omega_1)F_n(\omega_2)|^2|F_n(\omega_1 + \omega_2)|^2} \quad (6.13)$$

where $F(\omega)$ represents the Fourier transform of a signal at frequency ω and $*$ denotes a complex conjugate. This is a statistical measure of the quadratic phase coupling (Nikias and Raghuvver 1987) determined by splitting a signal into several parts, computing the ‘bispectrum’ (one of the terms in the numerator) of individual parts and eventually summing them up. Wave interactions that preserve the same phase relation over the different parts of the time series result in a particularly strong $B(\omega_1, \omega_2)$. The HOSA Toolbox for MATLAB (Swami et al. 1998) is used for this purpose.

We compute the bicoherence for a time series of zonal velocity, u_ϕ , that we split into 16 segments overlapping by 50%. For each segment, 4096 points are used for the Fast Fourier Transform. $B(\omega_1, \omega_2)$ attains a high value for all identified triadic resonances, as shown in figure 6.23. For example, take the peak of $(\omega_1, \omega_2) = (0.61, 0.11)$ representing the coupling for the (4, 1) mode and $m = 1$ SI mode seen in this regime. $B(0.61, 0.11)$ has a very high value as these modes are phase coupled to the (3, 2) mode, having a frequency of $0.61 + 0.11 = 0.72$. The couplings with higher frequencies denote triadic resonances between pairs of higher harmonics of the (3, 2), (4, 1) and (10, 3) modes and the higher harmonics of the $m = 1$ fundamental mode. Strong self-interactions along the main diagonal can also be seen, especially for the dominant (3, 2) mode.

The major modes forming triadic resonances at $E = 10^{-5}$ and the degree to which they satisfy the frequency criteria are shown in figure 6.24. The pairs forming triads with the fundamental instability are [(5, 2), $m1EA$], [(4, 3), (5, 2)], [(3, 2), (6, 1)] and [(10, 3), (3, 2)], where $m1EA$ refers to the $m = 1$ EA inertial mode which could not be clearly identified.

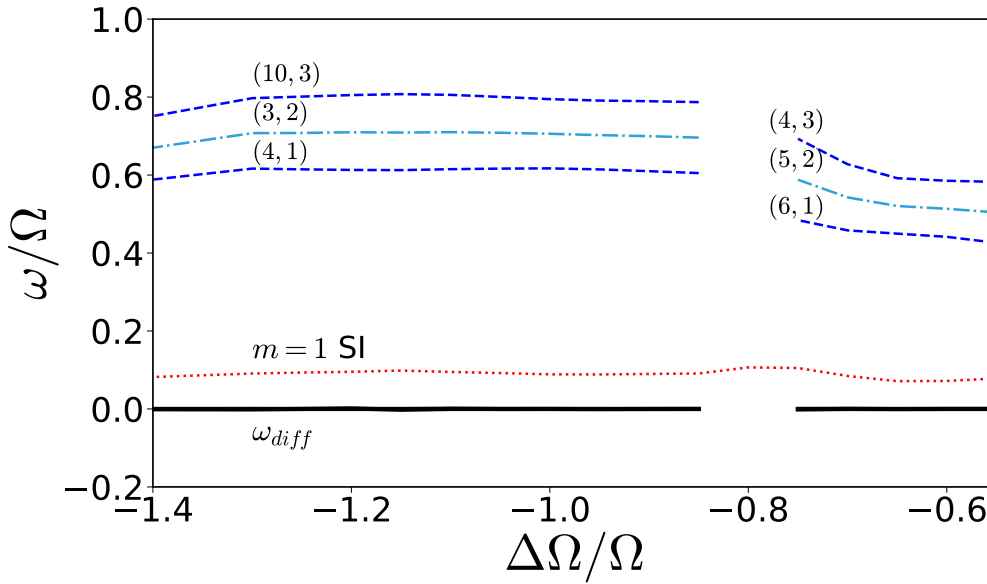


Figure 6.24: Triadic resonances at $E = 10^{-5}$. ω_{diff} refers to the lines of various frequency differences which form triadic resonances. ω_{diff} is close to zero at all times.

These triads have also been found in experiments at BTU C-S (Hoff et al. 2016b,a).

6.9 Onset of inertial modes

Since pairs of the ‘fast’ inertial EA modes form triadic resonances with the $m = 1$ fundamental instability, there are two possibilities:

- i. The EA modes are secondary instabilities of the equatorially symmetric (ES) modes - the $m = 1$ SI and its higher harmonics. This mechanism would be similar that of the shear and elliptical instabilities of precessing flow (Kerswell 1993), where a background flow becomes unstable to two inertial modes and the three form a triadic resonance. For the present system this would mean that the pairs of EA modes are to be interpreted as an instability of the SI and could only appear together and always at the same time.
- ii. The EA modes are instabilities of the background flow. If the background flow ($m = 0$) becomes unstable, it would give rise to not two, but a single EA mode which would then dominate the solution.

To determine whether the fundamental $m = 1$ instability is essential for the appearance of fast inertial modes, we suppress its onset by restricting the symmetry in numerical simulations. We choose the onset of the EA modes at $E = 10^{-4}$ as a test case since it is computationally less demanding. We initiate our simulations from an axisymmetric state and add an initial random noise perturbation to all spherical harmonic coefficients. Thereafter, we allow only all axisymmetric $m = 0$ modes and all EA modes to grow.

We find that at $Ro = -0.7$ all EA modes decay away as seen from the negative growth rates γ in panel (a) of figure 6.25. At $Ro = -0.8$, we find the onset of the first EA mode,

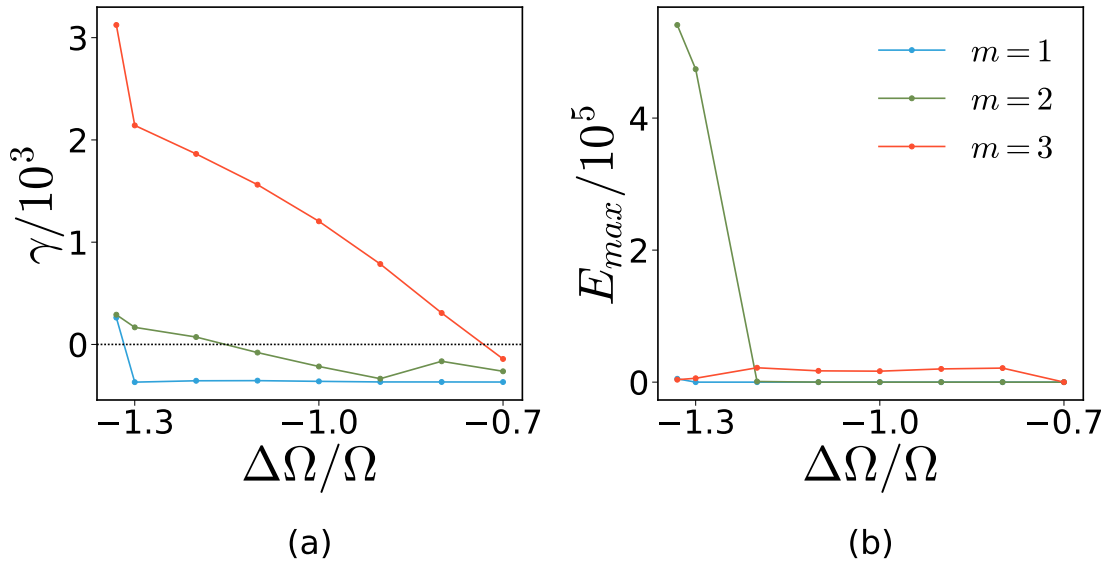


Figure 6.25: (a) Growth rates γ and (b) saturation energies (E_{max}) of EA modes at different Ro . Horizontal line in (a) marks zero growth rate.

which is the (4, 3) mode, not observed in the full system at $E = 10^{-4}$. Till $Ro = -1.1$, this is the only instability in the system. However, at $Ro = -1.2$, the (3, 2) mode has a positive growth rate, grows to a higher saturation value than the existing (4, 3) mode and remains as the dominant mode thereafter as can be seen in panel (b) of figure 6.25. Finally, at $Ro = -1.33$, where the onset of EA modes takes place for the full system, we find the emergence of an $m = 1$ EA mode, which could not be identified owing to its twisted structure. In the absence of any equatorially symmetric mode, there are no triads in the system.

The above observations show that the fast inertial modes are secondary instabilities of the background flow and even though the equatorially symmetric instabilities of the system are not essential to their onset, they play a key role in selecting the modes that are allowed to emerge while shifting the critical value of Ro by a small amount. The resonant triads are not a prerequisite for the appearance of the EA modes but a consequence of the fact that the $m = 1$ SI mode is already present when these modes set in.

6.10 Conclusion

The experiment at BTU C-S allowed exploring the spherical Couette system in a parameter regime also accessible to numerical simulations. We have used the two codes MAGIC and XSHELLS for a detailed study at Ekman numbers $E = 10^{-4}$ and $E = 10^{-5}$ and a close comparison to the experiment for the latter parameter.

All the principle regimes and modes discovered in the experiment are recovered by the numerics. The complete access to the full solution in the simulations not only confirmed the sometimes challenging mode identifications in the laboratory but also revealed additional instabilities. At both Ekman numbers a fundamental Stewartson layer instability

(SI) with wave number $m = 1$ is the first non-axisymmetric instability. This is followed by a regime consisting of ‘fast’ equatorially antisymmetric (EA) inertial modes. We find the initial dominant mode to be a more complex (5, 2) mode at $E = 10^{-5}$ as compared to the (3, 2) mode at $E = 10^{-4}$, most likely due to a smaller viscous dissipation at a lower Ekman number. They are modified by the presence of the background flow and therefore differ from the respective eigenmodes of a rotating spherical shell. However, the modifications are small enough to still allow a clear identification in most cases. By artificially exciting the inertial mode (3, 2) at different differential rotation rates we could trace how its frequency increases from a perfect match with the eigenmode prediction at $Ro = 0$ to close to the value found for the full simulations at $Ro = -1.33$. Not surprisingly, their shape is mostly affected at the Stewartson layer and inside the tangent cylinder where the shear exerted by the background flow is strongest.

A striking feature of the EA modes is that they always come in pairs that form resonant triads with the SI. Triads are found for many wave phenomena and require that the non-linear interaction between two modes matches the wave number, frequency and equatorial symmetry of a third mode. It seems surprising that such resonances exist but the dense spectrum of inertial modes may see to that, or at least significantly increase the likelihood for triads to occur. More exploration is certainly required to clarify this point. Modifications due to the background flow and the SI could also play a role.

To explore whether the triads with the SI are essential for facilitating the onset for the EA modes we conducted numerical experiments where the SI was suppressed. Since fast inertial modes were still excited and could exist as the only non-axisymmetric instability in the system we conclude that the triads are mostly a consequence of an EA mode onset and not a condition. Once, for example, the (3, 2) mode has set in, the triadic resonance with the $m = 1$ SI immediately feeds energy into the (4, 1) mode. The existence of the triads certainly changes the system behaviour in the sense that the EA mode onset is shifted and that other EA modes set in than preferred for a pure axisymmetric background flow.

The resonance more easily allows the system to drain energy from the imposed differential rotation. The system therefore seem to prefer the resonances and manages to maintain them over a larger range of differential rotation. However, at $E = 10^{-5}$ we find a cessation of triads at intermediate differential rotation rates. The background flow and nonlinear interaction may have modified the modes so such that the resonance becomes infeasible. However, at a larger $|Ro|$ value another triad with the fundamental SI becomes possible and the respective new EA modes set in. A succession of several EA modes has been reported for the 3-metre experiment (Triana 2011), when Ro is decreased to more negative values. We speculate that this has a similar origin, though the triadic pairs have not been clearly identified for this experiment. For a very low Rossby number, however, the (4, 1) mode clearly dominates the flow without any other strong mode being present. This shows that triads are not required to support EA modes but are preferred under certain conditions.

Finally, we note that the critical magnitude of differential rotation needed to excite the $m = 1$ SI or the EA modes seem to decrease with Ekman number. Further investigations at lower Ekman numbers are therefore necessary to understand the scaling of these regime boundaries. A scaling of $E^{1/5}$ for the transition to the turbulent regime has already been found in the experiments by Hoff et al. (2016b). Such scaling laws would also allow

further insight into the experiments of [Triana \(2011\)](#) as well as into the hydrodynamics of astrophysical objects which are at parameter regimes beyond the reach of numerical investigations.

7 The turbulent regime

*“Big whorls have little whorls
Which feed on their velocity,
And little whorls have lesser whorls
And so on to viscosity.”*

Lewis Fry Richardson

7.1 Introduction

The turbulent regime of the spherical Couette system for $Ro < 0$ was mentioned in chapter 6. However, we feel the results in this regime deserve a separate chapter. This chapter compares results from simulations with observations of two experiments - those of Hoff et al. (2016b) at BTU-CS, Germany and of Triana (2011) in Maryland, USA. The turbulent regime raises two fundamental and difficult to answer questions - (i) how to explain the features observed in the turbulent regime? and (ii) what is the mechanism by which the flow transitions to turbulence?

In what follows, we shall attempt to answer these questions using insights from our numerical simulations. A brief theoretical background to rotational turbulence is provided, dealing with only the most relevant topics.

7.2 Theoretical background

Turbulent flows are ubiquitous in nature, examples ranging from a jet emerging from a fire hose to the solar wind. The extreme sensitivity of the Navier-Stokes equation to initial conditions and the high degree of coupling of various spatio-temporal scales in turbulent flows, make it impossible to describe them analytically. Direct numerical simulations provide a good description till certain length scales but the available computing power limits the spatial resolution. In the absence of exact solutions to the equations of motion and computational limitations, one turns towards statistical measures of flow properties over ensemble averages, in volume or time.

The most well-known breakthrough in turbulence theory is that due to Kolmogorov (1941a,b) and Obukhov (1941) who described the energy spectrum in a homogeneous (independent of position), isotropic (independent of direction) turbulent flow to be

$$E(k) = \alpha \epsilon^{2/3} k^{-5/3} \quad (7.1)$$

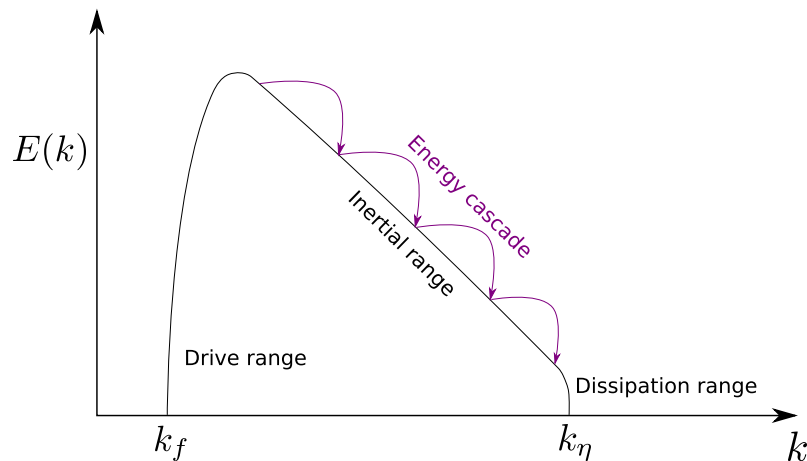


Figure 7.1: The basic idea of turbulence. There are three distinct scales - (i) the driving range k_f where energy is injected into the system, (ii) the inertial range where this energy then cascades down to smaller scales in the inertial range, without any dissipation, and finally (iii) the dissipation range where the energy is dissipated away by small scales, near k_η . x -axis represents wavenumber k while the y -axis shows kinetic energy. Based upon a figure by Frank Jenko.

where, α is a constant, ϵ is the rate of viscous dissipation and k is the wavenumber and $E(k)$ is the energy content in wavenumber k . The range of velocity scales over which this is valid is called the *inertial range*. The very basic statistical idea of turbulence can be summarised as follows: there are three distinct scales defined by whether energy production, transfer or dissipation takes place on a certain scale. The first of these, called the drive range are the scales, typically large, at which the system is driven and energy is pumped in to the system. The second range is the inertial range where transfer of energy takes place from the drive range to smaller scales via an energy cascade, called the ‘Richardson cascade’ after Lewis Fry Richardson. This cascade is assumed to be *local* in nature and takes place without any dissipation. Locality of interactions implies that flow at a certain length scale only interacts with flows of the same or nearby length scales. The interaction takes place between flows with wavevectors that form a triadic resonance $\mathbf{k}_1 + \mathbf{k}_2 + \mathbf{k}_3 = 0$ (Tennekes and Lumley 1972, Waleffe 1992). The final range of scales is the dissipation range where this energy is dissipated in small scales. This is illustrated schematically in figure 7.1.

2D and rotational turbulence

Kraichnan (1967) derived the spectrum for 2D turbulence, where the length scales along a certain axis (k_\parallel) are very different from those perpendicular (k_\perp) to it and the flow becomes independent of one axis (note that this is much like the Taylor-Proudman theorem, discussed in section 2.1.2). Leith (1968) and Batchelor (1969) further developed this work. The main result of ‘KBL theory’ is that there are two cascades for 2D turbulence - an ‘inverse’ energy cascade where energy goes from the driving scale to larger scales with $k^{-5/3}$ scaling and a ‘forward’ cascade of enstrophy (mean-squared vorticity, an invariant

for 2D incompressible flows) with a scaling of k^{-3} .

Waleffe (1992) projected a fluid velocity field onto a set of inertial waves and studied their *nonlocal* interactions meaning that a certain scale of motion need not necessarily interact with only scales close to it as was previously assumed for the inertial range of motions. Waleffe (1993) showed that under rapid rotation such nonlocal triadic interactions between different modes of decomposition made the flow tend towards a two dimensional state. Chen et al. (2005) considered Fourier modes of a periodic box and showed numerically that there is a subclass of ‘slow’ modes which are aligned with the rotation axis and decouple from the rest of the ‘fast’ modes, having independent dynamics of their own. They provided proof of a ‘dynamic Taylor-Proudman’ theorem which shows that the resonant interactions of three ‘slow’ modes yields a 2D, three component Navier-Stokes equation. Other experimental (e.g. Baroud et al. 2003, Yarom et al. 2013) and numerical (e.g. Sen et al. 2012) studies also concur that rotational turbulence can be described by invoking the formalism of 2D turbulence.

Note that rotational turbulence only occurs when $Re \gg 1$ and $Ro_u < 1$, where Re and Ro_u are the Reynolds and flow Rossby numbers defined as

$$Re = \frac{UL}{\nu} \text{ and } Ro_u = \frac{U}{\Omega L}. \quad (7.2)$$

The first one describes the importance of inertial advection with respect to viscous dissipation while the second describes the importance of inertia to the Coriolis force. Re is named after Reynolds (1883) who popularised the idea of Stokes (1851) that it is the critical parameter that determines when a flow transitions from being laminar to turbulent. Ro_u , named after Carl-Gustaf Rossby, tells us how much a flow is influenced by rotation. Thus, ‘rotational turbulence’ takes place when the flow is turbulent but still strongly influenced by rotation.

Wave turbulence

According to Nazarenko (2011), *wave turbulence* is defined as “out-of-equilibrium statistical mechanics of random nonlinear waves”. This provides an alternative formalism of turbulence in the form of weakly nonlinear wave interactions which is valid for cases where equations of motion can be linearised. In a rotating system, these take place through inertial waves. Smith and Waleffe (1999) used the wave turbulence formalism for a rapidly rotating system in terms of triadic resonant interaction of inertial waves to obtain the Smith-Waleffe spectrum

$$E(k) \sim \Omega^2 k^{-3} \quad (7.3)$$

for an inverse energy cascade for $k < k_f$. They conclude that there is an inverse cascade to large scales which are aligned with the rotation axis resulting in the flow becoming quasi-2D. However, inertial waves have an anisotropic dispersion relation, $\omega = 2\Omega k_{\parallel}/k_{\perp}$. Galtier (2003) looked at weak wave turbulence in terms of inertial waves and found that the anisotropic spectrum follows

$$E(k) \sim k_{\perp}^{-5/2} k_{\parallel}^{-1/2} \quad (7.4)$$

and that the energy cascade is towards smaller scales. Here, \parallel and \perp are with respect to the rotation axis. Rhines (1975) looked at turbulence in terms of interacting Rossby waves for geophysical application and found a scaling of k^{-5} . Davidson et al. (2006) and Staplehurst et al. (2008) postulated theoretically and showed experimentally how a blob of vorticity would radiate inertial waves in all directions, but with the energy content being highest on the rotation axis. This would lead to the creation of columnar eddies and tend to make the flow two dimensional.

Both formalisms of 2D as well as wave turbulence provide a good description of rotational turbulence. Duran-Matute et al. (2013) performed experimental and theoretical studies of the importance of inertial waves in energy cascades and found a cut-off at 2Ω in the temporal spectrum of the flow velocity beyond which there was a decay in the energy indicating that energy transfers occur due to inertial wave interactions. Yarom and Sharon (2014) performed experimental studies describing rotational turbulence and concluded that the whole 3D flow field can be well described by 3D wave turbulence due to inertial waves, and that a quasi-2D formalism might not be needed.

The body of work in rotating turbulence is large and a more detailed review is beyond the scope of this work. For a more detailed introduction to the theory of turbulence, we refer to classical books such as Tennekes and Lumley (1972), Frisch (1995), Pope (2000), Nazarenko (2011) and Davidson (2013).

7.3 Turbulent regime of spherical Couette flow

As explained in chapter 6, three distinct regimes of the spherical Couette flow have been observed in experiments by Hoff et al. (2016b) at BTU C-S. Two of these, namely, the fundamental instability and inertial mode regime were discussed in section 6.6. Here, we focus on the third turbulent regime. Hoff et al. (2016b) found that at a fixed Ekman number E , as the Rossby number, $Ro = \Delta\Omega/\Omega$ is increased to higher magnitudes, at a certain critical value, the velocity spectrum becomes very broadband, with inertial mode peaks still visible, but with a high energy background. This is accompanied by a jump in the mode frequency of the dominant inertial modes, while still maintaining their triadic resonance with the fundamental $m = 1$ Stewartson instability (SI). The critical Ro for transition depends on the Ekman number and a scaling law of $Ro_c \propto E^{1/5}$ was suggested by Hoff et al. (2016b). However, the experiments did not go very deep into the turbulent regime. In our simulations at $E = 10^{-4}$, a similar transition is observed at $Ro = -2.3$. Below we compare several observations from the numerical simulations in this regime with those of the experiment.

7.3.1 Temporal spectrum

Figure 7.2 shows the temporal spectrum in the turbulent regime from three different sources and different parameter regimes - (a) from MagIC simulations at $E = 10^{-4}$, (b) at $E = 1.52 \times 10^{-5}$ from the experiments by Hoff et al. (2016b) at BTU C-S and (c) the three metre experiment at Maryland, USA, whose Ekman numbers are extremely low ($\leq 10^{-7}$) and not achievable through present day computational resources. Despite spanning 4 decades in Ekman number, all the spectra have three common features - (i) they are all

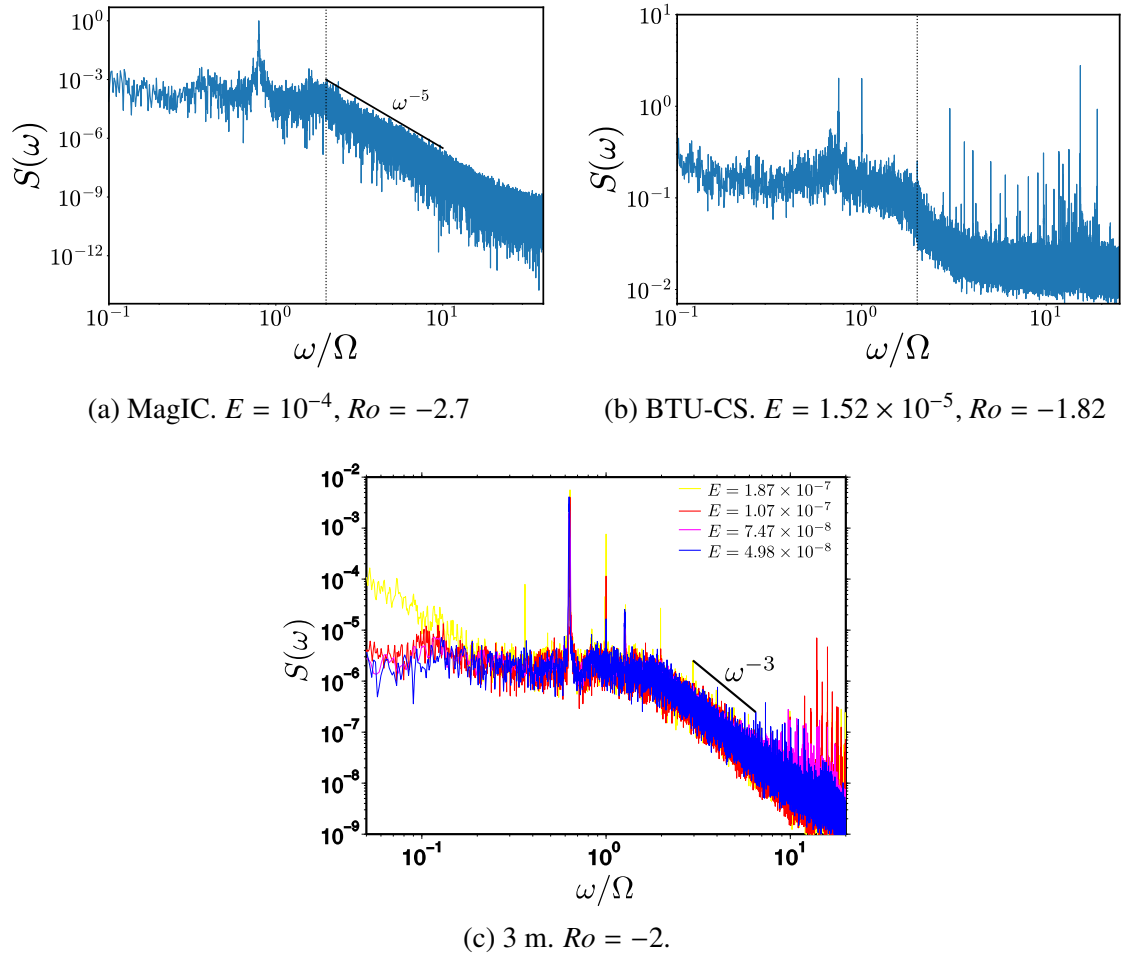


Figure 7.2: Temporal spectra in the turbulent regime for (a) MagIC simulation, (b) experiment by Hoff et al. (2016b) and (c) 3-metre experiment. The x -axis shows angular frequency in terms of the outer boundary rotation rate. The y -axis shows the power $S(\omega)$ in a frequency ω/Ω . All of them show a ‘knee’ at $\omega/\Omega = 2$. Data for figure (b) provided by Michael Hoff. Figure (c) taken from Triana (2011).

broadband with a high energy content over a large span of frequencies, (ii) they all retain a peak representing a dominant inertial mode and most importantly, (iii) they have a clear ‘knee’ at $\omega/\Omega = 2$. This points towards a common nature of turbulence in the spherical Couette system that is independent of the Ekman number. The sharp knee at $\omega/\Omega = 2$ is a clear indication of turbulence via inertial wave triad interactions (Duran-Matute et al. 2013, Clark di Leoni et al. 2015).

Triana (2011) noted a decay in energy of the form ω^{-3} beyond the 2Ω knee, which has an exponent similar to that of the Smith-Waleffe spectrum (Smith and Waleffe 1999) and of an enstrophy cascade in KBL theory and might be indicative of a strong influence of rotation on the flow. However, the regime where this is observed, there is a strong spectral peak of the (4, 1) inertial mode, whose presence makes the flow far from two dimensional, making both theories inapplicable. The simulations of MagIC show a decay which falls as ω^{-5} whose exponent looks similar to the β -plane scaling of k^{-5} due to Rhines (1975),

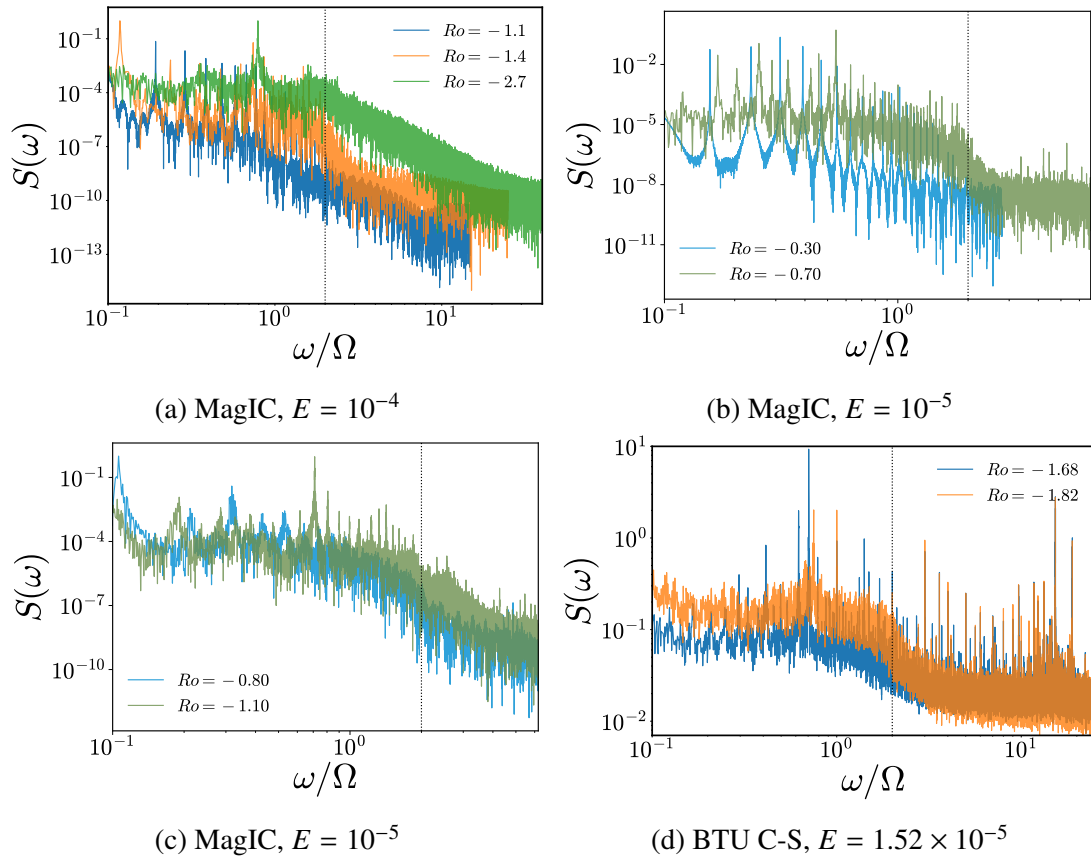


Figure 7.3: Temporal spectra in different regimes for MagIC simulations at $E = 10^{-4}$ and $E = 10^{-5}$ in panel (a), (b) and (c) and from BTU C-S at $E = 1.52 \times 10^{-5}$ in panel (d). Axes similar to figure 7.2. Experimental data provided by Michael Hoff.

where the Coriolis force is parametrised as a linear function of latitude with a slope of β . This may not be directly applicable to the spherical Couette system, certainly not to one with a wide-gap such as ours as the β -plane approximation only works for shallow fluids. Comparing exponents in temporal and spatial spectra is of course questionable, especially since Taylor’s hypothesis (Taylor 1938) of eddies getting ‘swept’ by background flow (giving $\omega = U_{rms}k$) is only valid when the perturbation to the background flow is very small. A more detailed analysis in this regard is thus certainly required.

A knee at 2Ω is visible in the inertial mode regime before the transition to turbulence as well. Figure 7.3 shows the temporal spectra in different regimes for simulations as well as experimental data. At $E = 10^{-4}$, no such knee can be seen for $Ro = -1.1$ where the onset of inertial modes has not yet taken place, as seen in panel (a). At $Ro = -1.4$ which, close to the critical onset value at $Ro = -1.33$ for equatorially antisymmetric (EA) inertial modes to set in, one can see a knee already starting to develop. The decay is steeper but short-lived in ω and levels off beyond $\omega/\Omega \approx 4$, unlike that in the turbulent regime for $Ro = -2.7$ where the decay is sustained through the whole frequency range. The noisy background around the peak of the dominant (3, 2) mode ends up in a higher energy state after the transition to the turbulent regime. In panels (b) and (c), one can see a clear ‘knee’

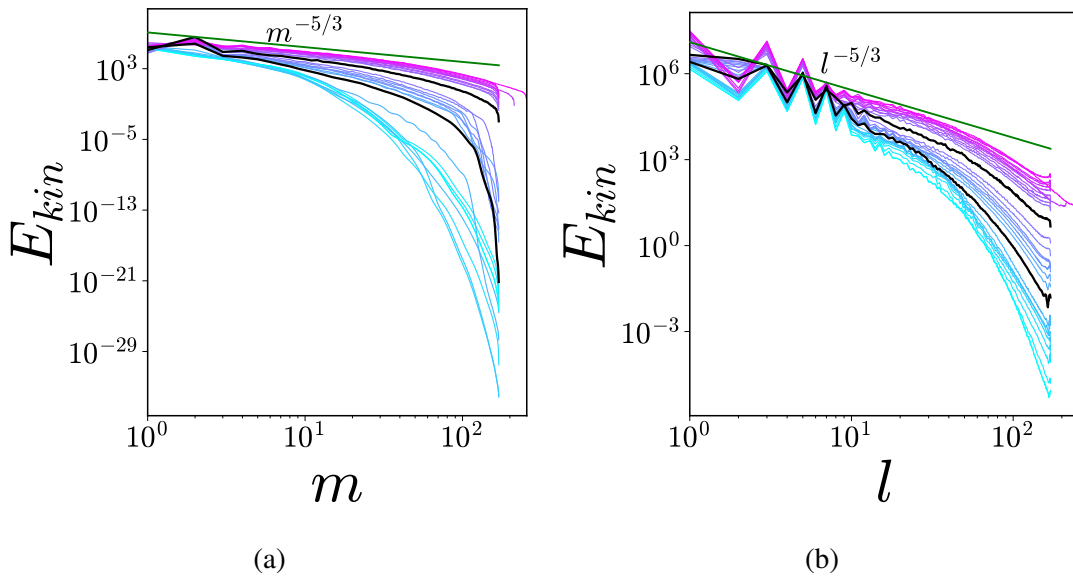


Figure 7.4: Spatial spectra in l and m for $-3.5 < Ro < -1$ at $E = 10^{-4}$. The solid green lines represent the classic Kolmogorov ($-5/3$) scaling. Darker colours show higher values of $|Ro|$. The lines for $Ro = -1.5$ and $Ro = -2.3$ have been plotted in black.

at 2Ω in the regimes where inertial modes are visible. In panel (d), the experimental data from BTU C-S shows a similar behaviour - presence of a ‘knee’ in both inertial mode and turbulent regimes - the one for the turbulent regime being more pronounced.

7.3.2 Spatial spectra

Though it is easy to get temporal spectra in experiments, obtaining information about the spatial spectra can be more tricky, especially in a spherical shell. In pseudo-spectral simulations this is fairly straightforward as one has access to the spectral coefficients. For a spherical harmonic decomposition, one would usually look at spatial spectra in terms of spherical harmonic degree l or order m .

Figure 7.4 shows the spatial spectra at different values of Ro at $E = 10^{-4}$ and compares it with the classical Kolmogorov ($-5/3$) scaling. Two prominent jumps can be observed in the spectra in m which have been marked with black lines in panel. One is at $Ro = -2.3$ where the transition to temporal broadband turbulence is observed. In the spatial spectrum, this is associated with a jump to a more Kolmogorov like scaling. Beyond $Ro = -2.3$, the spectrum can be seen to be getting closer and closer to the ($-5/3$) scaling, showing a progressive transition towards homogeneous and isotropic turbulence. The other jump in the form of the spatial spectrum occurs at $Ro = -1.5$. The spectral power between $Ro = -1.5$ and $Ro = -2.2$ can be scaled roughly as $m^{-5/2}$ or $l^{-5/2}$, as shown in figures 7.5a and 7.5b, which is reminiscent of the Galtier spectrum (equation 7.4) showing that this regime can be described in terms of weak inertial wave turbulence. This is also the case for the inertial mode regime at $E = 10^{-5}$, as shown in figures 7.5c and 7.5d, where a jump at $Ro \approx -0.5$ is seen when the transition to inertial mode regime occurs. Due to numerical difficulties of resolving small spatial scales, we could not proceed towards the

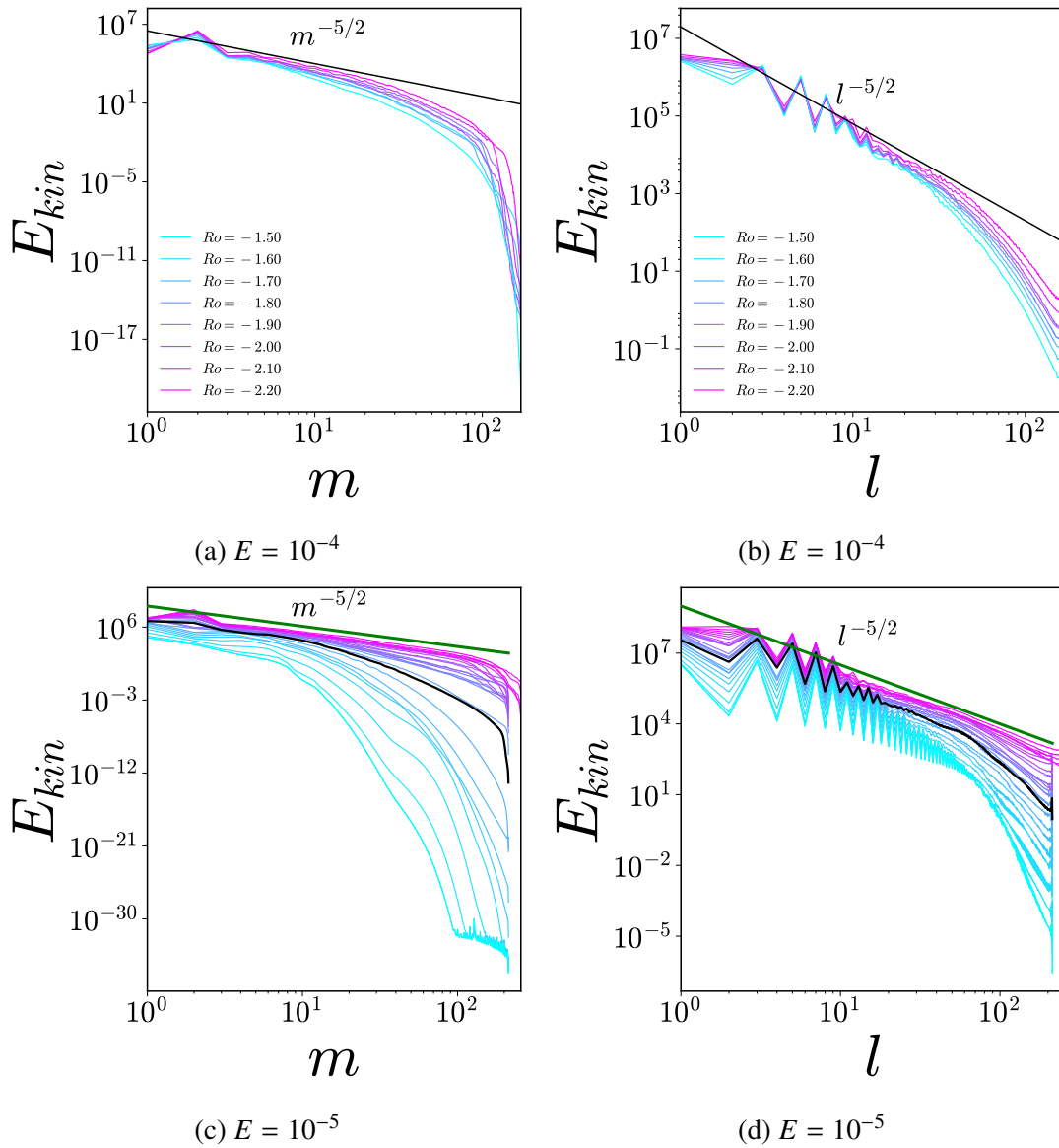


Figure 7.5: (a) and (b) show spatial spectra in the inertial mode regime for $E = 10^{-4}$ while (c) and (d) show spectra in all regimes at $E = 10^{-5}$. Straight lines at the top show a $(-5/2)$ scaling. Black lines in (c) and (d) show where a change in spectral behaviour is expected.

region of broadband temporal spectrum.

As shown in figure 7.6a, $Ro = -1.5$ is the point where the $(3, 2)$ inertial mode becomes the dominant mode of the system. After the transition to the isotropic turbulent regime, the energy in the dominant $(3, 2)$ mode seems to suddenly drop by a large amount, showing a sudden transition to a regime where rotation plays a less important role, as also inferred above from the spatial spectra. This sudden drop in the energy of the dominant $(3, 2)$ mode is also seen in the experiments at BTU C-S, as shown in figure 7.6b. For MagIC simulations at $E = 10^{-5}$, one also sees the rise in the $(3, 2)$ mode energy, as shown in figure 7.6c, where numerical difficulties stopped us from pursuing more negative Ro .

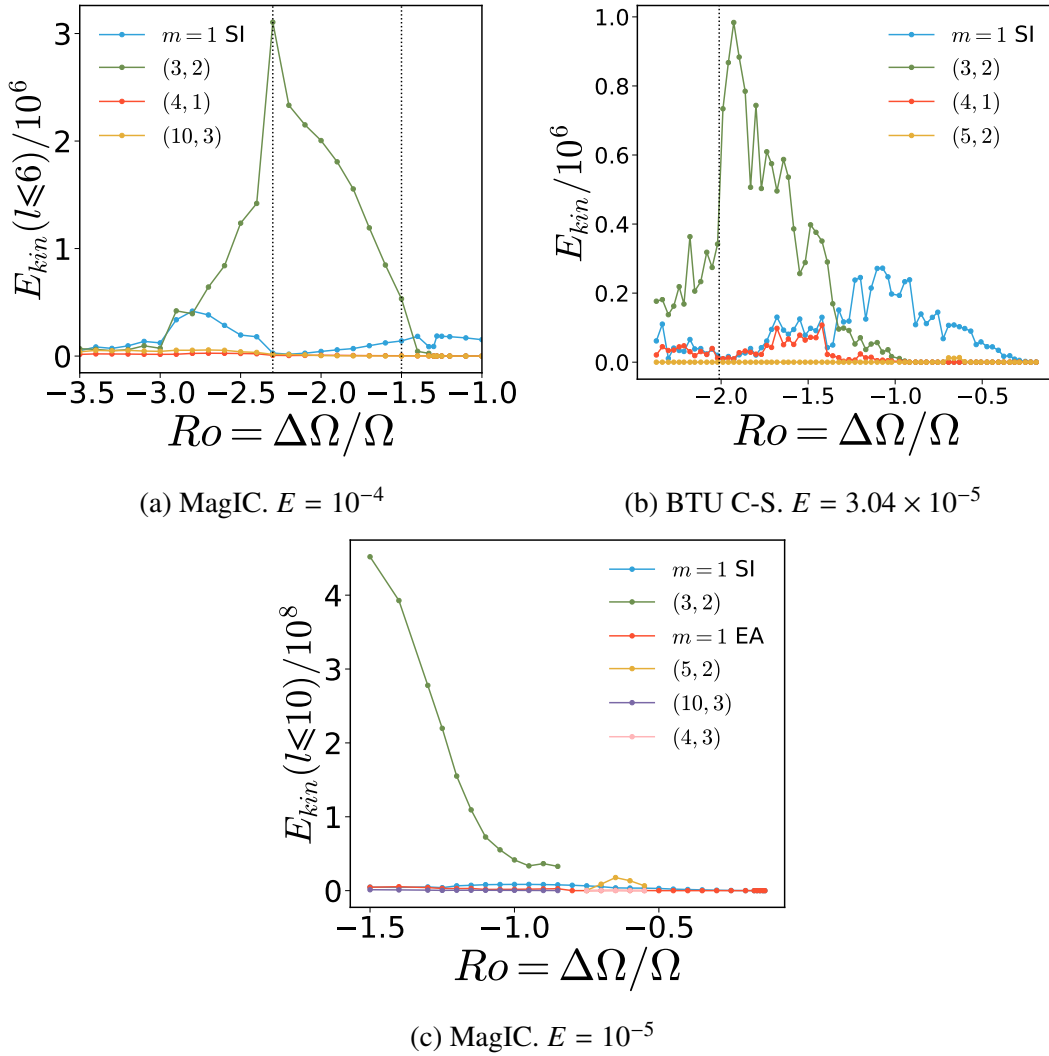


Figure 7.6: Non-dimensional energies of different modes in the system. (a) and (c) show MagIC simulations while (b) shows experiments at BTU C-S at $E = 3.04 \times 10^{-5}$. The vertical dotted lines in (a) mark the Ro where the (3,2) mode becomes dominant ($Ro = -1.5$) and for the transition to broadband temporal spectrum ($Ro = -2.3$). Vertical dotted line in (b) marks the transition to broadband turbulence.

7.3.3 Flow and Torque

One can find clear signatures of a transition to broadband turbulence in the variation of the time-averaged kinetic energy and torque with Ro . Section 5.1 discussed torque scaling with the outer sphere stationary where two distinct regimes were found - one varying linearly with $\Delta\Omega$ and one as $\Delta\Omega^{3/2}$. We saw that the torque scaling at more extreme $\Delta\Omega$ would scale asymptotically as $\Delta\Omega^2$. Here, when the outer boundary is rotating, the torque scaling looks quite different. One can see the different scalings in figures 7.7b and 7.7d, that change in accordance with the hydrodynamic flow regimes observed. This is accompanied by changes in the kinetic energy behaviour as well.

At very low values of $|\Delta\Omega|$ the torque scales nearly linearly and the kinetic energy (KE)

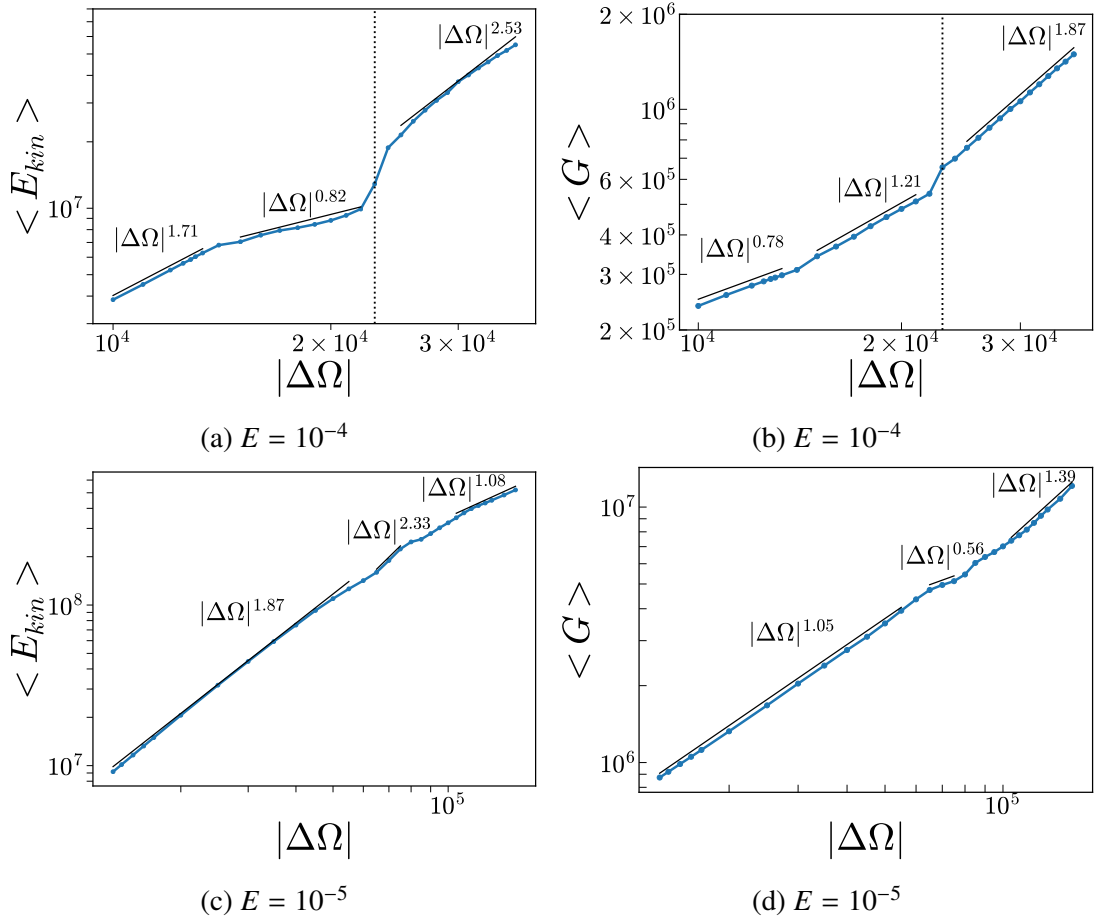


Figure 7.7: Time-averaged kinetic energy E_{kin} and torque G on the inner sphere versus $|\Delta\Omega|$. The transition to the turbulent regime at $E = 10^{-4}$ has been marked with the vertical dotted line.

scales close to $|\Delta\Omega|^2$ till the onset of EA inertial modes at both values of E , as expected for a laminar flow. A transition in this behaviour takes place once EA inertial modes emerge. At $E = 10^{-4}$, we find a $\approx 50\%$ decrease in the KE scaling and a similar increase in the torque scaling, indicating that these instabilities efficiently dissipate energy and transport angular momentum. This can be seen in an increase in the scaling of viscous dissipation, shown in figure 7.8, where the scaling of viscous dissipation increases by almost six fold in the inertial mode regime. A better visualisation is offered by figure 7.9a showing the azimuthal average of u_ϕ along with the meridional circulation at $E = 10^{-4}$. At $Ro = -1$, almost all the meridional circulation is confined close to the tangent cylinder. At $Ro = -2$, in the EA inertial mode regime, little vortices can be seen developing outside the tangent cylinder and close to the outer boundary and the background flow seems to be spreading out gradually into the bulk. These small scale structures would cause a more efficient viscous dissipation, and the broadening of the background flow profile would start to transport angular momentum more efficiently. After the flow transitions to broadband turbulence, both scalings - KE and torque - increase again, with a three fold increase in the KE scaling and a $\approx 50\%$ increase in the torque scaling. Thus, the viscous dissipation

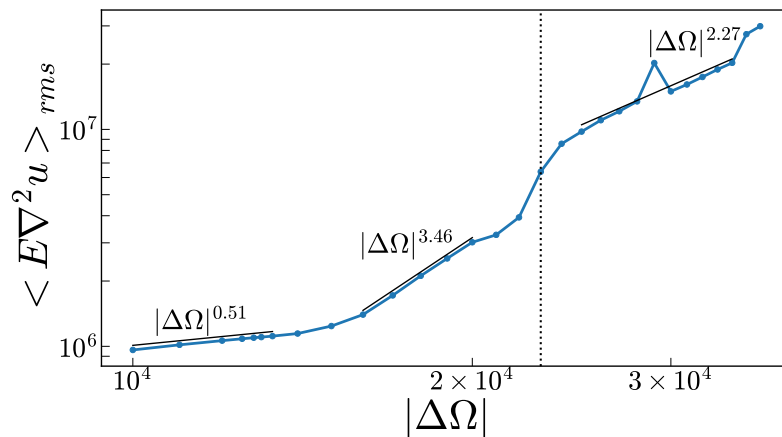


Figure 7.8: RMS values of viscous dissipation at different $|\Delta\Omega|$ at $E = 10^{-4}$. Vertical lines mark transition to temporal broadband turbulence.

is less efficient in this regime, as seen in figure 7.8 while the angular momentum transport is more efficient. The solutions in this regime (last three panels of figure 7.9a) show that the fluid differential rotation which was mostly confined to the tangent cylinder (TC) diffuses out into the bulk outside. The Stewartson layer boundary between the two fluid rotation rates (differential and solid-body) is not very well-defined any more and becomes diffuse.

This breakdown of the Stewartson layer can also be observed in figure 7.9 which shows how the well-defined Stewartson layer close to the tangent cylinder starts to become more diffuse beyond $Ro = -2.3$, leading to a more efficient angular momentum transport, as observed in the torque scalings. In particular, at $Ro = -2.5$ in figure 7.9a, one can see the development of two circulation cells attached to the boundary layer on the inner sphere which seem to be directly aiding the transport of high angular momentum fluid by being connected to larger circulation cells in the bulk. A more clearer picture of this can be found at $Ro = -3.5$ where this phenomenon is more extreme. This is also visualised in figure 7.10 which shows the evolution of background flow with Ro and shows that it matches well with experimental observations. Hoff et al. (2016b) say that the cause of this transition might be Görtler vortices (Görtler 1955) produced by the instability of the boundary layer at the equator which are known to cause an increase in mean flow (Ghasemi V et al. 2016), thus explaining the sudden increase in the kinetic energy scaling of the flow. The Ekman layer at the equator of the inner sphere scales as $E^{1/5}$ (Stewartson 1966), just like the Ekman layer at critical latitudes. If the instability of the Ekman layer at the equator causes the onset of the Görtler vortices, this might help explain the $E^{1/5}$ scaling observed in experiments.

At $E = 10^{-5}$, there are two inertial mode regimes - with the (5, 2) and (3, 2) modes being the dominant ones in each regime. As shown in figure 7.7c and 7.7d, the scaling behaviour in the laminar regime before onset of any EA mode is similar to that for $E = 10^{-4}$. However, in the first inertial mode regime, the KE scaling increases by about 25% while the torque scaling decreases by about 50%, showing that the instabilities in this regime are neither efficient in viscous dissipation nor in transporting angular momentum.

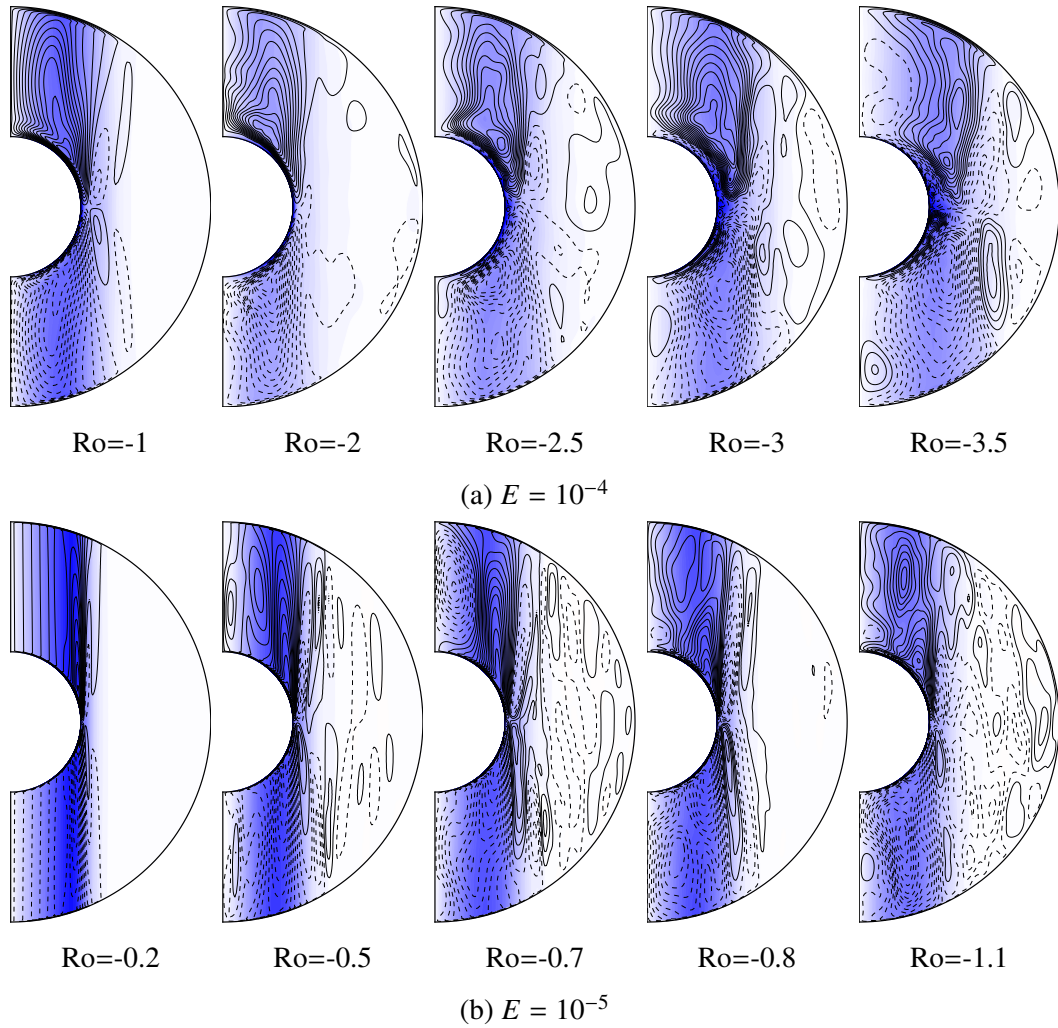


Figure 7.9: Azimuthal averages of zonal velocity, u_ϕ at different parameters from MagIC simulations. The lines represent meridional circulation - solid (dotted) lines show clockwise (anti-clockwise) circulations. Colours represent zonal velocity with blue corresponding to negative or retrograde motion.

This is different from the behaviour observed in the inertial mode regime at $E = 10^{-4}$. However, as one can see for $Ro = -0.7$ in figure 7.9b, the flow is composed of small scale vortices in the whole bulk of the fluid which would imply a high viscous dissipation and angular momentum transport. This is followed by a regime where the inertial modes disappear and the meridional circulation becomes constrained to live inside the tangent cylinder again, as seen for $Ro = -0.8$ in figure 7.9b. Thereafter, we get a behaviour similar to that observed in the inertial mode regime for $E = 10^{-4}$ - the KE scaling decreases while the torque scaling increases showing that the (3, 2) and others modes present in this regime are more dissipative and are efficient in transporting angular momentum than the EA modes seen before.

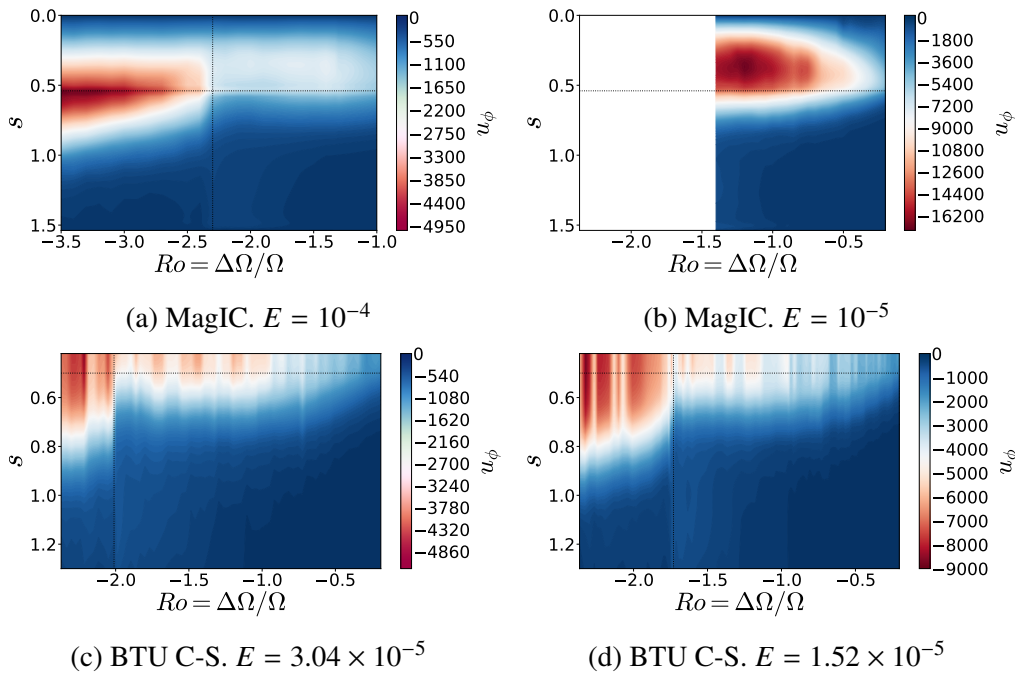


Figure 7.10: Variation of background flow profiles with Ro . (a) and (b) show simulations from MagIC while (c) and (d) show experimental data from BTU C-S. s is the cylindrical radius. The dotted horizontal and vertical lines mark the position of the tangent cylinder and the Ro for transition to the ‘turbulent’ regime, respectively. The x -axis in (b) has been extended to the same range as (d) for ease of comparison - no data is available for the white patch. All velocities have been non-dimensionalised. Due to large uncertainties in close to the centre experiments, the s values start from a finite value rather than zero. Experimental data provided by Michael Hoff.

7.3.4 A new mode

At $E = 10^{-4}$, around $Ro = -2.7$, a new mode emerges and becomes the dominating large-scale structure in the flow solution. This is an equatorially symmetric columnar mode with $m = 2$. Its structure at $Ro = -3$ is shown in figure 7.11 and it drifts with a frequency around $\omega/\Omega \approx 0.4$. This mode could not be identified as a full sphere inertial mode. At the beginning of the chapter, in section 7.2, we cited a number of studies which suggest that turbulence in the presence of rotation gives rise to columnar structures associated with the rotation axis. However, these studies are all based on the assumption that rotation is the dominant force in the system, which is not the case any more in the regime for homogeneous and isotropic turbulence. The force balance is discussed below.

7.4 Critical Balance - criteria for transition?

We conjectured before that there is a transition from a weak-inertial mode wave turbulence towards a homogeneous and isotropic turbulent regime. We try to predict this transition using an argument similar to the lines of the Zeman scale (Zeman 1994) which predicts

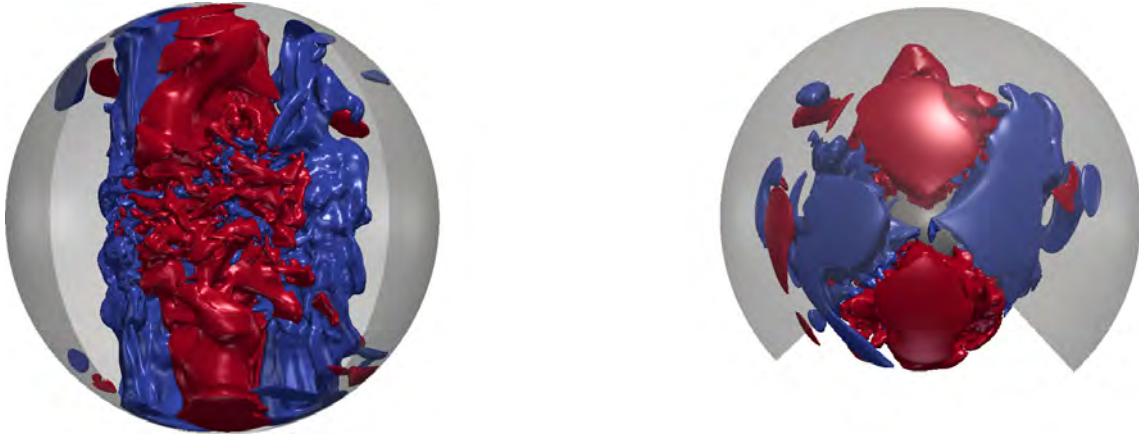


Figure 7.11: Isosurfaces of non-axisymmetric cylindrical radial velocity u_s , at $Ro = -3$, $E = 10^{-4}$.

that if the scale at which the eddy turnover time-scale matches the inertial wave time-scale is k_Ω , then the energy spectrum for $k < k_\Omega$ would be dominated by rotation and that for $k > k_\Omega$ would be the Kolmogorov spectrum for homogeneous and isotropic turbulence. For our system, the criteria for the eddy turnover time-scale matching the inertial wave time-scale can be written as a balance between the non-linear term and the Coriolis force in the Navier-Stokes equation

$$|\mathbf{u} \cdot \nabla \mathbf{u}| \sim |2\boldsymbol{\Omega} \times \mathbf{u}| \Rightarrow l/u_l \sim 1/2\Omega \quad (7.5)$$

To check this balance, we plot the force balance in figure 7.12 showing the time-averaged RMS (in volume) magnitude of the different terms in the Navier-Stokes equation obtained from MagIC simulations as function of Ro at $E = 10^{-4}$. As can be seen, the Coriolis force dominates the dynamics till the transition to the turbulent regime. The transition then takes place exactly when the magnitude of the non-linear term matches the Coriolis force. In the isotropic turbulent regime, inertia dominates the force balance, leading to a more homogeneous and isotropic system. To check whether this is a more generic criteria or simply a coincidence, one should continue this work and test the same at different Ekman numbers.

7.5 Triadic resonances in the turbulent regime

The last chapter focused on triadic resonances in the ‘inertial mode’ regime. Here, we see if they still exist in the ‘turbulent’ regime. Hoff et al. (2016b) find that the triadic resonances that existed in the inertial mode regime, still continue to exist in the turbulent regime. However, they did not go more negative Ro in the turbulent regime. MagIC simulations at $E = 10^{-4}$ lose the triads around $Ro = -2.9$ and the new $m = 2$ mode mentioned above becomes the dominant large-scale structure, though signatures of the previously dominant but distorted (3, 2) mode are still visible.

Let us now turn towards a much more turbulent case - the 3-metre experiment at Maryland, USA. According to the $E^{1/5}$ scaling law derived by Hoff et al. (2016b) for the

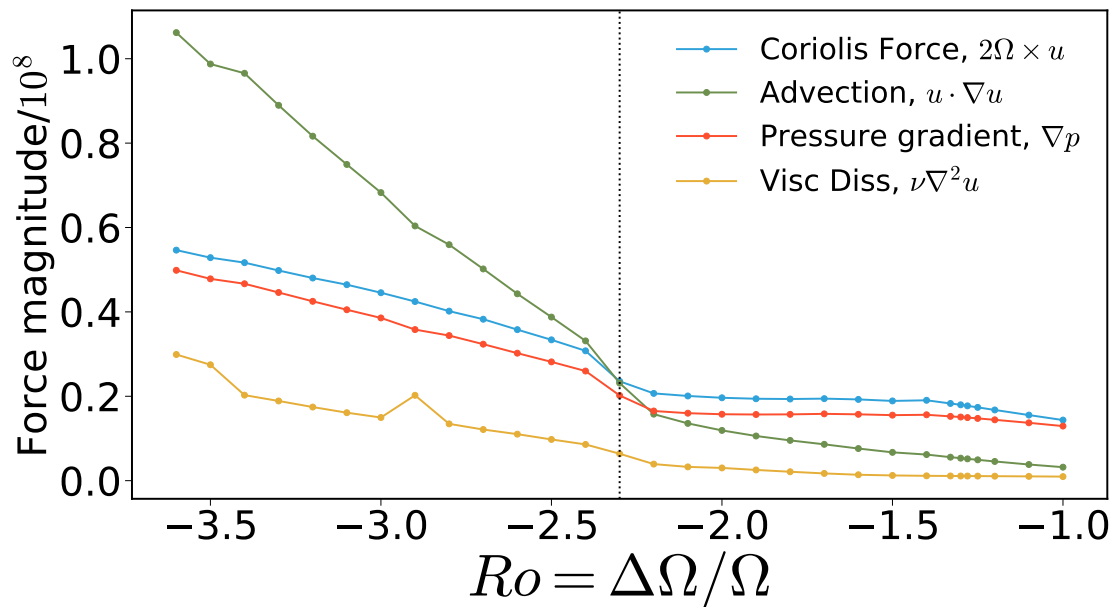


Figure 7.12: Time averaged non-dimensional magnitude of forces affecting the dynamics of flow from MagIC simulations at $E = 10^{-4}$. The vertical dotted line marks the transition to the turbulent regime. Note that the transition takes place exactly when advection balances the Coriolis force. The dominant force balance changes from the Coriolis force to advective transport.

critical Ro for transition, the 3-metre experiment was always well inside the turbulent regime. This offers us a unique possibility to observe possible inertial mode triads in the turbulent regime. Figure 7.13 shows the data from the 3-metre experiment. The two lines at the top mark the dominant frequencies at different Ro over the whole range. The solid line at the bottom shows their difference which almost always lies in the broad peak of the $m = 1$ Stewartson layer instability. Unfortunately, for most of these cases, one of the lines forming the triad pair was not identified. In a few cases where they have been identified, the wavenumber criteria for triadic resonances matches as well.

7.6 Conclusion

We explored the turbulent regime of the spherical Couette flow for negative differential rotation, $Ro < 0$. We found excellent agreements between experiments and simulations while comparing possible observables. It was seen that in all cases, the temporal spectra in the turbulent regime has a sharp decay beyond $\omega/\Omega = 2$, indicating that the turbulent energy transfers take place via triadic resonances of inertial waves. This sharp ‘knee’, though less pronounced, is also present in the ‘inertial mode’ regime where the broadband background of the temporal spectra has less energy compared to the inertial mode peaks. This would indicate that the energy transfers via inertial waves already begin in the ‘inertial mode’ regime and become progressively more efficient at more negative Ro . In the ‘inertial mode’ regime, the spatial spectra show a scaling of $m^{-5/2}$ and $l^{-5/2}$ which

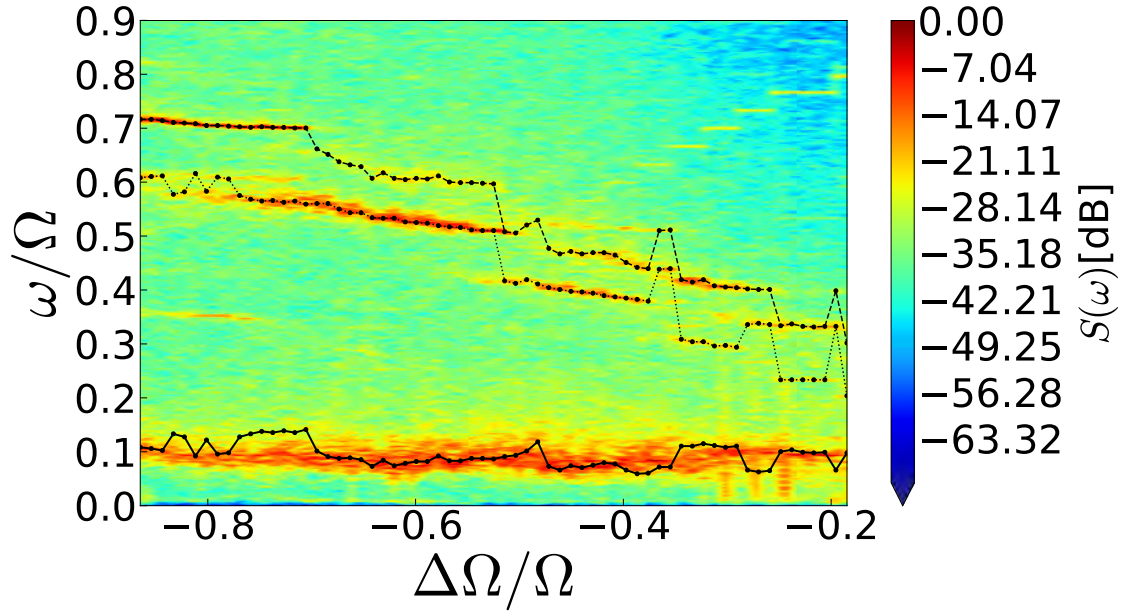


Figure 7.13: The search for triadic resonances in the pressure probe spectra of the 3-metre experiment at Maryland, USA. x -axis shows $Ro = \Delta\Omega/\Omega$ while y -axis shows the frequency ω/Ω . The colormap gives the power $S(\omega)$ in ω/Ω . The two lines above mark positions of dominant frequencies while the solid line at the bottom shows their difference. The differences mostly lie in the broad band of the $m = 1$ mode below. Data from Santiago Triana.

is similar to the spectrum given by Galtier (2003) for ‘weak inertial-wave’ turbulence, i.e, for weak nonlinear interactions between inertial waves as can be seen in the temporal spectra as well. When the temporal spectrum becomes broadband and all inertial mode frequencies seem to be resonantly excited, the spatial spectra get asymptotically close to the Kolmogorov ($-5/3$) scaling. Prominent ‘jumps’ can be seen in the spectra which correspond to either the appearance of a dominant inertial mode in the system or the transition to Kolmogorov-like turbulence. The transitions between different hydrodynamic regimes are also marked with changes in slopes of kinetic energy and torque on the inner sphere. These slopes have been quantified for the first time in this study.

Besides the spectra, the transition to the turbulent regime is also marked by sudden changes in the slopes of kinetic energy and torque on the inner sphere as a function of Ro . At $E = 10^{-4}$, the flow solutions show a breakdown of the Stewartson shear layer and vortices and small circulation cells developing in the bulk of the fluid. These transport angular momentum very efficiently and match the observations of the background flow in experiments at BTU C-S. According to Hoff et al. (2016b), these might be Görtler vortices emerging due to an instability of the Ekman layer at the inner sphere equator, the width of which scales as $E^{1/5}$, hinting towards a possible origin of the similar scaling of the critical Ro for transition found by Hoff et al. (2016b).

To determine a criteria for this transition from rotation dominated inertial wave turbulence to homogeneous and isotropic turbulence, we turned to the concept of Zeman scale

in turbulence where the inertial wave time-scale matches the eddy turnover time and determines whether the turbulent spectrum at a certain scale will be dominated by rotation or be isotropic. An analysis of the dominant forces in the system showed that the transition takes place exactly where the nonlinear advection term matches in magnitude with the Coriolis force implying that the system transitions from a rotation dominated regime to an inertia dominated isotropic regime.

A new $m = 2$ mode is seen to emerge in the turbulent regime of the MagIC simulations at $E = 10^4$. The experiments at BTU C-S did not go to sufficiently negative Ro in the turbulent regime to observe new modes. This mode could not be identified with a corresponding full sphere inertial mode and could be a result of large-scale columnar structure formation by small scale turbulent eddies as proposed by several studies (Waleffe 1993, Smith and Waleffe 1999, Davidson et al. 2006, Staplehurst et al. 2008). However, these studies were all in a rotation dominated regime and further investigation is needed for their applicability to an inertia dominated regime under the influence of rotation. Lastly, inertial mode pairs forming triadic resonances with the $m = 1$ Stewartson layer instability could be identified in the data of the 3-metre experiment at Maryland, USA, showing that the system “prefers” these resonances even in a highly turbulent regime.

Landau (1944b) proposed that transition of a flow to turbulence takes place due to bifurcations that lead to oscillations of velocity at certain frequencies f_i , i being an integer. When i becomes too large, the flow appears chaotic and turbulent. Contradicting this picture, Ruelle and Takens (1971), using abstract mathematics, proposed an alternative scenario where after three or four time-dependent bifurcations, one should lose any periodicity of the flow. Gollub and Swinney (1975) found the transition to turbulence in the case of a cylindrical Taylor-Couette setup to consist of periodic states which disappeared and gave way to aperiodic behaviour confirming the Ruelle and Takens (1971) scenario. The transition was sharp and non-hysteretic. In our simulations as well as in experiments at BTU C-S, one always find dominant spectral peaks even deep into the turbulent regime. In fact, in the 3-metre experiment, where the flow was always turbulent, one found very clear spectral peaks, favouring the scenario of Landau (1944b).

The spherical Couette system provides a unique playground for exploring rotational turbulence. Though a large number of interesting observations were made in our simulations and in experiments, their complete understanding remains limited. The remarkable similarity of observations over several orders of magnitude of Ekman numbers shows the close similarity in the turbulent states. A more detailed analysis of the flow using simulations at other Ekman numbers would provide further insight into this turbulent state.

8 MHD Theory

“It is of great advantage to the student of any subject to read the original memoirs on that subject, for science is always most completely assimilated when it is in the nascent state . . .”

James Clerk Maxwell

Electromagnetic interactions between moving conductors and magnetic fields have been studied extensively since the time of Faraday. But what if the conductor is a fluid, such as liquid iron in the interior of the Earth, the plasma inside a star or liquid metals in industry? To understand fluid motion and magnetic field interactions in such scenarios, one needs to combine the realms of hydrodynamics and electromagnetic theory.

This chapter introduces the reader to the basics of magnetohydrodynamics (MHD). MHD is a vast subject in itself, and discussing it in great detail is beyond the scope of this text. For greater insights into magnetohydrodynamics, a good place to start would be the book of [Davidson \(2001\)](#) and the notes of [Jones \(2008\)](#) and [Spruit \(2013\)](#).

8.1 Pre-Maxwell and induction equations

Maxwell’s equations form the foundation of electromagnetic theory and are necessary to understand magnetic fields and their interactions with conductors. Since most magnetohydrodynamic phenomena in the universe take place at speeds much lower than that of light, the displacement current is ignored and one considers ‘pre-Maxwell’ equations. They can be written as

$$\nabla \times \mathbf{E} = -\frac{\partial \mathbf{B}}{\partial t}, \quad (8.1a)$$

$$\nabla \times \mathbf{B} = \mu \mathbf{J}, \quad (8.1b)$$

$$\nabla \cdot \mathbf{B} = 0, \quad (8.1c)$$

$$\nabla \cdot \mathbf{E} = \rho_e / \epsilon, \quad (8.1d)$$

where, \mathbf{E} , \mathbf{B} and \mathbf{J} represent magnetic field, electric field and current density, respectively. μ is the magnetic permeability of vacuum. ρ_e is the charge density, c is the speed of light and ϵ is the dielectric constant. In vacuum, $1/\mu\epsilon = c^2$.

The first equation is Faraday's law of induction, the second is Ampere's law relating the magnetic field generated to the current flowing in the conductor. The third equation says that there are no magnetic monopoles while the fourth relates the electric field in a region to the density of electric monopoles (charges).

In a frame of reference moving with a velocity \mathbf{u} , where Galilean transformation would imply $\mathbf{x} \rightarrow \mathbf{x} - \mathbf{u}t$, the form of the pre-Maxwell equations remain the same. The only difference is that the resultant electric field in the moving reference frame is not only the native electric field in the system, but is also has a contribution from the movement of magnetic field. Thus, $\mathbf{E} \rightarrow \mathbf{E} + \mathbf{u} \times \mathbf{B}$. To arrive at an equation for the evolution of the magnetic field we begin with the classical resistive Ohm's law,

$$\mathbf{J} = \sigma(\mathbf{E} + \mathbf{u} \times \mathbf{B}). \quad (8.2)$$

From equations (8.1a), (8.1b) and (8.2) we get

$$\begin{aligned} \frac{\partial \mathbf{B}}{\partial t} &= \nabla \times \left(-\frac{\nabla \times \mathbf{B}}{\mu\sigma} + \mathbf{u} \times \mathbf{B} \right) \\ &= \nabla \times (\mathbf{u} \times \mathbf{B}) - \nabla \times \left(\frac{\nabla \times \mathbf{B}}{\mu\sigma} \right). \end{aligned} \quad (8.3)$$

The quantity $\lambda = 1/\mu\sigma$ is called the *magnetic diffusivity*. Thus the above equation can be rewritten to give

$$\frac{\partial \mathbf{B}}{\partial t} = \nabla \times (\mathbf{u} \times \mathbf{B}) - \nabla \times (\lambda \nabla \times \mathbf{B}). \quad (8.4)$$

Equation (8.4) is called the *induction equation*. We will deal with conductors consisting of a single fluid where \mathbf{u} would refer to the flow field. For conductors whose conductivity and hence magnetic diffusivity is constant in space, one can use the vector identity $\nabla \times \nabla \times \mathbf{B} = \nabla(\nabla \cdot \mathbf{B}) - \nabla^2 \mathbf{B} = -\nabla^2 \mathbf{B}$, and write

$$\frac{\partial \mathbf{B}}{\partial t} = \nabla \times (\mathbf{u} \times \mathbf{B}) + \lambda \nabla^2 \mathbf{B}. \quad (8.5)$$

The ratio of the typical magnitudes of the two terms on the RHS is an important quantity called the magnetic Reynolds number

$$Rm = \frac{|\nabla \times (\mathbf{u} \times \mathbf{B})|}{|\lambda \nabla^2 \mathbf{B}|} \sim \frac{UB/L}{\lambda B/L^2} = \frac{UL}{\lambda}, \quad (8.6)$$

where U and L represent the characteristic velocity and the characteristic length scale of the flow. The similarity to the flow Reynolds number $Re = UL/\nu$ is evident. Rm provides a measure for the ratio of induction to diffusion. We distinguish two limiting cases:

Case I: $Rm \rightarrow 0$

In this case, the induction equation reduces to a diffusion equation

$$\frac{\partial \mathbf{B}}{\partial t} = \lambda \nabla^2 \mathbf{B}. \quad (8.7)$$

Any initial magnetic field in the fluid simply decays away through Ohmic dissipation in a characteristic time τ_λ given by $B/\tau_\lambda = \lambda B/L^2 \Rightarrow \tau_\lambda = L^2/\lambda$, known as the magnetic diffusion time.

Case II: $Rm \rightarrow \infty$

In this case, the diffusion term is negligible and one obtains

$$\frac{\partial \mathbf{B}}{\partial t} = \nabla \times (\mathbf{u} \times \mathbf{B}). \quad (8.8)$$

For any solenoidal field \mathbf{G} , $\nabla \cdot \mathbf{G} = 0$, one can show that

$$\frac{d}{dt} \int_{\partial W} \mathbf{G} \cdot d\mathbf{S} = \int_{\partial W} \left[\frac{\partial \mathbf{G}}{\partial t} - \nabla \times (\mathbf{u} \times \mathbf{G}) \right] \cdot d\mathbf{S} \quad (8.9)$$

where ∂W is a material surface embedded in a fluid and moving with it. A formal proof can be found on page 40 of Davidson (2001). Qualitatively, it shows that the flux of \mathbf{G} through a material area ∂W changes due to two reasons - changes in \mathbf{G} itself and changes in the area while it moves with the fluid. Using equations (8.8) and (8.9), we get

$$\frac{d}{dt} \int_{\partial W} \mathbf{B} \cdot d\mathbf{S} = 0 \quad (8.10)$$

This is an important result known as Alfvén's theorem or the *frozen flux* theorem. Physically it means that when $Rm \rightarrow \infty$, the flux of magnetic field through an area co-moving with the fluid remains constant. Thus, the magnetic field lines remain *frozen* in the fluid and move along with it, without having the freedom to diffuse away.

The first term on the RHS of (8.5) can be written as: $\nabla \times (\mathbf{u} \times \mathbf{B}) = \mathbf{B} \cdot \nabla \mathbf{u} - \mathbf{u} \cdot \nabla \mathbf{B}$. Substituting this into the induction equation gives

$$\frac{\partial \mathbf{B}}{\partial t} + \underbrace{\mathbf{u} \cdot \nabla \mathbf{B}}_{\text{Advection}} = \underbrace{\mathbf{B} \cdot \nabla \mathbf{u}}_{\text{Stretching}} + \underbrace{\lambda \nabla^2 \mathbf{B}}_{\text{Diffusion}}. \quad (8.11)$$

Thus, the magnetic fields evolves through three processes: advection of the field by the flow, stretching of magnetic field lines in the direction of the flow and diffusion of the magnetic field through the fluid.

8.2 The Lorentz force

The induction equation shows how the flow of a conducting fluid affects the magnetic field. The magnetic field, too, affects the fluid through the Lorentz force, $\mathbf{F}_L = \mathbf{J} \times \mathbf{B} = (1/\mu)(\nabla \times \mathbf{B}) \times \mathbf{B}$. Adding this additional body force to the Navier-Stokes equation in a rotating frame (2.18) yields

$$\frac{\partial \mathbf{u}}{\partial t} + \mathbf{u} \cdot \nabla \mathbf{u} = \underbrace{-\nabla p}_{\text{Pressure gradient}} - \underbrace{2\boldsymbol{\Omega} \times \mathbf{u}}_{\text{Coriolis force}} + \underbrace{\frac{1}{\mu}(\nabla \times \mathbf{B}) \times \mathbf{B}}_{\text{Lorentz force}} + \underbrace{\nu \nabla^2 \mathbf{u}}_{\text{Viscous force}}. \quad (8.12)$$

The Lorentz force can be written as

$$\frac{1}{\mu}(\nabla \times \mathbf{B}) \times \mathbf{B} = \underbrace{-\frac{\nabla|\mathbf{B}|^2}{2\mu}}_{\text{Magnetic pressure}} + \underbrace{\frac{\mathbf{B} \cdot \nabla \mathbf{B}}{\mu}}_{\text{Magnetic tension}} \quad (8.13)$$

Note how similar the above expression is to the stress tensor decomposition into pressure and deviatoric stresses and takes the form of a magnetic stress tensor:

$$\tau_{ij}^B = \left(-\mathbf{B}^2/2\mu\right)\delta_{ij} + B_i B_j/\mu \quad (8.14)$$

Thus, the Lorentz force can be thought of as an additional set of stresses on the fluid, with the magnetic pressure adding to the effective pressure, while the magnetic tension adds to the deviatoric stresses on the fluid. These stresses are often referred to as Maxwell stresses. The magnetic tension along field lines makes the magnetic field lines act like a set of strings under tension (like a guitar), which can give rise to wave phenomena as well as a magnetic analogue of the Taylor-Proudman constraint, both of which we discuss below.

8.3 Waves due to the Lorentz force

One of the most important effects of the Lorentz force, in particular the magnetic tension, is to give rise to waves. In the absence of other forces, the simplest of these are Alfvén Waves, while in the presence of rotation, we get magneto-Coriolis waves, which can also be thought of as magnetically modified version of inertial waves from chapter 2. Much of the material below is based on [Finlay \(2008\)](#) to which one can refer for further details on MHD waves.

8.3.1 Alfvén waves

The simplest form of magnetically influenced waves are the Alfvén waves, named after [Alfvén \(1942\)](#) who first described them. Consider a highly conducting fluid at rest in an inertial frame under the influence of a constant uniform magnetic field \mathbf{B} . Consider that at some instant the fluid receives a small velocity perturbation \mathbf{u} and the corresponding small perturbation to the magnetic field is \mathbf{b} .

Using the frozen flux approximation for high Rm , we can write the linearised equation of motion and the linearised induction equation

$$\frac{\partial \mathbf{u}}{\partial t} = \underbrace{-\frac{1}{\rho}\nabla p}_{\text{Effective pressure including magnetic pressure}} + \underbrace{\frac{1}{\rho\mu}(\mathbf{B} \cdot \nabla)\mathbf{b} + (\mathbf{b} \cdot \nabla)\mathbf{B}}_{\text{Magnetic tension}}, \quad (8.15a)$$

$$\frac{\partial \mathbf{b}}{\partial t} = -(\mathbf{u} \cdot \nabla)\mathbf{B} + (\mathbf{B} \cdot \nabla)\mathbf{u}, \quad (8.15b)$$

The terms involving $\nabla \mathbf{B}$ are zero since \mathbf{B} is taken to be uniform. Taking the curl of (8.15a), we get the equation for the evolution of fluid vorticity $\boldsymbol{\xi} = \nabla \times \mathbf{u}$:

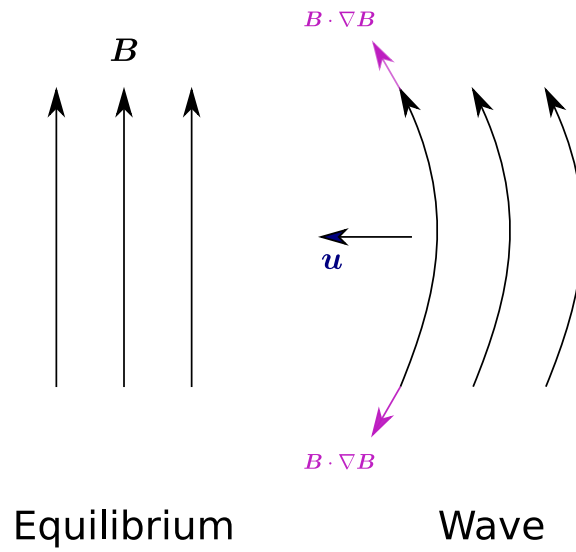


Figure 8.1: Example of an Alfvén wave. The magnetic tension in the field lines acts as a restoring mechanism for the waves. \mathbf{u} here is the velocity of the fluid as forced upon by the magnetic field lines.

$$\frac{\partial \boldsymbol{\xi}}{\partial t} = \frac{1}{\rho\mu} (\mathbf{B} \cdot \nabla) (\nabla \times \mathbf{b}). \quad (8.16)$$

Taking the curl of (8.15b) yields

$$\nabla \times \frac{\partial \mathbf{b}}{\partial t} = (\mathbf{B} \cdot \nabla) \boldsymbol{\xi}. \quad (8.17)$$

Taking a time derivative of (8.16) and substituting (8.17), leads to

$$\frac{\partial^2 \boldsymbol{\xi}}{\partial t^2} = \frac{1}{\rho\mu} (\mathbf{B} \cdot \nabla)^2 \boldsymbol{\xi}, \quad (8.18)$$

which is the Alfvén wave equation. The restoring force, as can be seen from the RHS, is due to the stretching of magnetic field lines by the flow. In other words, magnetic field lines, when stretched, react back on the flow in the form of waves, just like strings under tension. In this case, the frozen flux theorem works in reverse - the fluid is forced to move as the magnetic fields want them to, not the other way round. This reaction is shown in figure 8.1.

Using a wave ansatz $\boldsymbol{\xi} \propto e^{i(\mathbf{k} \cdot \mathbf{r} - \omega t)}$, one obtains the dispersion relation for Alfvén waves,

$$\omega_A^2 = \frac{B^2 (\mathbf{k} \cdot \hat{\mathbf{B}})^2}{\rho\mu}. \quad (8.19)$$

Thus,

$$\omega_A = \pm v_A (\mathbf{k} \cdot \hat{\mathbf{B}}), \quad (8.20)$$

where $v_A = B / \sqrt{\rho\mu}$ is known as the Alfvén velocity, which is the speed at which Alfvén waves travel along the field lines. Their phase velocity is equal to their group velocity and

depends on the angle between waves and the background magnetic field and is independent of $|\mathbf{k}|$. They are thus non-dispersive. The waves are transverse with particle motions being linearly polarised.

8.3.2 Magneto-Coriolis waves

Now let us add rotation to the system. The new equations for the perturbations are

$$\frac{\partial \mathbf{u}}{\partial t} = \underbrace{-\frac{1}{\rho} \nabla p}_{\text{Effective pressure including magnetic pressure}} + \underbrace{\frac{1}{\rho\mu} (\mathbf{B} \cdot \nabla) \mathbf{b}}_{\text{Magnetic tension}} - \underbrace{2\boldsymbol{\Omega} \times \mathbf{u}}_{\text{Coriolis force}}, \quad (8.21a)$$

$$\frac{\partial \mathbf{b}}{\partial t} = (\mathbf{B} \cdot \nabla) \mathbf{u}. \quad (8.21b)$$

As before, we start by taking the curl of both equations, which gives us

$$\frac{\partial \boldsymbol{\xi}}{\partial t} = 2\boldsymbol{\Omega} \cdot \nabla \mathbf{u} + \frac{1}{\rho\mu} (\mathbf{B} \cdot \nabla) (\nabla \times \mathbf{b}) \quad (8.22a)$$

$$\frac{\partial (\nabla \times \mathbf{b})}{\partial t} = (\mathbf{B} \cdot \nabla) \boldsymbol{\xi}. \quad (8.22b)$$

Note that if it were a steady state and the Lorentz force was not present, we would get back the Taylor-Proudman constraint (2.20) from (8.22a). Taking a time-derivative of (8.22a) and using (8.22b) gives

$$\frac{\partial^2 \boldsymbol{\xi}}{\partial t^2} = 2(\boldsymbol{\Omega} \cdot \nabla) \frac{\partial \mathbf{u}}{\partial t} + \frac{1}{\rho\mu} (\mathbf{B} \cdot \nabla)^2 \boldsymbol{\xi}. \quad (8.23)$$

Taking the curl of this and using the fact that $\nabla \times \boldsymbol{\xi} = \nabla \times \nabla \times \mathbf{u} = -\nabla^2 \mathbf{u}$, we get

$$-2(\boldsymbol{\Omega} \cdot \nabla) \frac{\partial \boldsymbol{\xi}}{\partial t} = \left(\frac{\partial^2}{\partial t^2} - \frac{1}{\rho\mu} (\mathbf{B} \cdot \nabla)^2 \right) \nabla^2 \mathbf{u}. \quad (8.24)$$

Taking a time-derivative of (8.24) and eliminating $\boldsymbol{\xi}$ from (8.23) and (8.24) gives the equation:

$$\left(\frac{\partial^2}{\partial t^2} - \frac{1}{\rho\mu} (\mathbf{B} \cdot \nabla)^2 \right)^2 \nabla^2 \mathbf{u} = -4(\boldsymbol{\Omega} \cdot \nabla)^2 \frac{\partial^2 \mathbf{u}}{\partial t^2}. \quad (8.25)$$

Equation (8.25) represents *magneto-Coriolis* waves (MC waves). These waves have the Coriolis and Lorentz forces as restoring forces and can thus be thought of as a combination of inertial and Alfvén waves.

Substituting a plane wave ansatz $\mathbf{u} \propto e^{i(\mathbf{k}\cdot\mathbf{r}-\omega t)}$ in equation (8.25) gives a quadratic equation in ω whose roots are

$$\omega_{MC} = \pm(\boldsymbol{\Omega} \cdot \hat{\mathbf{k}}) \pm \left((\boldsymbol{\Omega} \cdot \hat{\mathbf{k}})^2 + \frac{1}{\rho\mu} (\mathbf{B} \cdot \mathbf{k})^2 \right)^{1/2}, \quad (8.26)$$

which is the dispersion relation for MC waves. Note that it can be written as

$$\omega_{MC} = \pm \frac{\omega_C}{2} \pm \left(\left(\frac{\omega_C}{2} \right)^2 + \omega_A^2 \right)^{1/2} \quad (8.27)$$

where, $\omega_C = \pm 2\mathbf{\Omega} \cdot \hat{\mathbf{k}}$ is the frequency of a pure inertial wave and $\omega_A = \pm(\mathbf{B} \cdot \mathbf{k})/\sqrt{\rho\mu}$ is the Alfvén wave frequency. The dispersion relation shows that an MC wave is simply the combination of an inertial and an Alfvén wave. Setting either $\mathbf{\Omega}$ or \mathbf{B} to zero allows one to recover the dispersion relation of a pure Alfvén or inertial wave, respectively. The dispersion relation (8.26) defines two distinct classes of MC waves:

- **Fast MC waves** When both terms in (8.26) have the same sign, the wave has a high frequency. Both forces, Coriolis and Lorentz, act in unison and give rise to a large restoring force.
- **Slow MC waves** When the two terms in (8.26) have opposite signs, the wave frequency is low because Coriolis and Lorentz forces act against each other and give rise to a small restoring force.

The two classes become very clearly distinct in the case when the inertial wave frequency is much larger than the Alfvén wave frequency, $\omega_C \gg \omega_A$. In this case, one can perform a Taylor series expansion in the small parameter ω_A/ω_C and obtain the dispersion relations for the two classes of waves by ignoring higher order terms:

$$\omega_{MC}^f = \pm \omega_C \left(1 + \frac{\omega_A^2}{\omega_C^2} \right), \quad (8.28a)$$

$$\omega_{MC}^s = \pm \frac{\omega_A^2}{\omega_C} = \pm \omega_A \left(\frac{\omega_A}{\omega_C} \right). \quad (8.28b)$$

Equation (8.28a) shows that a fast MC wave is essentially an inertial wave modified slightly by the magnetic field (ω_A^2/ω_C^2 is a small quantity) with its frequency being higher than that of a pure inertial wave. Thus, fast MC waves can have frequencies higher than 2Ω . For a slow MC wave, equation (8.28b) shows that the Lorentz force is the primary restoring force for these waves with the Coriolis force opposing it. These waves are of interest to geophysicists as their time-period $\tau_{MC} = 2\Omega L^2/v_A^2$ is equal to about 300 years for the parameters of the Earth and is thus similar to the time-scale of wave-like secular variation observed in the Earth's magnetic field (Finlay and Jackson 2003).

In the presence of temperature gradients, buoyancy comes in as a third restoring force and the waves generated are then called Magnetic Archimedes Coriolis (MAC) waves - a topic of great interest in geodynamo research (e.g. Braginsky 1993).

8.3.3 Lorentz force and differential rotation: Ferraro's law of isorotation

As one can guess by now, strong magnetic tension inhibits fluid motion. Thus, magnetic tension would try to align fluid motions along field lines. This is the magnetic equivalent

of the Taylor-Proudman theorem and is known as *Ferraro's law of isorotation* after [Ferraro \(1937\)](#). Consider an axisymmetric magnetic field \mathbf{B} ($\partial\mathbf{B}/\partial\phi = 0$) permeating a fluid with velocity \mathbf{u} that is differentially rotating about an axis with

$$\mathbf{u} = s\bar{\omega}(s, z)\hat{\phi}, \quad (8.29)$$

where we have used cylindrical coordinates (s, z, ϕ) . \mathbf{B} can be separated into an azimuthal contribution (toroidal field) and a non-azimuthal one (poloidal field).

$$\mathbf{B} = \mathbf{B}_p(s, z, t) + B_\phi(s, z, t)\hat{\phi} \quad (8.30)$$

In the limit of high magnetic Reynolds number, one can ignore diffusion and the induction equation would give

$$\frac{\partial\mathbf{B}_p}{\partial t} = 0, \quad (8.31a)$$

$$\frac{\partial B_\phi}{\partial t} = s(\mathbf{B}_p \cdot \nabla)\bar{\omega}, \quad (8.31b)$$

which, in a steady state yields

$$\mathbf{B}_p \cdot \nabla\bar{\omega} = 0, \quad (8.32)$$

indicating that lines of isorotation are aligned with the poloidal magnetic field lines. This is known as *Ferraro's law of isorotation*. Taking the analysis further and including the linearised Navier-Stokes equation would yield the equation for *torsional Alfvén waves*

$$\frac{\partial^2\bar{\omega}}{\partial t^2} = v_{TA}^2 \frac{\partial^2\bar{\omega}}{\partial z^2} \quad (8.33)$$

where, $v_{TA} = \pm B_p / \sqrt{\rho\mu}$ is the speed of the torsional Alfvén waves.

8.4 Magneto-Coriolis modes

In a bounded container rotating with a rotation rate Ω in a magnetic field \mathbf{B} , any velocity perturbation \mathbf{u} would grow according to the MC wave equation (8.25). However, in this case, it wouldn't give rise to plane waves and must satisfy the boundary condition $\mathbf{u} \cdot \hat{\mathbf{n}} = 0$, where $\hat{\mathbf{n}}$ is the normal to the surface of the container.

The two most significant studies of magneto-Coriolis modes were by [Hide \(1966\)](#) and [Malkus \(1967\)](#). They are explained below in brief

Hide's β -plane model

[Hide \(1966\)](#) developed a model for MC modes in a spherical shell whose motions are roughly parallel to the rotation axis, thus concentrating on local fluid motions in eastward ($\hat{\mathbf{x}}$) and northward ($\hat{\mathbf{y}}$) directions in a spherical shell and the evolution of z -vorticity (ξ_z). Following [Rossby et al. \(1939\)](#), he assumed that the Coriolis force varies linearly with latitude, often referred to as the β -plane approximation, because of the parameter β

defining the slope of the variation. The simplification results in the Coriolis force having components $-fu_y$ and fu_x in the east and northward directions, respectively, where $f = 2\Omega \cos \theta + (2\Omega/r_o) \sin \theta$ $y = f_0 + \beta y$. Hide argued that β should change its sign in thick spherical shells.

In Hide's scenario, the background magnetic field \mathbf{B} is uniform making a constant arbitrary angle with the \hat{x} direction. For simplicity, let us consider the case when \mathbf{B} is directed along \hat{x} . The equations for the perturbations (\mathbf{u}, \mathbf{b}) are

$$\frac{\partial u_x}{\partial t} - \beta y u_y = -\frac{1}{\rho} \frac{\partial p}{\partial x}, \quad (8.34a)$$

$$\frac{\partial u_y}{\partial t} + \beta y u_x = -\frac{1}{\rho} \frac{\partial p}{\partial y} + \frac{B}{\rho \mu} \left(\frac{\partial b_y}{\partial x} - \frac{\partial b_x}{\partial y} \right), \quad (8.34b)$$

$$\frac{\partial b_x}{\partial t} = B \frac{\partial u_x}{\partial x}, \quad (8.34c)$$

$$\frac{\partial b_y}{\partial t} = B \frac{\partial u_y}{\partial x}, \quad (8.34d)$$

These can be manipulated to yield an equation for the evolution of z -component of vorticity ($\nabla_H^2 = \partial^2/\partial x^2 + \partial^2/\partial y^2$),

$$\left(\frac{\partial^2}{\partial t^2} - \frac{B^2}{\rho \mu} \frac{\partial^2}{\partial x^2} \right) \nabla_H^2 \xi_z + \beta \frac{\partial}{\partial t} \left(\frac{\partial \xi_z}{\partial t} \right) = 0, \quad (8.35)$$

which is satisfied by plane-wave equations for the form $\xi \propto e^{i(kx+ky-\omega t)}$, k being the wavenumber and ω the angular frequency. They satisfy the dispersion relation

$$\omega = -\frac{\beta}{2k} \pm \frac{\beta}{2k} \left(1 + \frac{4B^2 k^4}{\rho \mu \beta^2} \right)^{1/2} \quad (8.36)$$

A Taylor expansion in $(4B^2 k^4/\rho \mu \beta^2)$ would yield two distinct classes of long-wavelength waves with

$$\omega_{Rossby} = -\frac{\beta}{k} \text{ and } \omega_{MC} = \frac{B^2 k^3}{\rho \mu \beta} \quad (8.37)$$

The first one can be identified as classical Rossby waves which are slow quasi-geostrophic inertial waves on a sphere and were first studied by Rossby et al. (1939). The second one looks similar in nature to the slow MC wave (8.28b) and are often referred to as an MC Rossby wave or Hide's wave. Recently, using numerical simulations Hori et al. (2015) have shown that these waves can be the key to gaining information about the toroidal magnetic field inside the Earth which is opaque to observations.

Malkus' MC modes in full sphere

Malkus (1967) investigated the problem of MC modes in a full sphere rotating at a rate Ω under the influence of a toroidal (azimuthal) magnetic field of the form $\mathbf{B} = Bs\hat{\phi}$ in cylindrical coordinates (s, z, ϕ) . Using the inertial mode ansatz $(\mathbf{u}, \mathbf{b}) \propto e^{i(m\phi-\omega t)}$, he was

successful in reducing the MC mode problem in a full sphere to resemble the Poincaré equation for inertial modes (2.45),

$$\left(\nabla^2 - \frac{4}{\omega_m^2} \frac{\partial^2}{\partial z^2}\right) p = 0. \quad (8.38)$$

where,

$$\omega_m = \frac{-\omega\rho + \frac{B^2 m^2}{\mu\omega}}{\Omega\rho + \frac{B^2 m}{\mu\omega}} \quad (8.39)$$

As in the case of inertial modes (section 2.3.2), ω_m are real and $|\omega_m| \leq 2\Omega$. Thus, one would obtain the same set of modes as that of a full sphere with their frequencies modified by the magnetic field. Note that in this case, the restriction on frequencies is on ω_m and thus ω may take values beyond 2Ω . Solving for ω gives

$$\omega = \frac{\omega_m \Omega}{2} \left[-1 \pm \left(1 + \frac{4B^2 m(m - \omega_m)}{\Omega^2 \omega_m^2 \rho \mu} \right)^{1/2} \right]. \quad (8.40)$$

A Taylor expansion in $\frac{4B^2 m(m - \omega_m)}{\Omega^2 \omega_m^2 \rho \mu}$ provides us with two classes of long-wavelength (small m) modes:

$$\omega_C \approx -\Omega\omega_m \text{ and } \omega_{MC} \approx \frac{B^2}{\Omega\rho\mu} \frac{m(m - \omega_m)}{\omega_m}. \quad (8.41)$$

ω_C represents a pure inertial mode, while ω_{MC} represents a slow MC mode in a full sphere.

8.5 Discussion

The above text provides a very fundamental knowledge of magnetohydrodynamic flows and MHD waves in the absence of thermal or density stratification. In chapter 1, we saw how hydromagnetic waves are very important in the context of geophysics as well as astrophysics. Thus, a study of these waves, especially in rotating spherical shells is quite imperative. The above theoretical background shall be useful in understanding the next chapter where we study the effect of an imposed magnetic field.

9 Magnetic Couette flow

*“I have had my results for a long time:
but I do not yet know how I am to
arrive at them”*

Carl Friedrich Gauss

We explored hydrodynamic instabilities of the spherical Couette system in chapter 6. In this chapter, we study the effect of an imposed magnetic field on the system when the fluid is conducting. We end the chapter with a short discussion on self-consistent dynamo action in the system.

9.1 Introduction

The question of whether and how magnetic fields interact with differential rotation is fundamental to understanding interior dynamics of astrophysical objects. However, simulations of self-consistent dynamo action in these objects are not able to control the strength of the magnetic field and differential rotation independently to study the parameter dependence. This motivates the study of the spherical Couette system under an imposed magnetic field.

We saw in chapter 3 that the solution by Proudman (1956) and Stewartson (1966) for the spherical Couette flow consists of a large change in the fluid rotation rate inside and outside the cylinder tangent to the inner core equator (the tangent cylinder or TC). This gives rise to a nested shear layer structure called the Stewartson layer consisting of three layers with thickness $O(E^{1/3})$, $O(E^{2/7})$ and $O(E^{1/4})$. In the presence of a magnetic field, the shear is modified by the magnetic tension. This gives rise to magnetic free shear layers called Shercliff layers after Shercliff (1962) who first described such layers in the context of magnetic pipe flows.

The difference arises because of the competing constraints of Taylor-Prouman theorem and the Ferraro isorotation law. In general, the type of solution depends on the magnetic boundary conditions and the magnetic field topology with magnetic field lines separating regions of constant angular velocity. The magnetic spherical Couette system was studied numerically by Hollerbach (1994) and analytically using asymptotic analysis by Kleorin et al. (1997) who studied the effect of an axisymmetric dipole field originating in the inner sphere, with regions outside both outer and inner boundaries insulating. As the field strength is increased, it was found that there is a gradual suppression of the nested Stewartson layer structure and a transition to a single Shercliff layer. The transition

takes place at slightly different field strengths for the three different nested layers, the first suppression being noticeable once $\Lambda > \mathcal{O}(E^{1/3})$, where Λ is the Elsasser number - a non-dimensional measure of magnetic energy. Around $\Lambda \sim \mathcal{O}(1)$, all three layers have merged into a single layer. Similar results were found by analytical investigations of the effect of an axial field by [Ingham \(1969\)](#) and [Vempaty and Loper \(1975, 1978\)](#) for cylindrical Taylor-Couette flow and numerical simulations by [Hollerbach \(1997\)](#) for a spherical Couette flow with a finitely conducting inner core. The latter study found that for weak fields, $\mathcal{O}(E^{1/2}) \leq \Lambda \leq \mathcal{O}(E^{-1/3})$, the main effect of the magnetic field is to enhance the rotation rate of the fluid inside TC through electromagnetic coupling with the inner core. For strong fields, $\Lambda \geq \mathcal{O}(E^{-1/3})$, the Ekman layer transitions to an Ekman-Hartmann layer (a magnetically modified boundary layer) of width $(E/\Lambda)^{1/2}$ and the three nested Stewartson layers merge together to form a single $(E/\Lambda)^{1/4}$ Shercliff layer. For conducting boundaries and different magnetic topologies, strong Lorentz forces can give rise to super and sub-rotating jets ([Starchenko 1997](#), [Dormy et al. 1998](#), [Hollerbach 2000, 2001](#)). [Soward and Dormy \(2010\)](#) performed an asymptotic analysis to map out the entire parameter space of dependence of the super-rotation of the jet on the outer boundary conductance with an inner conducting sphere.

The above studies discuss axisymmetric solutions at very low Re or Ro . Instabilities of the Shercliff layer in the spherical Couette flow at finite Re were first studied by [Hollerbach and Skinner \(2001\)](#) for an axial field, and a stationary outer boundary. Further development took place with studies by [Hollerbach \(2009\)](#) and [Gissinger et al. \(2011\)](#), with the last one having a rotating outer boundary and thus a Stewartson layer. [Gissinger et al. \(2011\)](#) found that a strong magnetic field can stabilise a hydrodynamically unstable Stewartson layer, but applying a stronger field causes instabilities of the Shercliff layer as already investigated by [Hollerbach and Skinner \(2001\)](#). [Wei and Hollerbach \(2008\)](#) considered the transition from a Stewartson layer instability to a Shercliff layer instability, but without any definite conclusions. The difference in the nature of instabilities is that, unlike in the case of the Stewartson layer, Shercliff layer instabilities do not depend on the sign of Ro .

The 60 cm and 3-metre experiments at Maryland USA use a weak axial magnetic field as a diagnostic to characterise the flow (e.g. [Kelley et al. 2007](#)). Since the fields are too weak to modify the flow significantly, the modes observed in [Kelley et al. \(2007\)](#) are probably close to inertial modes without the effect of magnetic field. Magnetic effects are more significant in the DTS experiment at Grenoble, France where the inner sphere is a permanent dipolar magnet. There one can observe clear magneto-Coriolis modes, the identifications of which have been verified by eigenmode computations and numerical simulations ([Schmitt et al. 2008](#), [Schmitt et al. 2013](#)). Numerical simulations suggest that if the fluid is strongly conducting, the spherical Couette flow can even give rise to a self-consistent dynamo (e.g. [Guervilly and Cardin 2010](#), [Cao et al. 2012](#)). A more detailed review of magnetic Couette flow can be found in the book by [Rüdiger et al. \(2013\)](#).

In this chapter, we study the effect of an imposed axial magnetic field on a spherical Couette setup with insulating boundaries. First we use a weak magnetic field as a diagnostic to detect inertial modes in the system, and compare the results with [Kelley et al. \(2007\)](#). Thereafter, we investigate the effect of stronger magnetic fields on some of the EA inertial modes found in our system.

9.2 Non-dimensional parameters

To non-dimensionalise the equations for the evolution of velocity and magnetic field in the spherical Couette system, we use the gap-width $L = r_o - r_i$ as the length scale and the viscous diffusion time, $\tau_v = L^2/\nu$ as the time scale. The magnetic field is scaled with $(\rho\mu\lambda\Omega_o)^{1/2}$. Using these scalings, the non-dimensional equations governing the evolution of velocity \mathbf{u} and magnetic field \mathbf{B} , can be written as (same as equations (4.1) - (4.3))

$$E \left(\frac{\partial \mathbf{u}}{\partial t} + \mathbf{u} \cdot \nabla \mathbf{u} \right) = -\nabla p - 2\hat{\mathbf{z}} \times \mathbf{u} + \frac{1}{Pm} (\nabla \times \mathbf{B}) \times \mathbf{B} + E \nabla^2 \mathbf{u}, \quad (9.1)$$

$$\frac{\partial \mathbf{B}}{\partial t} = \nabla \times (\mathbf{u} \times \mathbf{B}) + \frac{1}{Pm} \nabla^2 \mathbf{B}, \quad (9.2)$$

$$\nabla \cdot \mathbf{u} = 0 \quad , \quad \nabla \cdot \mathbf{B} = 0 \quad (9.3)$$

where, $E = \nu/\Omega_o L^2$ is the Ekman number, and Pm is called the magnetic Prandtl number, defined as

$$Pm = \frac{\nu}{\lambda}, \quad (9.4)$$

the ratio between the kinematic viscosity and the magnetic diffusivity. Another non-dimensional quantity of interest is the Elsasser number, defined as

$$\Lambda = \frac{B^2}{\rho\mu\lambda\Omega_o} = \frac{\text{Lorentz}}{\text{Coriolis}} \quad (9.5)$$

which is the ratio between the Lorentz and the Coriolis forces and is non-dimensional measure of the magnetic energy in our scaling.

9.3 Magnetic field as a diagnostic

Like in the 60 cm experiment (Kelley et al. 2007), we impose an axial magnetic field on the spherical Couette setup in our simulations with MagIC, as shown in figure 9.1. The amplitude of the field is kept very low so that the Lorentz forces are too weak to influence the fluid dynamics, but the induced field can be used as a diagnostic. The magnetic Prandtl numbers were kept at low values such as $Pm = 0.01$ and $Pm = 10^{-4}$ in order to let the magnetic field diffuse quickly.

The evolution of the induced field is given by the induction equation:

$$\frac{\partial \mathbf{b}}{\partial t} = \nabla \times (\mathbf{u} \times \mathbf{B}) + \frac{1}{Pm} \nabla^2 \mathbf{b} \quad (9.6)$$

where, \mathbf{B} is the applied field, \mathbf{b} is the induced field and $|\mathbf{b}| \ll |\mathbf{B}|$. Thus, if \mathbf{B} is known and \mathbf{b} is detected, one can integrate (9.6) for the velocity structure. The inertial modes in Kelley et al. (2007) were identified based on comparing induction patterns obtained from experiments to those obtained from numerics. The structure of the induction pattern on the surface of the spherical shell is given by the selection rules of Bullard and Gellman (1954). An axial magnetic field $B\hat{\mathbf{z}}$ has an azimuthal wavenumber of $m_0 = 0$ and a polar

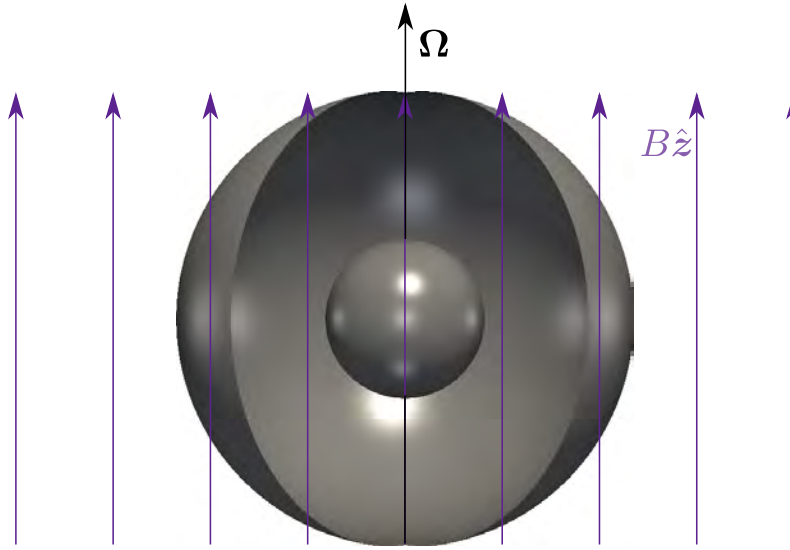


Figure 9.1: The spherical Couette system with a uniform magnetic field \mathbf{B} imposed along the rotation axis.

wavenumber of $l_0 = 1$. If the surface structure of the inertial mode and the induced field resemble spherical harmonics Y_{lm} and $Y_{l_{mag}m_{mag}}$, respectively, then using the selection rules, one gets:

- $m + m_0 + m_{mag} = 0$, implying that $m_{mag} = m$.
- The magnitudes of l , l_0 and l_{mag} must be able to form sides of a triangle, which is only possible when $|l - l_{mag}| = 1$. This implies that \mathbf{u} and \mathbf{b} have opposite equatorial symmetries.
- In addition, \mathbf{u} and \mathbf{b} have identical drift frequencies.

Figure 9.2 shows the induction patterns for some of the major inertial modes identified at $E = 10^{-4}$ and $E = 10^{-5}$. One can see that due to the selection rules, the equatorially antisymmetric inertial modes have equatorially symmetric magnetic induction patterns with the same azimuthal symmetry as the mode.

In the absence of any external sources (outside the outer boundary), the magnetic field can be written in terms of a potential ψ satisfying the Laplace equation

$$\nabla^2 \psi = 0. \quad (9.7)$$

ψ can be expanded as follows:

$$\psi(r, \theta, \phi, t) = \frac{r_o}{\mu_0} \sum_{l=1}^{l_{max}} \sum_{m=0}^l \left(\frac{r_o}{r}\right)^{l+1} P_l^m(\cos \theta) (g_{lm}(t) \cos m\phi + h_{lm}(t) \sin m\phi) \quad (9.8)$$

where g_{lm} and h_{lm} are known as the Gauss coefficients.

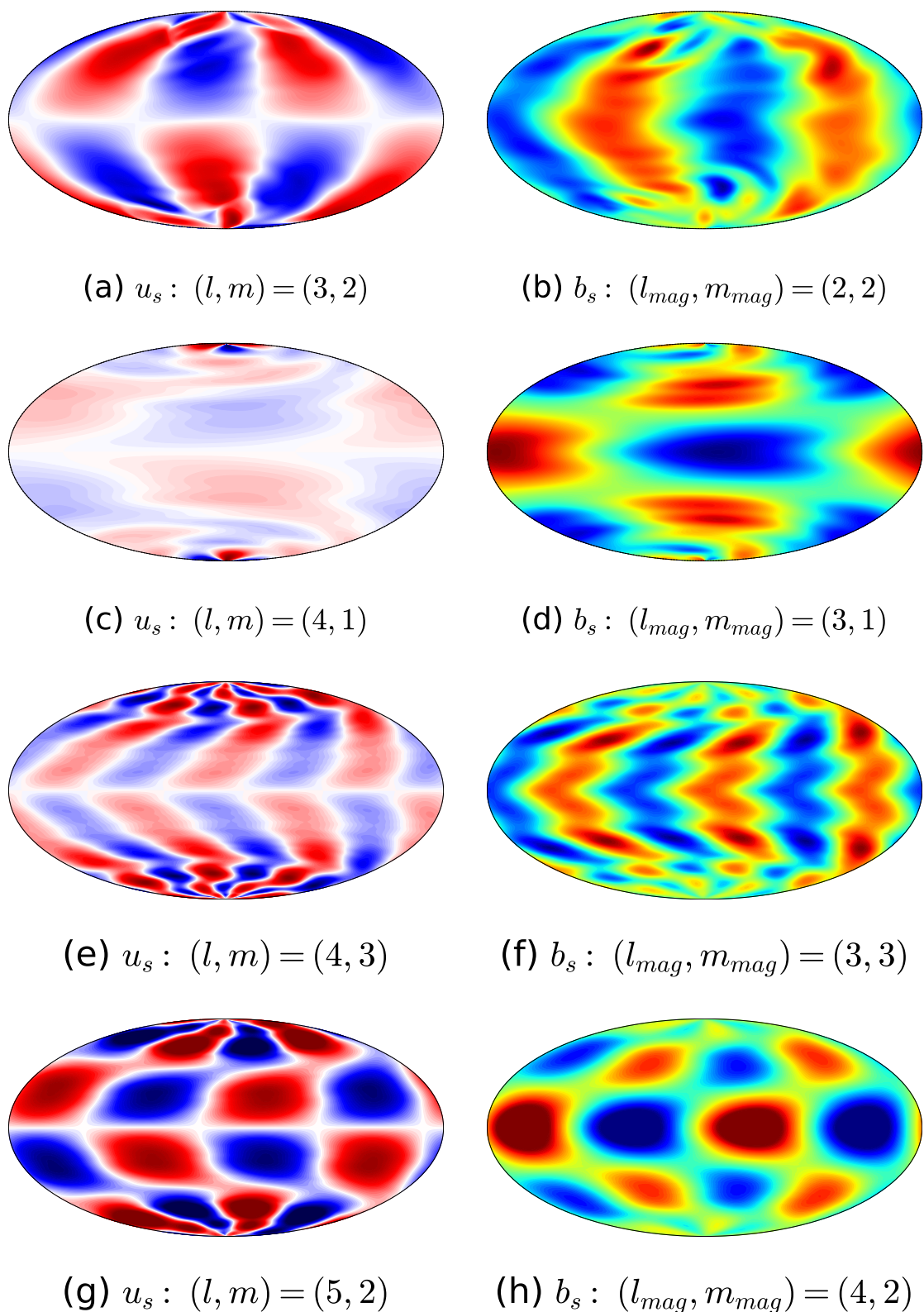


Figure 9.2: The major inertial modes identified at $E = 10^{-4}$ and $E = 10^{-5}$ and their magnetic induction patterns on a Hammer projection. Colours show cylindrical radial velocity and magnetic field u_s and b_s , respectively. Colours towards red indicate positive (outward) while colours towards blue indicate negative (inwards). Compare with figure 7 of Kelley et al. (2007).

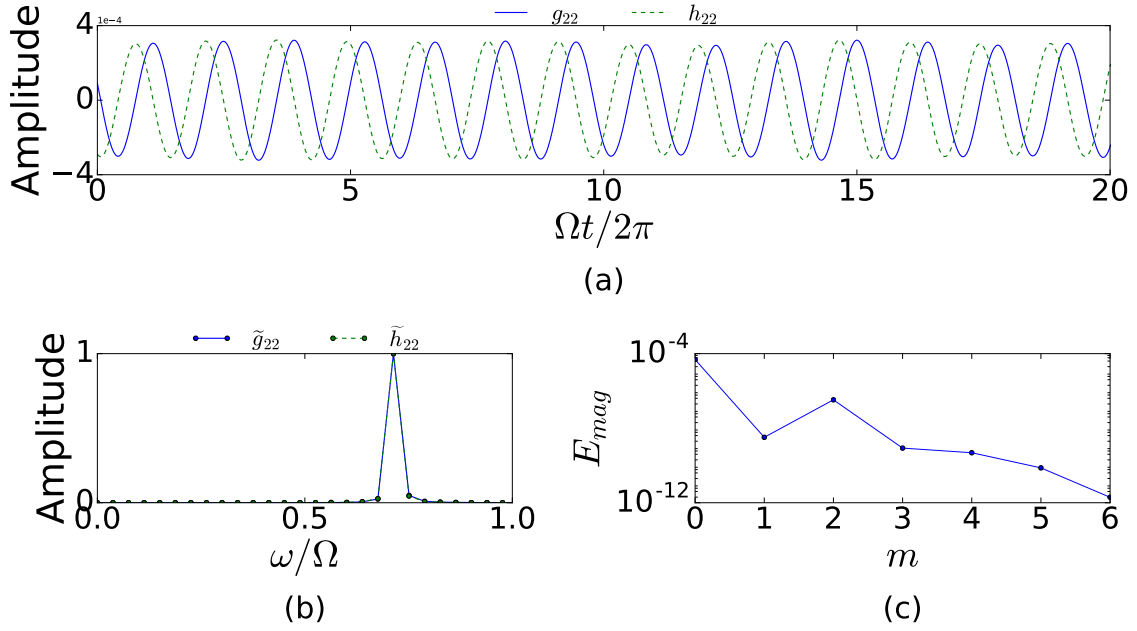


Figure 9.3: Oscillation of Gauss Coefficients g_{lm} and h_{lm} . (a) The oscillating coefficients g_{22} and h_{22} . (b) Fourier transform of the coefficients denoted by \sim on the top. (c) Magnetic energy vs spherical harmonic order - peak at $m = 2$ clearly visible. One recovers the drift frequency of the inertial mode from the oscillations of these coefficients.

The drift frequency of an inertial mode can be recovered by an analysis of the oscillations in the Gauss coefficients of the right azimuthal and equatorial symmetry (same m and equatorially symmetric: $l - m = \text{even}$). This has been shown in figure 9.3. The Fourier analysis of the coefficients g_{22} and h_{22} yields a dominant frequency the same as that of the (3, 2) mode at $E = 10^{-4}$ and $Ro = -2$. Panel (c) gives the energy in different m , showing that the modes with $m \leq 3$ are the most dominant ones as seen from the kinetic energy spectrum in chapter 6, section 6.6.1.3.

9.4 Magneto-Coriolis modes

We increase the imposed field strength to explore its effect on the flow dynamics, in particular, on the EA inertial modes. The theoretical analysis proceeds in a similar manner as in for magneto-Coriolis waves in section 8.3.2. Consider velocity and pressure perturbations \mathbf{u} and p in a fluid rotating in a container at a rate $\boldsymbol{\Omega}$ in the presence of a background magnetic field $\mathbf{B} = B\hat{\mathbf{z}}$. The velocity and pressure perturbations and the induced field \mathbf{b} obey

$$\frac{\partial \mathbf{u}}{\partial t} = -\frac{1}{\rho} \nabla p + \frac{1}{\rho \mu} (\mathbf{B} \cdot \nabla) \mathbf{b} - 2\boldsymbol{\Omega} \times \mathbf{u}, \quad (9.9a)$$

$$\frac{\partial \mathbf{b}}{\partial t} = (\mathbf{B} \cdot \nabla) \mathbf{u}. \quad (9.9b)$$

Using the wave ansatz in azimuth, $(\mathbf{u}, \mathbf{b}, p) \propto e^{i(m\phi - \omega t)}$, we obtain the equations

$$-i\omega \mathbf{u} = -\frac{1}{\rho} \nabla p + \frac{1}{\rho\mu} (\mathbf{B} \cdot \nabla) \mathbf{b} - 2\boldsymbol{\Omega} \times \mathbf{u}, \quad (9.10a)$$

$$-i\omega \mathbf{b} = (\mathbf{B} \cdot \nabla) \mathbf{u}. \quad (9.10b)$$

Eliminating \mathbf{b} from the two equations gives

$$-i\omega \mathbf{u} + \frac{1}{\rho} \nabla p + 2\boldsymbol{\Omega} \times \mathbf{u} = \frac{i}{\omega} \frac{1}{\rho\mu} (\mathbf{B} \cdot \nabla)^2 \mathbf{u}. \quad (9.11)$$

Using our usual non-dimensionalisation scalings for length and time and the strength B of the magnetic field to scale the magnetic field, we can rewrite this in a non-dimensional form as

$$-i\omega \mathbf{u} + \nabla p + 2\hat{\mathbf{z}} \times \mathbf{u} = \frac{i}{\omega} Le^2 (\hat{\mathbf{z}} \cdot \nabla)^2 \mathbf{u}, \quad (9.12)$$

where,

$$Le = \frac{B}{(\rho\mu)^{1/2} \Omega L} = \frac{v_A}{\Omega L} = \left(\frac{\Lambda E}{Pm} \right)^{1/2}, \quad (9.13)$$

is the Lehnert number which measures the ratio of the Alfvén speed v_A to the speed of an inertial wave. As can be inferred from the definition, Le determines the wave that would play a major role in the dynamics of the fluid. For $Le^2 \ll 1$, one can expand the velocity and pressure perturbations as

$$\mathbf{u} = \mathbf{u}_0 + Le^2 \mathbf{u}_1 + Le^4 \mathbf{u}_2 + \dots, \quad (9.14a)$$

$$p = p_0 + Le^2 p_1 + Le^4 p_2 + \dots \quad (9.14b)$$

Comparing like order terms in Le^2 , leads to

$$-i\omega \mathbf{u}_0 + \nabla p_0 + 2\hat{\mathbf{z}} \times \mathbf{u}_0 = 0, \quad (9.15a)$$

$$-i\omega \mathbf{u}_1 + \nabla p_1 + 2\hat{\mathbf{z}} \times \mathbf{u}_1 = \frac{i}{\omega} (\hat{\mathbf{z}} \cdot \nabla)^2 \mathbf{u}_1, \quad (9.15b)$$

$$-i\omega \mathbf{u}_i + \nabla p_i + 2\hat{\mathbf{z}} \times \mathbf{u}_i = 0, \text{ for all } i > 1, \quad (9.15c)$$

where i is an integer. The equation for \mathbf{u}_0 and p_0 and for all $\mathbf{u}_i, i > 1$ is the inertial mode equation (2.44a). Thus the zero order perturbation to the velocity and pressure evolve as inertial modes, which are slightly modified by the magnetic field, for higher orders in Le^2 . Note that we would also come to a similar conclusion from the definition of Le and the fact that the LHS of equation (9.12) looks the same as that of an inertial mode equation with the RHS being slightly different from zero for low Le . Thus, the Lorentz force contributes to the force balance, but the main balance is still decided by the pressure gradient and the Coriolis force. In our simulations, the highest value attained by Le^2 is 0.01.

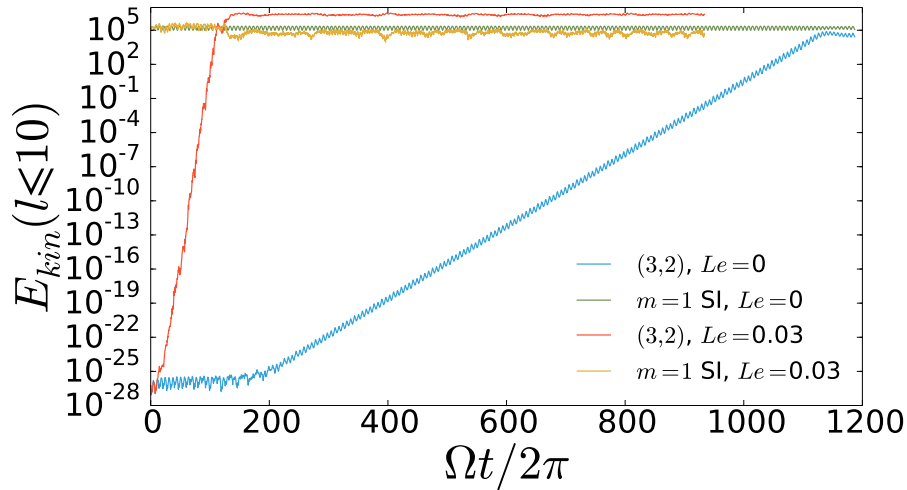


Figure 9.4: Effect of a magnetic field on the onset of an EA inertial mode. $E = 10^{-4}$, $Ro = -1.33$.

We perform our simulations at $E = 10^{-4}$ where the (3, 2) mode comes in as the most dominant EA inertial mode at $Ro = -1.33$. The Pm is kept fixed at 0.01. We initialise our simulations from a flow solution at $Ro = -1.3$ where only the $m = 1$ Stewartson layer instability (SI) is present as the dominant large scale structure. Figure 9.4 shows the effect of the magnetic field on the growth of the (3, 2) inertial mode. Even with a small magnetic field magnitude of $\Lambda = 0.09$, $Le = 0.03$, the growth rate increases by more than an order of magnitude. Moreover, the final saturation energy of the (3, 2) mode surpasses that of the $m = 1$ SI. This effect is seen for all the EA modes and their growth rates are roughly the same. Thus, the magnetic field seems to promote the growth of the EA inertial modes. The variation of growth rate of the (3, 2) mode and hence, the other major EA modes with magnetic field strength (Le or Λ) is shown in figure 9.5a. The sudden increase in growth rate when imposing a weak magnetic field can also be seen here. The growth rate seems to increase at high field strengths. A similar exercise at $Ro = -1.3$ did not yield an onset of any EA modes showing that the magnetic field does not cause a change in the critical Ro necessary for the onset of EA inertial modes.

The frequencies of the different EA modes do not show a simple dependence on the magnetic field strength, as shown in figure 9.5b. The frequency of the (3, 2) mode remains nearly constant. The $m = 1$ EA mode frequency suddenly decreases between $Le = 0.03$ and $Le = 0.035$, but increases again between $Le = 0.075$ and $Le = 0.08$, changing its frequency from one close to a (4, 1) to one close to a (6, 1) mode and back again. This points towards transitions to different magnetically modified modes. 9.6 illustrates the related structural changes. The $m = 1$ EA mode does not form a triad with the (3, 2) and $m = 1$ SI beyond $Le = 0.03$. The case of the $m = 3$ is relatively simple. The (10, 3) mode that forms a triad with the (3, 2) and $m = 1$ SI is detectable till $Le = 0.03$. From $Le = 0.035$ onwards, the (4, 3) mode sets in as the dominant $m = 3$ EA mode and remains so, without forming any identifiable triads. The mode energies in figure 9.7 show that the (3, 2) mode remains dominant throughout and has a peak at $Le = 0.05$.

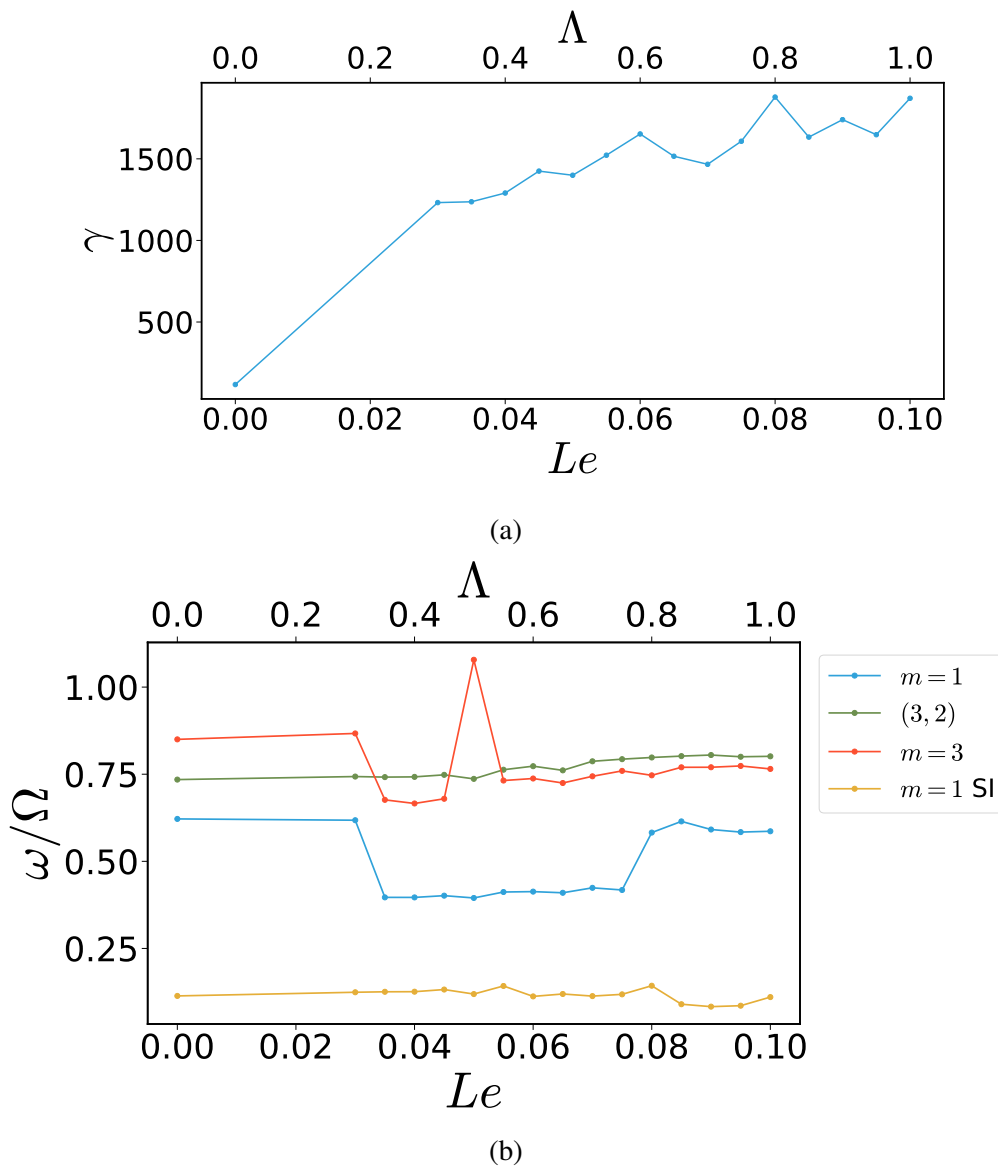


Figure 9.5: Variation of (a) growth rate γ and (b) frequency of EA inertial modes with magnetic field strength, measure by the Lehnert (Le) and Elsasser numbers (Λ).

Delayed imposition - EA mode quenching

The effect of the magnetic field trying to make the flow aligned with the rotation axis can be seen when the field is imposed after the onset of the EA modes has taken place in the purely hydrodynamic case. This is shown in figure 9.8, which shows the onset of $(3,2)$ EA mode at $E = 10^{-4}$, $Ro = -1.33$ and the time at which the magnetic field is imposed is indicated by the vertical line. One can see that the $(3,2)$ mode survives at a lower energy when the magnetic field strength is weak. However, with a small increase in magnetic field strength, the mode exponentially decays. The decay is faster for a stronger magnetic field. This can be understood in terms of magnetic tension trying to align the flow with the rotation axis and thus, effectively filtering out any mode that is equatorially

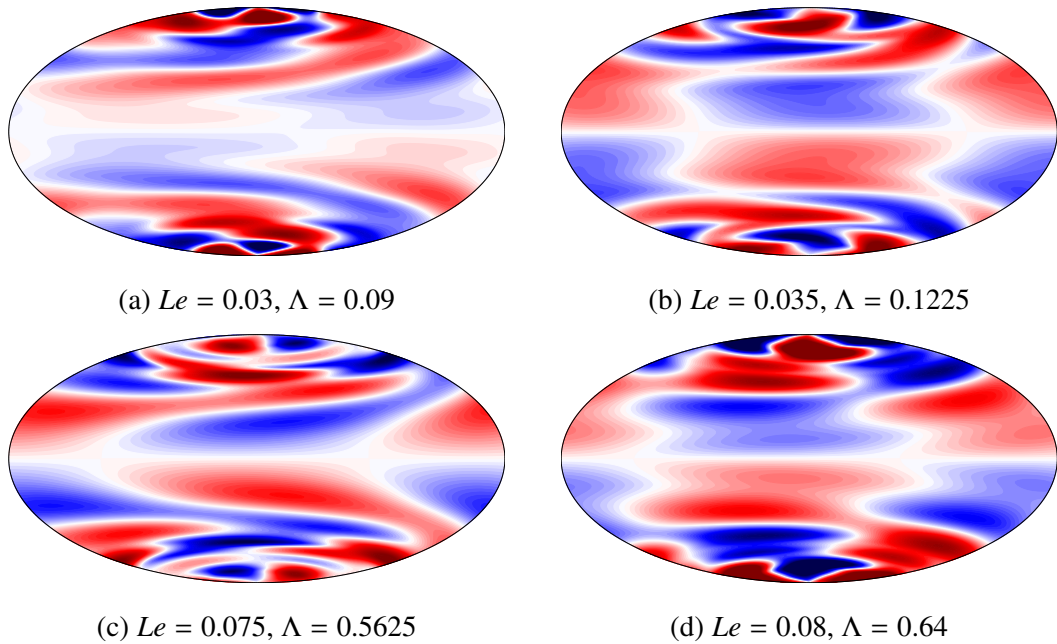


Figure 9.6: Change in the structure of the $m = 1$ EA mode with magnetic field strength. Shown here are colormaps of pressure at the outer boundary - red is positive (outwards) while blue is negative (inwards).

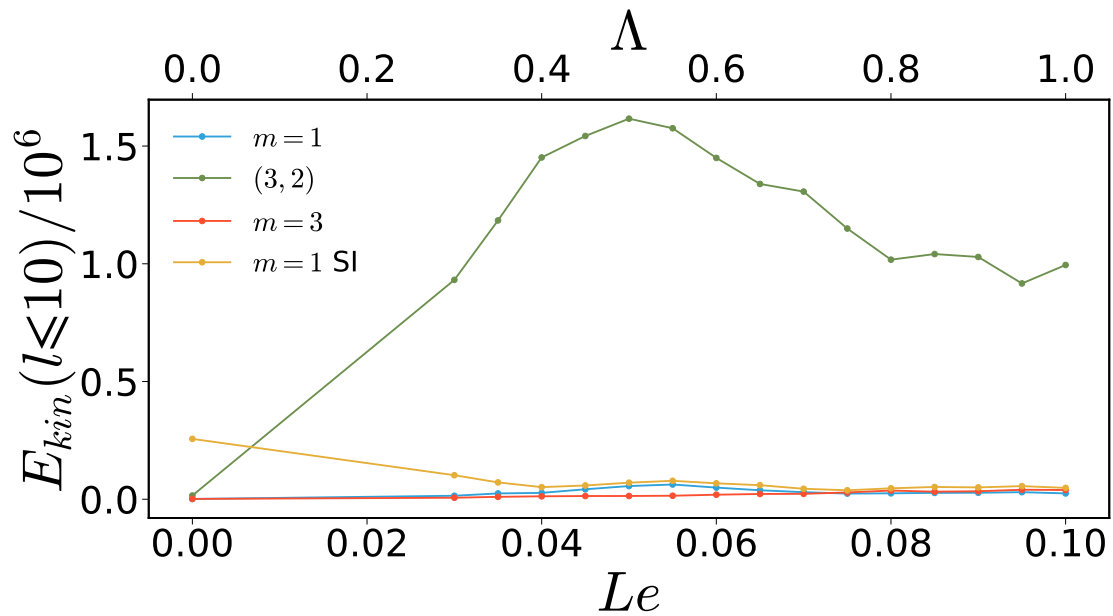


Figure 9.7: Kinetic energies (spherical harmonic expansion $l \leq 10$) of different EA modes. The (3, 2) mode is always the dominant mode.

antisymmetric. The effect is stronger for a stronger magnetic field.

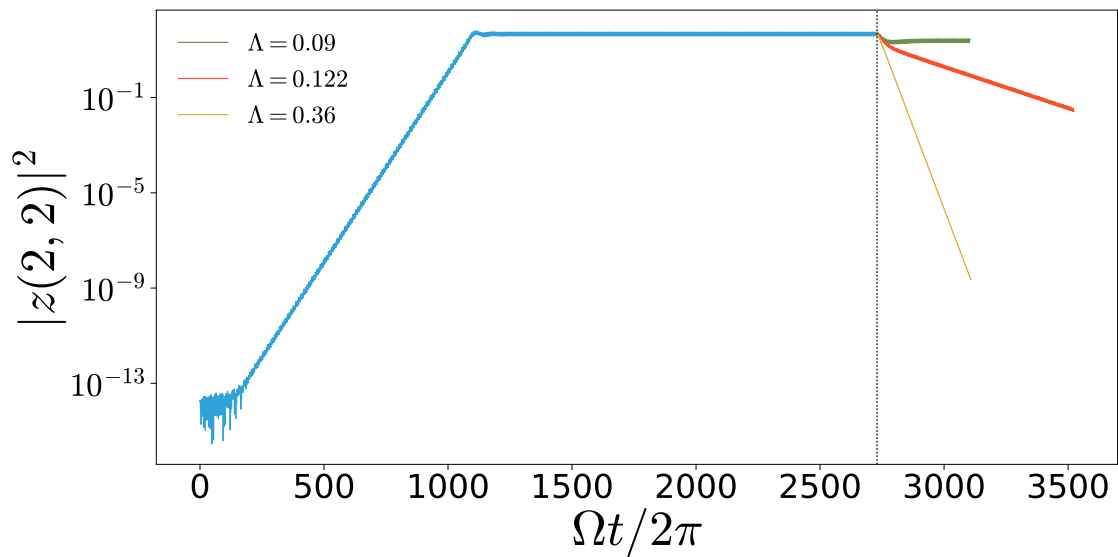


Figure 9.8: Quenching of EA modes by magnetic field. Shown on the y-axis is the squared amplitude of the toroidal (2, 2) coefficient - an indication of the energy in the (3, 2) mode. $Le = 0.03, 0.035$ and 0.06 . The time when the magnetic field is imposed is indicated by the vertical dashed line.

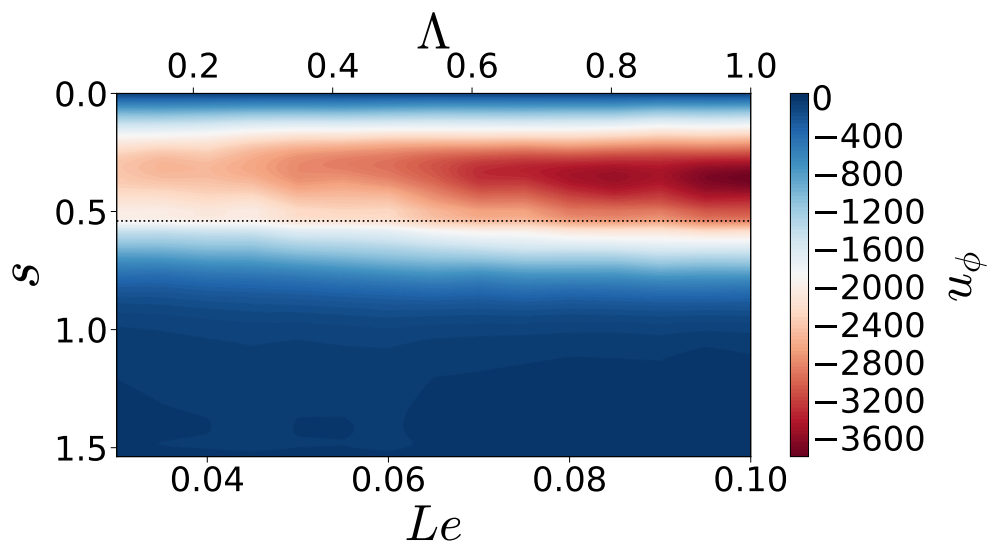


Figure 9.9: z -averaged zonal velocity u_ϕ profiles as a function of magnetic field strength. The y-axis shows cylindrical radius s . Horizontal dotted line marks the position of the tangent cylinder.

9.5 Flow and torque

Figure 9.9 shows the change in background flow profile as the magnetic field strength is increased. The fluid outside the tangent cylinder remains in solid body rotation with the

outer boundary. However, the fluid inside the tangent cylinder spins up as the magnetic field strength is increased. This is possibly due to an electromagnetic coupling of the fluid through the magnetic field lines, adding to the viscous coupling that exists in the absence of the magnetic field. Such an increase in fluid rotation rate was also noted by [Hollerbach \(1997\)](#) for the case of a finitely conducting inner sphere.

Figure 9.10 shows that as the magnetic field strength is increased, the torque on the inner sphere goes down. This shows that even though the fluid inside the tangent cylinder is spun up, the efficiency of angular momentum transport reduces. The spinning up of the fluid inside the tangent cylinder leads to an increase in the kinetic energy of the fluid, as illustrated in figure 9.10b. The increase in flow speeds has two effects - (i) it increases the strength of the induced field through the induction term in the induction equation leading to enhanced ohmic dissipation and (ii) it leads to an enhanced viscous dissipation. These are shown in figure 9.10c. These results are similar to those found by [Hollerbach \(1997\)](#), but for a conducting inner sphere.

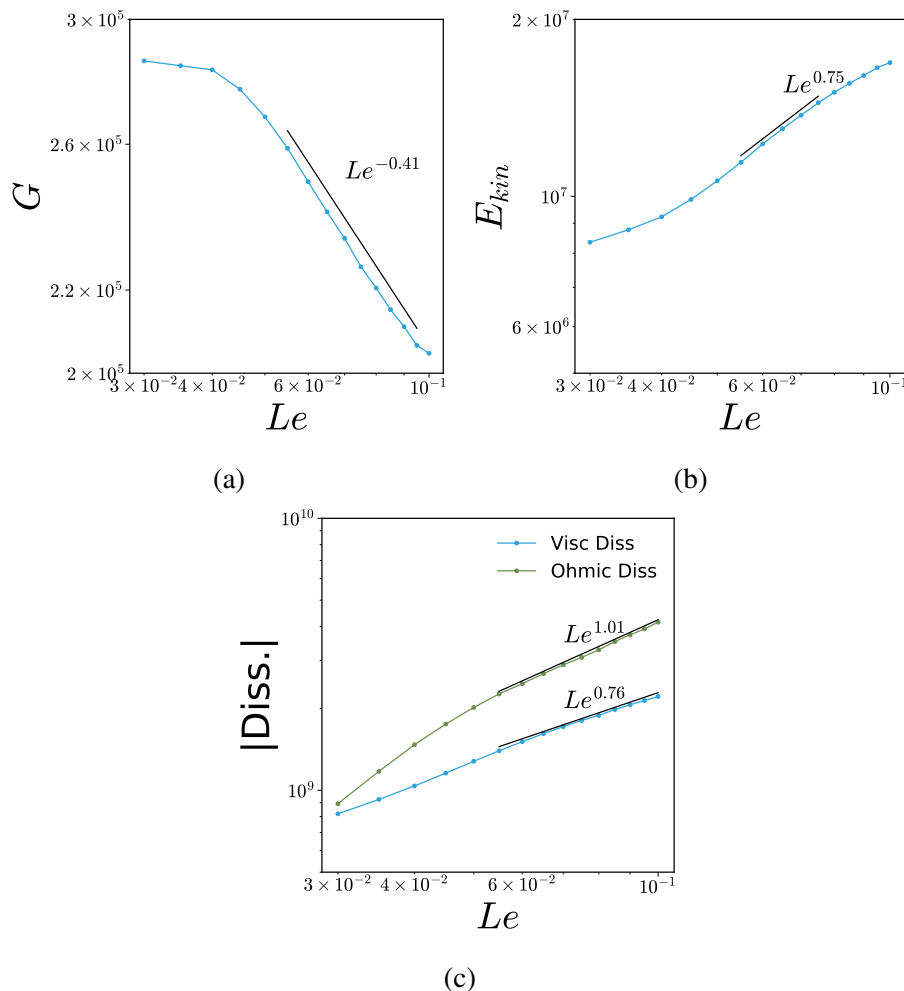


Figure 9.10: (a) shows the variation of torque G on the inner sphere with Le , (b) shows the variation of kinetic energy and (c) shows ohmic and viscous dissipation versus Le . Black lines show straight line fits.

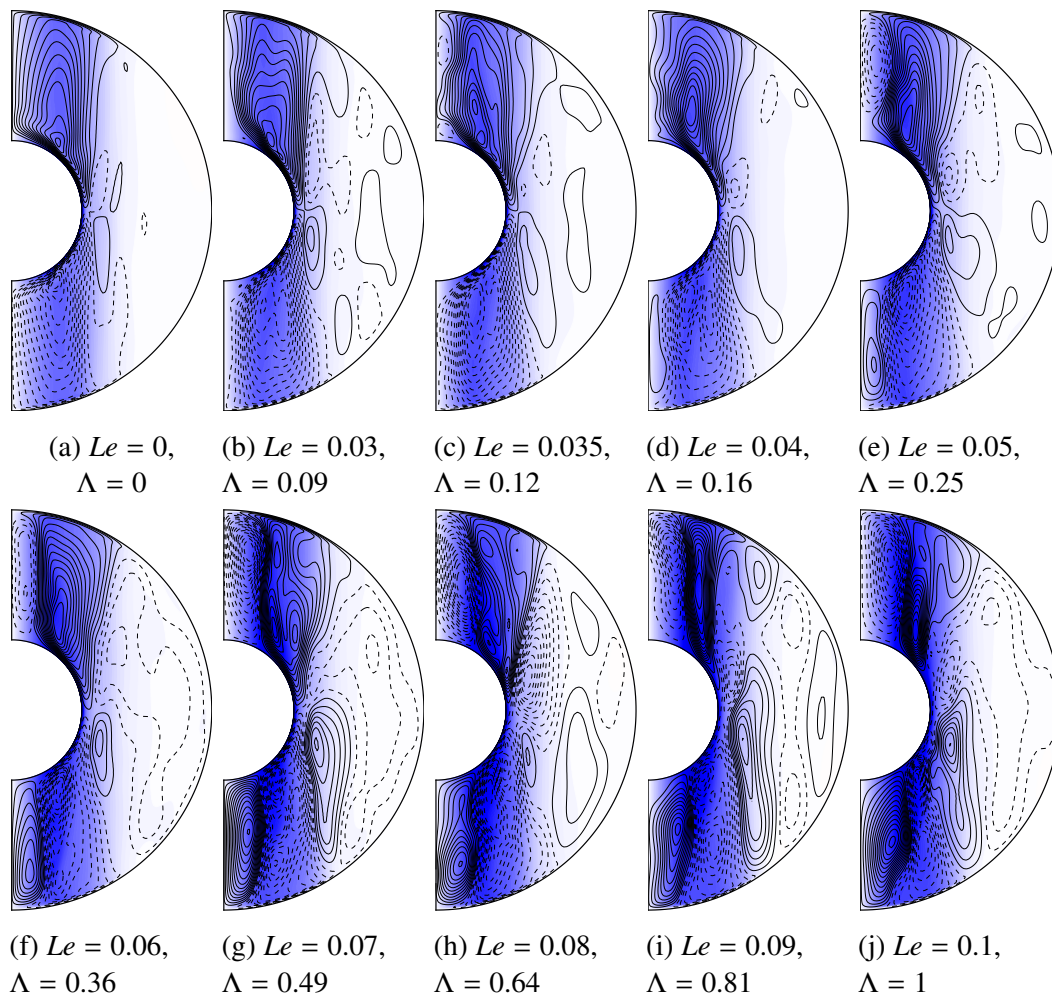


Figure 9.11: Change in axisymmetric flow structure. Colour shows azimuthal average of zonal velocity u_ϕ with blue indicating a retrograde flow and lines show meridional circulation - dotted lines being anti-clockwise and solid lines clockwise.

Figure 9.11 shows azimuthally averaged zonal velocity and the meridional circulation at different magnetic field strengths. Around $Le = 0.05$, secondary circulation cells start to develop close to the rotation axis and stay as a dominant flow structure thereafter. A tendency of the flow to get aligned with the rotation axis is seen at high field strengths. The meridional circulation structure is very similar to that observed at high magnetic field strengths by [Tilgner \(1999b\)](#) for a precessing flow under the influence of a magnetic field.

9.6 Discussion

We found new and intriguing effects of an externally imposed axial magnetic field on inertial modes in a spherical Couette setup. We started initially with a weak field and compared it with diagnostics from experiments of [Kelley et al. \(2007\)](#), finding excellent agreements. Thereafter we increased the magnetic field magnitude to explore magnetic

modifications of the inertial modes. It was seen that the growth rate of the fast EA inertial modes increases by more than an order of magnitude even in the presence of a magnetic field which is not very strong ($Le = 0.03$) and is achievable in experiments. Around $Le = 0.035$, the EA modes with $m = 1$ and $m = 3$ were modified quite heavily both in terms of frequency and structure while the $(3, 2)$ mode was only slightly modified in frequency and not modified at all in structure. The largest magnetic field that can be achieved in the 3-metre experiments corresponds to $\Lambda = 14.4$ (table 1 in [Zimmerman et al. 2014](#)). Taking typical experimental Ekman number $E = 10^{-8}$ and $Pm = 10^{-6}$ for liquid sodium, one ends up with $Le = 0.38$. For the 60 cm experiment at Maryland, USA, this would vary between $Le = 0.01$ and $Le = 0.18$ depending on the rotation rate (using data from [Kelley et al. 2007](#)). Thus, frequency and structure of the inertial modes observed in these experiments could be modified quite heavily by the magnetic field, depending on the mode being identified. We also saw that whether the growth of an EA mode would be promoted or suppressed by the magnetic field depends on when the magnetic field is imposed. An EA mode which onsets purely hydrodynamically is suppressed by an imposed axial magnetic field, while the growth and saturation for the same mode is promoted when the mode onsets in the presence of the magnetic field.

The magnetic field also introduces other effects such as spinning up of the fluid and newly formed circulation cells inside the tangent cylinder. This leads to an increase in the flow kinetic energy as well as enhanced viscous dissipation. At high magnetic field strengths ($Le \leq 0.1$ in our simulations), the flow structures show a tendency to get aligned with the rotation axis.

Though several interesting effects of a magnetic field were observed, their physical explanations still remain to be answered. One could start by exploring force balances in space and time of the various cases, in particular investigating the interactions of the Lorentz and the Coriolis forces, and exploring similar effects at other parameters where such fast EA inertial modes are observed.

10 Conclusions and Outlook

“Wir müssen wissen - wir werden wissen!”
(We must know - we will know!)

David Hilbert

Brief summary of results

In this study, we used direct numerical simulations (DNS) with an aim of studying a several aspects of a differentially rotating fluid in a spherical shell. The motivation for studying such a system was two fold. The first being the fact that the interiors of planets and stars consist of fluid layers in rotating spherical shells, and thus, an understanding of the fluid dynamics of such a system would provide insights into the interiors of these astrophysical objects. Secondly, there are experiments, both hydro- and magneto-hydrodynamic, which use this setup with the aforementioned motivation, but with limited diagnostics. Direct numerical simulations of the setup could help confirm experimental observations and provide a better understanding of the fluid and MHD instabilities taking place inside the experiments. This is especially true for liquid sodium experiments in opaque containers where the fluid is not even visible. DNS have the advantage of having access to specific modes of flow and magnetic fields as well as to values of all variables and forces at each individual grid point. An insight of such depth is not possible with experimental investigations.

We began by exploring the case when the outer boundary is stationary (chapter 5). As the inner boundary rotation rate is increased, a radial jet starts to emerge after a certain rotation rate. The width of this jet as well as the torque on the inner sphere was scaled with the Reynolds number of the flow at the equator of the inner boundary (Re_i). Both scalings agreed well with past studies of a rotating sphere in an unbounded fluid as well as with experiments of [Sorokin et al. \(1966\)](#) for a spherical Couette flow.

For the case of a rapidly rotating outer boundary, we ran simulations for both senses of differential rotation, but with different objectives. For positive differential rotation, we attempted to reproduce the the torque bistability observed in the water experiments of [Zimmerman \(2010\)](#). For negative differential rotation, we performed a close comparison of the transition into different hydrodynamic regimes with the experiments of [Hoff et al. \(2016b\)](#), with the aim of answering the long standing open question of the onset of fast equatorially antisymmetric (EA) inertial modes in the spherical Couette system ([Kelley et al. 2010](#), [Rieutord et al. 2012](#)).

For positive differential rotation (chapter 5), we found some similarities with [Zimmerman \(2010\)](#) in the temporal spectra of the torque when comparing a transient high torque state with a low torque state in steady state. The flow solutions showed that the low torque state has a region of fast rotating fluid close to the tangent cylinder, as envisaged by [Zimmerman \(2010\)](#) and that the zonal velocity profile looks more flat in the high torque state. The question that we could not answer was how a cyclic disintegration and rebuilding of such a flow might take place. Simulations at a faster outer boundary rotation rates might be turbulent enough to achieve a torque bistability as observed in the experiments and help bridge the gap in parameters.

Varying differential rotation in a negative sense (chapters 6 - 7), excellent agreements were found between the hydrodynamic regimes and the fast EA inertial modes observed in the simulations and those observed in the experiments of [Hoff et al. \(2016b\)](#). This work was carried out in collaboration with Santiago Triana from the Royal Observatory of Belgium and Michael Hoff from BTU C-S. The observed fast equatorially antisymmetric (EA) modes also corresponded well with those from experiments at Maryland, USA ([Kelley et al. 2007](#), [Triana 2011](#)), especially for faster outer boundary rotation rates. Using an artificial excitation and numerical truncation experiments we were able to conclude two key points. First, the background flow heavily modifies the inertial modes and can explain departures of their frequencies and structures from theoretical eigenmodes of a full sphere or spherical shell. Second, the equatorially symmetric (ES) instabilities that set in before the onset of the fast EA modes are not necessary for their onset, indicating that the fast EA modes might onset due to an instability of the axisymmetric background flow. However the ES instabilities play a role in selecting which modes onset in the system. This study helped provide clues towards answering the question of onset of EA inertial modes by differential rotation.

After increasing the differential rotation magnitude in a negative sense, the temporal spectrum of the flow was seen to become broadband at a very sharp and well-defined critical differential rotation rate. A study of this ‘turbulent regime’ was performed in chapter 7 with two goals in mind - characterising the flow in this regime and investigating the mechanism of transition to turbulence. In both the inertial mode regime as well as this ‘turbulent’ regime, we found a sharp decay of the temporal spectrum beyond 2Ω where Ω is the rotation rate of the outer boundary. The decay was better pronounced in the turbulent regime. This decay has been seen in experiments as well ([Triana 2011](#), [Hoff et al. 2016b](#)) and indicates that the energy exchanges in the turbulent flow must be occurring through interactions of inertial waves which can only have frequencies till 2Ω . The spatial energy spectra indicated that the inertial mode regime is in a state of weak inertial-wave turbulence ([Galtier 2003](#)), which eventually transitions to a state of homogeneous and isotropic turbulence with an energy spectrum given by [Kolmogorov \(1941a,b\)](#) and [Obukhov \(1941\)](#). The transition takes place exactly when the time-average of the mean squared value of the inertial term in our simulations matches that of the Coriolis term, indicating that it is a competition between the eddy turnover time-scale and the inertial wave time scale, similar to the concept of a Zeman scale in turbulence ([Zeman 1994](#)). What was thought to be a sharp transition to turbulence is in fact a transition from rotation dominated turbulence to a more homogeneous and isotropic turbulence. Since, periodic features remain in the flow even in the isotropic turbulent regime, the [Landau \(1944b\)](#) mechanism of the transition to turbulence seems to be favoured as compared to

the mechanism of [Ruelle and Takens \(1971\)](#). This is in contrast to what has been found in the past for a Taylor-Couette flow ([Gollub and Swinney 1975](#)). This study provided a lot of insights into the turbulent state of the spherical Couette system.

Chapter 8 introduced some fundamentals of magnetohydrodynamics which was necessary to understand chapter 9 where I imposed an external axial magnetic field on the spherical Couette setup with the aim of verifying the experimental diagnostics of [Kelley et al. \(2007\)](#) as well as understanding the effect of a strong magnetic field on the EA inertial modes. For a weak magnetic field, I found excellent agreements with the findings of [Kelley et al. \(2007\)](#). For a strong field, however, I observed some intriguing results which have never been reported before. I found that imposing a magnetic field during the onset of an EA mode increased its growth rate by more than an order of magnitude. While for some modes it had a very mild effect on the frequency and structure, for others it had a more profound effect with one mode being replaced by another of the same azimuthal and equatorial symmetry. In addition, I found that the fluid differential rotation increases inside the tangent cylinder as the magnetic field strength is increased, accompanied with a decrease in the torque on the inner sphere and an increase in the fluid kinetic energy and ohmic and viscous dissipation. With a strong magnetic field, the background flow structures tended to align with the rotation axis. These results show that a magnetic field can increase the growth rate of an EA inertial mode and might influence it heavily depending on the type of mode excited.

Conclusions

We see that the spherical Couette system provides us with a plethora of intriguing fluid dynamic and MHD phenomena. One curious aspect of the system is the formation of triadic resonances of inertial modes. At all outer boundary rotation and differential rotation rates we explored, pairs of fast EA modes formed a triadic resonance with the fundamental $m = 1$ instability. This was also shown to be true for the 3-metre experiment where the flow was in a much more turbulent state. Nonlinear interaction with the background flow and between different modes is the only pathway of exchange of energy available in this system. This can be easily tested by turning off the nonlinear term in the simulations, whence all modes decay away except for the axisymmetric background flow. Being the only mechanism of energy exchange, the system chooses to be in a state where this mechanism acts most efficiently, leading to resonances. Even though we found in chapter 6 that the equatorially symmetric modes are not necessary for the onset of an EA mode, their role in mode selection comes from the criteria for triadic resonances. Once a dominant EA mode has onset, only those inertial modes can onset which form a triadic resonance with the dominant EA mode and the existing equatorially symmetric instability. Triadic resonances between inertial waves are crucial for energy exchanges among various scales in the turbulent regime, as was shown in chapter 7.

In the regime of homogeneous and isotropic turbulence, we found the onset of an equatorially symmetric mode which could not be explained. Such columnar structures have been predicted by studies in rotational turbulence (e.g. [Davidson et al. 2006](#)) under the assumption that the influence of rotation on the flow is strong, which we showed was not the case as the spatial spectra resembled the classical Kolmogorov spectrum for homogeneous and isotropic turbulence. This has also been seen in the 3-metre experiment

where a single strong signal corresponding to an inertial mode was observed in the most turbulent state of the flow. This mode was not accompanied by any other modes and thus, did not form triads. In chapter 9, we saw that in the presence of a magnetic field, the inertial modes were amplified, modified and no longer formed triads.

Though inertial modes are classically thought to be excited due to external oscillatory mechanisms (precession, libration, tidal excitation, [Le Bars et al. 2015](#)), we showed that an instability of the background flow by differential rotation can also trigger them. The magnitude of differential rotation required to trigger the onset of these modes decreases with an increase in the outer boundary rotation. Thus, for real astrophysical objects, where the Coriolis force plays a much larger role in the dynamics, the differential rotation required for the onset of these modes would be a very small fraction of the outer boundary rotation rate. The same can be said about the critical differential rotation required for the transition to a homogeneous and isotropic turbulent regime. Inertial modes have been observed in the Earth ([Aldridge and Lumb 1987](#)) as well as in stars as inertia-gravity modes (e.g. [Neiner et al. 2012](#), [Pápics et al. 2012](#)) and can be effective in transporting angular momentum (e.g. [Rogers et al. 2013](#)). Especially in the presence of a magnetic field, we found that the onset of an EA mode due to differential rotation was enhanced. Thus, the presence of these modes is quite likely in astrophysical objects.

In figure 10.1, we plot all the available data from our simulations and experiments at BTU C-S and try to scale the various hydrodynamic regimes to extreme parameters of astrophysical objects. One of the objects chosen is a B-type main sequence star KIC 10526294 where part of the envelope is estimated to be counter rotating ([Triana et al. 2015](#)). The Earth where the core is supposed to be co-rotating ([Song 2000](#), [Tkalčić et al. 2013](#)), is also plotted on the same plot as our simulations and experiments for a perspective. One can think of it as plotting a terrestrial planet with the same rotation rate as the Earth but where the inner core counter rotates at the same rate as the estimates for Earth. Though such a linear extrapolation is a gross oversimplification, it tells us that the star KIC 10526294 might be in a state of homogeneous and isotropic turbulence, while the Earth-like planet might have a Stewartson layer instability.

Outlook

This study found new and intriguing results about the spherical Couette system while opening up doors to new questions. For example, though we found that the fast EA inertial modes can onset due to instabilities of the axisymmetric background flow, we do not know what determines the growth rate of the EA modes, especially in the presence of other instabilities. In addition, we found that the boundaries of the hydrodynamic regimes depend on the outer boundary rotation rate. Performing simulations with several different outer boundary rotation rates would provide a better answer towards how these regime boundaries scale with the outer boundary rotation rate, thus enabling us to extrapolate our findings to real astrophysical objects.

In our simulations, the regime of broadband turbulence was only investigated for one outer boundary rotation rate. We saw that a criteria for transition from rotation dominated turbulence to homogeneous and isotropic turbulence was an exact match between the eddy turnover time-scale and the inertial wave time-scale. This criteria needs to be verified for other outer boundary rotation rates to test if what we observed is a mere coincidence. The

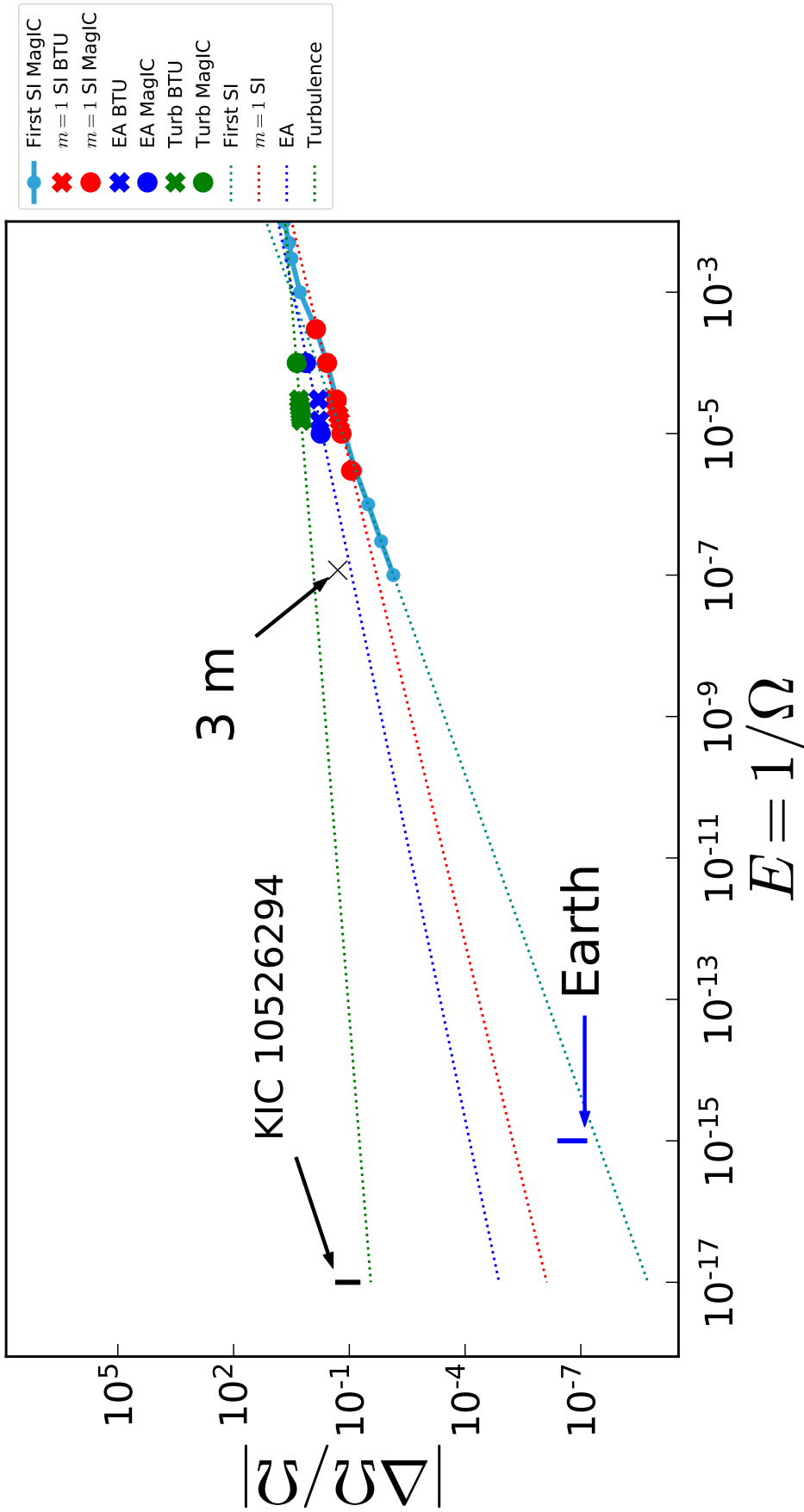


Figure 10.1: Scaling different regime boundaries to extreme parameters of astrophysical objects. Dotted lines are straight line fits to symbols of the same color. Crosses are experimental data for regime onsets from BTU Cottbus-Senfenberg, while filled circles are data from MagIC simulations. KIC 10526294 is a B-type main sequence star and the data for its rotation rate and differential rotation is based on [Triana et al. \(2015\)](#). Data for its differential rotation magnitude is based on estimates due to [Song \(2000\)](#), [Tkalić et al. \(2013\)](#). Data for the 3-metre experiment from Santiago Triana. Abbreviations: SI - onset of Stewartson layer Instability, EA - onset of equatorially antisymmetric fast inertial modes, Turb - onset of temporal broadband turbulence.

experiments of [Hoff et al. \(2016b\)](#) obtained a scaling law of $Ro_c \propto E^{1/5}$ for the critical differential rotation rate for transition to the isotropic turbulent regime. However, this law was obtained over a small range of outer boundary rotation rates. This law could be tested with simulations at other rotation rates of the outer boundary as well. In addition, different hydrodynamic regime boundaries may also exist in terms of outer boundary rotation and not just differential rotation which is worth exploring if one wants to infer something about real astrophysical objects.

The imposed magnetic field left us with several open questions. It is curious as to why the magnetic field leads to such a drastic change in the growth rate of the EA modes when one would expect it to try to align fluid motions along the axis. Even more intriguing is the fact that the expected behaviour is found when the magnetic field is imposed after the EA modes have set in, whereby it quenches the modes. This in turn gets us back to the question that we do not understand the reason for the growth rates of these EA modes, even in the purely hydrodynamic case. The change in mode frequency and structure due to the magnetic field was also not understood. These are completely new results not reported or explored before.

The possibilities of future work with this setup are endless. One could start by building on the present study and trying to answer some of the open questions by further studies of hydrodynamic regimes at different outer boundary rotation rates. The artificial excitation of inertial modes used in this study can be further used to perform a detailed study of the nonlinear interactions of background flow and an inertial mode, or nonlinear interactions of different user-defined inertial modes. Another interesting aspect would be the effect of an imposed axial magnetic field on EA inertial modes which has only been briefly explored here and is a completely new territory. Other completely unexplored territories are stable stratification of the fluid inside and taking into account fluid compressibility. These could have direct applications to stars, especially with regards to magnetic field interactions and angular momentum transport.

Ongoing and planned studies building on this work include a systematic study of parameter variations outer and inner boundary rotation rates as well as imposed magnetic field strengths. Though a lot of past work has been done in this regard, they have mostly focussed on either a stationary outer boundary ([Hollerbach and Skinner 2001](#)) or a fixed ratio of inner to outer boundary rotation ([Gissinger et al. 2011](#)). Another ongoing study is on spherical Couette dynamos which could have possible applications to stellar radiative zones. There have only been two such studies in this regard ([Guervilly and Cardin 2010](#), [Cao et al. 2012](#)) in a limited parameter space and an expanded parameter regime is waiting to be explored.

Bibliography

- Adams, M. (2016). *Magnetic and acoustic investigations of turbulent spherical flow*. PhD thesis, University of Maryland, College Park.
- Aerts, C., Christensen-Dalsgaard, J., and Kurtz, D. W. (2010). *Asteroseismology*. Springer Science & Business Media.
- Aldridge, K., Seyed-Mahmoud, B., Henderson, G., and van Wijngaarden, W. (1997). Elliptical instability of the Earth's fluid core. *Physics of the Earth and Planetary Interiors*, 103:365–374.
- Aldridge, K. D. (1967). *An experimental study of axisymmetric inertial oscillations of a rotating liquid sphere*. PhD thesis, Massachusetts Institute of Technology.
- Aldridge, K. D. and Lumb, L. I. (1987). Inertial waves identified in the earth's fluid outer core. *Nature*, 325:421–423.
- Alfvén, H. (1942). Existence of Electromagnetic-Hydrodynamic Waves. *Nature*, 150:405–406.
- Aubert, J., Finlay, C. C., and Fournier, A. (2013). Bottom-up control of geomagnetic secular variation by the earth's inner core. *Nature*, 502(7470):219–223. Letter.
- Aubert, J., Gastine, T., and Fournier, A. (2017). Spherical convective dynamos in the rapidly rotating asymptotic regime. *Journal of Fluid Mechanics*, 813:558–593.
- Ayachit, U. (2015). *The ParaView Guide: A Parallel Visualization Application*. Kitware, Inc., USA.
- Backus, G. (1958). A class of self-sustaining dissipative spherical dynamos. *Annals of Physics*, 4(4):372 – 447.
- Balbus, S. A. and Hawley, J. F. (1998). Instability, turbulence, and enhanced transport in accretion disks. *Reviews of modern physics*, 70(1):1.
- Banks, W. H. H. (1965). The boundary layer on a rotating sphere. *The Quarterly Journal of Mechanics and Applied Mathematics*, 18(4):443–454.
- Baroud, C. N., Plapp, B. B., Swinney, H. L., and She, Z.-S. (2003). Scaling in three-dimensional and quasi-two-dimensional rotating turbulent flows. *Physics of Fluids*, 15(8):2091–2104.

- Baruteau, C. and Rieutord, M. (2013). Inertial waves in a differentially rotating spherical shell. *Journal of Fluid Mechanics*, 719:47–81.
- Batchelor, G. K. (1969). Computation of the energy spectrum in homogeneous two-dimensional turbulence. *The Physics of Fluids*, 12(12):II–233.
- Bellan, P. M. (2008). *Fundamentals of Plasma Physics*. Cambridge University Press.
- Bethe, H. A. (1939). Energy production in stars. *Physical Review*, 55(5):434.
- Biermann, L. (1932). Untersuchungen über den inneren aufbau der sterne. iv. konvektion-zonen im innern der sterne.(veröffentlichungen der universitäts-sterne-warte göttingen, nr. 27.) mit 5 abbildungen. *Zeitschrift für Astrophysik*, 5:117.
- Bjerknes, V., Bjerknes, J., Solberg, H., and Bergeron, T. (1933). *Physikalische Hydrodynamik*. Springer-Verlag Berlin Heidelberg.
- Boisson, J. and Dubrulle, B. (2011). Three-dimensional magnetic field reconstruction in the vks experiment through galerkin transforms. *New Journal of Physics*, 13(2):023037.
- Bondi, H. and Lyttleton, R. A. (1953). On the dynamical theory of the rotation of the earth. II. The effect of precession on the motion of the liquid core. *Proceedings of the Cambridge Philosophical Society*, 49:498.
- Borucki, W. J., Koch, D., Basri, G., Brown, T., Caldwell, D., Devore, E., Dunham, E., Gautier, T., Geary, J., Gilliland, R., Gould, A., Howell, S., and Jenkins, J. (2003). Kepler Mission: a mission to find Earth-size planets in the habitable zone. In Fridlund, M., Henning, T., and Lacoste, H., editors, *Earths: DARWIN/TPF and the Search for Extrasolar Terrestrial Planets*, volume 539 of *ESA Special Publication*, pages 69–81.
- Bourgoin, M., Marié, L., Pétrélis, F., Gasquet, C., Guigon, A., Luciani, J.-B., Moulin, M., Namer, F., Burguete, J., Chiffaudel, A., Daviaud, F., Fauve, S., Odier, P., and Pinton, J.-F. (2002). Magnetohydrodynamics measurements in the von kármán sodium experiment. *Physics of Fluids (1994-present)*, 14(9):3046–3058.
- Bowden, F. P. and Lord, R. G. (1963). The aerodynamic resistance to a sphere rotating at high speed. *Proceedings of the Royal Society of London A: Mathematical, Physical and Engineering Sciences*, 271(1345):143–153.
- Braginsky, S. I. (1984). Short-period geomagnetic secular variation. *Geophysical & Astrophysical Fluid Dynamics*, 30(1-2):1–78.
- Braginsky, S. I. (1993). Mac-oscillations of the hidden ocean of the core. *Journal of geomagnetism and geoelectricity*, 45(11-12):1517–1538.
- Braginsky, S. I. and Roberts, P. H. (1995). Equations governing convection in earth’s core and the geodynamo. *Geophysical and Astrophysical Fluid Dynamics*, 79:1–97.
- Braithwaite, J. (2006). A differential rotation driven dynamo in a stably stratified star. *A&A*, 449(2):451–460.

- Braithwaite, J. and Spruit, H. C. (2015). Magnetic fields in non-convective regions of stars. *ArXiv e-prints*.
- Bratukhin, I. (1961). On the evaluation of the critical Reynolds number for the flow of fluid between two rotating spherical surfaces. *Journal of Applied Mathematics and Mechanics*, 25(5):1286 – 1299.
- Brito, D., Alboussiere, T., Cardin, P., Gagniere, N., Jault, D., La Rizza, P., Masson, J.-P., Nataf, H.-C., and Schmitt, D. (2011). Zonal shear and super-rotation in a magnetized spherical Couette-flow experiment. *Physical Review E*, 83(6):066310.
- Brown, T. M., Latham, D. W., Everett, M. E., and Esquerdo, G. A. (2011). Kepler Input Catalog: Photometric Calibration and Stellar Classification. *AJ*, 142:112.
- Bryan, G. H. (1889). The waves on a rotating liquid spheroid of finite ellipticity. *Philosophical Transactions of the Royal Society of London A: Mathematical, Physical and Engineering Sciences*, 180:187–219.
- Buffett, B. (2012). Earth science: Geomagnetism under scrutiny. *Nature*, 485(7398):319–320.
- Buffett, B. (2014). Geomagnetic fluctuations reveal stable stratification at the top of the earth's core. *Nature*, 507(7493):484–487. Letter.
- Buffett, B. A. and Seagle, C. T. (2010). Stratification of the top of the core due to chemical interactions with the mantle. *Journal of Geophysical Research: Solid Earth*, 115(B4):n/a–n/a. B04407.
- Bullard, E. and Gellman, H. (1954). Homogeneous dynamos and terrestrial magnetism. *Philosophical Transactions of the Royal Society of London Series A*, 247:213–278.
- Bullard, E. C. (1949). The magnetic field within the Earth. *Proceedings of the Royal Society of London Series A*, 197:433–453.
- Bullard, E. C., Freedman, C., Gellman, H., and Nixon, J. (1950). The westward drift of the Earth's magnetic field. *Philosophical Transactions of the Royal Society of London Series A*, 243:67–92.
- Busse, F. H. (1968). Shear flow instabilities in rotating systems. *Journal of Fluid Mechanics*, 33:577–589.
- Cantiello, M., Mankovich, C., Bildsten, L., Christensen-Dalsgaard, J., and Paxton, B. (2014). Angular momentum transport within evolved low-mass stars. *The Astrophysical Journal*, 788(1):93.
- Cao, H., Russell, C. T., Wicht, J., Christensen, U. R., and Dougherty, M. K. (2012). Saturn's high degree magnetic moments: Evidence for a unique planetary dynamo. *Icarus*, 221(1):388 – 394.
- Cardin, P. and Olson, P. (2007). 8.11 - experiments on core dynamics. In Schubert, G., editor, *Treatise on Geophysics*, pages 319 – 343. Elsevier, Amsterdam.

- Cartan, E. (1922). Sur les petites oscillations d'une masse fluide. *Bulletin des Sciences Mathématiques*, 46:317–352 and 356–369.
- Cébron, D., Le Bars, M., Moutou, C., and Le Gal, P. (2012a). Elliptical instability in terrestrial planets and moons. *A&A*, 539:A78.
- Cébron, D., Le Bars, M., Noir, J., and Aurnou, J. M. (2012b). Libration driven elliptical instability. *Physics of Fluids*, 24(6):061703.
- Chandrasekhar, S. (1939). *An introduction to the study of stellar structure*. Chicago, Ill., The University of Chicago press [1939].
- Charbonneau, P. and Steiner, O. (2012). *Solar and Stellar Dynamos: Saas-Fee Advanced Course 39 Swiss Society for Astrophysics and Astronomy*. Saas-Fee Advanced Course. Springer Berlin Heidelberg.
- Chen, Q., Chen, S., Eyink, G. L., and Holm, D. D. (2005). Resonant interactions in rotating homogeneous three-dimensional turbulence. *Journal of Fluid Mechanics*, 542:139–164.
- Chossat, P. and Iooss, G. (1994). *The Couette-Taylor Problem*, volume 102 of *Applied Mathematical Sciences*. Springer New York.
- Christensen, U. and Wicht, J. (2007). 8.08 - numerical dynamo simulations. In Schubert, G., editor, *Treatise on Geophysics*, pages 245 – 282. Elsevier, Amsterdam.
- Christensen, U. R. (2006). A deep dynamo generating mercury's magnetic field. *Nature*, 444(7122):1056–1058.
- Christensen, U. R. (2015). Iron snow dynamo models for ganymede. *Icarus*, 247:248 – 259.
- Clark di Leoni, P., Cobelli, P. J., and Mininni, P. D. (2015). The spatio-temporal spectrum of turbulent flows. *The European Physical Journal E*, 38(12):136.
- Cooper, C. M., Wallace, J., Brookhart, M., Clark, M., Collins, C., Ding, W. X., Flanagan, K., Khalzov, I., Li, Y., Milhone, J., Nornberg, M., Nonn, P., Weisberg, D., Whyte, D. G., Zweibel, E., and Forest, C. B. (2014). The Madison plasma dynamo experiment: A facility for studying laboratory plasma astrophysics. *Physics of Plasmas*, 21(1):013505.
- Courant, R., Friedrichs, K., and Lewy, H. (1928). Über die partiellen Differenzgleichungen der mathematischen Physik. *Mathematische Annalen*, 100:32–74.
- Cowling, T. G. (1933). The magnetic field of sunspots. *MNRAS*, 94:39–48.
- Cowling, T. G. (1934). The stability of gaseous stars. *Monthly Notices of the Royal Astronomical Society*, 94:768–782.
- Cowling, T. G. (1957). The dynamo maintenance of steady magnetic fields. *The Quarterly Journal of Mechanics and Applied Mathematics*, 10(1):129.

- Craik, A. D. D. (1989). The stability of unbounded two- and three-dimensional flows subject to body forces - Some exact solutions. *Journal of Fluid Mechanics*, 198:275–292.
- Davidson, P. (2013). *Turbulence in Rotating, Stratified and Electrically Conducting Fluids*. Cambridge University Press.
- Davidson, P. A. (2001). *An introduction to magnetohydrodynamics*, volume 25. Cambridge university press.
- Davidson, P. A., Staplehurst, P. J., and Dalziel, S. B. (2006). On the evolution of eddies in a rapidly rotating system. *Journal of Fluid Mechanics*, 557:135–144.
- Dennis, S., Ingham, D., and Singh, S. (1981). The steady flow of a viscous fluid due to a rotating sphere. *Quarterly Journal of Mechanics and Applied Mathematics*, 34(3):361–381.
- Dietrich, W. and Wicht, J. (2013). A hemispherical dynamo model: Implications for the martian crustal magnetization. *Physics of the Earth and Planetary Interiors*, 217:10 – 21.
- Domingo, V., Fleck, B., and Poland, A. I. (1995). SOHO: The Solar and Heliospheric Observatory. *Space Sci. Rev.*, 72:81–84.
- Dormy, E., Cardin, P., and Jault, D. (1998). Mhd flow in a slightly differentially rotating spherical shell, with conducting inner core, in a dipolar magnetic field. *Earth and Planetary Science Letters*, 160(1–2):15 – 30.
- Dudley, M. L. and James, R. W. (1989). Time-dependent kinematic dynamos with stationary flows. *Proceedings of the Royal Society of London A: Mathematical, Physical and Engineering Sciences*, 425(1869):407–429.
- Duran-Matute, M., Flór, J.-B., Godefert, F. S., and Jause-Labert, C. (2013). Turbulence and columnar vortex formation through inertial-wave focusing. *Physical Review E*, 87(4):041001.
- Eddington, A. S. (1920). The internal constitution of the stars. *Science*, 52(1341):233–240.
- Egbers, C. and Rath, H. (1995). The existence of Taylor vortices and wide-gap instabilities in spherical Couette flow. *Acta Mechanica*, 111(3-4):125–140.
- Ekman, V. W. et al. (1905). On the influence of the earth's rotation on ocean-currents.
- Elsasser, W. M. (1939). Origin of the Earth's Magnetic Field. *Nature*, 143:374–375.
- Elsasser, W. M. (1946). Induction Effects in Terrestrial Magnetism Part II. The Secular Variation. *Physical Review*, 70:202–212.
- Elsasser, W. M. (1950). The Earth's Interior and Geomagnetism. *Reviews of Modern Physics*, 22:1–35.

- Emden, R. (1907). *Gaskugeln: anwendungen der mechanischen wärmetheorie auf kosmologische und meteorologische probleme*. Gaskugeln: Anwendungen der mechanischen wärmetheorie auf kosmologische und meteorologische probleme. B. Teubner.
- Ferraro, V. C. A. (1937). The non-uniform rotation of the sun and its magnetic field. *Monthly Notices of the Royal Astronomical Society*, 97:458.
- Figueroa, A., Schaeffer, N., Nataf, H.-C., and Schmitt, D. (2013). Modes and instabilities in magnetized spherical couette flow. *Journal of Fluid Mechanics*, 716:445–469.
- Finke, K. and Tilgner, A. (2012). Simulations of the kinematic dynamo onset of spherical couette flows with smooth and rough boundaries. *Phys. Rev. E*, 86:016310.
- Finlay, C. C. (2008). Course 8 waves in the presence of magnetic fields, rotation and convection. In Cardin, P. and Cugliandolo, L., editors, *Dynamos*, volume 88 of *Les Houches*, pages 403 – 450. Elsevier.
- Finlay, C. C. and Jackson, A. (2003). Equatorially dominated magnetic field change at the surface of earth's core. *Science*, 300(5628):2084–2086.
- Fox, J. (1964). *Boundary layers on rotating spheres and other axisymmetric shapes*. National Aeronautics and Space Administration.
- Frisch, U. (1995). *Turbulence: The Legacy of A. N. Kolmogorov*. Cambridge University Press.
- Früh, W.-G. and Read, P. L. (1999). Experiments on a barotropic rotating shear layer. part 1. instability and steady vortices. *Journal of Fluid Mechanics*, 383:143–173.
- Fuller, J., Lecoanet, D., Cantiello, M., and Brown, B. (2014). Angular momentum transport via internal gravity waves in evolving stars. *The Astrophysical Journal*, 796(1):17.
- Fultz, D. (1959). A note on overstability and the elastoid-inertia oscillations of kelvin, solberg, and bjerknes. *Journal of Meteorology*, 16(2):199–208.
- Gailitis, A., Lielausis, O., Dement'ev, S., Platacis, E., Cifersons, A., Gerbeth, G., Gundrum, T., Stefani, F., Christen, M., Hänel, H., and Will, G. (2000). Detection of a flow induced magnetic field eigenmode in the riga dynamo facility. *Phys. Rev. Lett.*, 84:4365–4368.
- Gailitis, A., Lielausis, O., Platacis, E., Gerbeth, G., and Stefani, F. (2002). *Colloquium* : Laboratory experiments on hydromagnetic dynamos. *Rev. Mod. Phys.*, 74:973–990.
- Galtier, S. (2003). Weak inertial-wave turbulence theory. *Physical Review E*, 68(1):015301.
- Gastine, T., Wicht, J., Duarte, L. D. V., Heimpel, M., and Becker, A. (2014). Explaining jupiter's magnetic field and equatorial jet dynamics. *Geophysical Research Letters*, 41(15):5410–5419.

- Ghasemi V, A., Klein, M., Harlander, U., Kurgansky, M. V., Schaller, E., and Will, A. (2016). Mean flow generation by görtler vortices in a rotating annulus with librating side walls. *Physics of Fluids*, 28(5):056603.
- Gilbert, W. (1600). *De Magnete, magneticisque corporibus, et de magno magnete tellure: Physiologia nova, plurimis & argumentis, & experimentis demonstrata*. London.
- Gissinger, C., Ji, H., and Goodman, J. (2011). Instabilities in magnetized spherical couette flow. *Phys. Rev. E*, 84:026308.
- Glatzmaier, G. A., Coe, R. S., Hongre, L., and Roberts, P. H. (1999). The role of the Earth's mantle in controlling the frequency of geomagnetic reversals. *Nature*, 401:885–890.
- Glatzmaier, G. A. and Roberts, P. H. (1995). A three-dimensional self-consistent computer simulation of a geomagnetic field reversal. *Nature*, 377(6546):203–209.
- Glatzmaier, G. A. and Roberts, P. H. (1996). Rotation and magnetism of earth's inner core. *Science*, 274(5294):1887–1891.
- Gollub, J. P. and Swinney, H. L. (1975). Onset of turbulence in a rotating fluid. *Physical Review Letters*, 35(14):927.
- Görtler, H. (1955). Dreidimensionales zur stabilitätstheorie laminarer grenzsichten. *ZAMM*, 35:326.
- Grannan, A. M., Le Bars, M., Cébron, D., and Aurnou, J. M. (2014). Experimental study of global-scale turbulence in a librating ellipsoid. *Physics of Fluids*, 26(12):126601.
- Greenspan, H. (1968). *The Theory of Rotating Fluids*. Cambridge University Press.
- Greenspan, H. P. (1964). On the transient motion of a contained rotating fluid. *Journal of Fluid Mechanics*, 20(4):673–696.
- Greenspan, H. P. (1965). On the general theory of contained rotating fluid motions. *Journal of Fluid Mechanics*, 22(3):449–462.
- Gubbins, D. and Zhang, K. (1993). Symmetry properties of the dynamo equations for palaeomagnetism and geomagnetism. *Physics of the Earth and Planetary Interiors*, 75:225–241.
- Guervilly, C. and Cardin, P. (2010). Numerical simulations of dynamos generated in spherical Couette flows. *Geophysical and Astrophysical Fluid Dynamics*, 104:221–248.
- Gutenberg, B. (1912). Ueber erdbebenwellen. vii a. beobachtungen an registrierungen von fernbeben in göttingen und folgerung über die konstitution des erdkörpers. *Nachrichten von der Gesellschaft der Wissenschaften zu Göttingen, Mathematisch-Physikalische Klasse*, pages 125 – 176. read 1912, published 1914.

- Haberman, W. L. (1962). Secondary flow about a sphere rotating in a viscous liquid inside a coaxially rotating spherical container. *Physics of Fluids*, 5(5):625–626.
- Hale, G. E. (1908). On the Probable Existence of a Magnetic Field in Sun-Spots. *The Astrophysical Journal*, 28:315.
- Halley, E. (1683). A theory of the variation of the magnetical compass. *Philosophical Transactions of the Royal Society of London*, 13:208 – 221.
- Herzenberg, A. (1958). Geomagnetic dynamos. *Philosophical Transactions of the Royal Society of London A: Mathematical, Physical and Engineering Sciences*, 250(986):543–583.
- Hide, R. (1966). Free hydromagnetic oscillations of the earth's core and the theory of the geomagnetic secular variation. *Philosophical Transactions of the Royal Society of London A: Mathematical, Physical and Engineering Sciences*, 259(1107):615–647.
- Hide, R. and Titman, C. W. (1967). Detached shear layers in a rotating fluid. *Journal of Fluid Mechanics*, 29:39–60.
- Hoff, M., Harlander, U., Egbers, C., and Triana, S. A. (2016a). Interagierende trägheitsmoden in einem differenziell rotierenden kugelspaltexperiment. In Egbers, C., Ruck, B., Leder, A., and Dopheide, D., editors, *Proceedings der 24. GALA-Fachtagung "Experimentelle Strömungsmechanik"*, pages 12–1 – 12–8. GALA e.V. (German Association for Laser Anemometry).
- Hoff, M., Harlander, U., and Triana, S. A. (2016b). Study of turbulence and interacting inertial modes in a differentially rotating spherical shell experiment. *Phys. Rev. Fluids*, 1:043701.
- Hollerbach, R. (1994). Magnetohydrodynamic ekman and stewartson layers in a rotating spherical shell. *Proceedings of the Royal Society of London A: Mathematical, Physical and Engineering Sciences*, 444(1921):333–346.
- Hollerbach, R. (1997). The influence of an axial field on magnetohydrodynamic ekman and stewartson layers, in the presence of a finitely conducting inner core. *Acta Astron. et Geophys. Univ. Cornenianae XIX*, 263:275.
- Hollerbach, R. (2000). *Magnetohydrodynamic flows in spherical shells*, pages 295–316. Springer Berlin Heidelberg, Berlin, Heidelberg.
- Hollerbach, R. (2001). Super- and counter-rotating jets and vortices in strongly magnetic spherical couette flow. In *Dynamo and Dynamics, a Mathematical Challenge*, pages 189–197. Springer.
- Hollerbach, R. (2003). Instabilities of the stewartson layer part 1. the dependence on the sign of ro . *Journal of Fluid Mechanics*, 492:289–302.
- Hollerbach, R. (2009). Non-axisymmetric instabilities in magnetic spherical couette flow. *Proceedings of the Royal Society of London A: Mathematical, Physical and Engineering Sciences*, 465(2107):2003–2013.

- Hollerbach, R., Futterer, B., More, T., and Egbers, C. (2004). Instabilities of the Stewartson layer part 2. supercritical mode transitions. *Theoretical and Computational Fluid Dynamics*, 18(2):197–204.
- Hollerbach, R., Junk, M., and Egbers, C. (2006). Non-axisymmetric instabilities in basic state spherical Couette flow. *Fluid Dynamics Research*, 38(4):257 – 273.
- Hollerbach, R. and Kerswell, R. R. (1995). Oscillatory internal shear layers in rotating and precessing flows. *Journal of Fluid Mechanics*, 298:327–339.
- Hollerbach, R. and Skinner, S. (2001). Instabilities of magnetically induced shear layers and jets. *Proceedings of the Royal Society of London A: Mathematical, Physical and Engineering Sciences*, 457(2008):785–802.
- Hori, K., Jones, C. A., and Teed, R. J. (2015). Slow magnetic Rossby waves in the Earth's core. *Geophys. Res. Lett.*, 42:6622–6629.
- Hough, S. S. (1897). On the application of harmonic analysis to the dynamical theory of the tides. part i. on Laplace's "oscillations of the first species," and on the dynamics of ocean currents. *Philosophical Transactions of the Royal Society of London A: Mathematical, Physical and Engineering Sciences*, 189:201–257.
- Howarth, L. (1951). Cxxix. note on the boundary layer on a rotating sphere. *The London, Edinburgh, and Dublin Philosophical Magazine and Journal of Science*, 42(334):1308–1315.
- Hunter, J. D. (2007). Matplotlib: A 2d graphics environment. *Computing In Science & Engineering*, 9(3):90–95.
- Ingham, D. (1969). Magnetohydrodynamic flow in a container. *The Physics of Fluids*, 12(2):389–396.
- Jeffreys, H. (1926). The rigidity of the earth's central core. *Geophysical Supplements to the Monthly Notices of the Royal Astronomical Society*, 1(7):371.
- Jones, C. A. (2008). Course 2 dynamo theory. In Cardin, P. and Cugliandolo, L., editors, *Dynamos*, volume 88 of *Les Houches*, pages 45 – 135. Elsevier.
- Jouve, L., Gastine, T., and Lignières, F. (2015). Three-dimensional evolution of magnetic fields in a differentially rotating stellar radiative zone. *A&A*, 575:A106.
- Kageyama, A. and Sato, T. (1995). Computer simulation of a magnetohydrodynamic dynamo. ii. *Physics of Plasmas*, 2(5):1421–1431.
- Kelley, D. H. (2009). *Rotating, Hydromagnetic Laboratory Experiment Modelling Planetary Cores*. PhD thesis, University of Maryland, College Park.
- Kelley, D. H., Triana, S. A., Zimmerman, D. S., and Lathrop, D. P. (2010). Selection of inertial modes in spherical Couette flow. *Phys. Rev. E*, 81:026311.

- Kelley, D. H., Triana, S. A., Zimmerman, D. S., Tilgner, A., and Lathrop, D. P. (2007). Inertial waves driven by differential rotation in a planetary geometry. *Geophysical & Astrophysical Fluid Dynamics*, 101(5-6):469–487.
- Kelvin, L. (1862). On the age of the sun's heat. *Macmillan's Magazine*.
- Kerswell, R. R. (1993). The instability of precessing flow. *Geophysical & Astrophysical Fluid Dynamics*, 72(1-4):107–144.
- Kerswell, R. R. (1995). On the internal shear layers spawned by the critical regions in oscillatory Ekman boundary layers. *Journal of Fluid Mechanics*, 298:311–325.
- Kerswell, R. R. (2002). Elliptical instability. *Annual Review of Fluid Mechanics*, 34:83–113.
- Kerswell, R. R. and Malkus, W. V. R. (1998). Tidal instability as the source for Io's magnetic signature. *Geophys. Res. Lett.*, 25:603–606.
- Kippenhahn, R. and Weigert, A. (1990). *Stellar structure and evolution*. Astronomy and astrophysics library. Springer.
- Kleeorin, N., Rogachevskii, I., Ruzmaikin, A., Soward, A., and Starchenko, S. (1997). Axisymmetric flow between differentially rotating spheres in a dipole magnetic field. *Journal of Fluid Mechanics*, 344:213–244.
- Koch, S., Harlander, U., Egbers, C., and Hollerbach, R. (2013). Inertial waves in a spherical shell induced by librations of the inner sphere: experimental and numerical results. *Fluid Dynamics Research*, 45(3):035504.
- Kolmogorov, A. N. (1941a). Dissipation of Energy in Locally Isotropic Turbulence. *Akademiia Nauk SSSR Doklady*, 32:16.
- Kolmogorov, A. N. (1941b). The Local Structure of Turbulence in Incompressible Viscous Fluid for Very Large Reynolds' Numbers. *Akademiia Nauk SSSR Doklady*, 30:301–305.
- Kraichnan, R. H. (1967). Inertial ranges in two-dimensional turbulence. *The Physics of Fluids*, 10(7):1417–1423.
- Kudlick, M. D. (1966). *On transient motions in a contained, rotating fluid*. PhD thesis, Massachusetts Institute of Technology.
- Kumar, S. and Roberts, P. H. (1975). A three-dimensional kinematic dynamo. *Proceedings of the Royal Society of London A: Mathematical, Physical and Engineering Sciences*, 344(1637):235–258.
- Lacaze, L., Le Gal, P., and Le Dizès, S. (2004). Elliptical instability in a rotating spheroid. *Journal of Fluid Mechanics*, 505:1–22.
- Lacaze, L., Le Gal, P., and Le Dizès, S. (2005). Elliptical instability of the flow in a rotating shell. *Physics of the Earth and Planetary Interiors*, 151:194–205.

- Landau, L. (1944a). A new exact solution of the navier-stokes equations. *Dokl. Akad. Nauk SSSR*, 43(7):299–301.
- Landau, L. D. (1944b). On the problem of turbulence. *Dokl. Akad. Nauk SSSR*, 44(8):339–349.
- Lane, H. J. (1870). On the theoretical temperature of the sun, under the hypothesis of a gaseous mass maintaining its volume by its internal heat, and depending on the laws of gases as known to terrestrial experiment. *American Journal of Science*, Series 2 Vol. 50(148):57–74.
- Larmor, J. (1919). How could a rotating body such as the sun become a magnet? *Report of the British Association for the Advancement of Science*, 87th Meeting:159–160.
- Lathrop, D. P., Fineberg, J., and Swinney, H. L. (1992). Turbulent flow between concentric rotating cylinders at large reynolds number. *Physical review letters*, 68(10):1515.
- Lathrop, D. P. and Forest, C. B. (2011). Magnetic dynamos in the lab. *Physics Today*, 64(7):40–45.
- Le Bars, M., Cébron, D., and Le Gal, P. (2015). Flows driven by libration, precession, and tides. *Annual Review of Fluid Mechanics*, 47(1):163–193.
- Le Bars, M., Lacaze, L., Le Dizès, S., Le Gal, P., and Rieutord, M. (2010). Tidal instability in stellar and planetary binary systems. *Physics of the Earth and Planetary Interiors*, 178:48–55.
- Le Bars, M., Le Dizès, S., and Le Gal, P. (2007). Coriolis effects on the elliptical instability in cylindrical and spherical rotating containers. *Journal of Fluid Mechanics*, 585:323.
- Lehmann, I. (1936). P'. *Publications du Bureau central séismologique internationale. Série A: Travaux scientifiques*, 14:87 – 115.
- Leith, C. E. (1968). Diffusion approximation for two-dimensional turbulence. *The Physics of Fluids*, 11(3):671–672.
- Lighthill, M. and Lighthill, J. (2001). *Waves in Fluids*. Cambridge Mathematical Library. Cambridge University Press.
- Longuet-Higgins, M. S. (1964). Planetary Waves on a Rotating Sphere. *Proceedings of the Royal Society of London Series A*, 279:446–473.
- Longuet-Higgins, M. S. (1965). Planetary Waves on a Rotating Sphere. II. *Proceedings of the Royal Society of London Series A*, 284:40–68.
- Longuet-Higgins, M. S. (1968). The Eigenfunctions of Laplace's Tidal Equations over a Sphere. *Philosophical Transactions of the Royal Society of London Series A*, 262:511–607.

- Lortz, D. (1968). Exact solutions of the hydromagnetic dynamo problem. *Plasma Physics*, 10(11):967.
- Maas, L. R. M. (2001). Wave focusing and ensuing mean flow due to symmetry breaking in rotating fluids. *Journal of Fluid Mechanics*, 437:13–28.
- Maas, L. R. M. (2005). Wave Attractors: Linear yet Nonlinear. *International Journal of Bifurcation and Chaos*, 15:2757–2782.
- Maeder, A. (2008). *Physics, formation and evolution of rotating stars*. Springer Science & Business Media.
- Maeder, A. and Meynet, G. (2000). The Evolution of Rotating Stars. *ARA&A*, 38:143–190.
- Maeder, A. and Meynet, G. (2004). Stellar evolution with rotation and magnetic fields-ii. general equations for the transport by tayler-spruit dynamo. *Astronomy & Astrophysics*, 422(1):225–237.
- Maeder, A. and Meynet, G. (2005). Stellar evolution with rotation and magnetic fields-iii. the interplay of circulation and dynamo. *Astronomy & Astrophysics*, 440(3):1041–1049.
- Maeder, A., Meynet, G., Lagarde, N., and Charbonnel, C. (2013). The thermohaline, richardson, rayleigh-taylor, solberg–høiland, and gsf criteria in rotating stars. *A & A*, 553:A1.
- Malkus, W. V. R. (1967). Hydromagnetic planetary waves. *Journal of Fluid Mechanics*, 28(04):793–802.
- Malkus, W. V. R. (1968). Precession of the earth as the cause of geomagnetism. *Science*, 160(3825):259–264.
- Manglik, A., Wicht, J., and Christensen, U. R. (2010). A dynamo model with double diffusive convection for mercury’s core. *Earth and Planetary Science Letters*, 289(3–4):619 – 628.
- Manohar, R. (1967). The boundary layer on a rotating sphere. *Zeitschrift für angewandte Mathematik und Physik ZAMP*, 18(3):320–330.
- MATLAB (2017). *Release 2017a*. The MathWorks Inc., Natick, Massachusetts.
- Matsui, H., Adams, M., Kelley, D., Triana, S., Zimmerman, D., Buffett, B., and Lathrop, D. (2011). Numerical and experimental investigation of shear-driven inertial oscillations in an earth-like geometry. *Physics of the Earth and Planetary Interiors*, 188(3–4):194 – 202. Proceedings of the 12th Symposium of {SEDI}.
- Mautino, A. (2016). *Inverse spectral methods in acoustic normal mode velocimetry of high Reynolds number spherical couette flows*. PhD thesis, University of Maryland, College Park.

- McComas, C. H. and Bretherton, F. P. (1977). Resonant interaction of oceanic internal waves. *Journal of Geophysical Research*, 82(9):1397–1412.
- Meynet, G. and Maeder, A. (2003). Stellar evolution with rotation and magnetic fields. *Astronomy and astrophysics: A European journal*, 411(3):543–552.
- Milbury, C., Schubert, G., Raymond, C. A., Smrekar, S. E., and Langlais, B. (2012). The history of mars’ dynamo as revealed by modeling magnetic anomalies near tyrrhenus mons and syrtis major. *Journal of Geophysical Research: Planets*, 117(E10):n/a–n/a. E10007.
- Monnereau, M., Calvet, M., Margerin, L., and Souriau, A. (2010). Lopsided growth of earth’s inner core. *Science*, 328(5981):1014–1017.
- Morize, C., Le Bars, M., Le Gal, P., and Tilgner, A. (2010). Experimental determination of zonal winds driven by tides. *Physical review letters*, 104(21):214501.
- Munson, B. R. and Joseph, D. D. (1971a). Viscous incompressible flow between concentric rotating spheres. part 1. basic flow. *Journal of Fluid Mechanics*, 49:289–303.
- Munson, B. R. and Joseph, D. D. (1971b). Viscous incompressible flow between concentric rotating spheres. part 2. hydrodynamic stability. *Journal of Fluid Mechanics*, 49:305–318.
- Munson, B. R. and Menguturk, M. (1975). Viscous incompressible flow between concentric rotating spheres. part 3. linear stability and experiments. *Journal of Fluid Mechanics*, 69:705–719.
- Nataf, H.-C. and Gagnière, N. (2008). On the peculiar nature of turbulence in planetary dynamos. *Comptes Rendus Physique*, 9(7):702 – 710.
- Nazarenko, S. (2011). *Wave Turbulence*. Lecture Notes in Physics. Springer Berlin Heidelberg.
- Neiner, C., Floquet, M., Samadi, R., Espinosa Lara, F., Frémat, Y., Mathis, S., Leroy, B., de Batz, B., Rainer, M., Poretti, E., Mathias, P., Guarro Fló, J., Buil, C., Ribeiro, J., Alecian, E., Andrade, L., Briquet, M., Diago, P. D., Emilio, M., Fabregat, J., Gutiérrez-Soto, J., Hubert, A.-M., Janot-Pacheco, E., Martayan, C., Semaan, T., Suso, J., and Zorec, J. (2012). Stochastic gravito-inertial modes discovered by CoRoT in the hot Be star HD 51452. *A&A*, 546:A47.
- Nikias, C. L. and Raghuveer, M. R. (1987). Bispectrum estimation: A digital signal processing framework. *Proceedings of the IEEE*, 75(7):869–891.
- Nimmo, F. (2007). 8.02 - energetics of the core. In Schubert, G., editor, *Treatise on Geophysics*, pages 31 – 65. Elsevier, Amsterdam.
- Obukhov, A. M. (1941). On the distribution of energy in the spectrum of turbulent flow. *Akademiia Nauk SSSR Doklady*, 32(1):22–24.
- Oldham, R. D. (1906). Earthquake Origins. *Nature*, 73:620–621.

- Olson, P. (2013). Experimental dynamos and the dynamics of planetary cores. *Annual Review of Earth and Planetary Sciences*, 41(1):153–181.
- Pápics, P. I., Briquet, M., Baglin, A., Poretti, E., Aerts, C., Degroote, P., Tkachenko, A., Morel, T., Zima, W., Niemczura, E., Rainer, M., Hareter, M., Baudin, F., Catala, C., Michel, E., Samadi, R., and Auvergne, M. (2012). Gravito-inertial and pressure modes detected in the B3 IV CoRoT target HD 43317. *A&A*, 542:A55.
- Parker, E. N. (1955). Hydromagnetic dynamo models. *The Astrophysical Journal*, 122:293.
- Pearson, C. E. (1967). A numerical study of the time-dependent viscous flow between two rotating spheres. *Journal of Fluid Mechanics*, 28:323–336.
- Pedlosky, J. (1987). *Geophysical fluid dynamics*. New York and Berlin, Springer-Verlag.
- Pérez, F. and Granger, B. E. (2007). IPython: a system for interactive scientific computing. *Computing in Science and Engineering*, 9(3):21–29.
- Phillips, O. M. (1963). Energy transfer in rotating fluids by reflection of inertial waves. *The Physics of Fluids*, 6(4):513–520.
- Poincaré, H. (1910). Sur la précession des corps déformables. *Bulletin Astronomique, Serie I*, 27:321–356.
- Ponomarenko, Y. B. (1973). Theory of the hydromagnetic generator. *Journal of Applied Mechanics and Technical Physics*, 14(6):775–778.
- Pope, S. (2000). *Turbulent Flows*. Cambridge University Press.
- Pozzo, M., Davies, C., Gubbins, D., and Alfe, D. (2012). Thermal and electrical conductivity of iron at earth's core conditions. *Nature*, 485(7398):355–358.
- Proudman, I. (1956). The almost-rigid rotation of viscous fluid between concentric spheres. *Journal of Fluid Mechanics*, 1:505–516.
- Proudman, J. (1916). On the motion of solids in a liquid possessing vorticity. *Proceedings of the Royal Society of London A: Mathematical, Physical and Engineering Sciences*, 92(642):408–424.
- Rabitti, A. and Maas, L. R. M. (2013). Meridional trapping and zonal propagation of inertial waves in a rotating fluid shell. *Journal of Fluid Mechanics*, 729:445–470.
- Rabitti, A. and Maas, L. R. M. (2014). Inertial wave rays in rotating spherical fluid domains. *Journal of Fluid Mechanics*, 758:621–654.
- Rayleigh, L. (1917). On the Dynamics of Revolving Fluids. *Proceedings of the Royal Society of London Series A*, 93:148–154.

- Reynolds, O. (1883). An Experimental Investigation of the Circumstances Which Determine Whether the Motion of Water Shall Be Direct or Sinuous, and of the Law of Resistance in Parallel Channels. *Philosophical Transactions of the Royal Society of London Series I*, 174:935–982.
- Rhines, P. B. (1975). Waves and turbulence on a beta-plane. *Journal of Fluid Mechanics*, 69(03):417–443.
- Ribner, H. S. (1957). Reflection, transmission, and amplification of sound by a moving medium. *The Journal of the Acoustical Society of America*, 29(4):435–441.
- Rieutord, M. (1991). Linear theory of rotating fluids using spherical harmonics part ii, time-periodic flows. *Geophysical & Astrophysical Fluid Dynamics*, 59(1-4):185–208.
- Rieutord, M., Georgeot, B., and Valdetaro, L. (2000). Wave attractors in rotating fluids: A paradigm for ill-posed cauchy problems. *Phys. Rev. Lett.*, 85:4277–4280.
- Rieutord, M., Georgeot, B., and Valdetaro, L. (2001). Inertial waves in a rotating spherical shell: attractors and asymptotic spectrum. *Journal of Fluid Mechanics*, 435:103–144.
- Rieutord, M., Triana, S. A., Zimmerman, D. S., and Lathrop, D. P. (2012). Excitation of inertial modes in an experimental spherical couette flow. *Phys. Rev. E*, 86:026304.
- Rieutord, M. and Valdetaro, L. (1997). Inertial waves in a rotating spherical shell. *Journal of Fluid Mechanics*, 341:77–99.
- Roberts, G. O. (1972a). Dynamo action of fluid motions with two-dimensional periodicity. *Philosophical Transactions of the Royal Society of London A: Mathematical, Physical and Engineering Sciences*, 271(1216):411–454.
- Roberts, P. (2007). 8.03 - theory of the geodynamo. In Schubert, G., editor, *Treatise on Geophysics*, pages 67 – 105. Elsevier, Amsterdam.
- Roberts, P. H. (1971). *Dynamo theory of geomagnetism*, pages 123 – 131. Number 28 in IAGA Bulletin. IUGG Publication Office, Paris.
- Roberts, P. H. (1972b). Kinematic dynamo models. *Philosophical Transactions of the Royal Society of London A: Mathematical, Physical and Engineering Sciences*, 272(1230):663–698.
- Roberts, P. H. and Stewartson, K. (1963). On the Stability of a Maclaurin Spheroid of Small Viscosity. *ApJ*, 137:777.
- Rogers, T. M., Lin, D. N. C., McElwaine, J. N., and Lau, H. H. B. (2013). Internal gravity waves in massive stars: Angular momentum transport. *The Astrophysical Journal*, 772(1):21.
- Rosby, C.-G. et al. (1939). Relation between variations in the intensity of the zonal circulation of the atmosphere and the displacements of the semi-permanent centers of action. *Journal of Marine Research*, 2(1):38–55.

- Rüdiger, G., Hollerbach, R., and Kitchatinov, L. L. (2013). *Magnetic processes in astrophysics: theory, simulations, experiments*. John Wiley & Sons.
- Ruelle, D. and Takens, F. (1971). On the nature of turbulence. *Communications in Mathematical Physics*, 20(3):167–192.
- Sauret, A., Cébron, D., Morize, C., and Le Bars, M. (2010). Experimental and numerical study of mean zonal flows generated by librations of a rotating spherical cavity. *Journal of Fluid Mechanics*, 662:260–268.
- Schaeffer, N. (2013). Efficient spherical harmonic transforms aimed at pseudospectral numerical simulations. *Geochemistry, Geophysics, Geosystems*, 14(3):751–758.
- Schaeffer, N. and Cardin, P. (2005). Quasigeostrophic model of the instabilities of the Stewartson layer in flat and depth-varying containers. *Physics of Fluids*, 17(10).
- Schaeffer, N., Jault, D., Nataf, H.-C., and Fournier, A. (2017). Turbulent geodynamo simulations: a leap towards earth's core. *Geophysical Journal International*, 211(1):1–29.
- Schmitt, D., Alboussière, T., Brito, D., Cardin, P., Gagnière, N., Jault, D., and Nataf, H.-C. (2008). Rotating spherical Couette flow in a dipolar magnetic field: experimental study of magneto-inertial waves. *Journal of Fluid Mechanics*, 604:175–197.
- Schmitt, D., Cardin, P., Rizza, P. L., and Nataf, H.-C. (2013). Magneto–coriolis waves in a spherical Couette flow experiment. *European Journal of Mechanics - B/Fluids*, 37:10–22.
- Schou, J., Antia, H., Basu, S., Bogart, R., Bush, R., Chitre, S., Christensen-Dalsgaard, J., Di Mauro, M., Dziembowski, W., Eff-Darwich, A., et al. (1998). Helioseismic studies of differential rotation in the solar envelope by the solar oscillations investigation using the Michelson Doppler Imager. *The Astrophysical Journal*, 505(1):390.
- Sen, A., Mininni, P. D., Rosenberg, D., and Pouquet, A. (2012). Anisotropy and nonuniversality in scaling laws of the large-scale energy spectrum in rotating turbulence. *Physical Review E*, 86(3):036319.
- Shercliff, J. (1962). Magnetohydrodynamic pipe flow part 2. high Hartmann number. *Journal of Fluid Mechanics*, 13(04):513–518.
- Singh, S. N. (1970). Laminar boundary layer on a rotating sphere. *The Physics of Fluids*, 13(10):2452–2454.
- Sisan, D. R. (2004). *Hydromagnetic turbulent instability in liquid sodium experiments*. PhD thesis, University of Maryland, College Park.
- Smith, L. M. and Waleffe, F. (1999). Transfer of energy to two-dimensional large scales in forced, rotating three-dimensional turbulence. *Physics of fluids*, 11(6):1608–1622.
- Song, X. (2000). Joint inversion for inner core rotation, inner core anisotropy, and mantle heterogeneity. *J. Geophys. Res.*, 105:7931–7943.

- Sorokin, M. P., Khlebutin, G. N., and Shaidurov, G. F. (1966). Study of the motion of a liquid between two rotating spherical surfaces. *Journal of Applied Mechanics and Technical Physics*, 7(6):73–74.
- Soward, A. and Dormy, E. (2010). Shear-layers in magnetohydrodynamic spherical Couette flow with conducting walls. *Journal of Fluid Mechanics*, 645:145–185.
- Spohn, T. (2007). 10.01 - overview. In Schubert, G., editor, *Treatise on Geophysics*, pages 1 – 26. Elsevier, Amsterdam.
- Spruit, H. C. (1999). Differential rotation and magnetic fields in stellar interiors. *A&A*, 349:189–202.
- Spruit, H. C. (2002). Dynamo action by differential rotation in a stably stratified stellar interior. *A&A*, 381:923–932.
- Spruit, H. C. (2008). Origin of neutron star magnetic fields. *AIP Conference Proceedings*, 983(1):391–398.
- Spruit, H. C. (2013). Essential Magnetohydrodynamics for Astrophysics. *ArXiv e-prints*.
- Squire, H. (1955). Radial jets. *Fifty Years of Boundary Layer Research*, pages 47–54.
- Staplehurst, P. J., Davidson, P. A., and Dalziel, S. B. (2008). Structure formation in homogeneous freely decaying rotating turbulence. *Journal of Fluid Mechanics*, 598:81–105.
- Starchenko, S. (1997). Magnetohydrodynamics of a viscous spherical layer rotating in a strong potential field. *Journal of Experimental and Theoretical Physics*, 85(6):1125–1137.
- Steenbeck, M., Krause, F., and Rädler, K.-H. (1966). Berechnung der mittleren Lorentz-Feldstärke $\bar{v} \times \mathcal{B}$ für ein elektrisch leitendes Medium in turbulenter, durch Coriolis-Kräfte beeinflusster Bewegung. *Zeitschrift Naturforschung Teil A*, 21:369.
- Stevenson, D. J. (2008). Metallic helium in massive planets. *Proceedings of the National Academy of Sciences*, 105(32):11035–11036.
- Stewartson, K. (1957). On almost rigid rotations. *Journal of Fluid Mechanics*, 3:17–26.
- Stewartson, K. (1958). On rotating laminar boundary layers. In *Grenzschichtforschung/Boundary Layer Research*, pages 59–71. Springer.
- Stewartson, K. (1966). On almost rigid rotations. part 2. *Journal of Fluid Mechanics*, 26:131–144.
- Stewartson, K. and Rickard, J. A. (1969). Pathological oscillations of a rotating fluid. *Journal of Fluid Mechanics*, 35(4):759–773.
- Stieglitz, R. and Müller, U. (2001). Experimental demonstration of a homogeneous two-scale dynamo. *Physics of Fluids (1994-present)*, 13(3):561–564.

- Stokes, G. G. (1851). On the Effect of the Internal Friction of Fluids on the Motion of Pendulums. *Transactions of the Cambridge Philosophical Society*, 9:8.
- Swami, A., Mendel, J. M., and Nikiyas, C. L. (1998). Higher-order spectral analysis toolbox. *The Mathworks, Inc.*
- Talon, S. and Charbonnel, C. (2008). Angular momentum transport by internal gravity waves. *A&A*, 482(2):597–605.
- Taylor, G. I. (1917). Motion of solids in fluids when the flow is not irrotational. *Proceedings of the Royal Society of London A: Mathematical, Physical and Engineering Sciences*, 93(648):99–113.
- Taylor, G. I. (1938). The spectrum of turbulence. *Proceedings of the Royal Society of London A: Mathematical, Physical and Engineering Sciences*, 164(919):476–490.
- Tennekes, H. and Lumley, J. (1972). *A First Course in Turbulence*. Pe Men Book Company.
- Tilgner, A. (1999a). Driven inertial oscillations in spherical shells. *Phys. Rev. E*, 59:1789–1794.
- Tilgner, A. (1999b). Magnetohydrodynamic flow in precessing spherical shells. *Journal of Fluid Mechanics*, 379:303–318.
- Tilgner, A. (2005). Precession driven dynamos. *Physics of Fluids*, 17(3):034104–034104.
- Tilgner, A. (2007a). 8.07 - rotational dynamics of the core. In Schubert, G., editor, *Treatise on Geophysics*, pages 207 – 243. Elsevier, Amsterdam.
- Tilgner, A. (2007b). Zonal wind driven by inertial modes. *Phys. Rev. Lett.*, 99:194501.
- Tkalčić, H., Young, M., Bodin, T., Ngo, S., and Sambridge, M. (2013). The shuffling rotation of the earth's inner core revealed by earthquake doublets. *Nature Geosci.*, 6(6):497–502. Article.
- Triana, S., Zimmerman, D., and Lathrop, D. (2012). Precessional states in a laboratory model of the earth's core. *Journal of Geophysical Research: Solid Earth*, 117(B4).
- Triana, S. A. (2011). *Inertial waves in a laboratory model of the Earth's core*. PhD thesis, University of Maryland, College Park.
- Triana, S. A., Moravveji, E., Pápics, P. I., Aerts, C., Kawaler, S. D., and Christensen-Dalsgaard, J. (2015). The Internal Rotation Profile of the B-type Star KIC 10526294 from Frequency Inversion of its Dipole Gravity Modes. *ApJ*, 810:16.
- van der Walt, S., Colbert, S. C., and Varoquaux, G. (2011). The numpy array: A structure for efficient numerical computation. *Computing in Science Engineering*, 13(2):22–30.
- van Heijst, G. J. F. and Kloosterziel, R. C. (1989). Tripolar vortices in a rotating fluid. *Nature*, 338(6216):569–571.

- Vanyo, J., Wilde, P., Cardin, P., and Olson, P. (1995). Experiments on precessing flows in the Earth's liquid core. *Geophysical Journal International*, 121:136–142.
- Vanyo, J. P. (1984). Earth core motions - Experiments with spheroids. *Geophysical Journal*, 77:173–183.
- Vempaty, S. and Loper, D. E. (1975). Hydromagnetic boundary layers in a rotating cylindrical container. *The Physics of Fluids*, 18(12):1678–1686.
- Vempaty, S. and Loper, D. E. (1978). Hydromagnetic free shear layers in rotating flows. *Zeitschrift für angewandte Mathematik und Physik ZAMP*, 29(3):450–461.
- Vidal, J. and Schaeffer, N. (2015). Quasi-geostrophic modes in the earth's fluid core with an outer stably stratified layer. *Geophysical Journal International*, 202(3):2182–2193.
- von Kármán, T. (1921). Über laminare und turbulente Reibung. *Zeitschrift Angewandte Mathematik und Mechanik*, 1:233–252.
- Waleffe, F. (1992). The nature of triad interactions in homogeneous turbulence. *Physics of Fluids*, 4:350–363.
- Waleffe, F. (1993). Inertial transfers in the helical decomposition. *Physics of Fluids*, 5:677–685.
- Walton, I. C. (1975). Viscous Shear Layers in an Oscillating Rotating Fluid. *Proceedings of the Royal Society of London Series A*, 344:101–110.
- Wei, X. and Hollerbach, R. (2008). Instabilities of shercliffe and stewartson layers in spherical couette flow. *Phys. Rev. E*, 78:026309.
- Wicht, J. (2002). Inner-core conductivity in numerical dynamo simulations. *Physics of the Earth and Planetary Interiors*, 132(4):281 – 302.
- Wicht, J. (2014). Flow instabilities in the wide-gap spherical couette system. *Journal of Fluid Mechanics*, 738:184–221.
- Wiechert, E. (1897). Ueber die massenvertheilung im innern der erde. *Nachrichten von der Gesellschaft der Wissenschaften zu Göttingen, Mathematisch-Physikalische Klasse*, pages 221–243.
- Wu, C.-C. and Roberts, P. H. (2013). On a dynamo driven topographically by longitudinal libration. *Geophysical & Astrophysical Fluid Dynamics*, 107(1-2):20–44.
- Yarom, E. and Sharon, E. (2014). Experimental observation of steady inertial wave turbulence in deep rotating flows. *Nature Physics*, 10(7):510–514.
- Yarom, E., Vardi, Y., and Sharon, E. (2013). Experimental quantification of inverse energy cascade in deep rotating turbulence. *Physics of Fluids*, 25(8):085105.
- Zandbergen, P. J. and Dijkstra, D. (1987). Von karman swirling flows. *Annual Review of Fluid Mechanics*, 19(1):465–491.

- Zeman, O. (1994). A note on the spectra and decay of rotating homogeneous turbulence. *Physics of Fluids*, 6(10):3221–3223.
- Zhang, K., Chan, K. H., Liao, X., and Aurnou, J. M. (2013). The non-resonant response of fluid in a rapidly rotating sphere undergoing longitudinal libration. *Journal of Fluid Mechanics*, 720:212–235.
- Zhang, K., Earnshaw, P., Liao, X., and Busse, F. H. (2001). On inertial waves in a rotating fluid sphere. *Journal of Fluid Mechanics*, 437:103–119.
- Zhang, Y. and Pedlosky, J. (2007). Triad instability of planetary rossby waves. *Journal of Physical Oceanography*, 37(8):2158–2171.
- Zimmerman, D. S. (2010). *Turbulent shear flow in a rapidly rotating spherical annulus*. PhD thesis, University of Maryland, College Park.
- Zimmerman, D. S., Triana, S. A., and Lathrop, D. P. (2011). Bi-stability in turbulent, rotating spherical couette flow. *Physics of Fluids (1994-present)*, 23(6):–.
- Zimmerman, D. S., Triana, S. A., Nataf, H.-C., and Lathrop, D. P. (2014). A turbulent, high magnetic reynolds number experimental model of earth’s core. *Journal of Geophysical Research: Solid Earth*, 119(6):4538–4557.

Sources of figures

The following list provides full sources of figures that were taken from external sources, in accordance with copyright agreements.

Figure	Source
1.1a	By Kelvinsong - Own work, CC BY-SA 3.0, https://commons.wikimedia.org/w/index.php?curid=23371669
1.1b	Illustration of the Sun By Kelvinsong - Own work, CC BY-SA 3.0, https://commons.wikimedia.org/w/index.php?curid=23966175
1.1b	Illustration of red giant by Paul G. Beck, Leuven University, Belgium
1.1c	By www.sun.org - http://www.sun.org/encyclopedia/stars , CC BY-SA 3.0, https://commons.wikimedia.org/w/index.php?curid=31093567
1.3a	Reprinted from Stieglitz, R. and Müller, U. (2001). Experimental demonstration of a homogeneous two-scale dynamo. <i>Physics of Fluids (1994-present)</i> , 13(3):561–564., with the permission of AIP Publishing. DOI: http://dx.doi.org/10.1063/1.1331315
1.3b	Reprinted figure with permission from Gailitis, A., Lielausis, O., Dement'ev, S., Platacis, E., Cifersons, A., Gerbeth, G., Gundrum, T., Stefani, F., Christen, M., Hänel, H., and Will, G. Detection of a flow induced magnetic field eigenmode in the riga dynamo facility. <i>Phys. Rev. Lett.</i> , 84:4365–4368, (2000) Copyright (2000) by the American Physical Society. Permission also obtained from Frank Stefani. DOI: https://doi.org/10.1103/PhysRevLett.84.4365
1.3c	Figure obtained from open access work Boisson, J. and Dubrulle, B. (2011). Three-dimensional magnetic field reconstruction in the VKS experiment through galerkin transforms. <i>New Journal of Physics</i> , 13(2):023037. DOI: https://doi.org/10.1088/1367-2630/13/2/023037
5.6a, 5.6b, 5.7	Reprinted from Zimmerman, D. S., Triana, S. A., and Lathrop, D. P. (2011). Bi-stability in turbulent, rotating spherical couette flow. <i>Physics of Fluids (1994-present)</i> , 23(6), with the permission of AIP Publishing. DOI: http://dx.doi.org/10.1063/1.3593465

Appendix

A Orthogonality and eigenvalues of Inertial modes

A.1 ω real and $|\omega| \leq 2$

Multiply the momentum equation (2.44a) with the complex conjugate \mathbf{Q}^\dagger and integrate over the whole volume W of the container. Doing so, we get

$$-i\omega \int_W \mathbf{Q}^\dagger \cdot \mathbf{Q} dV + 2 \int_W \mathbf{Q}^\dagger \cdot (\hat{\mathbf{z}} \times \mathbf{Q}) dV = - \int_W \mathbf{Q}^\dagger \cdot \nabla \phi dV. \quad (\text{A.1})$$

Consider the term on the RHS. Since $\nabla \cdot \mathbf{Q}^\dagger = 0$, one can write $\mathbf{Q}^\dagger \cdot \nabla \phi = \nabla \cdot (\mathbf{Q}^\dagger \phi)$ and we would get

$$\begin{aligned} \int_W \mathbf{Q}^\dagger \cdot \nabla \phi dV &= \int_W \nabla \cdot (\mathbf{Q}^\dagger \phi) dV \\ &= \int_{\partial W} \phi (\mathbf{Q}^\dagger \cdot \hat{\mathbf{n}}) dS \\ &= 0, \end{aligned} \quad (\text{A.2})$$

where we have used the divergence theorem and the boundary condition that $\mathbf{Q}^\dagger \cdot \hat{\mathbf{n}} = 0$ on the surface ∂W of the container. This term being zero, we get,

$$\begin{aligned} \omega &= -2i \frac{\int_W \mathbf{Q}^\dagger \cdot (\hat{\mathbf{z}} \times \mathbf{Q}) dV}{\int_W \mathbf{Q}^\dagger \cdot \mathbf{Q} dV} \\ &= -2i \frac{\int_W \hat{\mathbf{z}} \cdot (\mathbf{Q} \times \mathbf{Q}^\dagger) dV}{\int_W \mathbf{Q}^\dagger \cdot \mathbf{Q} dV} \\ &= 4 \frac{\int_W \hat{\mathbf{z}} \cdot (\mathbf{Q}_R \times \mathbf{Q}_I) dV}{\int_W (\mathbf{Q}_R^2 + \mathbf{Q}_I^2) dV}, \end{aligned} \quad (\text{A.3})$$

where, $\mathbf{Q} = \mathbf{Q}_R + i\mathbf{Q}_I$. Equation (A.3) proves that ω is real. Taking a closer look at the numerator,

$$\begin{aligned}
\int_W \hat{\mathbf{z}} \cdot (\mathbf{Q}_R \times \mathbf{Q}_I) dV &\leq \int_W |\mathbf{Q}_R \times \mathbf{Q}_I| dV \\
&\leq \int_W |\mathbf{Q}_R| |\mathbf{Q}_I| dV \\
&\leq \frac{1}{2} \int_W (\mathbf{Q}_R^2 + \mathbf{Q}_I^2) dV,
\end{aligned} \tag{A.4}$$

where in the last step we have used the inequality: arithmetic mean \geq geometric mean. Substituting in equation (A.3), we obtain

$$|\omega| \leq 2, \tag{A.5}$$

or, in the dimensional form,

$$|\omega| \leq 2\Omega. \tag{A.6}$$

A.2 Orthogonality

Consider two eigenmodes, \mathbf{Q}_m and \mathbf{Q}_n , associated with eigenvalues ω_m and ω_n , respectively such that $\omega_m \neq \omega_n$. Doing a similar exercise as equation (A.1), but this time, multiplying the equation for \mathbf{Q}_n with \mathbf{Q}_m^\dagger and vice-versa, one can write the following equations

$$-i\omega_n \mathbf{Q}_m^\dagger \cdot \mathbf{Q}_n + 2\mathbf{Q}_m^\dagger \cdot \hat{\mathbf{z}} \times \mathbf{Q}_n = -\mathbf{Q}_m^\dagger \cdot \nabla \Phi_n, \tag{A.7a}$$

$$i\omega_m \mathbf{Q}_n \cdot \mathbf{Q}_m^\dagger + 2\mathbf{Q}_n \cdot \hat{\mathbf{z}} \times \mathbf{Q}_m^\dagger = -\mathbf{Q}_n \cdot \nabla \Phi_m^\dagger. \tag{A.7b}$$

If we add the two equations and integrate over the volume W of the container, we would find, as before, that the terms on the RHS would vanish owing to the boundary condition $\mathbf{Q} \cdot \hat{\mathbf{n}} = 0$ on ∂W . In addition, since $\mathbf{Q}_m^\dagger \cdot (\hat{\mathbf{z}} \times \mathbf{Q}_n) = -\mathbf{Q}_n \cdot (\hat{\mathbf{z}} \times \mathbf{Q}_m^\dagger)$, the sum of the second terms on the LHS also vanishes. Thus, we are left with

$$(\omega_m - \omega_n) \int_W \mathbf{Q}_m^\dagger \cdot \mathbf{Q}_n dV = 0. \tag{A.8}$$

Since, $\omega_m - \omega_n \neq 0$, we get

$$\int_W \mathbf{Q}_m^\dagger \cdot \mathbf{Q}_n dV = 0. \tag{A.9}$$

Equation (A.9) shows that inertial modes are orthogonal.

B List of dimensionless numbers

Symbol	Name	Definition	Note
E	Ekman number	$E = \frac{\nu}{\Omega L}$	Represents importance of viscous dissipation with respect to the influence by rotation in the form of Coriolis force. Named after Ekman et al. (1905) who showed that boundary layer thickness in a rotating system scales as $E^{1/2}$.
Ro_u	flow Rossby number	$Ro_u = \frac{U}{\Omega L}$	Represents the importance of inertial advection with respect to the Coriolis force, and hence is a measure of how much the flow is influenced by rotation. Named after Carl-Gustaf Rossby and is the traditional definition of Rossby number.
Ro	Rossby number	$Ro = \frac{\Delta\Omega}{\Omega}$	Quantifies the amount of differential rotation between the inner and outer sphere in a spherical Couette flow. Used in this context by Hollerbach (2003) .
Re	Reynolds number	$Re = \frac{UL}{\nu}$	Represents the importance of inertial with respect to viscous dissipation and is the critical quantity determining transition from laminar to turbulent flow. Named after Reynolds (1883) who popularised this idea of Stokes (1851) .
Pm	Magnetic Prandtl number	$Pm = \frac{\nu}{\lambda}$	Ratio between viscous and ohmic dissipation in an MHD flow. Named after Ludwig Prandtl.
Rm	Magnetic Reynolds number	$Rm = \frac{UL}{\lambda}$	Represents the importance of advection of magnetic field with respect to diffusion.
Le	Lehnert number	$Le = \frac{B}{\Omega L \sqrt{\mu\rho}}$	Ratio of the Alfvén speed to the speed of an inertial wave

Publications

Refereed publications

(submitted) Triadic resonances in the wide-gap spherical Couette system, [A. Barik](#), S. A. Triana, M. Hoff, J. Wicht, *Journal of Fluid Mechanics*

Conference contributions

Talks

1. **(Invited)** Inertial and magneto-Coriolis modes in the spherical Couette flow, *3rd ANR IMAG-INE Meeting*, L'Institut de Recherche en Astrophysique et Planétologie (IRAP), Toulouse, France, 27 - 28 Feb, 2017
2. Hydrodynamic regimes of the spherical Couette flow, *17th MHD Days*, Max Planck Institute for Solar System Research, Göttingen, Germany, 31 Nov - 2 Dec, 2016
3. Spherical Couette Dynamos, *16th MHD Days*, Technische Universität Ilmenau, Ilmenau, Germany, 7 - 9 Dec, 2015
4. Flow instabilities in the Spherical Couette System, *19th International Couette-Taylor Workshop*, Brandenburg University of Technology, Cottbus, Germany, 22 - 24 June, 2015
5. Spherical Couette Flow: Getting closer to experiments, *International Conference on Rayleigh-Bénard Turbulence 2015*, Max Planck Institute for Dynamics and Self-Organization, Göttingen, Germany, 1 - 5 June, 2015
6. Spherical Couette Flow, *Stellar and planetary dynamos*, Georg-August-Universität Göttingen, Göttingen, Germany, 26 - 29 May, 2015
7. **(Invited)** Spherical Couette flow simulations, *Workshop on Geomagnetic Prediction*, hosted by the CIDER project, UC Berkley, Berkley, California, USA, 13 December, 2014
8. Effect of gravity environment on dynamo action in spherical shells, *15th MHD Days*, Leibniz-Institut für Astrophysik Potsdam (AIP), Potsdam, Germany, 2 - 3 December, 2014
9. **(Invited)** Flow instabilities in the wide-gap spherical Couette system, *Workshop on Geomagnetic Prediction*, hosted by the CIDER project, University of Maryland, College Park, USA, 7 - 8 July, 2014 (presented online through Adobe Connect)

Posters

1. Identification and onset of inertial modes in the wide-gap spherical Couette system, *AGU Fall Meeting*, San Francisco, USA, December 12 - 16, 2016
2. Flow Instabilities in spherical Couette Flow, *12th International School/ Symposium for Space Simulations (ISSS-12)*, Prague, Czech Republic, July 6 - 10, 2015

Acknowledgements

I would like to thank the International Max Planck Research School for Solar System Science at the University of Göttingen (IMPRS) for funding my PhD and providing me with an opportunity to complete this work.

Johannes deserves a huge thank you for taking care of me for these past years. He has been a mentor, a teacher, a guide and even a counsellor at times - calming me down whenever I seemed stressed and stressing me when I seemed too calm. He was always reassuring and talking to him always made me feel like things are going to be all right.

I would like to thank Uli and Andreas for being part of my Thesis Advisory Committee and providing valuable advice. I thank Uli for inviting me to the institute back in 2011 and giving the young me a golden opportunity to be a part of this wonderful research group - a saga that culminated in this thesis. Andreas helped me through several discussions which led to the resolution of many challenges that I faced in my research. I thank him dearly for that.

I would like to thank the past members of the group - Domenico, Rakesh, Andrea, Lucía, Wieland and Thomas who always did and are still helping me out at every step. Thomas has been a great mentor and a huge influence on my life as a researcher and a programmer.

I would like to thank Santiago and Michael who were not just collaborators but soon became good friends as well. I thank Santiago for teaching me a lot and helping me out with everything I asked. Without them, my work would have been incomplete.

Sonja - thank you for being an amazing coordinator and for the number of times I would have been in deep trouble if it weren't for you.

I thank Patricio, Jörn and Theo for going through parts of my thesis and providing valuable feedback. Patricio and Jörn, I apologise for pestering you so much.

I thank my officemates - Andrea, Benjamin, David, Domenico, Gesa, Hans and Rakesh for making the office so lively. I especially thank Andrea and Gesa for being my translators and helping me survive in Germany.

I would like to thank Fatima and Theo for inspiring me to play the guitar and making me take it up seriously (Theo: "Practice"). I thank Ati and Rénard for being my mom-friends, Emanuelle for amazing scientific discussions, Holly for being shiny and Abbey for her strong sense of care.

I thank my band who gave given me some of the best moments of my life. Abbey, Alessandro, Bastian, Chi Ju, David, Earl, Emanuelle, Fatima, Felix, Hans, Helge, Holly, Kenny, Robin, Theo - thank you all. It was a pleasure and an honour to perform with you.

My friends here at the institute have given me the best years of my life. Each and every one of them has contributed to making Göttingen feel like home and not some foreign land. If I have forgotten to mention someone, know that you all of you are close to my heart.

I would like to thank my mom and dad for all their love and sacrifices. I wouldn't be who I am today if it were not for them. Dieter and Drusilla, thank you for giving me a second family in a far away land.

Finally, thank you Anindita, my love. Thank you for being there for me all the time. Without you, this work as well as this life would be incomplete.

Curriculum vitae

Personal

Name: Ankit Barik
Date of birth: 12 November 1990
Nationality: Indian

Education

2013 – 2017 PhD studies
Research School International Max Plank Research School for Solar System Science at the University of Göttingen, Göttingen, Germany
Thesis Inertial modes, turbulence and magnetic effects in a differentially rotating spherical shell
Supervisors Dr. Johannes Wicht, Prof. Dr. Ulrich R. Christensen and Prof. Dr. Andreas Tilgner

2008 – 2013 Integrated MSc. (Hons) in Exploration Geophysics (Bachelors + Masters)
Institute Indian Institute of Technology, Kharagpur, Kharagpur, India
Thesis Effect of gravity environment on dynamo action in rotating spherical shells
Supervisors Dr. Johannes Wicht, Prof. W.K. Mohanty

Ankit Barik: Inertial modes, turbulence and magnetic effects in a differentially rotating spherical shell

The study of a fluid trapped inside a spherical shell is of fundamental interest in fluid mechanics, having given rise to numerous theoretical and experimental studies. This is also a geometric feature shared by geo- and astrophysical objects such as the interior and atmosphere of the Earth, the interiors of stars, gas giants, exoplanets and so on. Driven by these motivations, the present work builds over past studies of the spherical Couette system - two concentric differentially rotating spheres with the space in between filled with a fluid. Despite the numerous theoretical and experimental investigations, several aspects of this system still remain elusive. Examples are the origin of special instabilities called 'inertial modes', transition to turbulence and the effect of magnetic fields on inertial modes. In the first part of this work, numerical simulations are compared with experiments. The focus is mainly on the origin of inertial modes in the system which are global oscillatory modes of a rotating fluid restored by the Coriolis force. Continuing this comparison, the work then focuses on the transition to turbulence and features of the turbulent regime. Lastly, an external axial magnetic field is applied to the setup with a conducting fluid and its effect on the flow is studied with special emphasis on the effect on inertial modes and rise of a class of magneto-Coriolis modes where the restoring forces consist of the Lorentz and Coriolis forces. Some aspects are compared to observations in magnetohydrodynamic experiments.